Study of electrical interfaces for electrostatic vibration energy harvesting

Armine Karami

Ph.D THESIS REPORT

in the field of

ELECTRICAL ENGINEERING

Paris doctoral school of computer science, telecommunications and electronics

Presented by

Armine KARAMI

to obtain the grade of

Ph.D from SORBONNE UNIVERSITÉ

Thesis title :

Study of electrical interfaces for electrostatic vibration energy harvesting

Defense on May 16th, 2018

Defense committee :

Adrien Badel	Prof., *Univ. Savoie Mont-Blanc*	Reviewer
Einar Halvorsen	Prof., *Univ. College of Southeast Norway*	Reviewer
Florence Ossart	Prof., *Sorbonne Université*	Committee member
Elena Blokhina	Associate prof., *Univ. College Dublin*	Committee member
Élie Lefeuvre	Prof., *Univ. Paris-Sud*	Committee member
Konstantin Turitsyn	Associate prof., *Massachusetts Institute of Technology*	Committee member
Jérome Juillard	Prof., *CentraleSupélec*	Invited member
Philippe Basset	Associate prof., *ESIEE Paris*	Second advisor
Dimitri Galayko	Associate prof., *Sorbonne Université*	Main advisor

Acknowledgments

First and foremost, I would like to thank my thesis supervisors, Dimitri Galayko and Philippe Basset. They have become, more than advisors, great friends, and I have learned a lot from them. They have both always trusted me during all of these three and a half years. Especially, I am immensely thankful to Dimitri Galayko. I have great memories of our scientific, philosophical, or more laid back discussions. He has always encouraged me in all my initiatives and investigations, some of which were solely originating from intellectual curiosity and deviated from our main objectives. He also agreed to let me take a lot of additional courses during my Ph.D. I thank him deeply for all of that.

I would also like to thank the laboratory of computer science (LIP6) of Sorbonne Université for allowing me to conduct my research in the best conditions. I particularly thank the head of the systems-on-chip department, Marie-Minerve Louërat, for her smooth and effective handling of all material issues. I have also always felt her interest in my work on the occasions where I could discuss scientific matters with her. I must also thank Sorbonne Université for my education from my Bachelor to my Ph.D. I also have overall good memories of the teaching that I have accomplished there.

I also express my sincere acknowledgments to all of our research collaborators. In particular, I address my sincere thanks to Jérôme Juillard from CentraleSupélec and Elena Blokhina from University College Dublin. They were both very supportive and always enthusiastic to discuss scientific matters. I am also deeply grateful to all members of my defense committee. In particular, the works of Prof. Halvorsen, Prof. Turitsyn and Prof. Lefeuvre were very inspiring and were foundational to a large part of the research I accomplished during this thesis. I would like to add particular thanks to Prof. Badel and Prof. Halvorsen for agreeing to review the present manuscript.

I am also thankful to all my teachers from elementary school to university. Some of them were true mentors, sometimes without even being aware of it. I especially thank Mr. Cote, my high-school mathematics teacher, Mr. Lebel, my middle-school history teacher, and Sylvain Feruglio, for introducing me to research during my masters.

I must also thank all my colleagues. Some of them have become true friends, including Amine, and my fellow Ph.D. students: Olivier, Éric and Mohammed. I am also deeply thankful to my group of close friends. I have known most of them from early childhood, and they are as a family to me. I thank you all, Rémi, Stanislas, Philippe, Damien, Clément, Yanis, Jordan, Simon, and all others that I have met more recently. I am also extremely grateful to my parents, my sister, and to all my family across Europe, Iran or the United States, for their tremendous support during the course of my studies. Last but not least, thank you, Estelle, I love you.

Contents

Overview of this work

This document is the report of a Ph.D thesis geared towards the study of novel electrical interfaces for electrostatic vibrations energy harvesters (e-VEHs). Vibration energy harvesting (VEH) is a candidate technique to power autonomous systems of small scales, such as the nodes of a wireless sensor network. Example of potential application areas of VEH include health care or structure health monitoring.

Relying on electrostatic transducers is one of the main investigated possibility to implement VEHs. One of the major motivations for this choice is the maturity of the technologies used to fabricate the micro-electromechanical electrostatic transducers. Another advantage of electrostatic systems is the high customizability of their dynamics, which can be used in order to improve their performances in various application cases. However, this customizability comes with high complexity in the design. This complexity is due to the conjunction of the nonlinear nature of the electrostatic force, to that of the switched electrical circuits used for the conditioning of the electrostatic transducer. The numerous optimization parameters and the wide variety of specifications that can be imposed in practical applications critically call for a deep understanding of electrostatic VEH systems, in order to enable the creation of systematic design flows. This study attempts to contribute to this understanding, from the point of view of the electrical interfaces.

This manuscript starts by an introduction chapter on the general principles of electrostatic vibration energy harvesters. After a brief exposure of the context and motivations for electrostatic vibration energy harvesting, it exposes part of the knowledge base that has been built in about twenty years of research carried out by several teams in the world. The notions are exposed in a way to maximize the self-containment of the manuscript, and all material specific to the field of electrostatic VEH that is needed to understand the manuscript is in principle enclosed in this introduction. This chapter ends by a quick review of different approaches that have been proposed so far to meet some of the current challenges in electrostatic vibration energy harvesting.

The first thematic part of the manuscript is composed of chapters 2 to 5. These chapters focus on a family of electrical interfaces for electrostatic vibration energy harvesters called charge-pump conditioning circuits. In brief, these conditioning circuit have the advantage that they allow energy conversion without the need for an active synchronization with the environmental vibrations.

A more detailed presentation of these conditioning circuits is done in chapter 2. This chapter lists different charge-pump conditioning circuits that have been proposed in the literature, and that will be referenced in the three following chapters. Some of these conditioning circuits are

quantitatively analyzed in the electrical domain when this analysis was not found in the literature. The presentation is made following a unifying framework: the listed circuits are presented as belonging to a same family, which is defined following formal criteria in the beginning of the chapter. In particular, the presented charge-pump conditioning circuits are split into two main subclasses, namely stable and unstable charge-pumps. Our unified presentation is thought as to be the root of a complete theory of charge-pump conditioning circuits, that is yet to build.

In chapter 3, a new generic topology of unstable charge-pump conditioning circuits is proposed, that we call by the name of series-parallel charge-pump conditioning circuits. This topology generalizes the Bennet's doubler circuit that is presented in chapter 2. The essential part of the chapter is a formal analysis of the topology, which results in a formal proof of its operation. The non-trivial dependence of transducer conditioning scheme implemented by the circuit on the values of its capacitors is unveiled by the analysis. As this circuit generalizes the Bennet's doubler, the analysis contains that of the latter, in particular of its transient dynamics which were not described quantitatively until now.

The chapter 4 carries out a comparison of the different charge-pump conditioning circuits presented in the two former chapters. Constraints that make such a comparison meaningful are set, and the comparison is first carried out in the electrical domain. Then, we present the results of experiments highlighting the prominent role of the electromechanical coupling on the dynamics of vibration energy harvesters using unstable charge-pump conditioning circuits. Subsequently, we present the basis of a semi-analytical method that we have developed in order to study and ultimately compare different charge-pump conditioning circuits, accounting for the electromechanical effects. We give results of its application in different contexts defined by different parameters of harmonic input, different unstable charge-pumps, and a couple of different mechanical parameters corresponding to realistic MEMS electrostatic transducers.

A method for the characterization of electrostatic vibration energy harvesters is presented in chapter 5. This method relies on a topology of charge-pump conditioning circuit that is briefly presented in chapter 2. The chapter starts with a more detailed analysis of the topology of this circuit. The main part of the chapter reports on an easy experimental procedure to measure the value of two important parameters for vibration energy harvesters. The first of those parameters is the value of the lumped voltage source accounting for, e.g., electret charging of the transducer. The second parameter is the capacitance variation under the transducer biasing set by a charge-pump conditioning circuit. Procedures for minimizing the measurement errors are given for both methods. A full experimental example for the application of the first method is reported, while some partial results are given for the second method.

The second thematic part of the manuscript is composed of chapter 6 and 7. It presents the concept of what we call "near-limits vibration energy harvesting", as well as an architecture suited for its implementation.

Chapter 6 lays down the foundations of the concept of near-limits kinetic energy harvesting, that we investigated during this work. This concept refers to a methodology for the design of electrostatic vibration energy harvesters that starts from an overall, top-down view of the system, rather than optimizing the mechanical or electrical part independently and only then studying the dynamics yielded by an electromechanical domain analysis. This approach allows, in principle, to build VEHs compatible with arbitrary types of vibrations. We start the chapter

by taking a step back from the work done in the first part of the manuscript, showing how this approach is different. We then derive the energy maximizing dynamics of an idealized vibration energy harvesting system, and discuss how the different sources of energy dissipation mitigate the optimality of the derived dynamics.

The chapter 7 presents the full architecture of an electrostatic vibration energy harvester that implements the concept of near-limits vibration energy harvesting settled in chapter 6. To this end, a mechanical control law and suited electrical interface, computing, and sensing parts are proposed. Then, the architecture is sized using realistic values for the mechanical parameters, and realistic models of the electrical components. The results show the proof of concept of our architecture, as well as the influence of some of the parameters on the system's performance. We then point out the optimization challenges that arise from our study, and give several examples of possible variations of our architecture that may be worth investigating in future works.

We conclude the manuscript with a general conclusion, where we present a summary of the main results obtained during this work, and of the future works that we think are worth pursuing.

Chapter 1

Introduction to electrostatic vibration energy harvesting

This introduction chapter serves both as a general, rather qualitative introduction to the field of electrostatic vibration energy harvesting (e-VEH), as well as an exposition of the knowledge base that is going to be used throughout this manuscript.

We start by reviewing some of the motivations behind vibration energy harvesting. We then focus on explaining the basic concepts of electrostatic vibration energy harvesting (e-VEH). After a simple situation illustrating the concept of e-VEH is presented, we then move on to the presentation of the lumped-parameter model of a complete e-VEH. Then, the role of the electrical conditioning circuits in e-VEH is more thoroughly discussed through some examples. The role of the electrical constraints on the comparison of different electrical conditioning schemes is highlighted. This section on conditioning circuits ends with a discussion on the study of the electromechanical coupling effects arising from the electrical conditioning of e-VEH's transducer. Next, we briefly discuss the fabrication of micro-electromechanical devices used as electrostatic transducers in e-VEH. We also report three state-of-the-art examples of devices to illustrate the different geometries of electrostatic transducers. In particular, the structure that is the basis of the devices used in experiments throughout this manuscript is presented. We then move on to the description of some experimental procedures to which we will make reference at multiple points throughout this manuscript. The chapter ends with a discussion on some challenges in e-VEH, as well as some examples of reported systems.

1.1 Motivations for electrostatic vibration energy harvesting

Sensing and data recording is appearing as the new paradigm of the 21^{th} century: smart cars, smart home, smart buildings and cities are the objects of very extensive and active research. They all need a large number of communicating sensors, preferably wireless, for installation and operation cost reduction or reliability improvement. The modern car has a few hundred sensors, and it is expected that the automotive industry will require 22 billion sensors by 2020. Today, most sensors are still powered using wires. Making them autonomous would ease the sensor installation and would, generally, offer a lighter and more reliable system. These ideas about

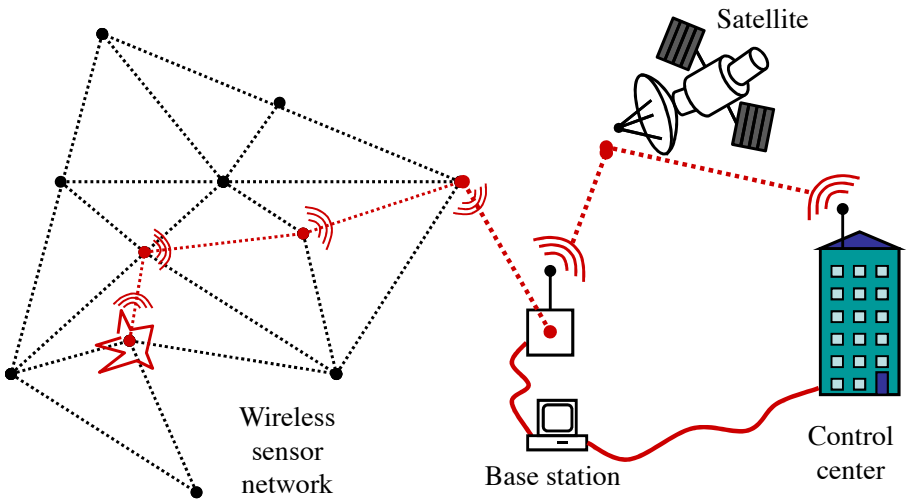

Figure 1.1: Principle of an ideal wireless sensor network (WSN) ecosystem: an event captured by an abandoned sensor node is transmitted to other nodes nearby.

smart environments take benefit from the Wireless Sensor Network (WSN) or the Internet of Thing [AIM10] (IoT) concepts. In WSN, all the sensors are provided with an embedded energy source and an antenna to wirelessly transmit data measurements. This communication system usually takes place in a star network where each sensor communicates with a master node. A better implementation of the network can be arranged if each sensor communicates with the closest node in order to progressively propagate the measured information to reach the base station (Fig. 1.1). For the IoT, the main idea is that any item of the daily life is able to communicate data through such a network.

For both WSNs and the IoT, independent and miniature power sources are usually preferable over wire powering. In the majority of cases, a battery is used, which may last from several days to several years, depending on its size and the application. However there are applications where a battery is not suitable for some reasons: a harsh environment degrades the battery too fast, an inaccessible location makes the cost of the battery replacement too high, or the ecological impact of battery use and disposal [RS03]. In these cases, a good solution is to convert energy from the ambient environment of the sensor. This is the modern concept of "energy harvesting".

There are many ways to harvest ambient energy. The most mature and efficient technique to this day is undoubtedly the use of photo-voltaic cells converting ambient light into electricity. Another technique is to use temperature gradients to generate electrical energy through the Seebeck effect. However, in some cases where no light or temperature gradient are available in the environment, less conventional energy sources have to be envisaged. In these cases, the kinetic energy communicated to the sensor by its surroundings vibrations is a good candidate for conversion into electricity, since these vibrations are present in the environment of many applications.

A vibration energy harvester, or VEH, is a system designed to carry out this energy conversion, and to make the converted energy available for use by an electronic system. The term VEH refers to systems of relatively small size, on the order of $1\,\mathrm{cm}^3$ or less, and of small mass, so that they do not impede with the operation of the device they supply. In general, the amount of converted energy is an increasing function of the device's size. VEHs generate electric power on scales ranging from the µW to the mW, depending on both the device size and the environ-

mental vibrations. Note that the idea of converting kinetic energy to electrical energy to supply electrical devices has existed since about the discovery of electricity. An example is the dynamo, invented in the late 19^{th} century. Such device uses a purposeful mechanical action in order to generate electrical energy, contrarily to VEH as we understand it, for which the vibrations, sometimes unwanted, are experienced by the system because of its environment, rather than being deliberately introduced. There also exist devices of very large scale that convert kinetic energy from environmental vibrations, such as from ocean waves [SJ09]. The scales of generated power are that of electrical power plants, that is, MW.

The fabrication of small-scale vibration energy harvesters has been enabled by recent developments in material science and microelectronics, which allow us to envisage miniaturized systems combining the vibration energy harvester and the electrical system supplied by this source, possibly without any battery. Three families are generally distinguished for this conversion of mechanical energy into electricity, depending on the mode of transduction used: electromagnetic, piezoelectric and electrostatic. Each family has its advantages and drawbacks, and a comparison requires a set of specifications given by a concrete application case. In this manuscript, we focus on devices using the electrostatic transduction mechanism. The advantages of electrostatic vibration energy harvesters that are often cited include compatibility with batch-fabrication processes, which have mature fabrication processes driven by the technologies of integrated circuits, as well as a better long term reliability.

There are numerous applications for vibration energy harvesting, even if there are few commercial products so far. For instance, mechanical structure health monitoring includes the monitoring of bridge oscillations, in which large WSN are buried, as Fig. 1.2 depicts. Structure health monitoring is also concerned with cracks in plane wings or changes in train rail fixtures with the aim to avoid deadly accidents. In all of these examples, it can be tedious and/or costly to replace end-of-life batteries. Other common examples include mechanical vibrations of the heart, for example, to power an implanted, leadless pacemaker, as depicted in Fig. 1.3. Commercial products nevertheless are beginning to emerge, through companies such as Wisepower srl, or Omron corporation.

The environmental vibrations from which electricity is to be converted can be of various forms, depending on the application. They can be periodic or non-periodic, harmonic or non-harmonic, regular or irregular, spread over a large frequency range or concentrated around single frequency. As depicted in Fig. 1.4, each environment has a specific vibration frequency spectrum and it is very difficult, if not impossible, to design a generic VEH: each application needs a dedicated device in order to optimize the power yield. A great research effort in the field of vibration energy harvesting is geared towards building systematic design flows for VEHs. Such a design flow is intended to enable the conception of VEHs that can be made compatible with targeted types of vibrations and under a given set of constraints (e.g., on the VEH's size), as dictated by the specification of each particular application.

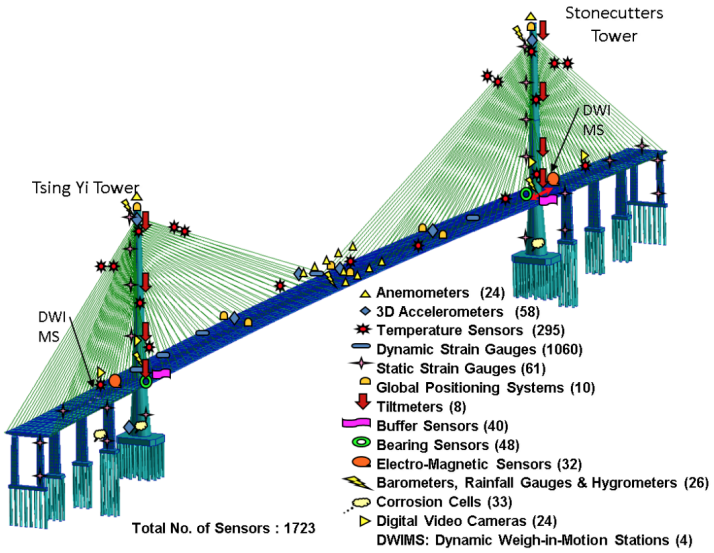

Figure 1.2: The wide variety and large number of sensors in a modern bridge [DST13].

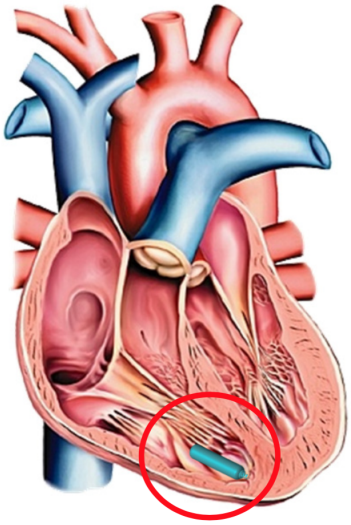

Figure 1.3: Schematic of the human heart with an implanted, leadless pacemaker [Det13].

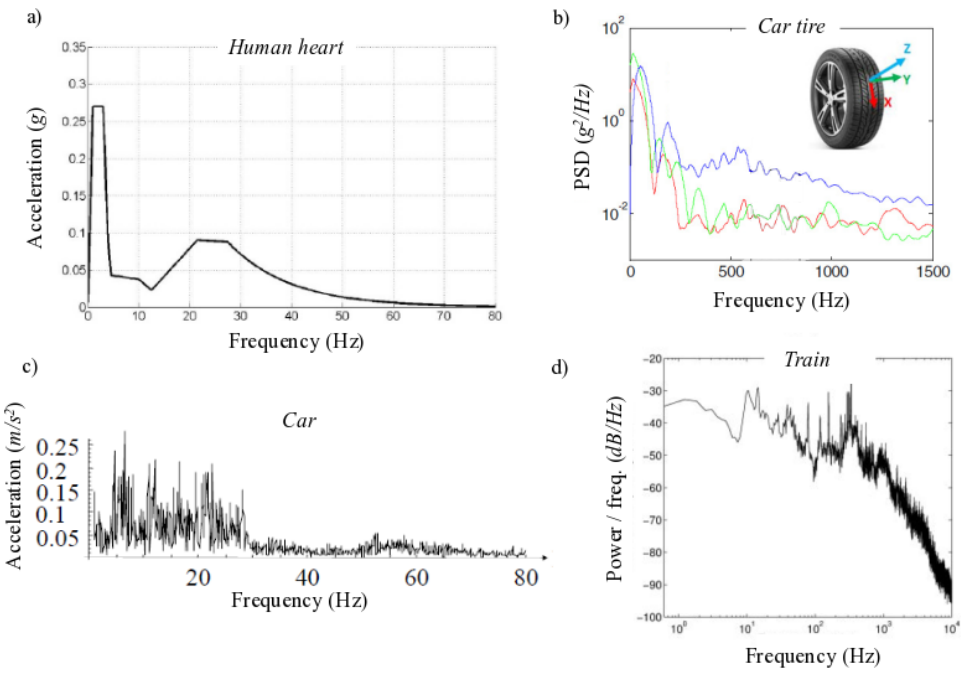

Figure 1.4: Examples of different vibration spectra published in the scientific literature: (a) typical shape of the acceleration spectrum in the right atrium of a human heart [Det13], (b) power spectral density of the acceleration measured on the inner surface of a car tire driving at 60 km/h [RAG13], (c) acceleration spectrum of a car [DJJ05], (d) acceleration of a train [VC14].

1.2 Introduction to electrostatic vibration energy harvesting

1.2.1 Operation principle on a simple example

Electrostatic vibration energy harvesters (referred to as e-VEHs, for electrostatic vibration energy harvesters, throughout this text) are VEHs that use electrostatic transducers in order to convert kinetic energy to electrical energy. Such transducers are in fact variable capacitors, and are electrically modeled as such. The variation of the capacitance is subsequent to a change in their geometry. This change in the geometry is itself subsequent to the work of an external mechanical force. In e-VEH, this force is the result of the system being submitted to its environmental vibrations.

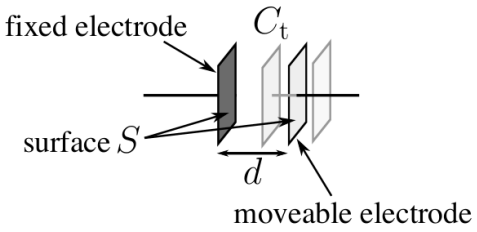

Figure 1.5: Schematic of an electrostatic transducer, that is, a variable capacitor. Here, the capacitance varies by the motion of the right electrode.

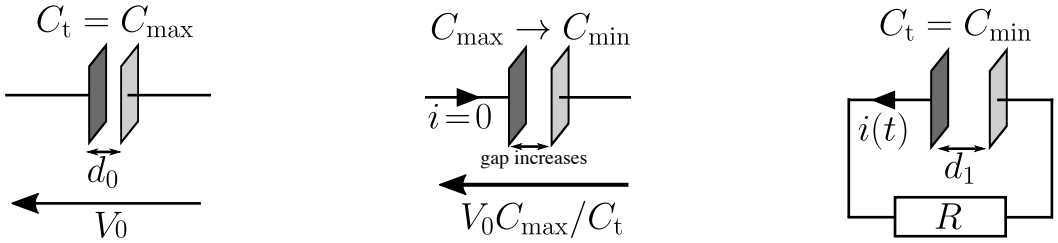

(a) We start from $C_t = C_{max}$, the transducer being charged with a voltage V_0.

(b) The gap increases thanks to an external mechanical action on one or both of the transducer's plates, while the transducer is isolated electrically: its voltage increases while its charge remains constant.

(c) When the gap reaches a value $d_1 > d_0$, the transducer is discharged in a resistance R.

Figure 1.6: Example illustrating the principle of e-VEH.

Let us give a simple examples that illustrates the operation of an e-VEH. Consider a planar capacitor C_t that has a movable electrode along an axis normal to the electrode plane, as depicted in Fig. 1.5. The other electrode is supposed to be unmovable. This type of variable capacitor is said to be of 'gap-closing' geometry, because its geometry varies by varying the length of the gap between its electrodes. Recall the capacitance formula for a planar capacitance:

$$C_t(d) = \varepsilon_0 \varepsilon_r \frac{S}{d} \tag{1.1}$$

where ε_0 is the vacuum permittivity constant, is the dielectric permittivity constant, S is the capacitance's electrode surface and d is the separating gap between the two electrodes. In the following example, let us assume that the sole varying parameter is d, so that the capacitance is

a function of d. In the rest of this manuscript, we suppose that the dielectric is either vacuum or air, for which $\varepsilon_\mathrm{r} \approx 1$, so that we drop the ε_r coefficient, hence lightening the notations.

Now, consider the sequence of events in Fig. 1.6. First, suppose that the gap between the capacitor's plates is of $d = d_0$. At this instant, the capacitor is charged by a voltage source to a voltage V_0. It hence stores the energy ${V_0}^2 C_\mathrm{t}(d_0)/2$. At a time t_1 corresponding to the end of the charging to V_0, the electrodes are supposed to move apart, until the gap reaches $d_1 > d_0$. During this movement, the transducer is isolated electrically so that the current flowing through it is effectively zero. Finally, when the gap has reached d_1, the transducer is connected to a resistor R in which it discharges, whilst the gap stays at d_1. The energy dissipated in the resistor is equal to the energy in the capacitor when the gap reached d_1. The capacitor provided more energy to the load R than it stored at $d = d_0$. In particular, the net energy ΔW, obtained by removing the initial energy in the capacitor is

$$\Delta W = \frac{1}{2} C_\mathrm{t}(d_1) {V_0}^2 \frac{C_\mathrm{t}^2(d_0)}{C_\mathrm{t}^2(d_1)} - \frac{1}{2} C_\mathrm{t}(d_0) {V_0}^2 = \varepsilon_0 {V_0}^2 \frac{S}{{d_0}^2}(d_1 - d_0) > 0 \tag{1.2}$$

The process described in this example needed a pre-bias of V_0 across the electrostatic transducer. In fact, the need for a pre-charge is a characteristic property of electrostatic transducers. This pre-charge can be provided by different means, such as an electrical energy tank in the system (see Sec. 1.3) or by particular materials called electrets (see Sec. 1.4.2).

1.2.2 Lumped-parameter model of an electrostatic vibration energy harvester

In the previous example, the displacement of the capacitor's mobile electrode was given as an input of the considered system. This example allowed for an intuitive understanding of the process on which e-VEH is based on.

In a physical setting, the energy has to be converted from some other form into the transducer's electrostatic field. In the context of e-VEH, it is converted from the mechanical domain. The converted energy amounts to the work of the external mechanical force responsible for the displacement of the mobile electrode. A full physical model of the e-VEH system is hence needed in order to fully describe the system's dynamics and hence the energy conversion process.

In this thesis, we deal with lineic inertial e-VEHs. Such e-VEH systems can be viewed as a box, or a frame, in which lies a mass of strictly inferior dimensions than that of the box. The transducer capacitance variation happens thanks to the displacement of an inertial mass along a constrained axis. The transducer's mobile electrode is supposed to be mechanically fixed to this mass. In turn, the mass displacement is a consequence of the e-VEH frame being accelerated by its surroundings vibrations. The displacement is a result of the dynamics of the whole system rather than be directly imposed such as it was in the example of Sec. 1.2.1.

The acceleration of the box, denoted by $A_\mathrm{ext}(t)$, translates to an equivalent force $\xi(t)$ acting on the e-VEH's inertial mass, which reads

$$\xi(t) \coloneqq -m A_\mathrm{ext}(t) \tag{1.3}$$

In the rest of the manuscript, the term input force and the notation $\xi(t)$ will refer to this force in the various contexts where it appears.

Let us now make these general ideas more precise by exposing a lumped model of an e-VEH. We start from a minimalistic lumped model, which we gradually enrich by adding details about the electrical and mechanical subsystems of an e-VEH.

1.2.2.1 Simplest physical model

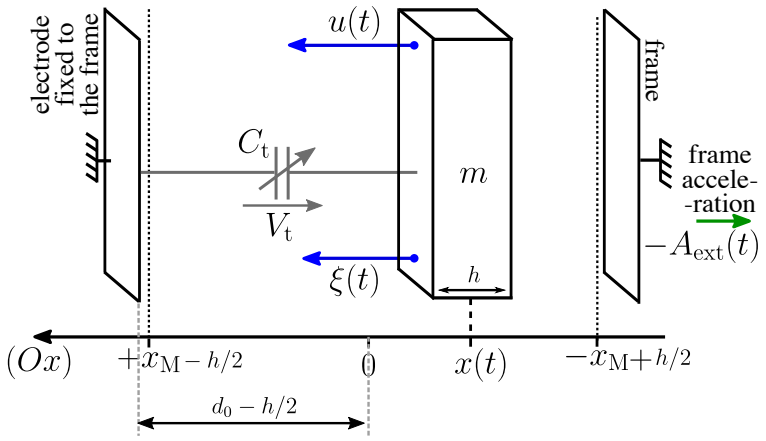

Figure 1.7: Generic model of an inertial e-VEH, based on a transducer of gap-closing geometry.

The conversion from electrical to mechanical energy means that there exists at least a force of electrical origin acting on the mass, adding up with the external mechanical force $\xi(t)$. With electrostatic transduction, this is done by the mass being fixed to the movable plate of the variable capacitor. We will consider that the other plate is fixed to the frame of the e-VEH. The force responsible for the energy conversion is hence the force acting on the mass because of the electrostatic field in between the two plates.

The simplest model that is widely encountered for lineic, inertial KEHs (we will omit the lineic and inertial adjectives from now on as it is all we are interested in in the present study) is given by the ODE (ordinary differential equation):

$$\begin{cases} m\ddot{x} = \xi(t) + u(t) \\ |x(t)| \leqslant x_M \end{cases} \tag{1.4}$$

where $x(t)$ denotes the displacement of the mass relatively to the e-VEH's frame. The (repeated) overdot stand for (repeated) derivation versus time. The force $u(t)$ is the transducer force responsible for the energy conversion between mechanical and electrical domains. Note that this model does not define the dynamics outside of the limits $\pm x_M$. The energy converted from the vibration into the energy of the transducer's electric field reads

$$W = \int_{t_0}^{t} u(t)\dot{x}(t)\,\mathrm{d}t \tag{1.5}$$

In the setting of electrostatic KEH we have that [PFC97]

$$u(t) = \frac{1}{2} V_{\mathrm{t}}^2(t) \frac{\partial C}{\partial x}(x(t)). \tag{1.6}$$

where V denotes the voltage across the transducer. In the following of this manuscript, the time dependence will often be dropped when it is clearly implied by the context.

Let us summarize this model on a schematic, depicted in Fig. 1.7. In this figure, the transducer's geometry is said to be gap-closing, as in the example of Sec. 1.2.1. The mass' left face forms the transducer's mobile electrode, while the electrode fixed to the frame is depicted on the left of the figure. The mobile mass moves between positions $\pm x_{\mathrm{M}}$.

In this configuration, the capacitance-versus-position function reads:

$$C_{\mathrm{t,GC}}(x) = \varepsilon_0 \frac{S}{d_0 - x} \tag{1.7}$$

and, from (1.6), the transducer force u reads:

$$u = \frac{1}{2} V_{\mathrm{t}}^2 \varepsilon_0 \frac{S}{(d_0 - x)^2}. \tag{1.8}$$

The gap-closing geometry is not the sole possible geometry of electrostatic transducers. Let us present two other geometries of 1-dof (1 degree of freedom) transducers: the symmetrical gap-closing geometry and the area-overlap geometry. For simplicity, we will keep the gap-closing geometry in the following figures of enriched models of the KEH (Sec. 1.2.2.2 and Sec. 1.2.2.3).

Electrostatic transducers of symmetrical gap-closing geometry are configured such as depicted in Fig. 1.8. The transducer consists in two differential capacitors: two electrodes are fixed and the corresponding mobile electrode moves in between them in a gap-closing fashion. Each face of the mobile mass constitutes an electrode for each of the two variable capacitors. The mobile mass, whose position relatively to the e-VEH frame is denoted by $x(t)$, is free to move along an axis (Ox), between positions $\pm x_{\mathrm{M}}$. The two differential capacitors are electrically configured as parallel capacitors, because the two fixed electrodes are electrically connected. Hence, the transducer capacitance C_{t} is the sum of these two differential capacitance values.

The capacitance-versus-displacement function for a symmetrical gap-closing transducer reads

$$C_{\mathrm{t,SGC}}(x) = \varepsilon_0 \frac{S}{d_0 - x} + \varepsilon_0 \frac{S}{d_0 + x} = \varepsilon_0 \frac{2Sd_0}{{d_0}^2 - x^2}, \tag{1.9}$$

and hence, from (1.6), the transducer force u reads:

$$u = \frac{1}{2} V_{\mathrm{t}}^2 \varepsilon_0 \frac{4Sd_0 x}{(d_0^2 - x^2)^2} \tag{1.10}$$

Electrostatic transducers of area-overlap geometry are configured such as depicted in Fig. 1.9. In this configuration, the gap between the mobile and fixed electrode is kept constant, but the overlapping area changes as the transducer is free to move in the direction corresponding to the l dimension of the mass (see the figure). Again, the mobile electrodes are fixed on the e-VEH's mass which is able to move along an axis (Ox) between positions $\pm x_{\mathrm{M}}$. The change

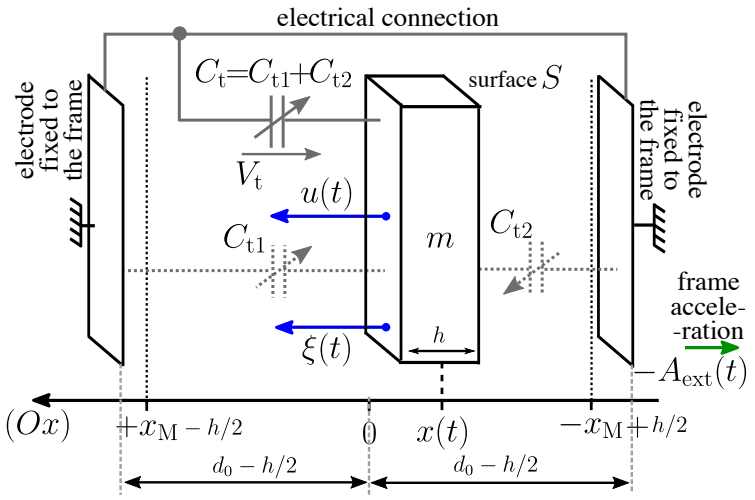

Figure 1.8: Generic model of an e-VEH based on a transducer of symmetrical gap-closing geometry.

of capacitance occurs because of the change in the capacitor overlapping area instead of the separating gap.

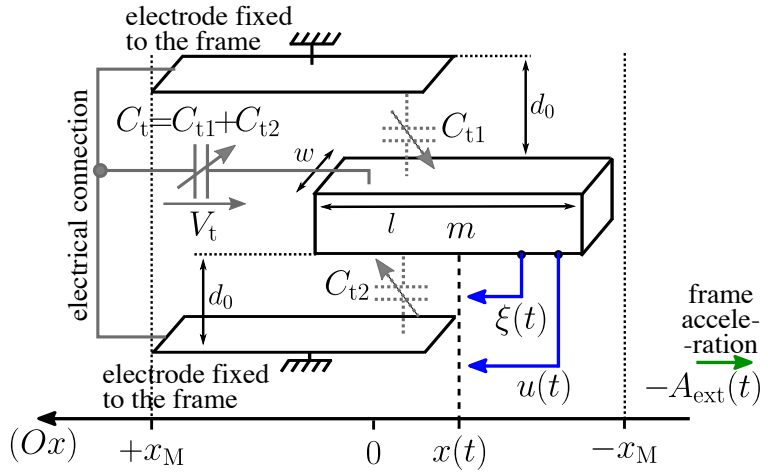

Figure 1.9: Generic model of an e-VEH based on a transducer of area-overlap geometry.

The capacitance-versus-displacement function for an area-overlap electrostatic transducer reads

$$C_{t,AO}(x) = 2\varepsilon_0 \frac{w(l+x)}{d_0}. \tag{1.11}$$

From (1.6), the transducer force u reads:

$$u = V_t^2 \varepsilon_0 \frac{w}{d_0}. \tag{1.12}$$

Here, we have represented an area-overlap geometry with a two-ended fixed electrode, but it can be one ended as well, the corresponding capacitance-versus-displacement function being obtained by dropping the factor 2 in (1.11), and modifying (1.12) accordingly.

An observation that can be made from (1.8), (1.10) and (1.12) is that an even downscaling of all transducer's dimensions leaves the electrostatic force unchanged. This property, as mentioned in Sec. 1.1, is one of the reasons why the electrostatic transduction mechanism interesting for

e-VEH at smaller scales.

Finally, note that there also exists differential transducers that are composed of two separate variable capacitors that vary in a complementary manner. We postpone the model of such a differential transducer to Chap.7 where it is used. Finally, note that other types of electrostatic transducers geometries are possible, such as transducers for which both the overlapping area and the gap vary, or transducers which are based on a variation of their dielectric material. We will not discuss such transducers in this manuscript.

1.2.2.2 Adding details about the electronics

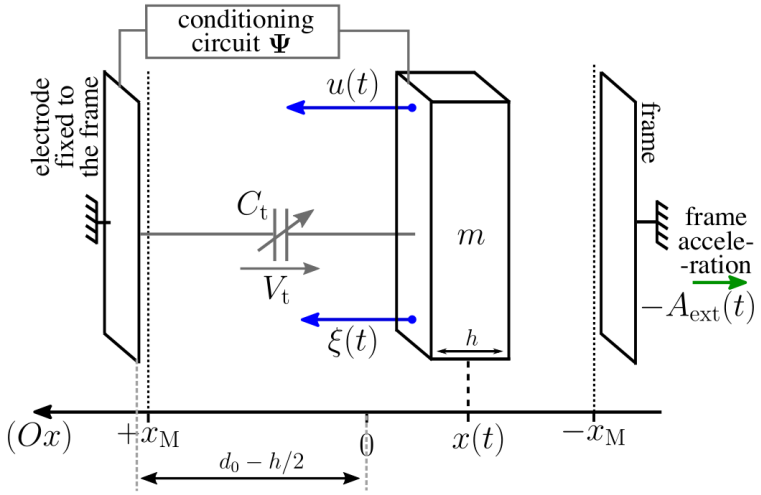

Figure 1.10: Generic model of an e-VEH based on a transducer of gap-closing geometry and biased by a conditioning circuit.

Both the previous model and the simplified example of Sec. 1.2.1 highlight that the energy conversion process depends on the evolution of the transducer's bias throughout its capacitance variation. This evolution of the transducer's biasing during its capacitance variation is called the electrical conditioning of the transducer. This conditioning is determined by an electronic circuit, called the *conditioning circuit*. This circuit can be described by a set of differential-algebraic relations $\mathbf{\Psi}$ that governs the evolution of V_t. We can thus further enrich the model:

$$\begin{cases} m\ddot{x} = \xi(t) + u(t) \\ |x(t)| \leqslant x_\mathrm{M} \\ \mathbf{\Psi}(\dot{\mathbf{V}}, \dot{\mathbf{I}}, \mathbf{V}, \mathbf{I}, x, \dot{x}, t) = 0 \end{cases} \tag{1.13}$$

where $\mathbf{V}$ and $\mathbf{I}$ are vectors of currents and voltages in the circuit. Hence, V_t is a coordinate of $\mathbf{V}$.

Let us illustrate an example of such a map for the introductory example of Se. 1.2.1. A circuit implementing the steps of this simple example is given in Fig. 1.11. Note that practical implementation implementations of conditioning circuits will differ from the illustrative circuit of Fig. 1.11, for reasons that are exposed below in Sec. 1.3.2.1.

In this circuit, we chose as the sole electrical state variables the voltage across and the current through the transducer. Hence we replace $\mathbf{V}$ with V_t and $\mathbf{I}$ with i_t. We denote by $C_\mathrm{t}(x)$

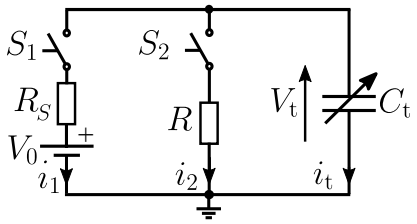

Figure 1.11: Circuit to implement the introductory example of transducer conditioning presented in Sec. 1.2.1.

the capacitance-versus-displacement function for the geometry of interest (e.g., (1.7), (1.9) or (1.11)). Note that we added a resistance R_S modeling the series resistance of the source V_0. Defining $\mathbf{\Psi} = (\Psi_1, \Psi_2)^\mathrm{T}$, we can describe the circuit above by, e.g.,

$$\begin{aligned}
\Psi_1(\dot{i_\mathrm{t}}, \dot{V_\mathrm{t}}, i_\mathrm{t}, V_\mathrm{t}, x, \dot{x}, t) &= i_\mathrm{t}(t) - \frac{\partial C}{\partial x}(x)\dot{x}(t)V_\mathrm{t}(t) - C_\mathrm{t}(x)\dot{V_\mathrm{t}}(t) \\
\Psi_2(\dot{i_\mathrm{t}}, \dot{V_\mathrm{t}}, i_\mathrm{t}, V_\mathrm{t}, x, \dot{x}, t) &= \begin{cases} V_0 - i_\mathrm{t}R_\mathrm{S}, & \text{if } x(t) \leqslant d_0 \\ i_\mathrm{t}(t), & \text{if } d_0 < x(t) < d_1 \\ V_\mathrm{t}(t) - i_\mathrm{t}(t)R, & \text{if } x(t) \geqslant d_1 \end{cases}
\end{aligned} \tag{1.14}$$

Evolution maps describing switched circuits dynamics, such as $\mathbf{\Psi}$ given above, give rise to dynamical systems where there may exist problems of well-posedness, depending on, e.g., the specified initial conditions, and that even if the circuit is decoupled from the mechanics (i.e., $x(t)$ or equivalently $C_\mathrm{t}(t)$ is an input). In fact, the systematic, quantitative study of such piecewise-linear circuits is covered by non-smooth analysis and the theory of differential inclusions [GBA12; ABB10]. This latter approach is used by the latest circuit simulators, that must be able to numerically solve a wide class of circuits. As the rest of this manuscript will show, almost all conditioning circuits used in e-VEH have such a switching behavior, but we do not need the same systematic approach as that used by circuit simulators. Specifically, we will never use the explicit description of a conditioning circuit in terms of the map $\mathbf{\Psi}$. Instead, the approach we will use in the rest of this work to analyze e-VEHs will be based on additional knowledge, gained from the electrical analysis and physical insight, on the particular topology of the conditioning circuit they use. Also note that another modeling strategy could be to use a $\mathbf{\Psi}$ map that describes smooth (yet, of course, nonlinear) models of these components (e.g., quadratic transistor model for switches) instead of the abruptly switching models. In this present section, we chose the abstract representation as a generic map $\mathbf{\Psi}$ in order to not induce any loss of generality on the electrical interface that can be used at this point. This view of the electrical interface will appear a few times throughout this manuscript, in Chap. 4 and in Chap. 6.

Finally, let us mention here that in the setting of the transducer connected to an electrical circuit, the parasitic capacitance due to the transducer's electrical environment (e.g., diodes input capacitances, or parasitic capacitances due to the connections) will superpose to that of the transducer. Hence, the effective capacitance of the transducer will be increased by a parasitic C_p, whose value depends on the electrical context.

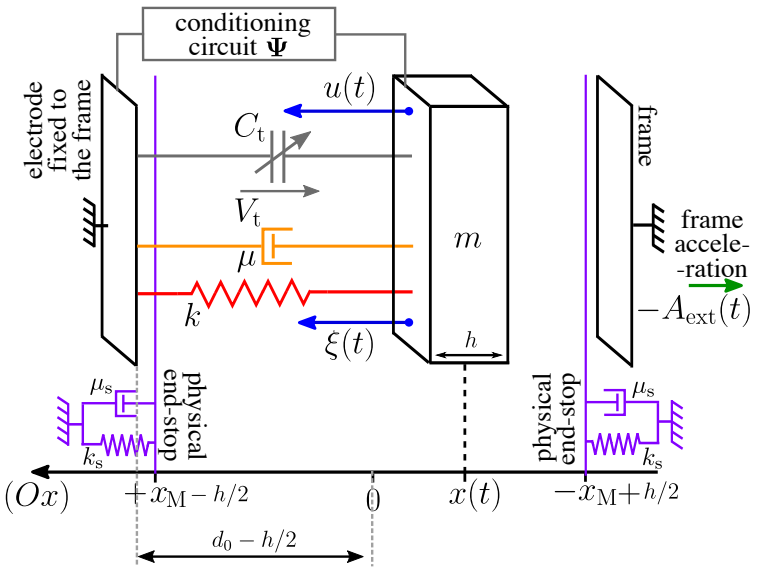

Figure 1.12: Generic model of an e-VEH based on a transducer of gap-closing geometry and biased by a conditioning circuit. The model accounts for forces of mechanical origin, here a linear spring, a linear damping and end-stops modeled by a spring-damper system.

1.2.2.3 Adding details about the mechanics

Finally, the model of an electrostatic vibration energy harvester has also to account for mechanical effects that originate from the mechanical structure of the transducer itself. Such effects are often intentionally added in order to improve the operation of the KEHs for specific application cases. Other times, they can be unwanted parasitic effects. We can encapsulate them into two additional terms to the original ODE: a term $-k(x)x$ which represents a conservative (i.e., solely position-dependent in the 1-dof context), and a term $-c(x,\dot{x})\dot{x}$ which accounts for parasitic damping effects.

$$\begin{cases} m\ddot{x} = \xi(t) + u(t) - k(x)x - c(x,\dot{x})\dot{x} \\ \mathbf{\Psi}(\dot{\mathbf{V}}, \dot{\mathbf{I}}, \mathbf{V}, \mathbf{I}, x, \dot{x}, t) = \mathbf{0} \end{cases} \tag{1.15}$$

One of the most encountered mechanical features of VEHs is the presence of a spring, that is at least present to suspend the inertial mass in the e-VEHs frame. Hence, the mechanical structure of such VEHs is a resonator. For example, $k(x) = k$ for a linear spring, in which case the e-VEH's mechanical structure is a linear resonator of natural frequency $\omega_0 = \sqrt{k/m}$. This term can also account for nonlinearities, either introduced or non-intentional. For example, the function $k(x) = k + k_2x^2$ gives rise to the celebrated Duffing equation [GH13] if one omits the transducer force $u(t)$. In fact, in the setting of electrostatic transduction for e-VEH, introducing such nonlinearities can be beneficial. Some examples will be given below in Sec. 1.6.1. In the same way, the parasitic damping term can be linear (that is, $c(x,\dot{x}) = c$), or nonlinear to account, e.g., for squeeze-film damping effects [Sen07].

The terms $k(x)$ and $c(x,\dot{x})$ can also account for a mechanical model of the end-stops. An end-stop can be modeled by a stiff spring and a linear damper, the latter being responsible for energy conversion in the collisions (e.g., lost into heat). In this case we remove the constraint

$|x(t)| \leqslant x_{\mathrm{M}}$ from (1.2.2.2), and write

$$\begin{aligned} k(x) &= \begin{cases} kx(t) & \text{if } |x(t)| \leqslant x_{\mathrm{M}} \\ kx(t) + k_{\mathrm{s}}|x(t) - x_{\mathrm{M}}| & \text{otherwise} \end{cases} \\ c(x, \dot{x}) &= \begin{cases} c_{\mathrm{s}}\dot{x}(t) & \text{if } |x(t)| \leqslant x_{\mathrm{M}} \\ c_{\mathrm{s}}\dot{x}(t) + c_{\mathrm{s}}\dot{x}(t) & \text{otherwise} \end{cases} \end{aligned} \tag{1.16}$$

A more abrupt model can be used, as it is done in the example of map $\boldsymbol{\Psi}$ above (i.e., reinitializing the mass' velocity as in [AB08]), but the model (1.16) is seemingly the most popular among e-VEH works, and has gone through extensive experimental validation [TLH15] and parameter-fitting [KHS15].

1.3 Conditioning circuits for electrostatic vibration energy harvesting

The electrical conditioning of an electrostatic transducer was defined in Sec. 1.2.2.2 as the evolution of the transducer's bias throughout its capacitance variation. The term conditioning scheme will refer to this same definition in the rest of this manuscript.

A conditioning scheme is implemented by a conditioning circuit. For example, the scheme of the example of Sec. 1.2.1 can be implemented by the conditioning circuit in Fig. 1.6. The above model suggests that the conditioning scheme and hence the conditioning circuit have an important role on the system's dynamics, and thus on energy generation.

This section is devoted to give more details on the electrical conditioning of e-VEHs. We start by presenting a geometrical tool summarizing the operation of conditioning circuits, called the charge-voltage diagram. Then, three fundamental examples of conditioning circuits are presented (constant-charge, constant-voltage and primitive). The example of the constant-charge conditioning will be used as an occasion to highlight the role of the conditioning circuit related to load energy delivery. In the end of the section, the fundamental difference between the electrical and electromechanical domain study of an e-VEH is discussed.

1.3.1 Charge-voltage diagram

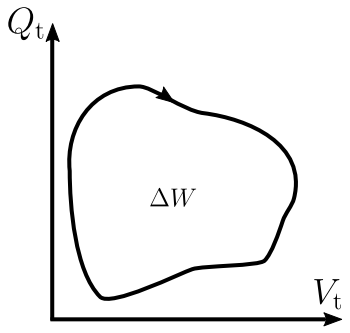

Figure 1.13: An example of a charge-voltage diagram presenting a loop.

The charge-voltage diagram is a convenient tool that will be used throughout this thesis to describe the operation of a conditioning circuit. This diagram is a parametric plot $(Q_\mathrm{t}(C_\mathrm{t}), V_\mathrm{t}(C_\mathrm{t}))$ in the charge-voltage plane, where $Q_\mathrm{t} = V_\mathrm{t} C_\mathrm{t}$ denotes the charge on the transducer. It summarizes the evolution of the charge and voltage biasing of the transducer as imposed by the conditioning circuit it is connected to, across the variation of C_t. A generic example of such a diagram is depicted in Fig. 1.13.

For a biasing of C_t throughout its variation that describes a loop in the charge-voltage diagram, the energy converted by the corresponding variation is the area enclosed by the loop. Indeed, the work done by the transducer force between two times t_1 and t_2 reads, according to (1.6)

$$W_\mathrm{u} = \frac{1}{2}\int_{t_1}^{t_2} {V_\mathrm{t}}^2 \frac{\partial C_\mathrm{t}}{\partial x}(x(t))\dot{x}(t)\,\mathrm{d}t = \frac{1}{2}\int_{C_\mathrm{t}(t_1)}^{C_\mathrm{t}(t_2)} {V_\mathrm{t}}^2\,\mathrm{d}C_\mathrm{t}. \tag{1.17}$$

The change of variable here can be made rigorous by breaking down the evolution of C_t between times t_1 and t_2 into monotonic evolution segments, so that V_t is a function of C_t on each of them. We also have that

$$C_\mathrm{t}(Q_\mathrm{t}, V_\mathrm{t}) = \frac{Q_\mathrm{t}}{V_\mathrm{t}} \implies \mathrm{d}C_\mathrm{t}(Q_\mathrm{t}, V_\mathrm{t}) = \frac{1}{V_\mathrm{t}}\,\mathrm{d}Q_\mathrm{t} - \frac{Q_\mathrm{t}}{{V_\mathrm{t}}^2}\,\mathrm{d}V_\mathrm{t}, \tag{1.18}$$

Integrating this differential form over the closed loop Γ parametrized by $(Q_\mathrm{t}(C_\mathrm{t}), V_\mathrm{t}(C_\mathrm{t}))$ yields, using Green-Riemann's theorem

$$W_\mathrm{u} = \frac{1}{2}\int_\Gamma {V_\mathrm{t}}^2\,\mathrm{d}C(Q_\mathrm{t}, V_\mathrm{t}) = \frac{1}{2}\int_\Gamma V_\mathrm{t}\,\mathrm{d}Q_\mathrm{t} - Q_\mathrm{t}\,\mathrm{d}V_\mathrm{t} = -\iint_{\overset{\circ}{\Gamma}} \mathrm{d}Q_\mathrm{t}\,\mathrm{d}V_\mathrm{t} \tag{1.19}$$

The rightmost quantity is the opposite of the signed area of the domain $\overset{\circ}{\Gamma}$ enclosed by Γ. The work done by the transducer force is hence negative if the loop's orientation is counter canonical (a person walking on the line sees the interior of the domain on its right, as in Fig. 1.13), in which case the area of $\overset{\circ}{\Gamma}$ represents energy converted from the mechanicam to the electrical domain. If C_t's variation describes the loop in the canonical orientation, the area enclosed in $\overset{\circ}{\Gamma}$ amounts to the energy converted from the electrical to the mechanical domain.

1.3.2 Examples of conditioning schemes and circuits

Let us describe three electrical conditioning schemes and give examples of associated conditioning circuits, namely the constant-charge, constant-voltage and primitive conditioning schemes. Chronologically, these conditioning schemes are the three first that were proposed in the field of e-VEH. They still are used in a variety of applications, with the primitive conditioning being extensively used for device test and characterization (see Sec. 1.5).

1.3.2.1 Constant-charge conditioning circuits

The constant-charge conditioning scheme consists in keeping the charge on the transducer constant while its capacitance decreases. Let us describe this conditioning scheme, while at the

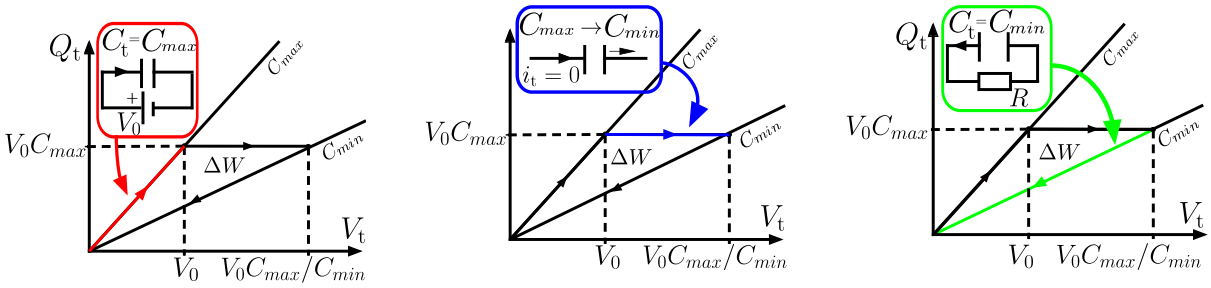

(a) Charging of C_t at $C_t = C_{max}$.

(b) C_t decreases while its charge is constant.

(c) Discharging of C_t at $C_t = C_{min}$.

Figure 1.14: The three steps of the constant-charge conditioning scheme explained on its charge-voltage diagram.

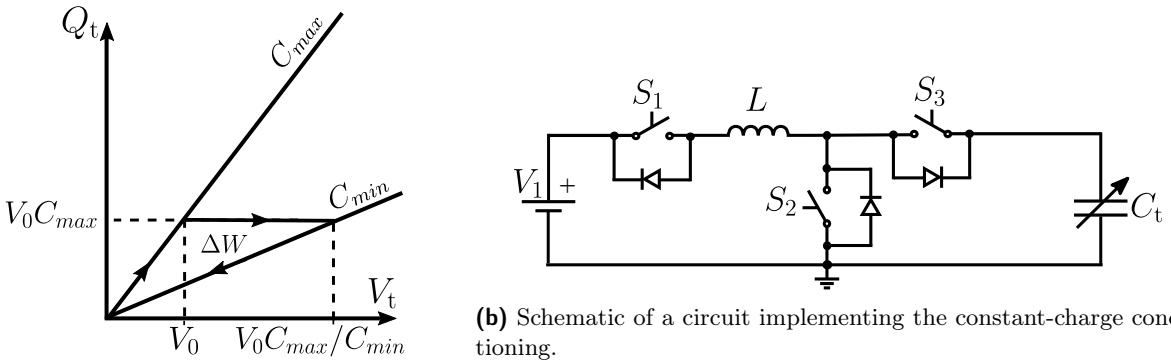

(a) Charge-voltage diagram for the constant-charge conditioning.

(b) Schematic of a circuit implementing the constant-charge conditioning.

Figure 1.15: Constant-charge conditioning of an electrostatic transducer.

same taking this opportunity to build the corresponding charge-voltage diagram following the Fig. 1.14.

Suppose the transducer's capacitance C_t continuously and cyclically varies between two extreme values C_{max} and C_{min} with $C_{max} > C_{min}$. Here, we are not interested in the whole system dynamics including the mechanics, but we consider this capacitance variation as an input, as we did in Sec. 1.2.1. This is often the case when first studying new conditioning schemes and circuits (see Sec. 1.3.4 below) and is called the electrical domain analysis.

When $C_t = C_{max}$, the transducer is charged to a voltage V_0 fast enough so that C_t remains equal to C_{max} during the whole process. This is the red segment in Fig. 1.14a. Then, C_t decreases while its charge is kept constant by being electrically isolated, until $C_t = C_{min}$, and its voltage increases such that $V_t(t) = V_0 C_{max}/C_t(t)$. This is the blue segment in Fig. 1.14b. At the instant when $C_t = C_{min}$, the transducer is discharged into a load resistor R, fast enough so that it happens while C_t remains equal to C_{min}. This is the green segment in Fig. 1.14c. Then, the transducer is kept discharged until $C_t = C_{max}$ and the cycle restarts. The obtained contour in the charge-voltage plane is triangular. It encloses the area ΔW, which reads

$$\Delta W = \frac{1}{2} C_{max} V_0 \left(\frac{C_{max}}{C_{min}} V_0 - V_0 \right) = \frac{1}{2} C_{max} {V_0}^2 \left(\frac{C_{max}}{C_{min}} - 1 \right) \tag{1.20}$$

In fact, this scheme correspond to the introductory example of Sec. 1.2.1: $C_t = C_{max}$ corresponds to the gap of d_0 and $C_t = C_{min}$ to the gap of d_1. The circuit depicted in Fig. 1.6

was presented as a circuit to implement this specific conditioning scheme, but it has several drawbacks that makes it unusable in practice:

- when the capacitance reaches $C_{\min}$, it is discharged at once through R. If R represents the load to be supplied, it is supplied in a pulsed pattern (every time $C_t = C_{\min}$), with a voltage ripple going from 0 to $V_0 C_{\max}/C_{\min}$. However, most electrical systems need to be supplied in a specific form, e.g., a steady DC voltage of given value ;
- when the capacitance is charged at $C_{\max}$, it is connected to a voltage source V_0. This voltage source is likely to be realized with a large capacitor, or at least modeled as such. It is a well known fact that such a direct connection results in the loss of a large part of the energy supplied by the initially charged capacitor [UJM16]. As the purpose of a VEH is to maximize its energy output, this is a rather bad solution.

This example of constant-charge conditioning is for us an opportunity to raise those two requirements that are in fact universal to all e-VEHs conditioning circuits. In particular, the first of these requirements shows that the load interfacing and the electrical conditioning are two different but coupled tasks which the e-VEHs electrical interface encompasses. Finally, another limitation of the circuit in Fig. 1.11, which this time is specific to the constant-charge conditioning scheme, is that the charge on the transducer $V_0 C_{\max}$ is imposed by the value of the voltage source V_0, which can have low value and hence result in small converted energy (see (1.20)).

A more realistic example of a circuit implementing the constant-charge conditioning scheme is depicted in Fig. 1.15b. Let us synthetically describe its operation. Suppose initially that $C_t = C_{\max}$ and that $V_t = 0$. The switches S_1 and S_2 are put in their ON state, thus magnetizing the inductor L. Then, they are turned off so that the inductor, in series with V_1, discharges into C_t through the diode anti-parallel to S_3. This process has to be quick enough so that C_t remains equal to $C_{\max}$. The amount of charge $V_0 C_{\max}$ can be modulated to any value greater than $V_1 C_{\max}$ by adequately timing the pulse width commanding switches S_1 and S_2. When C_t decreases from $C_{\max}$ to $C_{\min}$, all switches remain in their off-state so that C_t's charge is constant. Finally, when C_t reaches $C_{\min}$, S_1 is set to ON so that C_t fully discharges into the source V_1 through L.

This circuit addresses the two points raised above by:

- moving the converted energy back into the voltage source V_0, which can be seen as the energy tank of the system. We can suppose that this is realized by, e.g., a large capacitor. In this case, an external regulation mechanism can hence either regulate the voltage across this capacitor, either move it to another capacitor whose voltage will be regulated. A load connected will see a steady DC voltage. Therefore, one can say that this circuit decouples the problem of transducer conditioning from the problem of load interfacing.

- carrying out the charging of the transducer at $C_{\max}$ and its discharge in the capacitive energy tank at $C_{\min}$ through an inductive energy buffer, reminiscing of a DC-DC converter topology. This allows, in principle, lossless transfers from V_1 to C_t and vice-versa.

Practical implementations of e-VEHs using a constant-charge conditioning circuit have been reported, e.g., in [MMA01]. It is important to note that the constant-charge conditioning circuits need to track the value of C_t in real-time in order to correctly implement the charging and

discharging events. Finally, note that parasitic elements of the conditioning circuit's components make the conditioning scheme deviate from the idealized constant-charge conditioning scheme depicted in Fig. 1.15a. For instance, in the example of Fig. 1.3.2.1 the leakage currents associated to the switches elements will prevent exact constant-charge operation when C_t decreases from C_max to C_min.

1.3.2.2 Constant-voltage conditioning circuit

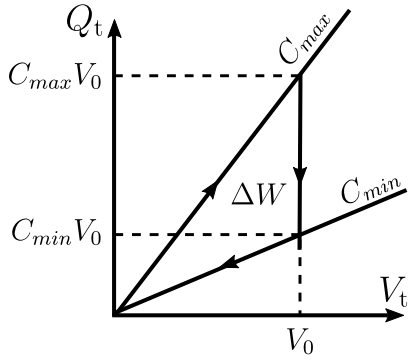

(a) Charge-voltage diagram for the constant-voltage transducer conditioning scheme.

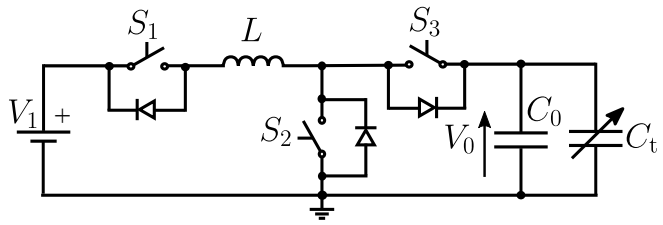

(b) Example of a circuit implementing the constant-voltage conditioning scheme.

Figure 1.16: Constant-voltage conditioning of an electrostatic transducer.

Instead of keeping the transducer charge constant through its decreasing, one may decide to fix the voltage across the transducer. This is the so-called constant-voltage conditioning scheme. It consists in keeping the voltage across the transducer fixed to a voltage V_0 while C_t decreases from C_max to C_min, and then keep it uncharged when it increases from C_min back to C_max. The corresponding charge-voltage diagram is depicted in Fig. 1.16a. The converted energy computed from the area of the cycle reads

$$\Delta W = \frac{1}{2}{V_0}^2(C_\mathrm{max} - C_\mathrm{min}) \tag{1.21}$$

An example of circuit architecture to implement the constant-voltage conditioning scheme described in Fig. 1.16a is depicted in Fig. 1.16b. This circuit essentially works in the same way as the constant-charge circuit in Fig. 1.15b, except that at $C_\mathrm{t} = C_\mathrm{max}$, it charges the capacitive system composed of C_t and a fixed capacitor $C_0 \gg C_\mathrm{max}$. When C_t decreases, the capacitance $\{C_\mathrm{t}$ in parallel with $C_0\}$ is kept at constant charge. Therefore, the voltage across C_t remains approximatively constant during its variation as C_0's value is much larger than C_t. Indeed, if the voltage across C_0 and C_t is equal to V_0 when L finishes being discharged, the charge conservation equation reads

$$V_0(C_\mathrm{max} + C_0) = V_1(C_\mathrm{t} + C_0),\ C_\mathrm{t} \in [C_\mathrm{min}\,; C_\mathrm{max}] \implies V_1 = V_0\frac{C_\mathrm{max} + C_0}{C_\mathrm{t} + C_0} \underset{C_\mathrm{max}/C_0 \to 0}{\sim} V_0. \tag{1.22}$$

Practical circuit designs implementing the constant-voltage conditioning scheme have been reported in the literature, e.g. by Torres *et al.* in [TR10]. As for the constant-charge case, constant-voltage conditioning circuits need synchronization with C_t's variation.

1.3.2.3 Primitive conditioning

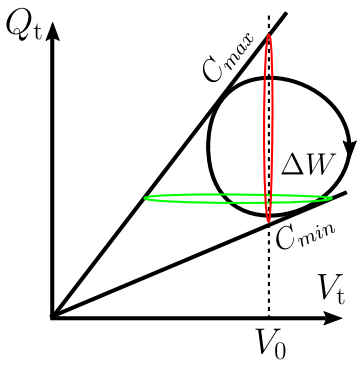

(a) Charge-voltage diagram for the primitive conditioning circuit in steady-state mode.

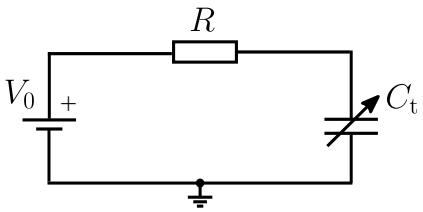

(b) The primitive conditioning circuit.

Figure 1.17: Primitive conditioning of an electrostatic transducer.

The primitive conditioning refers to both a conditioning scheme and the conditioning circuit that is tied to it. It consists in using the transducer in series with the loading resistance and a voltage source, as depicted in Fig. 1.3.2.3.

Contrarily to the constant-charge and constant-voltage conditioning circuits of Sec. 1.3.2.1 and Sec. 1.3.2.2, with the primitive conditioning circuit, the converted power at each cycle of variation of C_t does not only depend on local extremum C_{max} and C_{min}, but rather on the capacitance variation function in between these two extrema. Plus, for a fixed variation of C_t, the circuit has a transient dynamics before reaching a steady-state operation, which is not the case for the two circuits described above. The voltage across R is alternating, and there is little control on it as it depends on the exact $C_t(t)$ variation. If R represents the electrical load that is to be supplied by the e-VEH, then this is incompatible with the need of a steady DC voltage of most electrical systems. For these two reasons, the primitive conditioning circuit is almost unusable as such in a practical e-VEH.

Yet, this circuit is useful in different settings. First, in some cases, the study of this circuit can serve as a benchmark of the performances of e-VEHs using more sophisticated electrical interfaces, that can be modeled by a resistive load under some hypotheses. These are essentially based on the assumption of a linear two-port lumped model of e-VEH, which coincides in structure with models of piezoelectric VEH (see [Til96; DSP10]). The primitive conditioning circuit is also used for e-VEH characterization purposes in different experimental settings for the characterization of e-VEHs. This is the subject of Sec. 1.5 below.

Let us mention that, regarding to the converted power, there exists a value of R that maximizes it, for a each capacitance variation function and voltage V_0. This can be understood by considering two extreme cases:

- when R is of relatively large value so that it tends to an open circuit, the charges on C_t do not change. The voltage across C_t hence alternates between two values $Q_{t,0}/C_{max}$ and $Q_{t,0}/\min$, where $Q_{t,0}$ denotes the initial charges on C_t (green contour in Fig. 1.17a) ;

- when R is of relatively small value so that it tends to a short circuit, the voltage across C_t seldom changes. In this case, the charge-voltage diagram tends to a vertical line passing

through points $(V_0, V_0 C_{\min})$ and $(V_0, V_0 C_{\max})$ (red contour in Fig. 1.17a).

A thorough analysis of this circuit can be found in [GBB13] and Chap. 8 of [BBG16].

1.3.3 Comparison of conditioning circuits

Given the previous examples of electrical interfaces, a legitimate interrogation is on the relative performances of different conditioning circuits. As for most of topics in engineering, this question is only meaningful if some constraints are set. We already have encountered such constraints in the presentation above: the constraint on the need for a regulated voltage to supply the load had *de facto* eliminated the primitive conditioning from being potentially usable in a practical e-VEH context where the resistor R represents the load to be supplied.

Another legitimate constraint that can be added is on the maximum voltage that the transducer can support. Let us denote this latter quantity by $V_{\max}$. In this case, it is easily shown that the maximal constant-charge conversion cycle, for given $C_{\max}$ and $C_{\min}$, amounts to

$$\Delta W = {V_{\max}}^2 \frac{C_{\min}}{C_{\max}} (C_{\max} - C_{\min}) \tag{1.23}$$

while the maximal constant-voltage conversion cycle is

$$\Delta W = {V_{\max}}^2 (C_{\max} - C_{\min}) \tag{1.24}$$

As $C_{\min}/C_{\max} < 1$, it is clear that the converted energy is superior with the constant-voltage circuit than with the constant-charge circuit in this setting.

However, this conclusion can be mitigated by the implementation of the circuits used for each of the conditioning schemes. For example, the circuit in Fig. 1.3.2.2 charges capacitors C_0 and C_t to the voltage V_0 through the inductive buffer L and the diode anti-parallel with the switch S_3. Let us consider the voltage drop V_T of this diode as the sole electrical non-ideality for simplicity. In this case, to implement the cycle achieving (1.23), the charge $V_{\max} C_{\min}$ must end up on C_t when $C_\mathrm{t} = C_{\max}$, and hence go through the diode. This implies that an energy of $V_\mathrm{T} V_{\max} C_{\min}$ is lost in the process in the anti-parallel diode of S_3. In the same way, with the constant-voltage conditioning circuit, a total charge of $V_{\max}(C_{\max} + C_0)$ has to be moved to C_t and C_0. Neglecting $C_{\max} V_{\max}$ for simplicity, the energy lost amounts to $V_{\max} C_0$. By subtracting the energy lost in the diode from the converted energies for both cases (1.23) and (1.24), it comes that the net converted energy remains larger with the constant-voltage conditioning circuit over its constant-charge counterpart if and only if, defining $\eta := C_{\max}/C_{\min}$

$$C_0 \leqslant C_{\min} \left(1 + \frac{V_{\max}}{V_\mathrm{T}} \frac{(\eta - 1)^2}{\eta} \right). \tag{1.25}$$

This may restrict C_0 to values that are too small in order to guarantee the constant-voltage operation (see (1.22). We could have taken into account the non-idealities linked to the inductor parasitic resistance, the other diodes or the switches ON-state resistance. That would have made the condition (1.25) even more restrictive. This is fundamentally due to the fact that the energy that this constant-voltage conditioning circuit needs to transfer in order to implement the energy conversion scheme is much larger than its constant-charge counterpart.

This simple example shows that comparing e-VEHs using different conditioning schemes depends on how each of them is implemented, i.e., on the conditioning circuit. Depending on the application constraints, different conditioning circuits implementing the same conditioning scheme will also have different performances. It is worth mentioning that Mitcheson *et al.* did an extensive comparison of two constant-charge and constant voltage conditioning circuits in [MG12]. Their study takes into account different parameters including the input characteristics, several electrical non-idealities, as well as the role of the electromechanical coupling on the complete e-VEH's system dynamics, that we now move on to discuss.

1.3.4 Electrical and electromechanical domain study

In the study of the circuits above, we started by an hypothesis on the variation of C_t in between extreme values C_max and C_min. This means that $C_\mathrm{t}(t)$ was considered as an input, just like in the introductory example of Sec. 1.2.1. Doing so allows one to isolate the analysis of the electrical interface from the rest of the e-VEH system, and is called the electrical domain analysis. Meaningful insights on the operation of a conditioning circuit can be drawn from such an analysis.

However, as the physical models in Sec. 1.2.2 show, in an e-VEH, the evolution of the transducer's capacitance value $C_\mathrm{t}(x(t))$ is a consequence of the inertial mass' position, which itself results from the overall dynamics of the system. The electrical and mechanical dynamics are interleaved within this system. Hence, it is ultimately necessary to study the dynamics of the complete e-VEH system, given a specific mechanical structure and conditioning circuit. This is referred to as the electromechanical domain analysis. This analysis is of major importance for purposes of design and optimization of e-VEHs, i.e., in order to explore the parameter space. For e-VEHs, this parameter space includes the device's dimensions (e.g., the transducer's gap at rest d_0, or the displacement limits x_M), its mechanical attributes (e.g., the spring stiffness k), the attributes of its electrical conditioning (e.g., V_0 for the constant-voltage conditioning circuit), or the type of input we wish to study (e.g., harmonic inputs with a given range of frequencies).

The nonlinear nature of the electrostatic force (1.6), and of the conditioning circuits such as the constant-charge or constant-voltage conditioning circuits that exhibit non-smooth, piecewise-defined dynamics, make the electromechanical domain analysis complex. Nonlinearity in the mechanical domain (such as the Duffing-type discussed in Sec. 1.2.2.3, or the collisions with the end-stops) make the analysis even trickier. The subsequent system can give birth to a wide variety of behaviors that are fundamentally due to its nonlinear dynamics.

To illustrate the nonlinearity on a simple, concrete example, consider the case of a resonant e-VEH, with gap-closing geometry, using the primitive conditioning circuit, and harmonic input force of frequency ω and amplitude ξ_0. Let us not bother about displacement limitations. The corresponding model reads:

$$\begin{cases} m\ddot{x} + kx + c\dot{x} \; - \dfrac{1}{2}Q_\mathrm{t}^2 \dfrac{x}{\varepsilon_0 d_0 S} & = \xi_0 \cos(\omega t) \\ \dot{Q}_\mathrm{t} + Q_\mathrm{t} \dfrac{{d_0}^2 - x^2}{2\varepsilon_0 R d_0 S} & = \dfrac{V_0}{R} \end{cases} \tag{1.26}$$

which have to be solved for x and Q_t for a given initial condition on x, $\dot{x}$ and Q_t. This example clearly shows the nonlinearity of the differential system modeling the e-VEH. Using a

conditioning circuit of higher order (higher dimensional state) and piecewise-defined dynamics further adds non-smooth nonlinearities. In general, such so-called nonlinear oscillators can have a rich variety of qualitatively different dynamics [GH13], and the structure of system yielded by e-VEH models is no exception. Yet, note that for some particular couples of (transducer geometry ; electrical interface) (the latter is essentially the primitive conditioning circuit), a linear model can capture the dynamics of the system. The subsequent model is called the linear two-ports model. It has been extensively studied for the analysis and optimization of such configurations of e-VEHs [TLH16].

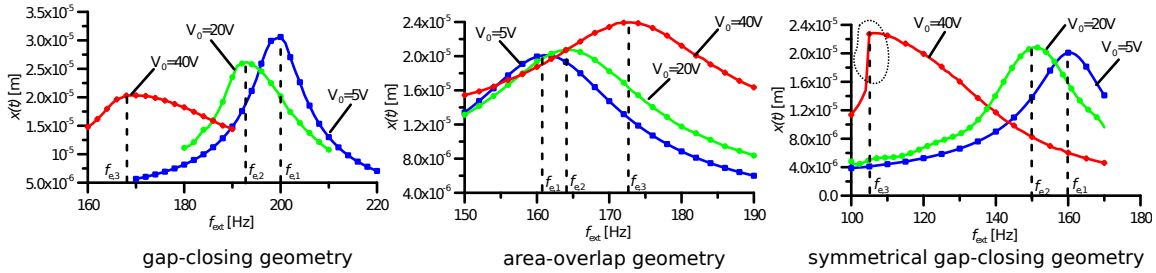

Figure 1.18: Amplitude of oscillating displacement $x(t)$ as a function of the frequency of the harmonic input force, for an e-VEH following the model (1.15) with linear stiffness, and using the primitive conditioning circuit with three different values of the voltage V_0. The plots are made for the three aforementioned geometries

In the electromechanical study of e-VEHs, an interesting metric is the response of the e-VEH, in terms of mass displacement, and/or converted power, to harmonic input forces of varying frequency. This figure carries interesting information about the performance of the harvester, and at the same time conveys informations about eventual nonlinear effects. For example, Fig. 1.18 depicts some obtained frequency responses for the primitive conditioning circuit with the model given above for all three presented geometries of electrostatic transducers, and of typical dimensions for small-scale devices. Each point corresponds to the steady-state amplitude of the oscillatory response in $x(t)$ obtained for harmonic inputs of fixed amplitude and varied frequency. The effect of the transducer force is clearly visible: whereas the steady-state amplitude for $V_0 = 5\,\mathrm{V}$ resembles that of the e-VEH's linear resonator (the electromechanical coupling is low because of the low voltage), when the voltage is varied, the response is shifted towards lower frequencies (spring-softening effect) or higher frequencies (spring-hardening effect) depending on the used transducer geometry. In particular, the red curve for the symmetrical gap closing, corresponding to the primitive conditioning circuit with $V_0 = 40\,\mathrm{V}$, shows a hallmark of nonlinear oscillators. It is an asymmetry in the amplitude vs. frequency curve, which is linked to a hysteresis in the frequency response. This phenomenon is often tied with multi-modality, which refers the fact that multiple oscillatory steady-state solutions $x(t)$ of different amplitudes coexist. Which will be observed in practice depends of the system's initial state, as well as the stability properties of the periodic orbit in the phase space that corresponds to each solution (see, e.g., Chap. 7 of [Kha02]). This type of behavior in the frequency domain is similar to that is witnessed with the Duffing equation (see, e.g., Chap. 4 of [GH13]).

For analysis, design and optimization purposes, it is desirable to be able to access and compute characteristics such as this frequency response, from other means than that of simulations. In order to do so, one can employ the so-called averaging or perturbation methods [BO13]. Such methods yield analytical approximations of the actual system's dynamics. Compared to simulations, not only this accelerates the computation time, but also yields insights on the relative role

of some of the system's parameters on the e-VEH's dynamics and hence on its performances in terms of converted energy.

These methods were used by our group in collaboration with Blokhina's group in multiple works, in order to carry out the electromechanical study of resonant e-VEHs using several electrical conditioning circuits, geometries of transducers, and mechanical features. For example, the work in [BGB13] studies the case of an e-VEH using the constant-charge conditioning circuit, while [OGB16] carries such a study for the primitive conditioning circuit. These works have shown evidence of multiple nonlinear phenomena that occur in e-VEHs studied as nonlinear oscillators. These phenomena include multi-modality, period-doubling and chaos. Notably, Blokhina *et al.*, in [BGH12], have applied perturbation methods to analytically derive the absolute limit of harvested energy for harmonically driven e-VEHs using the constant-charge conditioning circuit. This physical limit cannot be surpassed in the hypothesis set by the model used by Blokhina *et al.*. The study of the constant-charge conditioning circuit in the electrical domain cannot lead to such physical limits.

Within the present work, the Sec. 4.3 in Chap. 4 will use a harmonic balance method in order to enable the comparison of several conditioning circuits studied in the electromechanical domain. This analysis is carried out using the knowledge of the electrical domain dynamics of these conditioning circuits.

1.4 Micro-electromechanical structures for electrostatic transducers

One of the main features that makes electrostatic transduction interesting for small-scale VEH is its compatibility with batch fabrication processes used for MEMS (micro-electromechanical system) device engineering. This enables mass production at low cost per device. In particular, the fabrication of silicon-based electrostatic transducers for KEH benefits from the maturity of the associated micro-machining technologies, based on the experience gained from using these technologies for integrated circuits fabrication.

In this section, we quickly describe the fabrication of such small-scale electrostatic transducers. We then present electret charging, a technique often used in e-VEHs in order to provide the preexisting biasing needed by the electrostatic transducer. This section ends with some examples of reported mechanical structures for e-VEHs. In particular, we present the structure of the devices that are used in experiments throughout this manuscript.

1.4.1 Structure fabrication

Let us briefly describe the silicon bulk process, used to fabricate the majority of reported micro-scale e-VEHs. Silicon bulk process fabrication technology consists of fabricating the movable parts by etching a crystalline silicon wafer over several tens or even hundreds of micrometers. MEMS technologies, similarly to ICs, are based on photolithography. This step is depicted in Fig. 1.19. For each material layer, the patterns to be etched are first designed using a Computer Assisted Design (CAD) software. These patterns are then reproduced on a metal layer (usually chrome) deposited on a quartz plate thanks to e-beam lithography. This quartz plate is called

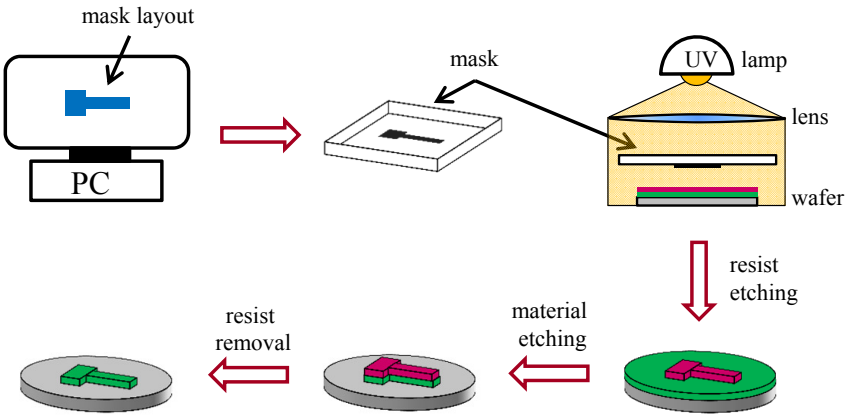

Figure 1.19: Simplified steps of photolithography.

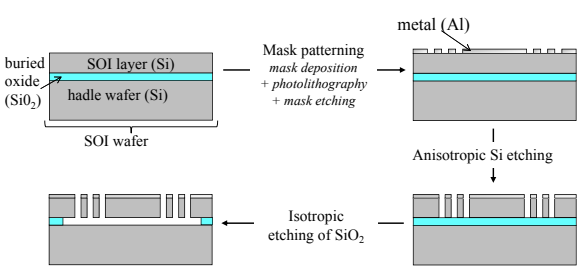

(a) Bulk process fabrications steps using SOI wafers.

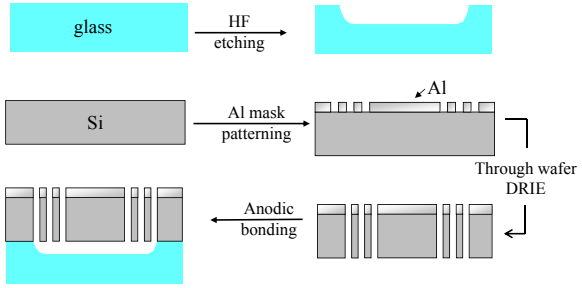

(b) Bulk process fabrications steps using silicon-glass.

Figure 1.20: Bulk processes for the fabrication of MEMS electrostatic transducers used in e-VEH.

a photo-mask and is now partially transparent. It will serve as a template to insolate by UV light a photoresist layer which is deposited on top of the wafer to be etched. Hence, the UV light insolates the resist only where the chrome has been removed from the mask. This creates a chemical reaction in the resist, making it easy to remove following the mask patterns.

The simplest way to obtain a bulk-silicon e-VEH is to use a Silicon On Insulator (SOI) wafer. SOI wafers are actually made of 2 silicon wafers separated by a thin insulating layer, generally made of silicon dioxide (SiO2). The bottom wafer, also called handle wafer, usually has no specific role except for supporting the top silicon wafer, the actual SOI layer.

In the simplest case, only three steps and one photomask are required to fabricate a device, as depicted in Fig. 1.20a. The first step consists of depositing a mask on top of the SOI layer, which is patterned by photolithography, and used as a protection layer for the silicon etching. Once the SOI layer has been vertically etched by Deep Reactive Ion Etching (DRIE), the buried oxide layer is isotropically etched by hydrofluoric acid.

With SOI wafers, the electrostatic transducer can only be made with vertical electrodes etched in the SOI layer. An alternative is to process two separate wafers and to bind them together. In this way, the transducer's electrodes can be made in the same layer, or can be located on both substrates. Usually, a silicon wafer contains the mobile electrode(s), and the second wafer, which is not necessarily made of silicon, is part of the e-VEH's frame and supports the fixed electrode(s). A bulk process using a two-wafer technology (one silicon and one glass wafers) is depicted in Fig. 1.20b. It requires two photomasks in order to obtain vertical electrodes in the silicon wafer.

Finally, let us mention that other technologies are also used for the fabrication of e-VEH's mechanical structure. One example is the usage of thin-films of polysilicon, which is also based on silicon micro-machining techniques. Another example has been reported by De Queiroz *et al.* in [QO16], with 3D-printed e-VEH structures made of acrylonitrile butadiene styrene, a thermoplastic polymer.

1.4.2 Built-in voltage

The property of e-VEHs that an initial bias is needed in order to bootstrap the energy conversion process makes necessary a pre charge. There are essentially two different ways to obtain this pre charge. The first way is to have an energy tank in the system, as in the foregoing conditioning circuits in which the voltage source V_1 plays this role. The other possibility is to make use of a type of active material called an electret.

1.4.2.1 Charging of a micro-electromechanical electrostatic transducer

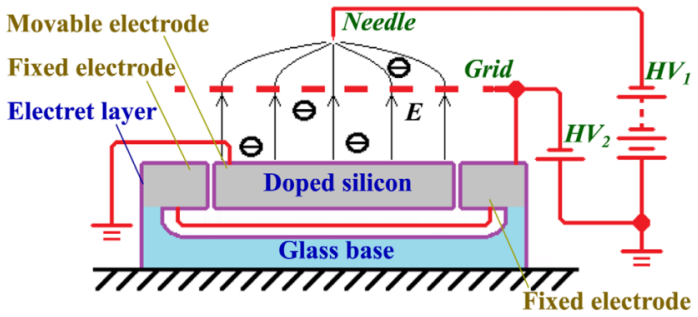

Figure 1.21: Simplified schematic of the Corona charging method of an electret layer. [LOC16]

The built-in voltage (i.e., electret) for electrostatic transducers is obtained by adding a layer of a dielectric material to the structure (e.g., parylene, silicon dioxide, Teflon or cytop), in which electrical charges are (quasi-)permanently trapped. There are several techniques allowing to obtain this charging. In particular, the Corona discharge method is used to obtain the electret-charged devices used in this manuscript. This method roughly consists in ionizing the air surrounding the device on which the dielectric layer is deposited. This is done by putting a conductive grid at high voltage on the top of the structure, while the movable part is grounded. The setup for the charging is depicted in Fig. 1.21, and more information about the charging process can be found in [LOC16]. Apart from Corona discharge, other methods to charge dielectric layers to obtain electrets include X-ray or vacuum UV charging [Suz11].

1.4.2.2 Electrical model of an electret charged electrostatic transducer

We now proceed to derive an electrical lumped model for electrostatic transducers having a charged dielectric layer (or electret) as described above.

Let us suppose that the additional thin dielectric layer has a thickness d_{E} and a relative dielectric constant ε_{E}. In this layer, a total charge of Q_{E} is trapped. This physical situation is depicted in Fig. 1.22a.

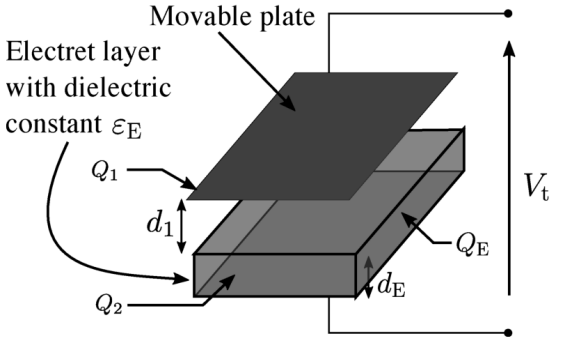

(a) Physical representation of an electrostatic transducer with a charged electret layer.

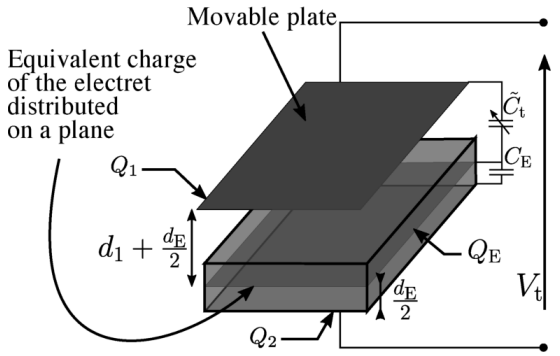

(b) Equivalent representation where the electret charges are distributed on a plane in the middle of the layer.

Figure 1.22: Electrostatic transducer with a charged electret layer.

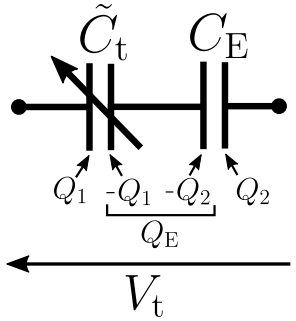

(a) Electrical model of a transducer with an electret layer.

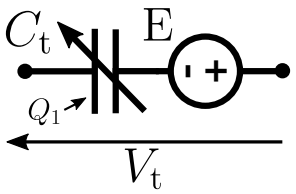

(b) Electrical model of a transducer with an electret layer, separating the variable capacitor and biasing elements.

Figure 1.23: Electrical modeling of an electrostatic transducer featuring a charged electret layer.

In order for the obtained transducer to be electrically neutral, as required by the theory of circuits for dipoles, the sum of the charges on both electrodes of the transducer plus the electret layer has to be null. If Q_1 and Q_2 denote the charges on each of the electrostatic transducer's electrodes, this translates to

$$Q_1 + Q_2 + Q_\mathrm{E} = 0. \tag{1.27}$$

Let us further suppose that the charge distribution across the electret layer is uniform. From the laws of electrostatics, we may equivalently consider that the charges Q_E in the dielectric layer are located on an infinite uniformly charged plane located in the middle of the dielectric layer, without changing the electrical field outside of the material [PFC97]. This equivalent transformation is depicted in Fig. 1.22b. As the planes are conductive, in this situation, we have two capacitors $\tilde{C}_\mathrm{t}$ and C_E connected in series, of values

$$\begin{aligned} \tilde{C}_\mathrm{t} &= \frac{2\varepsilon_0\varepsilon_\mathrm{E} S}{2\varepsilon_\mathrm{E} d_1 + d_\mathrm{E}}, \\ C_\mathrm{E} &= \frac{2\varepsilon_0\varepsilon_\mathrm{E} S}{d_\mathrm{E}}. \end{aligned} \tag{1.28}$$

where d_1 is the gap in between the dielectric material and the electrode at the other end. As before, we suppose that the part of this gap outside the deposited layer is made of air, such that its relative dielectric constant can be assumed to be 1. The obtained equivalent capacitance is denoted by C_t. Denoting by $\tilde{V}_\mathrm{t}$ the voltage across $\tilde{C}_\mathrm{t}$ and by E the voltage across C_E, we can now write

$$V_\mathrm{t} = \tilde{V}_\mathrm{t} - E = \frac{Q_1}{\tilde{C}_\mathrm{t}} - \frac{Q_2}{C_\mathrm{E}} \tag{1.29}$$

which, by (1.27), becomes

$$V_\mathrm{t} = Q_1 \left(\frac{1}{\tilde{C}_\mathrm{t}} + \frac{1}{C_\mathrm{E}} \right) + Q_\mathrm{E} \frac{1}{C_\mathrm{E}} = \frac{Q_1}{C_\mathrm{t}} + E \tag{1.30}$$

Thus, the lumped electrical model of an electret e-VEH is a dipole constituted of a variable capacitor C_t and a DC voltage source of value E. It is depicted in Fig. 1.23b. This is the model of the electret we are going to use in the rest of this manuscript.

For this derivation, we made the hypothesis of a dielectric layer that is infinite in the directions of the electrodes plane, as well as an hypothesis of uniform charge distribution. Note that Le *et al.* have derived an lumped electrical model of transducers supposing finite patches of charged dieletric by accounting for the boundary effects [LH17]. Also, Chap. 5 presents a method allowing for the measurement of an equivalent voltages source E for the electret, for non-necessarily uniform charge distributions across the electret layer.

1.4.3 Examples of reported structures

Let us briefly present some fabricated electrostatic transducers for e-VEH that were reported until now.

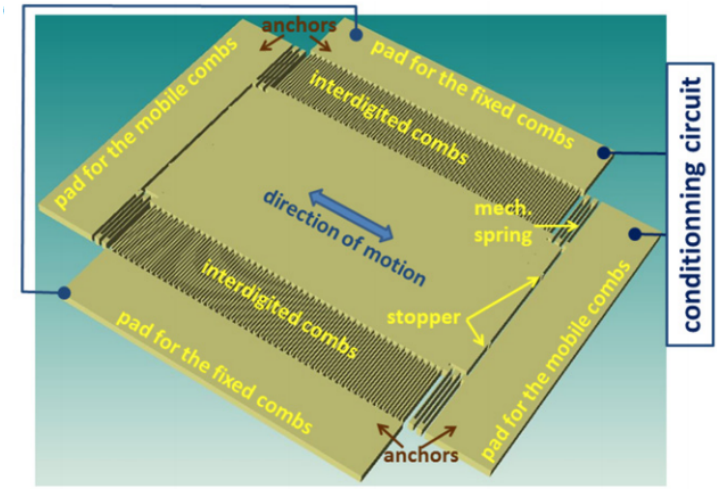

(a) Schematic of the device.

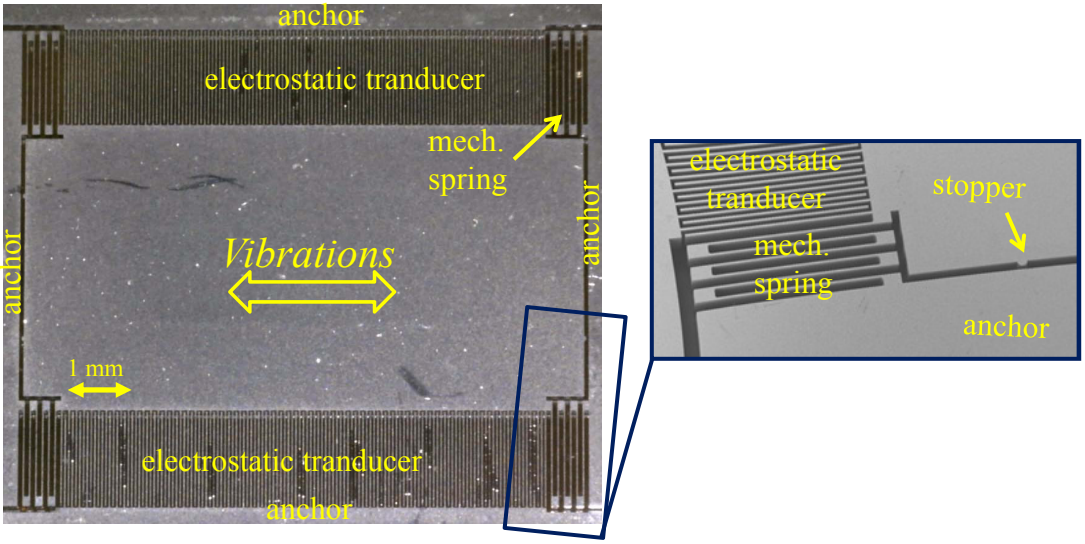

(b) Annotated top-view picture of the device.

Figure 1.24: Mechanical structure of a symmetrical gap-closing electrostatic transducer fabricated by our group [Gui12], and used throughout this manuscrit.

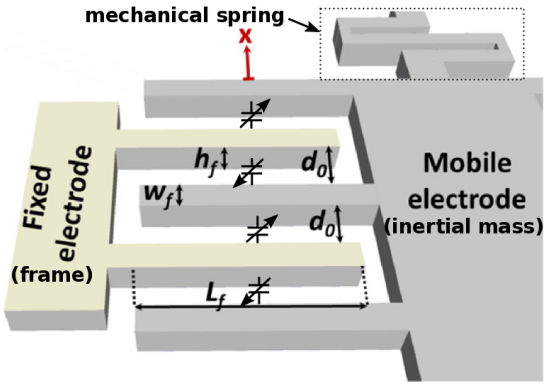

Figure 1.25: A close-up schematic on the fingers of an interdigitated, symmetrical gap-closing electrostatic transducer such as the one depicted in Fig. 1.24. [Gui12]

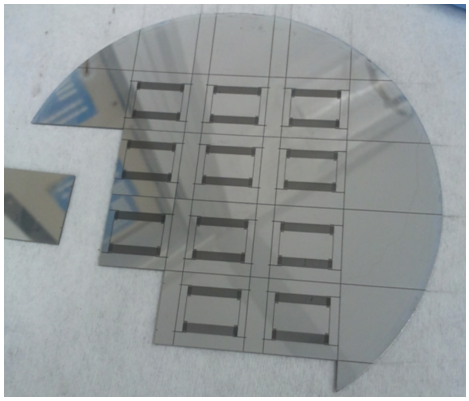

Figure 1.26: A wafer with several devices of the structure depicted in Fig. 1.24. [Gui12]

1.4.3.1 The symmetrical gap-closing structure used in this work

The mechanical structure depicted in Fig. 1.24 is fabricated at ESIEE Paris. It is the structure on which all of the transducers used in experimental work in this thesis are based on. Its mobile part is entirely fabricated in silicon, and is fixed on a glass wafer, following the process presented above and illustrated in Fig. 1.20b.

The device has the structure of a mechanical resonator. The springs are engineered in order to only allow movement on one axis. The electrostatic transducer is of symmetrical gap-closing geometry, obtained thanks to interdigitated fingers. The total capacitance is the sum of all symmetrical gap closing capacitances formed by the fingers, as Fig. 1.25 clarifies. The figure 1.24 also shows the mechanical end-stops or stoppers, that take the form of a small outgrowth at both ends of the inertial mass, colliding with the structure's frame in order to prevent electrode contact.

If the device has a total of N fingers (so $N/2$ at each side of the mass, see Fig. 1.24 where they are called "combs"), with the dimensions notations of Fig. 1.25, the device's capacitance versus displacement reads

$$C_{\mathrm{t}}(x) = \varepsilon_0 \frac{2 d_0 L_{\mathrm{f}} h_{\mathrm{f}}}{{d_0}^2 - x^2} \tag{1.31}$$

This is simply obtained by substituting the right geometrical parameters in (1.9): the total surface is the surface of each finger ($L_{\mathrm{f}} \times h_{\mathrm{f}}$) times the total number of fingers (N). If we further denote by d_{st} the gap between the device and the frame at the end-stop outgrowth (the distance between the "stopper" and the "anchor" in Fig. 1.24b), then the transducer's maximal capacitance that can be attained by the

$$C_{\max} = C_{\mathrm{t}}(d_{\mathrm{st}}) = \varepsilon_0 \frac{2 d_0 L_{\mathrm{f}} h_{\mathrm{f}}}{{d_0}^2 - {d_{\mathrm{st}}}^2}, \tag{1.32}$$

while the capacitance at rest ($x = 0$) which is also the minimal capacitance for the symmetrical gap-closing geometry, reads

$$C_{\min} = C_{\mathrm{t}}(0) = \varepsilon_0 \frac{2 L_{\mathrm{f}} h_{\mathrm{f}}}{d_0}. \tag{1.33}$$

In the following of the manuscript, we will refer to the values of the geometrical parameters of a device "as read on the layout". This means that the corresponding values are computed from the values of the geometrical parameters, as read on the layout file used for the fabrication (produced at step 1 in Fig 1.19). This will be also the case for the overall inertial mass dimension, from which we can get the mass value, by multiplying it by the silicon density. The same also goes for the value of the linear spring constant lumped parameter, which we deduct from the geometry of the silicon beams that constitute the physical springs. Given the geometry of the beams forming the springs, we use the so-called "clamped-free" formula, which gives the equivalent, lumped stiffness of each spring of the structure, and reads $k_0 = E h_{\mathrm{b}} {w_{\mathrm{b}}}^3 / {l_{\mathrm{b}}}^3 / N_{\mathrm{k}}$. In this formula, E is the silicon's Young modulus that we will take equal to 192 GPa, w_b is the width of each beam forming the spring, l_{b} is the length of each beam forming the spring (one sees on Fig. 1.24b that all the beams have the same width and length), and N_{k} is the number of parallel beams of length l_{b} that form each spring. The linear spring constant is then obtained by adding the linear spring constants of the four springs of the structure, that is, $k = 4k_0$, as each spring is identical in this structure.

Finally, note that a device that we will encounter in this manuscript and that is based on the structure structure described above, is charged by an electret (Chap. 5). This charging is obtained by a parylene layer which is deposited on the device, and then charged by the Corona technique, as discussed in the previous subsection.

1.4.3.2 Example of a gap-closing structure

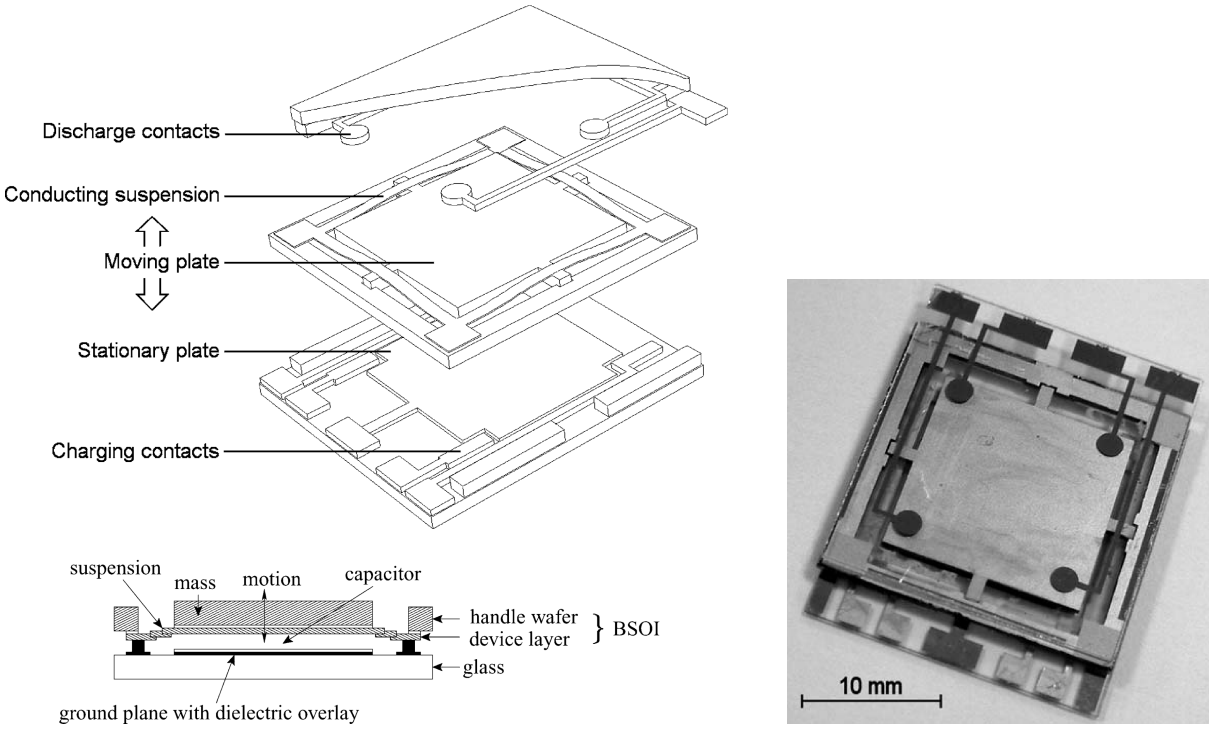

(a) Schematic of the device.

(b) Top-view picture of the device.

Figure 1.27: Mechanical structure of a gap-closing electrostatic transducer by the group of Miao *et al.* [MMH06].

The device depicted in Fig. 1.27 was fabricated by Miao *et al.* [MMH06]. It is an example of a gap-closing geometry, made of two rectangular plates. The inertial mass is the transducer's mobile electrode: the structure of the device is similar to what is depicted in the schematic of Fig. 1.12.

The device is obtained by separately fabricating the three parts of the structure, visible on the exploded view in Fig. 1.27a, on different wafers. The inertial mass is engineered in silicon following a bulk process. It is separated from the e-VEH's frame by DRIE. The mass that is the transducer's mobile electrode is suspended to the frame using polyimide suspensions, thus forming a resonator of low spring stiffness k. The mechanical end-stops are used as charging and discharging end-stops in this device.

1.4.3.3 Example of an area-overlap structure

Finally, let us show an example of an area overlap transducer, depicted in Fig. 1.28. As for the symmetrical gap closing device of Sec. 1.24, it has an interdigitated geometry. This structure was reported by Koga *et al.* [KMH17], fabricated using an SOI-based bulk-process. The device

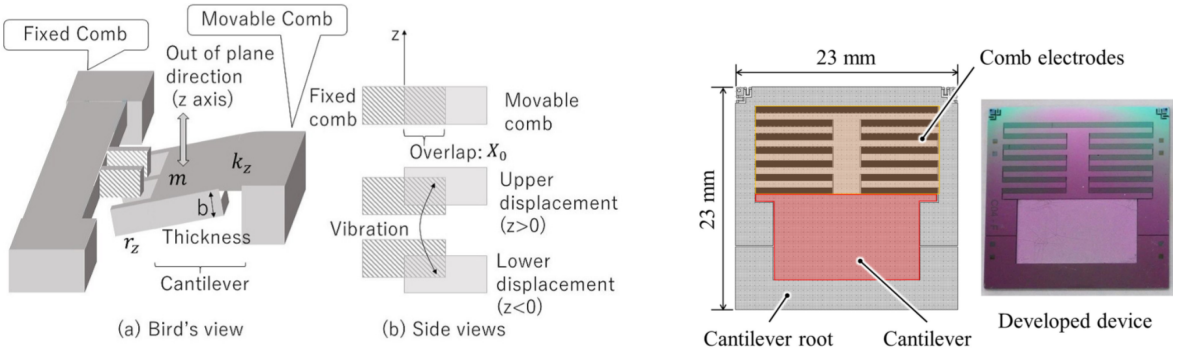

(a) Schematic of the device. **(b)** Top-view picture of the device.

Figure 1.28: Mechanical structure of an area-overlap electrostatic transducer by the group of Koga *et al.* [KMH17].

as reported in this work features an electret layer, obtained by a different technique from the Corona charging described above, namely electro-thermal polarization in silicon oxide using potassium ions.

1.5 Experimental considerations

Throughout this document, results of experiments will be presented at various points. An annotated picture giving an overview of the experimental setup can be found in Fig. 1.29. The mechanical shaker and its controller allow one to submit an inertial e-VEH fixed to its plate to a given, bounded acceleration function.

Below, we describe two experiments that will be referenced at multiple occasions throughout this thesis.

1.5.1 Synchronous detection

The synchronous detection technique allows for the measurement of the the transducer's variable capacitance value evolution over time, that is, $C_\mathrm{t}(t)$. The experimental setup used for this measurement is depicted in Fig. 1.30. The transducer is put in the same electrical configuration as for the primitive conditioning circuit presented in Sec. 1.3.2.3. The electrostatic device that is to be characterized is attached to the movable plate of the shaker. A sinusoidal signal of frequency ω_c and low amplitude is fed to the circuit, as depicted in the experimental setup figure.

While the shaker vibrates at the amplitude and frequency for which $C_\mathrm{t}(t)$ is desired to be measured, both the carrier signal and the voltage across the resistor are read through two amplifiers. Hence, the RC_t cell acts as a variable cutoff frequency high-pass filter. In particular, at each time t, the instantaneous phase shift $\theta(t)$ between the carrier signal and the voltage across the resistor is a function of $C_\mathrm{t}(t)$. Inverting the relation, $C_\mathrm{t}(t)$ can be expressed as

$$C_\mathrm{t}(t) = \frac{1}{\tan(\theta(t))R_\mathrm{s}\omega_\mathrm{c}} \tag{1.34}$$

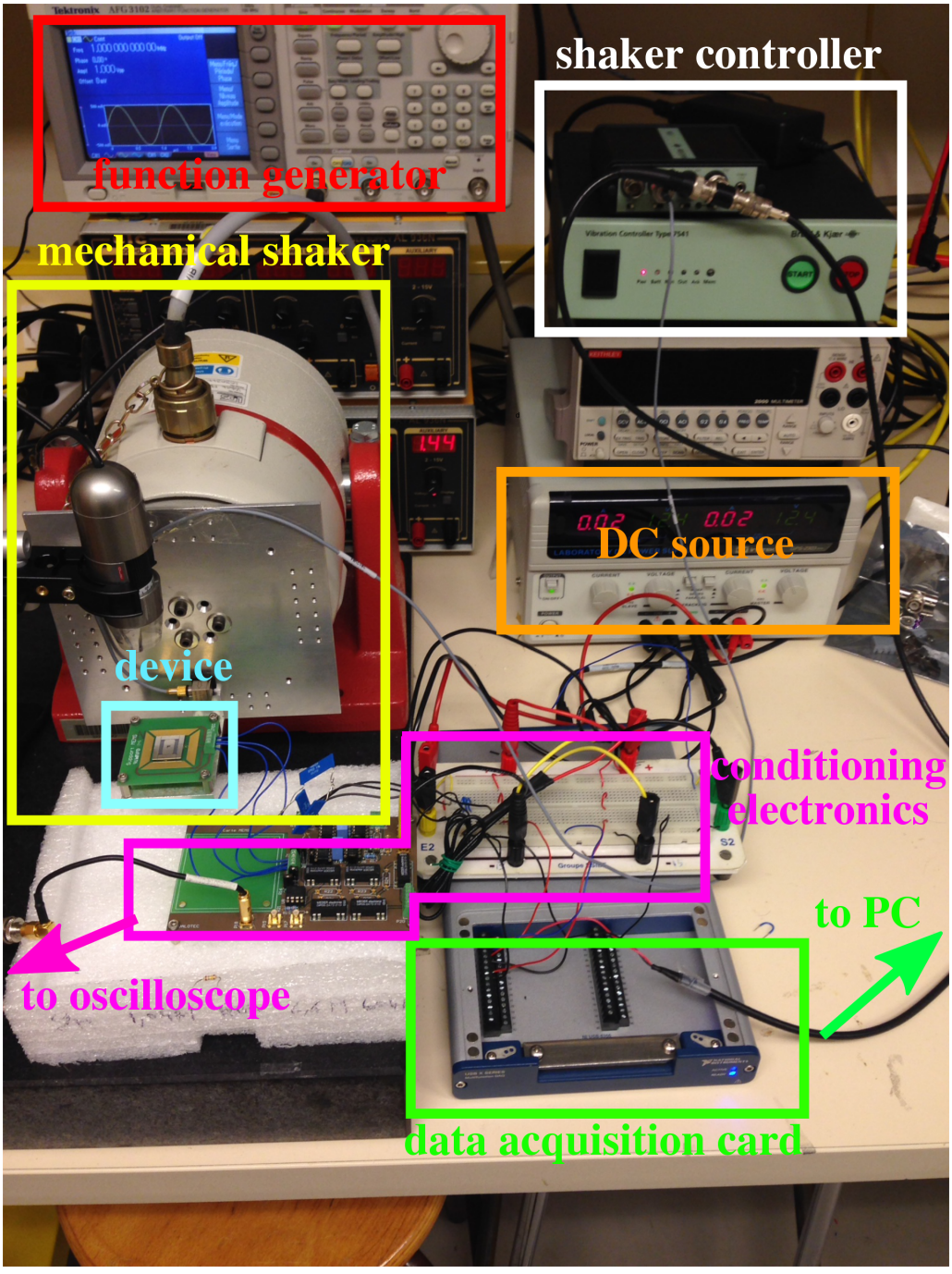

Figure 1.29: Overview of the experimental setup for the experiments done in this thesis.

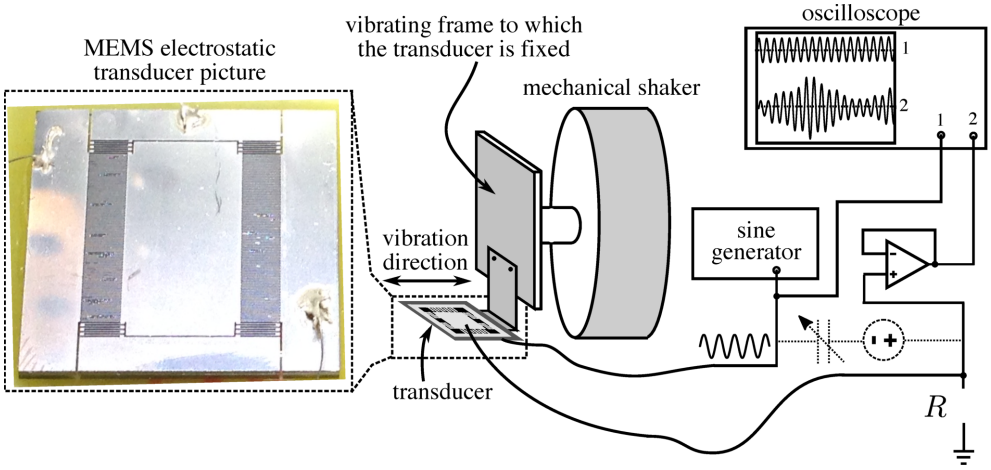

Figure 1.30: Experimental setup for dynamic $C_t(t)$ measurement by synchronous detection.

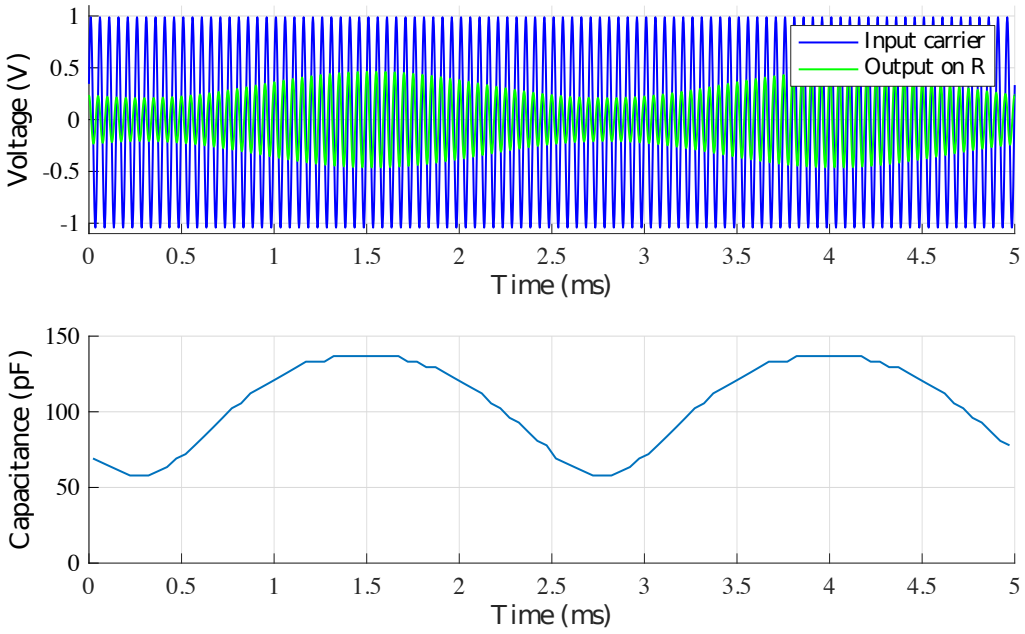

Figure 1.31: Experimental example of a synchronous detection measurement on a device similar to that of Fig. 1.24. On top, the measured waveforms, and under it, the processed waveforms in order to obtain $C_t(t)$.

The value of $C_t(t)$ can be recovered by computing the phase shift between the two measured waveforms over a period of time that corresponds to as much periods of variation of C_t as desired. The results for an example of such a measurement, on a device of the same structure than that of Fig. 1.24, is depicted in Fig. 1.31. The results were obtained by submitting the device to input vibrations of 1 g amplitude and 160 Hz frequency, corresponding to the natural resonant frequency of the mechanical resonator.

1.5.2 Frequency sweep

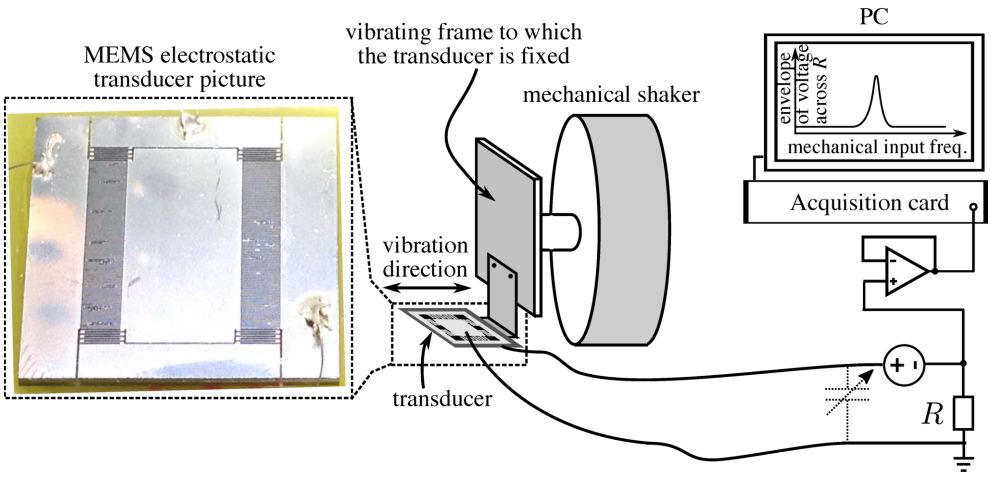

Figure 1.32: Experimental setup for the frequency response characterization of an e-VEH's resonator.

The primitive conditioning circuit configuration is also used in order to measure the frequency profile of an e-VEH's mechanical resonator. To do so, a sinusoidal input acceleration is generated by the shaker. This input acceleration has fixed amplitude and a frequency that slowly varies in time, sweeping from a frequency f_1 to a frequency f_2. The slow variation ensures quasi-static behavior, that is, for each value of the frequency, we may consider that the system does not exhibit a transient behavior due to the change in the input's characteristics. Usually, the first sweep is followed by a downsweep from f_2 to f_1, to exhibit possible nonlinear characteristics of the mechanical resonator, such as hysteresis in the frequency response. For each instantaneous value of the frequency input, fed from the shaker to a data acquisition card, the amplitude of the measured voltage across R is measured. This gives an idea of the response of the resonator at each frequency relatively to the others, as larger displacement and hence larger capacitance variation results in a larger voltage swing across the resistor. This is true given that the value of R is chosen close to the optimal load value discussed in Sec. 1.3.2.3, for the expected variation of C_t near resonance and the used value of the voltage source. The corresponding experimental set-up is depicted in Fig. 1.32. Note that the depicted voltage source can model an eventual electret charging of the transducer.

An example of results of frequency profile characterization, obtained with a device similar to the device presented in Sec. 1.4.3.1, is depicted in Fig. 1.33. The input acceleration used was of 0.3 g. One clearly sees that the linear resonator behavior of the mechanical structure, with a natural frequency of $f_0 = 160$ Hz.

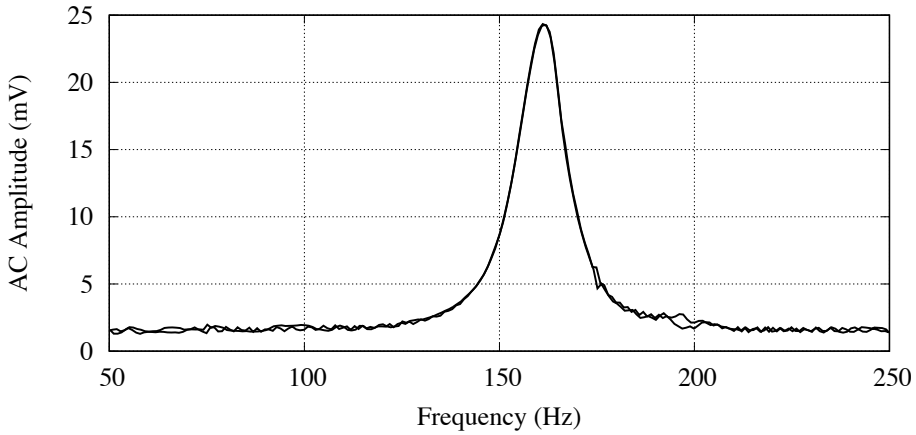

Figure 1.33: Example of a frequency response measured on an electrostatic transducer similar to that of Fig. 1.24.

1.6 Challenges and answers in electrostatic vibration energy harvesting

Over the past twenty years, the research community has investigated the creation of systematic e-VEHs design flows adaptable to different application contexts. Often, such a context is characterized by the form and characteristics of the vibrations that the e-VEH is going to be submitted to. Other context can for example put more emphasis on low fabrication costs, or on the compatibility with human tissue (e.g., as reported by Deterre in [Det13] for a pacemaker application). In e-VEH, the input force characteristics are often summarized in terms of their frequency spectra, as depicted in Fig. 1.4. In fact, a large research effort in e-VEH was put into enabling the design of harvesters that could maximize the amount of converted energy from vibrations of various spectra.

We propose to sort the ideas reported in the literature to maximize the energy output of e-VEHs in three different categories. First, some works are concerned with the enhancement of the e-VEH performance through the design of its mechanical part. Such works often start the design by an idea gained from the mechanical dynamics of the system, aiming for a maximal amplitude of the displacement of the e-VEH's inertial mass. They are the subject of Sec. 1.6.1. The second category encompasses attempts to improve e-VEHs performances starting by an electrical domain study of the electrostatic transducer's conditioning circuits. This is the subject of Sec. 1.6.2. The third category designates the works in which the approach starts from a system-level view of the e-VEH, equally considering the electrical and mechanical parts in a single model. The subsequent decisions on the design of both the electrical and mechanical part are then made on the basis of the system's dynamics captured by this model.

This classification may seem rather porous, because some mechanical designs of the first category then go through analysis when conjuncted to different electrical interfaces. In the same way, electrical interfaces of the second category are often studied in conjunction with the electromechanical coupling effect, as discussed in Sec. 1.3.4. However, the important distinction is in the view (mechanical, electrical or whole system) from which the design ideas originated.

Let us now briefly review some reported works falling into each of these categories. As we are interested in how these ideas can be helpful from a systematic design methodology point-of-

view, we report the basic ideas behind each reported technique, rather than a mere comparison of each realization in terms of harvested energy. A meaningful comparison would require setting very precise specification anyway, as we already pointed out at multiple occasions throughout this chapter. We end this introduction chapter by situating the work done in this thesis within the proposed classification.

1.6.1 Answers from the mechanics

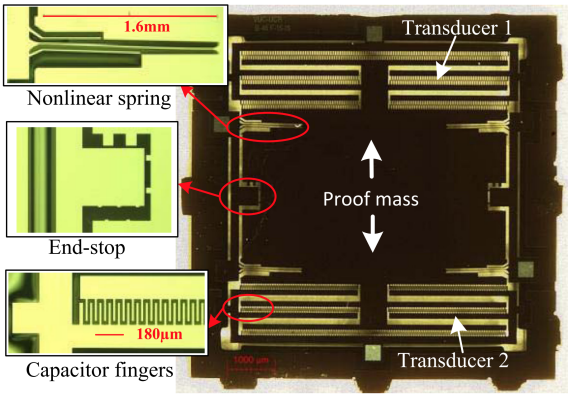

Figure 1.34: Top view annotated picture of an area-overlap electrostatic transducer with springs engineered in order for the resonator to exhibit a bistable potential function [NHP13].

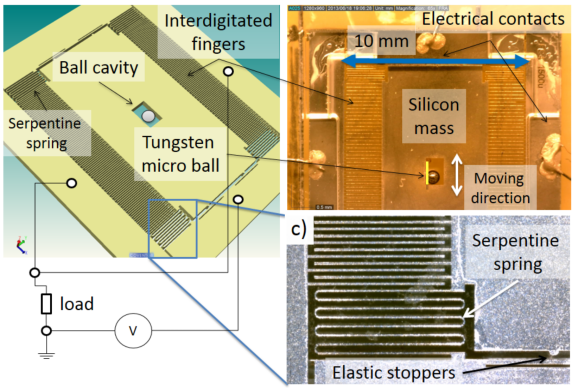

Figure 1.35: Schematic and top view annotated picture of a gap-closing electrostatic transducer with a cavity in which lies a tungsten micro-ball for frequency up conversion [CBM14].

The vast majority of reported inertial e-VEHs are based on a resonant structure, at least because of the necessary suspension of the inertial mass inside the frame of the system. In many reported e-VEHs, the spring-mass system is purposefully designed in a way that the resonant frequency of the subsequent resonator matches that of the targeted application. The motivation for deliberately building the e-VEH upon a resonant mechanical part is to increase the amplitude of the inertial mass' movement from harmonic input vibrations of small amplitudes.

However, resonant systems have a limited bandwidth and hence poorly respond to out-of-tune vibrations in terms of the inertial mass' movement. From this observations, many works proceeded to designing the e-VEHs mechanical part so as to introduce different kinds of nonlinearities, which result in improved bandwidth. Also, because mass decreases with decreased device dimensions, and the natural frequency of a linear resonator is inversely proportional to the square root of the mass, smaller scale devices are seldom compatible with low frequency vibrations.

Hence, many techniques were investigated in order to improve the response of e-VEHs to either low-frequency inputs, either large-bandwidth inputs, in terms of the amplitude of the resulting inertial mass movement. A first example is the use of bi-stability. This refers to the quartic potential function (resulting in $k(x) = k + k_3x^3$ in (1.15)) of the so-called bi-stable nonlinear resonators, which exhibit two stable equilibra instead of only one with quadratic potentials ($k(x) = -k$ in (1.15)) of linear resonators. Some experimental investigations, e.g., in [CVG09], show that such structures can be beneficial in order to convert energy from wide-band vibration inputs. The structure of Nguyen *et al.*, reported in [NHP13] and depicted here in Fig. 1.34, is an example of a bi-stable e-VEH mechanical structure.

Another investigated possibility is to use frequency-up conversion. This terms refers to the implementation of a mechanism to convert vibrations of low frequencies to inputs to which a underlying linear resonator is responsive. An e-VEH with a frequency-up conversion feature has been proposed by Cottone *et al.* in [CBM14], and it is depicted in Fig. 1.35. The frequency up-conversion happens thanks to the free movement of a micro-ball inside a cavity trenched in the inertial mass. Under vibrations of low frequencies, this ball regularly excites the underlying resonator by impulses happening at each collisions. As a result, the resonator's mass oscillates with increased amplitude at its natural frequency.

Other examples of methods to improve the bandwidth of the e-VEHs input vibration-to-displacement response include using the nonlinearity induced by the e-VEH's end-stops, and/or softening or hardening springs [BGC14].

Furthermore, parasitic mechanical damping due to air friction is responsible for a shortfall in the converted energy. To this end, the vacuum-packaging of e-VEHs was investigated, for example by Elfrink *et al.* in [ERK10]. Although this latter work is applied to the piezoelectric transduction case, vacuum packaging is also compatible with electrostatic VEHs. Some other works done in our group have investigated new geometries for interdigitated electrostatic transducers in order to reduce mechanical friction effects. See, e.g., [LMG17] by Lu *et al.*.

1.6.2 Answers from the electronics

The study of conditioning circuits for electrostatic transducers has drawn a lot of attention from teams of researcher in electrical and electronics engineering worldwide. The dependence of the harvested energy on the electrical conditioning scheme of the electrostatic transducer has been identified very quickly, as well as the points raised in Sec. 1.3.2.1, particularly on the coupled but distincts tasks of transducer conditioning and load supply regulation. The seminal and celebrated work of Meninger *et al.* in [MMA01] had already pointed out this distinction. The same work carried out a comparison of the constant-charge and constant-voltage conditioning schemes, although on the sole basis of the electrical conditioning scheme. Subsequent works, such as the previously cited work by Mitcheson *et al.* in [MG12], carried out a more advanced comparison of these two conditioning schemes.

In parallel, research has been done on the circuit design side in order to come up with low power realizations of each of these conditioning circuits, as for the practical realization of the constant-voltage conditioning circuit that we have already cited previously, by Torres *et al.* in [TR10]. It is implemented in Bi-CMOS technology, and a picture of the chip is shown in Fig. 1.36.

The two constant-charge and constant-voltage circuits need a command synchronized with the mass' external vibrations. This can be difficult or costly to achieve in terms of energy consumption, especially if the input vibrations are of high frequencies. Subsequently, Roundy *et al.*, in [RWR03], have reported a conditioning circuit that allows the e-VEH to convert energy without needing synchronization. This circuit implements a different conditioning scheme than that of the constant-charge or constant-voltage conditioning circuits. Since then, many other circuits based on Roundy's circuit have been reported. All of these circuits show some common characteristics. These circuits, that will be referred to as ''charge-pump conditioning circuits"

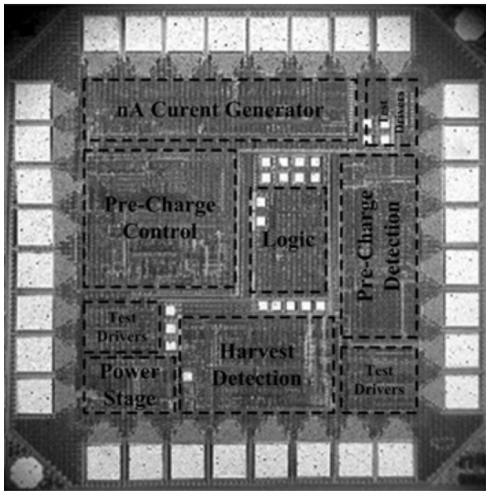

Figure 1.36: Annotated picture of a Bi-CMOS chip implementing the constant-voltage conditioning circuit, by Torres *et al.* [TR10].

throughout this thesis, are the subject of the four next chapters of this manuscript.

Also, note that in many cases, the practical implementation of e-VEHs' electrical interfaces can be challenging due to high-voltage and low-power requirements. We will witness such relatively high voltage values in Chap. 4 and, more dramatically, this requirement will be a very stringent constraint in Chap. 7. Many works were hence directed towards the implementation of all types of conditioning circuits under these constraints [KBH13; Dud14; SLN15].

Finally, it is worth noting that research on improvement of electret charging techniques and materials is conducted with the goal of increasing the obtained potentials, as well as their durability. See, e.g., Tao's work in [TWT17].

1.6.3 Answers from an overall system view of electrostatic vibration energy harvesters

The celebrated work of Mitcheson *et al.* in [MGY04] proposes a classification of several generic architectures of VEHs that are defined by the mathematical form of the transduction force. It sets some limits to the energy conversion accounting for some specific mathematical forms of the transducer force $u(t)$. In particular, it shows that a mere, uncontrolled maximization of the mass displacement, as the works categorized in Sec. 1.6.1 target, does not necessarily yield maximized converted energy. The optimal dynamics are shown to depend on the harmonic input's characteristics, the mechanical parameters such as the linear damping coefficient, and on the form of the transducer force, which in turn depends on which electrical interface that is used. Similar conclusions in a more general setting were drawn by Halvorsen *et al.* in [HLM13]. Halvorsen has also shown in [Hal13], that bistable resonators discussed in Sec. 1.6.1 have, in principle, the same performance compared to their linear counterparts. The experimental results obtained, in, e.g., [CVG09] showing the contrary are in fact due to a suboptimal electrical configuration of the VEH. Again, this shows that the mere isolated optimization of the mechanical behavior of the e-VEH does not necessarily yield optimal e-VEH systems.

In the same way, the optimum performances derived by an electrical domain analysis of an

e-VEH using a given conditioning circuit can be mitigated by the study in the electromechanical domain. This was discussed above in Sec. 1.3.4, and will be shown again in Sec. 4.2 of Chap. 4.

Hence, some theoretical works tackled the design of e-VEHs by starting the analysis from an overall view at the system level. This means that the design decisions originate from the analysis of e-VEH models encompassing both the electrical and mechanical dynamics, such as the models in Sec. 1.12. Because of their complexity, some simplifying hypothesis have to be made, thus restricting the corresponding e-VEH design, but in a controlled manner. For example, the work of Truong *et al.* in [TLH16] starts from the so-called linear two-port model of e-VEHs. This supposes that the corresponding design is constrained to e-VEHs configurations that can be accurately described by this model. These include at least the differential area-overlap electrostatic traducers using particular electrical interfaces which can be viewed as a resistive load. In the context of an e-VEH described by this model, Truong *et al.*'s work guarantees to optimize the converted energy for such e-VEHs by a proper choice of the model's stiffness and electrical load. As a result, it also yields an explicit relation with the bounds on harvested energy that are set by the used model.

The work of Truong *et al.* deals with harmonic vibration inputs, but a similar approach had already been proposed by Halvorsen in [Hal08], in the case of inputs given in terms of their probabilistic distribution (Gaussian) and frequency content (white noise). Such an approach to the design of VEHs has also been investigated extensively with the piezoelectric transduction mechanism, for which the two-port model seems to be descriptive of a wider variety of situations than for e-VEHs. Such works include that of Badel in [Bad05].

On the other hand, in parallel with this thesis, Hosseinloo *et al.*, in [HT15b], proposed the sketch of a system whose architecture is derived from the study of the most generic model of harvester (see (1.4)). Its dynamics are subsequently customizable, and can be chosen in order to maximize the amount of harvested energy from vibrations of, in principle, arbitrary forms. We followed such an approach during this work. We present its principles and clarify the underlying hypotheses in Chap. 6. The architecture of an e-VEH suited to implement these principles is presented in Chap. 7.

1.6.4 Where does this study fit ?

With regard to the foregoing classification, the two main parts of the studies done during this thesis can be categorized as follows.

The first part of this work is concerned with analyzing and extending an existing class of conditioning circuits, the charge-pump conditioning circuits. Roundy's circuit mentioned above is the fundamental example of such circuits. In this thesis, these circuits are first studied in the electrical domain, that is, without considering the whole system dynamics. The motivation behind the use of these circuits originates from their features inferred from an electrical domain analysis. These features are the auto-synchronized property, the absence of inductors, as well as the self-increasing bias (or unstable) property that will be thoroughly discussed in the next chapters. The electromechanical coupling effect is then introduced in the study in order to compare the different conditioning circuits of this class, in Chap. 4. Since the approach taken in this first part of the thesis starts from electronics, it belongs to the approaches categorized in

Sec. 1.6.2.

The second part of the thesis starts from a different methodological approach, first considering a simplified version of the overall e-VEH's lumped model. General principles are derived from this model. This results in an architecture of e-VEH that, in principle, can harvests energy from vibrations of arbitrary forms. This architecture is based on an active mechanical control that is itself synthesized by the e-VEH's electrical interface. This approach follows that of Hosseinloo *et al.* [HT15b], and can be placed in the same category, that is Sec. 1.6.3 above.

Chapter 2

Charge-pump conditioning circuits

The former chapter introduced the prominent role of the conditioning circuit in e-VEHs. The present chapter is devoted to the presentation of a specific family of conditioning circuits, called "charge-pump" conditioning circuits, and which will be the main subject of our study for the three forthcoming chapters. Such conditioning circuits have gained increasing interest because of advantages such that their auto-synchronization with the transducer's capacitance variation, or the fact that they do not comprise inductors.

This chapter attempts to give an unified presentation of the family of charge-pump conditioning circuits. A list of conditioning circuits reported in the literature is presented within this framework. Plus, some of these conditioning circuits (in Sec. 2.3.1.1 and Sec. 2.3.1.2) were already reported in previous works, but are formally analyzed in this chapter, as such analysis was not found in the literature. The role of this chapter is hence twofold: firstly, it presents our unified vision of charge-pump conditioning circuits. Secondly, we use it as an opportunity to list different conditioning circuits that will be referenced through the rest of this manuscript.

The analysis done in this chapter is limited to the electrical domain: here, the transducer is considered a time-varying capacitor, whose value is considered as an input (see Sec. 1.3.4).

The unified presentation and the identification of several of the following circuits as belonging to this same family of charge-pumps was partly published in [GDK15].

2.1 Introduction to charge-pump conditioning circuits

2.1.1 Notations and preliminaries

The notation and terminology given here will be used throughout the present chapter, as well as in the two following, namely Chap. 3 and Chap. 4.

As stated above, this chapter is concerned with the description of a class of conditioning circuits in the electrical domain. This means that the value of the transducer's variable capacitance is considered as an input. We suppose in the following that C_t is time-varying between maximum and minimum values C_max and C_min (not necessarily periodically).

In this chapter and the next, we define a cycle of variation of the capacitance C_t as its variation from its minimal value C_min, to C_max back to C_min, as depicted in Fig. 2.1. Depending on the context, we may sometimes start the analysis of a conditioning circuit from the instant when $C_\mathrm{t} = C_\mathrm{max}$, to $C_\mathrm{t} = C_\mathrm{min}$ and back to $C_\mathrm{t} = C_\mathrm{max}$. The cycles of variation of C_t are indexed by positive integers in the following. We also remind that V_t and Q_t respectively denote the voltage across C_t and the charge it stores.

The quantities indexed by $\overline{n}$ represent the value of the quantity at the instant corresponding the the cycle n, when $C_\mathrm{t} = C_\mathrm{max}$. The quantities index by $\underline{n}$ represent the value of the quantity at the instant corresponding to the cycle n when $C_\mathrm{t} = C_\mathrm{min}$. Fig. 2.1 illustrates these notations. If $t_{\underline{\mathrm{n}}}$ is the time in cycle n when $C_\mathrm{t} = C_\mathrm{max}$ and $t_{\overline{\mathrm{n}}}$ is the time in cycle n when $C_\mathrm{t} = C_\mathrm{min}$, then we choose the convention that

$$\ldots < t_{\underline{\mathrm{n-1}}} < t_{\overline{\mathrm{n-1}}} < t_{\underline{\mathrm{n}}} < t_{\overline{\mathrm{n}}} < t_{\underline{\mathrm{n+1}}} < t_{\overline{\mathrm{n+1}}} < \ldots \tag{2.1}$$

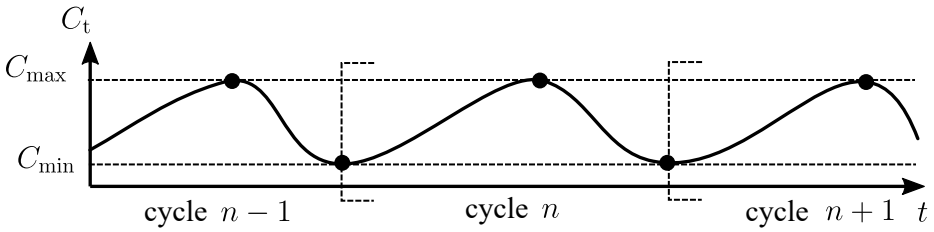

Figure 2.1: Explanation of the cycles of variation of C_t and of the notations.

Also, let us define

$$\eta \coloneqq \frac{C_\mathrm{max}}{C_\mathrm{min}}. \tag{2.2}$$

Finally, note that all the circuit analysis done in this chapter suppose idealized electrical components. In particular, the diodes are supposed to follow the ideal current-voltage law, with zero diode threshold voltage.

2.1.2 The ideal charge-pump

Consider the circuit depicted in Fig. 2.2a, with $0 < V_\mathrm{L} < V_\mathrm{R}$. This circuit will be referred to as the ideal charge-pump circuit in the rest of the manuscript. Its charge-voltage diagram in Fig. 2.2b is the ideal rectangular charge-voltage diagram. Note that the (natural) convention of voltage measurement for C_t depicted here will be used throughout all of the manuscript. It will also be the case for all of the fixed capacitors in all the encountered circuits. More precisely, the voltage orientation for any capacitor is supposed to be oriented in a bottom-top fashion in each of the circuit topologies depicted within this manuscript.

The transducer's electrical model comprises a fixed voltage source $E > 0$, that accounts for an eventual built-in voltage (e.g., obtained from electret charging, see Sec. 1.4.2) of the transducer. If the transducer is devoid of built-in voltage, it suffices to set $E = 0$.

The operation of this circuit can be summarized as such: the variation of C_t allows it to pump charges from a low potential $V_\mathrm{L} + E$ to a higher potential $V_\mathrm{R} + E$, thus increasing their energy.

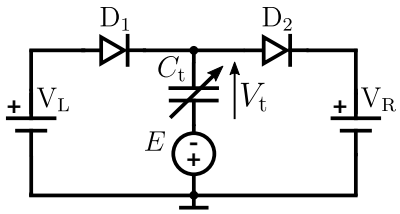

(a) Idealized charge-pump.

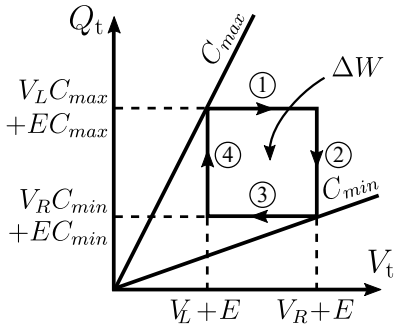

(b) Charge-voltage diagram for the idealized charge-pump

Figure 2.2: Schematic and charge-voltage diagram of the idealized charge-pump.

Let us analyze the behavior of this circuit when C_t is varying such as described above, in order to derive the corresponding charge-voltage diagram, depicted in Fig. 2.2b. In the following, at the scale of one cycle of C_t's variation we will implicitly re-parametrize time in terms of C_t. This is possible because the evolution of C_t is monotonic from C_min to C_max and monotonic from C_max to C_min, thereby defining two one-to-one mappings between time and C_t. Which one of the two is used throughout the variation of C_t in the following descriptions is clear from the context, as we always state "C_t is decreasing" or "C_t is increasing".

We consider a variation cycle of C_t with initially $C_\mathrm{t} = C_\mathrm{max}$. We further suppose that initially, $V_\mathrm{t} = V_\mathrm{L} + E$: we will check at the end of the analysis that we can always suppose so. When C_t decreases from C_max, the voltage across it increases while its charge remains equal to $(V_\mathrm{L} + E)C_\mathrm{max}$, as the diode D_1 blocks conduction. This is the segment ① on the charge-voltage diagram in Fig. 2.2b, corresponding to a constant-charge operation. We hence have

$$C_\mathrm{t} \in [C_1\,; C_\mathrm{max}], \quad \begin{cases} Q_\mathrm{t} = (V_\mathrm{L} + E)C_\mathrm{max}, \\ V_\mathrm{t} = \dfrac{(V_\mathrm{L} + E)C_\mathrm{max}}{C_\mathrm{t}}, \end{cases} \tag{2.3}$$

where

$$C_1 := \frac{V_\mathrm{L} + E}{V_\mathrm{R} + E} C_\mathrm{max} \tag{2.4}$$

This value is effectively attained by C_t (that is, $C_1 > C_\mathrm{min}$) if we suppose that

$$\eta \geqslant \frac{V_\mathrm{R} + E}{V_\mathrm{L} + E} \tag{2.5}$$

Let us continue the analysis with this last hypothesis taken for granted. In this case, when $C_\mathrm{t} = C_1$, it becomes connected to V_R through the diode D_2 and push charges to the potential V_R until it reaches C_min. This corresponds to the segment ② on the charge-voltage diagram in Fig. 2.2a. We have:

$$C_\mathrm{t} \in [C_\mathrm{min}\,; C_1], \quad \begin{cases} Q_\mathrm{t} = (V_\mathrm{R} + E)C_\mathrm{t}, \\ V_\mathrm{t} = V_\mathrm{R} + E. \end{cases} \tag{2.6}$$

Then, a symmetrical process happens: at $C_\mathrm{t} = C_\mathrm{max}$, $V_\mathrm{t} = V_\mathrm{L} + E$, and C_t starts decreasing while the voltage across it decreases and its charge remains equal to $V_\mathrm{R}C_\mathrm{min}$. This is the

segment ③ on the charge-voltage diagram in Fig. 2.2a. We have:

$$C_\mathrm{t} \in [C_\mathrm{min}\,; C_2], \quad \begin{cases} Q_\mathrm{t} = (V_\mathrm{R} + E)C_\mathrm{min}, \\ V_\mathrm{t} = \dfrac{(V_\mathrm{R} + E)C_\mathrm{min}}{C_\mathrm{t}}, \end{cases} \tag{2.7}$$

where

$$C_2 \coloneqq \frac{V_\mathrm{R} + E}{V_\mathrm{L} + E} C_\mathrm{min}. \tag{2.8}$$

which is necessarily attained (that is, $C_2 < C_\mathrm{max}$) under the hypothesis (2.5). Then, when $C_\mathrm{t} = C_2$, it becomes connected to V_L through D_1 and pumps charges from the potential V_L until it reaches C_max. Thus, for this segment, which is labeled ④ on the charge-voltage diagram in Fig. 2.2a, we have:

$$C_\mathrm{t} \in [C_2\,; C_\mathrm{max}], \quad \begin{cases} Q_\mathrm{t} = (V_\mathrm{L} + E)C_\mathrm{t}, \\ V_\mathrm{t} = V_\mathrm{L} + E. \end{cases} \tag{2.9}$$

The process cyclically continues as we are back at to the initial state where $V_\mathrm{t} = V_\mathrm{L}$ and $C_\mathrm{t} = C_\mathrm{max}$.

This almost completes the description of the circuit for a complete cycle of variation of C_t. We now only need to make sure that our initial hypothesis that $V_\mathrm{t} = V_\mathrm{L}$ when $C_\mathrm{t} = C_\mathrm{max}$ does not induce a loss of generality. Let us suppose that $C_\mathrm{t} = C_\mathrm{min}$, and denote by $V_{\mathrm{t},0} > 0$ the value of V_t at that instant, without other additional hypothesis other than that set by the circuit topology, namely that

$$V_\mathrm{L} + E \leqslant V_{\mathrm{t},0} \leqslant V_\mathrm{R} \ + E \tag{2.10}$$

Hence, when C_t increases,

$$C_\mathrm{t} \in [C_\mathrm{min}\,; C_0], \quad V_\mathrm{t} = \frac{V_{\mathrm{t},0} C_\mathrm{min}}{C_\mathrm{t}} \tag{2.11}$$

where

$$C_0 \coloneqq \frac{\mathrm{V}_{\mathrm{t},0}}{V_\mathrm{L} + E} C_\mathrm{min}. \tag{2.12}$$

If (2.5) is satisfied, then as we also have (2.10), C_t necessarily attains C_0 (that is, $C_0 < C_\mathrm{max}$). When it does, D_1 connects C_t and C_L, so that at $C_\mathrm{t} = C_\mathrm{max}$, we have $V_\mathrm{t} = V_\mathrm{L} + E$. From this point on, the preceding analysis can be followed. In summary, the conversion scheme corresponding to the charge-voltage diagram in Fig. 2.2b is reached by the circuit from any initial value of $V_\mathrm{t} \in [V_\mathrm{L} + E\,; V_\mathrm{R} + E]$ and in at most one cycle of variation of C_t, if and only if $\eta > (V_\mathrm{R} + E)/(V_\mathrm{L} + E)$.

If this latter condition is not fulfilled, then C_t has not enough variation amplitude to pump the charges from potential $V_\mathrm{L} + E$ to $V_\mathrm{R} + E$, and no current ever flows within the circuit. In this case V_t merely alternates between two voltage values while Q_t remains constant throughout C_t's variation. Thus, no energy conversion occurs in this setting. This can be seen geometrically, as no rectangle with sides parallel to the Q-axis located at $V_\mathrm{R} + E$ and $V_\mathrm{L} + E$ can fit between the lines of slope C_max and C_min in this case.

The energy converted per cycle ΔW is then readily found by computing the area of the

charge-voltage diagram:

$$\begin{cases} \Delta W = (V_{\mathrm{R}} - V_{\mathrm{L}})(V_{\mathrm{L}} C_{\max} - V_{\mathrm{R}} C_{\min} + E(C_{\max} - C_{\min})) & \text{if } \dfrac{C_{\max}}{C_{\min}} > \dfrac{V_{\mathrm{R}} + E}{V_{\mathrm{L}} + E}, \\ 0 & \text{otherwise.} \end{cases} \tag{2.13}$$

that we shall rewrite

$$\begin{cases} \Delta W(V_{\mathrm{L}}, V_{\mathrm{R}}) = C_{\min}(V_{\mathrm{R}} - V_{\mathrm{L}})(\eta V_{\mathrm{L}} - V_{\mathrm{R}} + E(\eta - 1)) & \text{if } \eta > \dfrac{V_{\mathrm{R}} + E}{V_{\mathrm{L}} + E}, \\ 0 & \text{otherwise.} \end{cases} \tag{2.14}$$

The twofold definition comes from the fact that for cases where (2.5) is not fulfilled, then the degenerated cycle has an area of zero. In the following of the manuscript, for simplicity, we only keep the first line of (2.14) in various contexts where we express the converted energy per cycle of C_{t}. This notation simplification eludes the fact that the converted energy is null (and not negative) when $\eta < (V_{\mathrm{R}} + E)/(V_{\mathrm{L}} + E)$.

We can make three important observations at this point:

- For any E and $\eta > 1$, $\Delta W(V_{\mathrm{L}}, V_{\mathrm{R}})$ is not upper-bounded in the half-plane $V_{\mathrm{L}} < V_{\mathrm{R}}$.
- The diodes D_1 and D_2 ensure the auto-synchronization of the circuit's topology reconfiguration with the capacitance variation. Hence, energy is being converted without the need of a switch synchronized with C_{t}'s variations.
- We did not discuss the implementation of the V_{R} and V_{L} voltage sources. One natural implementation would be to use capacitors of large values, charged to the V_{L} and V_{R} voltages. Proceed to this substitution yields the Roundy's charge-pump, presented hereafter.

2.1.3 The fundamental example of charge-pump: the Roundy's circuit

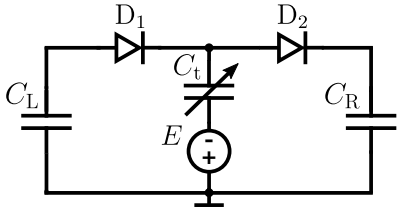

(a) Schematic of the charge-pump conditioning circuit proposed by Roundy *et al.*

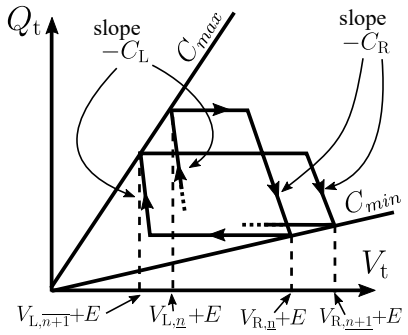

(b) Charge-voltage diagram for one cycle of operation of the Roundy's charge-pump. The slopes have been greatly exaggerated so to highlight the differences with the ideal rectangular charge-voltage diagram.

Figure 2.3: Schematic and charge-voltage diagram for the Roundy's charge-pump.

Roundy *et al.* were the first to report a charge-pump conditioning circuit for electrostatic vibration energy harvesting in [RWR03]. It is depicted in Fig. 2.3a. Compared to the idealized

charge-pump of Fig. 2.2a, Roundy's charge-pump is obtained by a mere substitution of the ideal voltage sources V_{R} and V_{L} with two fixed capacitors.

Let us give the full analysis of Roundy's charge-pump, without simplification assumptions, and for $E \geqslant 0$. The following analysis is not found in the literature to the best of the author's knowledge. Note that the polarity of the transducer could be inverted, which yields in different dynamics in the case of $E > 0$, but we will only deal with the polarity as depicted in Fig. 2.3a in this manuscript. The goal of this analysis is to derive the autonomous evolution laws of the circuit's state. This last sentence implies the major difference of the Roundy's charge-pump with the idealized charge-pump: contrarily to the latter, the former has non-trivial dynamics over multiples cycles of the capacitance variation. In other words, its electrical state defined as the voltages across C_{L}, C_{R} and C_{t} at a given instant of C_{t}'s variation cycle (e.g., $C_{\mathrm{t}} = C_{\max}$) evolves throughout the consecutive cycles of C_{t}'s variation. We will discuss these differences at the end of the analysis.

Consider a cycle n, at the initial instant when $C_{\mathrm{t}} = C_{\max}$, so that the analysis starts when C_{t} starts decreasing. We also suppose that $V_{\mathrm{t},\overline{\mathrm{n}}} = V_{\mathrm{CL},\overline{\mathrm{n}}} + E$. We label the current cycle n, so that the voltage across C_{t}, C_{L} and C_{R} are respectively initially denoted by $V_{\mathrm{t},\overline{\mathrm{n}}}$, $V_{\mathrm{CL},\overline{\mathrm{n}}}$ and $V_{\mathrm{CR},\overline{\mathrm{n}}}$. When C_{t} starts decreasing towards $C_{\min}$, the transducer is kept at constant charge, while its voltage increases, as in (2.3). Defining

$$C_1 \coloneqq \frac{V_{\mathrm{CL},\overline{\mathrm{n}}} + E}{V_{\mathrm{CR},\overline{\mathrm{n}}} + E} C_{\max} \tag{2.15}$$

it comes that if

$$\eta > \frac{V_{\mathrm{CR},\overline{\mathrm{n}}} + E}{V_{\mathrm{t},\overline{\mathrm{n}}} + E} \left(= \frac{V_{\mathrm{CR},\overline{\mathrm{n}}} + E}{V_{\mathrm{CL},\overline{\mathrm{n}}} + E} \right), \tag{2.16}$$

then C_{t} reaches C_1 as $C_1 > C_{\min}$. When that happens, the diode D_2 connects C_{t} and C_{R}, while C_{t} continues to decrease towards $C_{\min}$. During this time, C_{t} pushes charges to C_{R}. The charge conservation equation reads

$$C_{\mathrm{t}} \in [C_{\min}\,; C_1], \quad V_{\mathrm{t},\overline{\mathrm{n}}} C_{\max} + V_{\mathrm{CR},\overline{\mathrm{n}}} C_{\mathrm{R}} = V_{\mathrm{t}} C_{\mathrm{t}} + V_{\mathrm{CR}} C_{\mathrm{R}} \tag{2.17}$$

and we have that

$$C_{\mathrm{t}} \in [C_{\min}\,; C_1], \quad V_{\mathrm{t}} = V_{\mathrm{CR}} + E, \tag{2.18}$$

so

$$C_{\mathrm{t}} \in [C_{\min}\,; C_1], \quad Q_{\mathrm{t}} = V_{\mathrm{t},\overline{\mathrm{n}}} C_{\max} + (V_{\mathrm{CR},\overline{\mathrm{n}}} + E - V_{\mathrm{t}}) C_{\mathrm{R}}. \tag{2.19}$$

In particular, at $C_{\mathrm{t}} = C_{\min}$

$$V_{\mathrm{t},\underline{\mathrm{n+1}}} = \frac{V_{\mathrm{t},\overline{\mathrm{n}}} C_{\max} + (V_{\mathrm{CR},\overline{\mathrm{n}}} - V_{\mathrm{CR},\underline{\mathrm{n+1}}}) C_{\mathrm{R}}}{C_{\min}}, \tag{2.20}$$

$$V_{\mathrm{t},\underline{\mathrm{n+1}}} = V_{\mathrm{CR},\underline{\mathrm{n+1}}} + E, \tag{2.21}$$

and, as D_1 blocked any charge exchange with C_{L};

$$V_{\mathrm{CL},\underline{\mathrm{n+1}}} = V_{\mathrm{CL},\overline{\mathrm{n}}}. \tag{2.22}$$

Let us now combine (2.20) and (2.21); it comes that

$$V_{\mathrm{t},\underline{\mathrm{n+1}}} = \frac{V_{\mathrm{t},\overline{\mathrm{n}}} C_{\max} + V_{\mathrm{CR},\overline{\mathrm{n}}} C_{\mathrm{R}} + E C_{\mathrm{R}}}{C_{\min} + C_{\mathrm{R}}}. \tag{2.23}$$

When C_{t} starts to increase from $C_{\min}$, D_2 prevents any charge exchange between C_{t} and C_{R}, so C_{t} is kept at constant charge while its voltage decreases. Defining

$$C_2 \coloneqq \frac{V_{\mathrm{CR},\underline{\mathrm{n+1}}} + E}{V_{\mathrm{CL},\underline{\mathrm{n+1}}} + E} C_{\min} \tag{2.24}$$

then when $C_{\mathrm{t}} = C_2$, D_1 connects C_{t} and C_{L}: C_{t} absorbs charges from C_{L} until it reaches $C_{\max}$. Note that C_2 is always reached by C_{t} as (2.16) is supposed to be satisfied. Indeed, the condition for C_2 to be reached is that $C_2 < C_{\max}$, or

$$\eta > \frac{V_{\mathrm{CR},\underline{\mathrm{n+1}}} + E}{V_{\mathrm{CL},\underline{\mathrm{n+1}}} + E} \tag{2.25}$$

but (2.23) indicates that

$$\frac{V_{\mathrm{CR},\underline{\mathrm{n+1}}} + E}{V_{\mathrm{CL},\underline{\mathrm{n+1}}} + E} = \frac{V_{\mathrm{CL},\overline{\mathrm{n}}} C_{\max} + C_{\mathrm{R}}(V_{\mathrm{CR},\overline{\mathrm{n}}} + E)}{V_{\mathrm{CL},\overline{\mathrm{n}}} C_{\min} + C_{\mathrm{R}}(V_{\mathrm{CL},\overline{\mathrm{n}}} + E)} \tag{2.26}$$

and our hypothesis (2.16) immediately implies (2.25). The charge conservation equation reads

$$C_{\mathrm{t}} \in [C_2\,; C_{\max}], \quad V_{\mathrm{t},\underline{\mathrm{n+1}}} C_{\min} + V_{\mathrm{CL},\underline{\mathrm{n+1}}} C_{\mathrm{L}} = V_{\mathrm{t}} C_{\mathrm{t}} + V_{\mathrm{CL}} C_{\mathrm{L}}, \tag{2.27}$$

and we have that

$$C_{\mathrm{t}} \in [C_2\,; C_{\max}], \quad V_{\mathrm{t}} = V_{\mathrm{CL}} + E \tag{2.28}$$

so

$$C_{\mathrm{t}} \in [C_2\,; C_{\max}], \quad Q_{\mathrm{t}} = V_{\mathrm{t},\underline{\mathrm{n+1}}} C_{\min} + (V_{\mathrm{CL},\underline{\mathrm{n+1}}} + E - V_{\mathrm{t}}) C_{\mathrm{L}}. \tag{2.29}$$

In particular, at $C_{\mathrm{t}} = C_{\max}$

$$V_{\mathrm{t},\overline{\mathrm{n+1}}} = \frac{V_{\mathrm{t},\underline{\mathrm{n+1}}} C_{\min} + (V_{\mathrm{CL},\underline{\mathrm{n+1}}} - V_{\mathrm{CL},\overline{\mathrm{n+1}}}) C_{\mathrm{L}}}{C_{\max}}, \tag{2.30}$$

$$V_{\mathrm{t},\overline{\mathrm{n+1}}} = V_{\mathrm{CL},\overline{\mathrm{n+1}}} + E, \tag{2.31}$$

and, as D_2 blocked any charge exchange with C_{R};

$$V_{\mathrm{CR},\overline{\mathrm{n+1}}} = V_{\mathrm{CR},\underline{\mathrm{n+1}}}. \tag{2.32}$$

By combining (2.30), (2.31) and (2.23)

$$\begin{aligned} V_{\mathrm{t},\overline{\mathrm{n+1}}} =& V_{\mathrm{t},\overline{\mathrm{n}}} \frac{C_{\max} C_{\min}}{(C_{\min} + C_{\mathrm{R}})(C_{\max} + C_{\mathrm{L}})} + \\ &+ V_{\mathrm{CR},\overline{\mathrm{n}}} \frac{C_{\min} C_{\mathrm{R}}}{(C_{\min} + C_{\mathrm{R}})(C_{\max} + C_{\mathrm{L}})} + V_{\mathrm{CL},\overline{\mathrm{n}}} \frac{C_{\mathrm{L}}}{C_{\max} + C_{\mathrm{L}}} + E \end{aligned} \tag{2.33}$$

but as we supposed that $V_{\mathrm{t},\overline{\mathrm{n}}} = V_{\mathrm{CL},\overline{\mathrm{n}}} + E$, this becomes

$$V_{\mathrm{t},\overline{\mathrm{n+1}}} = h_{11} V_{\mathrm{t},\overline{\mathrm{n}}} + h_{12} V_{\mathrm{CR},\overline{\mathrm{n}}} + h_{13} E \tag{2.34}$$

where we have defined

$$\begin{aligned} h_{11} &\coloneqq \frac{C_{\min} C_{\mathrm{L}} + C_{\mathrm{L}} C_{\mathrm{R}} + C_{\max} C_{\min}}{(C_{\min} + C_{\mathrm{R}})(C_{\max} + C_{\mathrm{L}})}, \\ h_{12} &\coloneqq \frac{C_{\min} C_{\mathrm{R}}}{(C_{\min} + C_{\mathrm{R}})(C_{\max} + C_{\mathrm{L}})}, \\ h_{13} &\coloneqq \frac{C_{\min} C_{\mathrm{R}}}{(C_{\min} + C_{\mathrm{R}})(C_{\max} + C_{\mathrm{L}})}. \end{aligned} \tag{2.35}$$

Using (2.21), (2.23) and (2.32)

$$V_{\mathrm{CR},\overline{\mathrm{n+1}}} = h_{21} V_{\mathrm{t},\overline{\mathrm{n}}} + h_{22} V_{\mathrm{CR},\overline{\mathrm{n}}} + h_{23} E \tag{2.36}$$

where

$$\begin{aligned} h_{21} &\coloneqq \frac{C_{\max}}{C_{\min} + C_{\mathrm{R}}}, \\ h_{22} &\coloneqq \frac{C_{\mathrm{R}}}{C_{\min} + C_{\mathrm{R}}}, \\ h_{23} &\coloneqq -\frac{C_{\min}}{C_{\min} + C_{\mathrm{R}}}. \end{aligned} \tag{2.37}$$

From these expressions and (2.16) at cycle n, it can be easily derived that the circuit's state at the cycle $n+1$ also satisfies the hypothesis that

$$\eta > \frac{V_{\mathrm{CR},\overline{\mathrm{n+1}}} + E}{V_{\mathrm{t},\overline{\mathrm{n+1}}} + E} \tag{2.38}$$

Therefore, we may now describe the circuit's dynamics at every cycle when $C_{\mathrm{t}} = C_{\max}$ by recurrence. Defining

$$\mathbf{A} \coloneqq \begin{pmatrix} h_{11} & h_{12} & h_{13} \\ h_{21} & h_{22} & h_{23} \\ 0 & 0 & 1 \end{pmatrix}, \tag{2.39}$$

so that the explicit evolution law is given by

$$\forall n \geqslant n_0, \quad \begin{pmatrix} V_{\mathrm{t},\overline{\mathrm{n}}} \\ V_{\mathrm{CR},\overline{\mathrm{n}}} \\ E \end{pmatrix} = \mathbf{A}^n \begin{pmatrix} V_{\mathrm{t},\overline{\mathrm{n_0}}} \\ V_{\mathrm{CR},\overline{\mathrm{n_0}}} \\ E \end{pmatrix} \tag{2.40}$$

where $V_{\mathrm{CR},\overline{\mathrm{n_0}}}$,$V_{\mathrm{CL},\overline{\mathrm{n_0}}}$ and $V_{\mathrm{t},\overline{\mathrm{n_0}}}$ satisfy the initial hypothesis (2.16). We spare the easy diagonal-

ization details to compute the n-th power of $\mathbf{A}$, and the final results yields:

$$\forall n \geqslant n_0, \quad \begin{aligned} V_{\mathrm{t},\overline{\mathrm{n}}} &= \frac{\begin{array}{r} C_{\min}(C_{\mathrm{R}}(V_{\mathrm{CR},\overline{\mathrm{n_0}}}+E)+V_{\mathrm{CR},\overline{\mathrm{n_0}}}(C_{\max}+C_{\mathrm{L}}))+ \\ +{\lambda_0}^{n-n_0}C_{\mathrm{R}}(C_{\max}V_{\mathrm{t},\overline{\mathrm{n_0}}}-C_{\min}(V_{\mathrm{CR},\overline{\mathrm{n_0}}}+E)) \end{array}}{C_{\min}C_{\mathrm{L}}+C_{\max}C_{\mathrm{R}}+C_{\max}C_{\min}} \\ V_{\mathrm{CR},\overline{\mathrm{n}}} &= \frac{\begin{array}{r} C_{\max}(V_{\mathrm{t},\overline{\mathrm{n_0}}}(C_{\max}+C_{\mathrm{L}})+C_{\mathrm{R}}V_{\mathrm{CR},\overline{\mathrm{n_0}}}-C_{\min}E)-C_{\min}C_{\mathrm{L}}E- \\ -{\lambda_0}^{n-n_0}(C_{\max}+C_{\mathrm{L}})(C_{\max}V_{\mathrm{t},\overline{\mathrm{n_0}}}-C_{\min}(V_{\mathrm{CR},\overline{\mathrm{n_0}}}+E)) \end{array}}{C_{\min}C_{\mathrm{L}}+C_{\max}C_{\mathrm{R}}+C_{\max}C_{\min}} \end{aligned} \tag{2.41}$$

where $V_{\mathrm{CR},\overline{\mathrm{n_0}}}$,$V_{\mathrm{CL},\overline{\mathrm{n_0}}}$ and $V_{\mathrm{t},\overline{\mathrm{n_0}}}$ satisfy the initial hypothesis (2.16), and where the eigenvalue λ_0 of $\mathbf{A}$ reads

$$\lambda_0 = \frac{C_{\mathrm{L}}C_{\mathrm{R}}}{(C_{\max}+C_{\mathrm{L}})(C_{\min}+C_{\mathrm{R}})} \tag{2.42}$$

The expression for $V_{\mathrm{t},\underline{\mathrm{n}}}$ for all $n \geqslant n_0$ can be obtained by applying (2.23) to $V_{\mathrm{t},\overline{\mathrm{n-1}}}$. We also have that $V_{\mathrm{CR},\underline{\mathrm{n}}} = V_{\mathrm{CR},\overline{\mathrm{n}}}$, (see (2.32)) for all $n \geqslant n_0$. To complete the description of the circuit's explicit state for $n \geqslant n_0$, $V_{\mathrm{CL},\overline{\mathrm{n}}} = V_{\mathrm{t},\overline{\mathrm{n}}} - E$ (see (2.31)), so that $V_{\mathrm{CL},\underline{\mathrm{n}}} = V_{\mathrm{t},\overline{\mathrm{n-1}}} - E$ (see (2.22)).

To make the analysis complete, it can be shown that from any initial state of the charge-pump, the steady-state operation mode described by (2.41) is reached after at most one cycle of variation of C_{t} if and only if (2.16) is fulfilled. This means that the initial hypothesis that we have made above $V_{\mathrm{t},\overline{\mathrm{n}}} = V_{\mathrm{CL},\overline{\mathrm{n}}} + E$ can be shown to be fulfilled in at most one cycle of variation of C_{t} from any initial state $(V_{\mathrm{t}}, V_{\mathrm{CL}}, V_{\mathrm{CR}})$ fulfilling $V_{\mathrm{CL}} + E \leqslant V_{\mathrm{t}} \leqslant V_{\mathrm{CR}} + E$ and $\eta > (V_{\mathrm{CR}} + E)/(V_{\mathrm{CL}} + E)$. Showing this is done similarly to above in Sec. 2.1.2, for the idealized charge-pump.

The foregoing analysis clearly shows a major difference with the ideal charge-pump of Sec. 2.1.2: changing the V_{L} and V_{R} constant voltage sources of Sec. 2.1.2 to finite-valued capacitors turns our ideal charge-pump into a discrete-time dynamical system. The state of this system can be chosen as the voltages across each capacitor at $C_{\mathrm{t}} = C_{\max}$. Note that here in (2.40) we diminished the state dimension by 1 by not including $V_{\mathrm{CL},\overline{\mathrm{n}}}$ in the state, as it is straightforwardly linked to $V_{\mathrm{t},\overline{\mathrm{n}}}$ and $V_{\mathrm{CR},\overline{\mathrm{n}}}$. On the other hand, we augmented the state dimension by 1 in order to account for the effect of E (but we could has well have considered an affine mapping).

The differences with the ideal charge-pump can be summarized by the cross-comparison of the charge-voltage diagram for the Roundy's circuit (Fig. 2.3b) and for the ideal charge-pump (Fig. 2.2b). The first difference (exaggerated on the figure) with the rectangular charge-voltage diagram of the idealized charge-pump is that the segments described by (2.6) and (2.9) have become respectively (2.19) and (2.29). These two latter equations define two segments in the charge-voltage plane that have a slope of respectively $-C_{\mathrm{R}}$ and $-C_{\mathrm{L}}$. Increasing C_{L} and C_{R} relatively to $C_{\max}$ makes the charge-voltage diagram of the circuit approach that of the idealized charge-pump, which has vertical segments. Hence, locally at the scale of one cycle, large C_{L} and C_{R} make Roundy's charge-pump approach the ideal charge-pump.

The other difference visible on the charge-voltage diagram is that the cycles are not closed, because the charge-pump state evolves throughout the cycles of C_{t}. Increasing C_{L} and C_{R} makes λ_0 in (2.42) approach 1, so that the greater C_{L} and C_{R} are, the more consecutive cycles are alike. This means that increasing C_{L} and C_{R} makes the long-term behavior of the Roundy's charge-

pump, seen as an evolving dynamical system, approach that of the ideal charge-pump, whose state remains unchanged from cycle-to-cycle. The two observations made in this paragraph and the former are somewhat intuitive here, because the voltage sources V_{L} and V_{R} are exactly substituted with large-valued capacitors. In fact, we will see next that any circuit fulfilling some specific requirements can be seen, at the scale of one cycle of C_{t}'s variation, as implementing the dynamics of the ideal charge-pump. This holds as long as the fixed capacitors of these circuits are chosen large enough. Such circuits define the family of "charge-pump conditioning circuits".

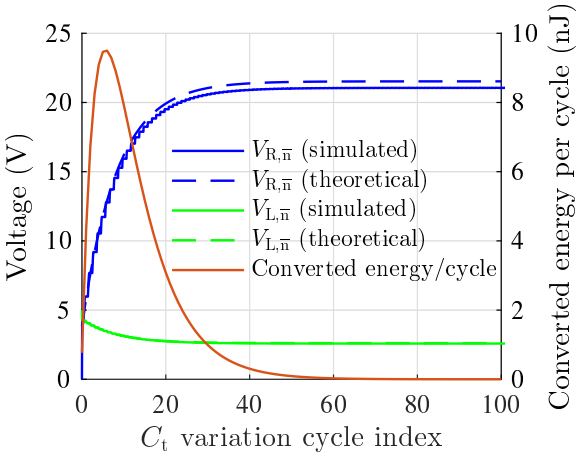

(a) Simulation of the Roundy's charge-pump: time-domain.

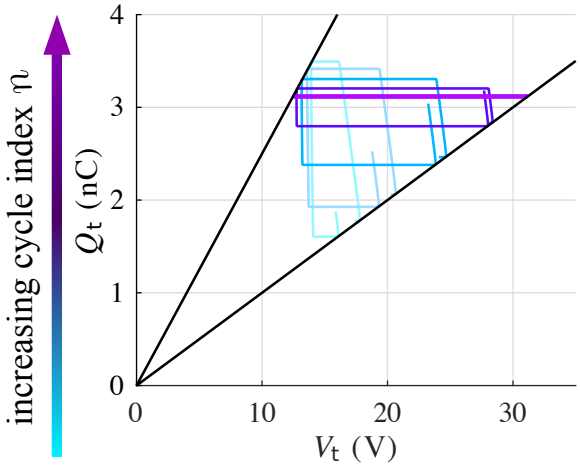

(b) Simulation of the Roundy's charge-pump: charge-voltage diagrams of some cycles.

Figure 2.4: Simulations of Roundy's charge-pump.

The plots in Fig. 2.4a give the results of a time-domain SPICE simulation of the Roundy's charge-pump. It operates with C_{t} varying between 250 pF and 100 pF, which are typical capacitance variation values encountered for micro-scale electrostatic transducers. We chose $C_{\mathrm{L}} = 10\,\mathrm{nF}$ and $C_{\mathrm{R}} = 1\,\mathrm{nF}$, deliberately not much larger than C_{t} to exacerbate the differences with the rectangular charge-voltage diagram approximation. The initial energy in the circuit was of 125 nW, and the built-in voltage $E = 10\,\mathrm{V}$. Note that the theoretical results derived above and the simulation results differ slightly. This is due to the diode non-idealities that are incorporated into the simulated model but not taken into account in the derivation above. Some charge-voltage diagrams at the scale of one cycle of C_{t} that correspond to different cycles of C_{t} throughout the evolution of the charge-pump in the simulation are depicted in Fig. 2.4b.

Finally, as $|\lambda_0| < 1$ (see (2.42)), it is immediate that $V_{\mathrm{CL},\overline{\mathrm{n}}}$, $V_{\mathrm{CR},\overline{\mathrm{n}}}$ and $V_{\mathrm{t},\overline{\mathrm{n}}}$ are bounded as n goes to infinity. We hence say that the Roundy charge-pump is a *stable* charge-pump.

2.2 Generalities about charge-pump conditioning circuits

2.2.1 Definition and operation at the scale of one cycle of C_{t}'s variation

Let us now give the definition of charge-pump conditioning circuits used in this work. From the general definition, some propositions concerning these circuits are given without proof. Because of lack of time, we could not integrate the formal proofs of these facts to this manuscript. The complete, formal context in which those proofs can be given requires a substantially longer

presentation, because it needs to lay down an abstract mathematical framework of charge-pump conditioning circuits based on a graph-theoretic language. We have worked on this subject within the course of this thesis. The description given below encompasses the main results that we have obtained, in a loosened level of formal language adapted to the rest of our study.

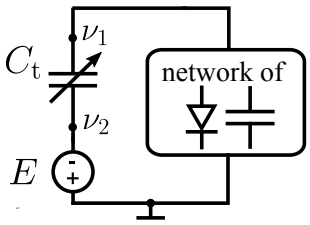

Figure 2.5: Generic network of diodes and fixed capacitors driven by a variable capacitor with eventual built-in voltage E.

Consider the family of all circuits that consist in a variable capacitor C_t in series with a voltage source E. The capacitor C_t varies as specified above in Sec. 2.1.1. It is connected at nodes ν_1 and ν_2 to a two-terminal network solely composed of fixed capacitors and diodes, and to the voltage source E. This configuration is depicted in Fig. 2.5. The two-terminal network is supposed to contain $N_\mathrm{C} \geqslant 1$ fixed capacitors and $N_\mathrm{D} \geqslant 2$ diodes. Further, we suppose that there are no dipoles in this network that are uniquely constituted of diodes other than single diodes. Let us call such a circuit a *candidate charge-pump*.

The voltage of all capacitors of the circuit, that is, the fixed capacitors C_i and the variable capacitor C_t, are labeled V_i and V_t respectively. We define the electrical state of such circuit as a vector $\mathbf{V} = (E, V_1, \ldots, V_{\mathrm{N_C}}, V_\mathrm{t})$. Notice that we have added E to the state, as we did in the analysis of Roundy's charge-pump.

In what follows, the notation $V_{\mathrm{t}n}(\overline{C})$ refers to the value of V_t when $C_\mathrm{t} = C$ during the (monotonic) increasing phase of C_t that occurs during the cycle n of C_t's variation. Similarly for $V_{\mathrm{t}n}(\underline{C})$ during the decreasing phase of C_t that occurs during cycle n of C_t's variation. The same notation goes for the charge Q_t across C_t.

We define a *charge-pump conditioning circuit* as a *candidate charge-pumps* that further fulfills the following condition: there exists a state $\mathbf{V}_{\overline{n}}$ of the charge-pump at $C_\mathrm{t} = C_\mathrm{max}$ of a cycle of variation of C_t (that we choose to index by n) such that:

- $\mathbf{V}_{\overline{n}}$ is *admissible given the circuit topology*. That is, the circuit's voltages, as constrained by Kirchhoff's laws, enforce the condition that $\mathbf{V}_{\mathrm{D}_i} \leqslant 0$, for $1 \leqslant i \leqslant N_\mathrm{D}$. Here, V_{D_i} denotes the voltage across the diode D_i of the network, oriented from the cathode to the anode. In addition, $V_{\mathrm{t}\overline{n}} > 0$ where V_t is oriented such that $V_\mathrm{t} = V_{\nu_1} - V_{\nu_2}$.
- there exists $C_{1,n} \in \,]C_\mathrm{min}\,; C_\mathrm{max}]$ such that when C_t starts to decrease from C_max, the circuit operates at constant charge up $C_\mathrm{t} = C_{1,n}$. That is: $\forall C_\mathrm{t} \in [C_{1,n}\,; C_\mathrm{max}], \partial_{C_\mathrm{t}} Q_{\mathrm{t}n}(\underline{C_\mathrm{t}}) = 0$. Then, for all $C_\mathrm{t} \in [C_{1,n}\,; C_\mathrm{max}]$, a current flows through C_t. The resulting charge-pump's state at $C_\mathrm{t} = C_\mathrm{min}$ of cycle $n+1$ is denoted by $\mathbf{V}_{\underline{n+1}}$ following the conventions of Sec. 2.1.1.
- Similarly, there exists $C_{2,n+1} \in \,]C_\mathrm{min}\,; C_\mathrm{max}[$ such that, when C_t starts to increase from C_min, the circuit operates at constant charge up to $C_\mathrm{t} = C_{2,n+1}$ (i.e., for $C_\mathrm{t} \in \,]C_\mathrm{min}\,; C_{2,n+1}[$). For $C_\mathrm{t} \in [C_\mathrm{min}\,; C_{2,n+1}]$, a current flows through C_t. The charge-pump's state at $C_\mathrm{t} = C_\mathrm{max}$ of cycle $n+1$ is denoted by $\mathbf{V}_{\overline{n+1}}$.

Such a state and the corresponding cycle of variation of C_t that provided by the definition will be called a *non-degenerated cycle* in the rest of this section. We will say that $\mathbf{V}_{\overline{n}}$ *provides* a non-degenerated cycle if it satisfies the requirement of the definition. This specifies that the cycle of C_t at which the charge-pump has this state at $C_\mathrm{t} = C_\mathrm{max}$ is chosen to be indexed as n.

Informally, a non-degenerated cycle is a cycle for which energy is converted thanks to C_t's variation, and ends-up in the circuit's fixed capacitors. A non-degenerated cycle has four segments as for the idealized charge-pump of Sec. 2.1.2: ① one segment at constant charge, followed by ② one segment at non-constant charge (but non-necessarily constant voltage unlike the idealized charge-pump), followed by ③ one segment at constant charge, followed by ④ one segment at non-constant charge (again, of non-necessarily constant voltage, unlike the idealized charge-pump). By this definition, the Roundy circuit is a charge-pump: it suffices to consider any initial state $(V_\mathrm{CR}, V_\mathrm{CL}, V_\mathrm{t})$ such that $V_\mathrm{CL} + E \leqslant V_\mathrm{t} \leqslant V_\mathrm{CR} + E$ and $\eta > (V_\mathrm{CR} + E)/(V_\mathrm{CL} + E)$

Our formal study yielded some results that give a precise meaning to the fact that charge-pump conditioning circuits approximate the ideal charge-pump of Fig. 2.2a. Before we state these results, we have add the following requirement to the topologies of charge-pump conditioning circuits: for any fixed capacitor C_i of the network, we either have that:

- the voltage across C_i increases when a positive current flows from ν_1 to ν_2 and decreases when a negative current flows from ν_1 to ν_2, or
- the voltage across C_i decreases when a positive current flows from ν_1 to ν_2 and increases when a negative current flows from ν_1 to ν_2.

We have conjectured that this requirement is implied by the definition of charge-pump given above, but we could not prove it. Hence, we add it as an additional hypothesis.

Let us consider any conditioning circuit. In the following, we also denote by $C_\perp$ the equivalent capacitance value of all the charge-pump's fixed capacitors put in series, that is, $C_\perp = (\sum_{i=1}^{N_\mathrm{C}} {C_i}^{-1})^{-1}$. The following properties hold:

- (i) Remember that V_t is oriented from ν_1 to ν_2. With this convention, we have that when C_t decreases, the current flowing through it is necessarily null or negative. Conversely, when C_t decreases, the current flowing through it is necessarily null or positive.
- (ii) Let $\mathbf{V}_{\overline{n}}$ provides a non-degenerated cycle. Then $\mathbf{V}_{\overline{n+1}}$ provides a non-degenerated cycle.
- (iii) Let $\mathbf{V}_{\overline{n}}$ provides a non-degenerated cycle. Then it is also a non-degenerated cycle for a charge pump of the same topology but with the fixed capacitors replaced with capacitors of larger values.
- (iv) Let $\mathbf{V}_{\overline{n_0}}$ provides a non-degenerated cycle. Let $\delta > 0$. There exists $\mathcal{C}_\delta > 0$ such that $C_\perp > \mathcal{C}_\delta$ implies that, for all cycle $n \geqslant n_0$, we have $|V_{\mathrm{t},\underline{\mathrm{n+1}}} - V_{\mathrm{t}n}(\underline{C_{1,n}})| < \delta$ and $|V_{\mathrm{t},\overline{\mathrm{n+1}}} - V_{\mathrm{t}n+1}(\overline{C_{2,n+1}})| < \delta$.

At this point, let us define, for a cycle n, $V_\mathrm{Ln} \coloneqq V_{\mathrm{t},\overline{\mathrm{n}}} - E$ and $V_\mathrm{Rn} \coloneqq V_{\mathrm{t},\underline{\mathrm{n+1}}} - E$. We further have the following properties:

- (v) Let $\mathbf{V}_{\overline{n}}$ provides a non-degenerated cycle. Given an integer N and $\delta > 0$, there exists a $\mathcal{C}_\delta > 0$ such that $C_\perp > \mathcal{C}_\delta$ implies that $\forall n_1, n_2 \in [\![\, 1\,;\, N \,]\!]$, we have that $|V_{\mathrm{Ln+n_1}} - V_{\mathrm{Ln+n_2}}| < \delta$

and $|V_{\mathrm{Rn+n_1}} - V_{\mathrm{Rn+n_2}}| < \delta$.

- (vi) Let $\mathbf{V}_{\overline{n_0}}$ provides a non-degenerated cycle. Let $\delta > 0$. There exists $\mathcal{C}_\delta > 0$ such that $C_\perp > \mathcal{C}_\delta$ implies that, for all cycle $n > n_0$, $|-\int_{t_{\overline{n}}}^{t_{\overline{n+1}}} i_\mathrm{t}(t)V_\mathrm{t}(t)\,\mathrm{d}t - \Delta W(V_{\mathrm{Ln}}, V_{\mathrm{Rn}})| < \delta$.
- (vii) There exists a piecewise-linear mapping $\mathbf{A}$ defined on the space of the charge-pump's admissible states onto itself, such that for any admissible $\mathbf{V}_{\overline{n}}$, we have $\mathbf{V}_{\overline{n+1}} = \mathbf{A}(\mathbf{V}_{\overline{n}})$. There is a finite number of subspaces of the space of the charge-pump's admissible states on which $\mathbf{A}$ is linear.

The property (i) means that C_t can be seen as a current source that gives positive charges to the fixed capacitors of the network when C_t decreases, and conversely receives positive charges from the fixed capacitors of the network when C_t increases.

The property (ii) means that as long as an initial state results in the charge-pump to operate in an energy-conversion mode, then all subsequent cycles of variation of C_t will also result in energy conversion. Our example of the Roundy charge-pump illustrates this fact, as if (2.16) is fulfilled, then (2.38) necessarily is.

The property (iii) is clear: one can always change the values of the fixed capacitors of a charge-pump without changing the non-degeneracy property of its states.

The property (iv) means that the voltage V_t in segments ② and ④ (segments at non-constant charge operation) can be considered constant, for a large enough choice of the fixed capacitors of the charge-pump. We had witnessed this with the simple example of the Roundy's charge-pump: choosing C_L and C_R large enough made the corresponding segments in the charge-voltage diagram approach vertical lines.

The property (v) means that for large enough values of the charge-pump's fixed capacitors, a finite number of consecutive states resulting from charge-pump operation can be considered to be the same. Because of this and the previous property, we will always drop the n index from $V_{\mathrm{L_n}}$ and $V_{\mathrm{R_n}}$ when referring to the local behavior of each charge-pump across a finite number of C_t's variation cycles. For a large enough choice of the circuit's capacitors, (iv) and (v) imply that the biasing of C_t across one cycle of its variation approaches that set by the ideal charge-pump circuit of Sec. 2.1.2. Therefore, V_L and V_R completely characterize the dynamics of the charge-pump at the local scale. We will therefore refer to these voltages as the cycle's *characteristic voltages* in the rest of this document.

The property (vi) is a result of the two previous points and states that the energy converted in a non-degenerated cycle can be approximated with arbitrary precision by that of the rectangular charge-voltage diagram of same V_L and V_R, for large enough values of the fixed capacitors.

A consequence of property (vii) is that the space of admissible states can be divided into a finite number of regions or subspaces on which the evolution of the charge-pump's state is given by a linear map. Each of these regions defines what we call an *operation mode* of the charge-pump. The Roundy's charge-pump analyzed above has only one of such operation modes. On the contrary, for example, the circuits presented in Sec. 2.2.2.2 have multiple operation modes. An explicit example of such piecewise-defined dynamics will be seen in the analysis of the series-parallel charge-pump topology in Chap 3.

In Fig. 2.6, a charge-voltage diagram for consecutive cycles of a general charge-pump condi-

tioning circuit is depicted, illustrating the consequence of the properties (i)-(vi).

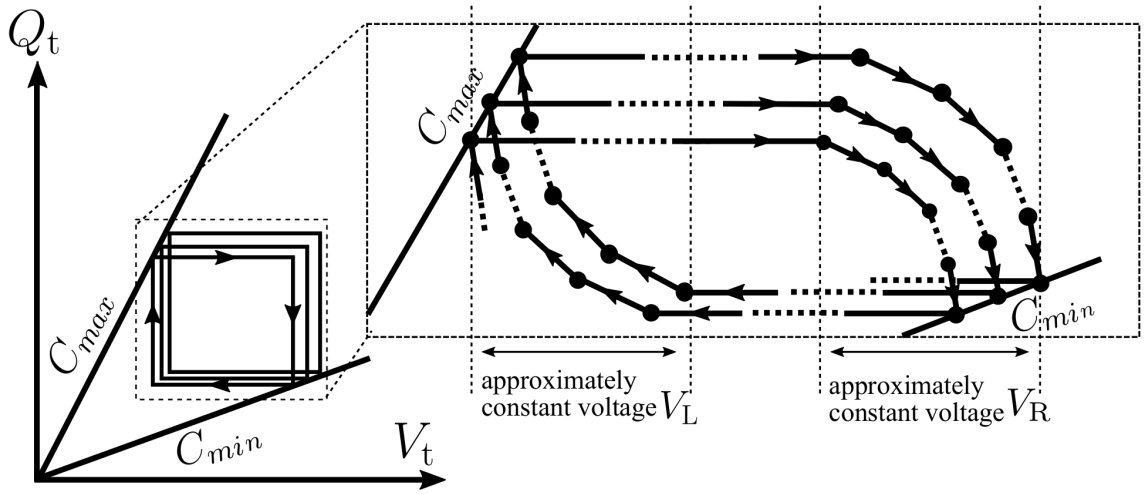

Figure 2.6: Three consecutive cycles of variation of C_t are approximated as closed rectangles. The magnification shows the actual evolution of C_t's biasing across the three cycles. Our analysis showed that in general, the charge-voltage diagram of any charge-pump will exhibit the piecewise-defined slopes that are visible on the magnification. In the case of Roundy's charge-pump, there was merely one slope value on the left and on the right voltages of the cycle. The analysis of the series-parallel topology in Chap. 3 will show charge-voltage diagrams that resembles that of the present figure, with piecewise-defined slopes.

In the following, we will not explicitly verify the definition of charge-pump conditioning circuit for each presented circuit. However, for all the charge-pumps that are explicitly analyzed in this work, a state fulfilling the definition will necessarily be considered in the process of the complete analysis of each charge-pump (as it was the case for Roundy's charge-pump).

In summary, the takeaway message from these results is that the circuits we are going to present now can all be considered to operate as the ideal charge-pump of Sec. 2.1.2, locally at the scale of a few consecutive cycles of C_t. This is true as long as the fixed capacitances of their topologies are chosen to have large enough values, which in practice means that the capacitors have to be large compared to C_{max}. However, in large timescales, the fact that they are evolving dynamical systems have some implications that we now discuss.

2.2.2 Long-term autonomous evolution

The previous discussion shows that, for large enough values of the capacitors, the difference in the biasing of C_t (in terms of V_L and V_R) between consecutive cycles of the capacitance variation can be made arbitrarily small by a proper choice of the circuit's fixed capacitors values (this is property (v) of Sec. 2.2.1). Still, the variation of C_t necessarily induces an *autonomous evolution* of the charge-pump's state starting from an initial, non-degenerated state.

The reason for this is simple: at the local scale of a non-degenerated cycle, the previous discussion shows that a charge-pump converts the energy $\Delta W(V_L, V_R)$ during this cycle. As the circuit has no dissipative element, the sum of the energy in the circuit's capacitors (including C_t) has to increase. Therefore, the overall energy in the circuit increases from cycle-to-cycle, meaning that at least two capacitors of the network have had their voltage changed. As a cycle's characteristic voltages V_L and V_R are mapped to the voltages across the circuit's fixed capacitors, they also evolve throughout the cycles of capacitance variation.

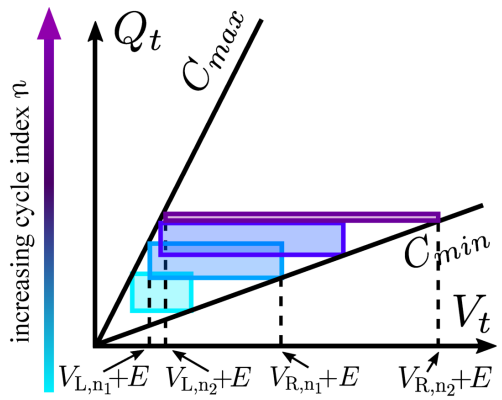

(a) Illustration of the evolution of the charge-voltage diagram for successive cycles of variation of C_t for stable charge-pump conditioning circuits.

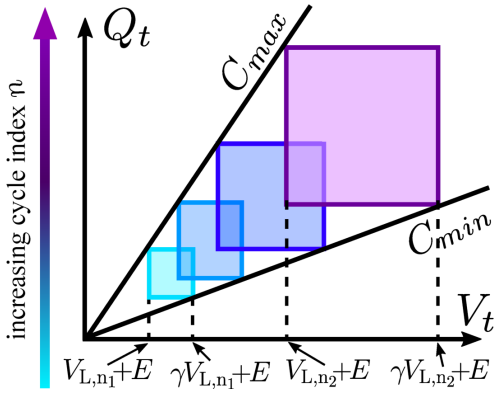

(b) Illustration of the evolution of the charge-voltage diagram for successive cycles of variation of C_t for fixed-ratio γ unstable charge-pump conditioning circuits.

From any non-degenerated initial cycle, the charge-pump evolves from cycle to cycle of C_t's variation accordingly to the piecewise-linear map $\mathbf{A}$. We admit without proof that $\mathbf{A}$ is necessarily such that there exists a subspace $\mathcal{V}$ of the space of all admissible states that is invariant by $\mathbf{A}$. In addition, we suppose that for any non-degenerated cycle $\mathbf{V}$, there exists n^* such that $\mathbf{A}^{(n^*)}(\mathbf{V}) \in \mathcal{V}$, where $\mathbf{A}^{(n^*)}$ denotes the n^*-th composition of $\mathbf{A}$. The subspace $\mathcal{V}$ defines an operation mode that we call the charge-pump's *steady-state* mode. The property given here means that from any initial non-degenerated cycle, the charge-pump will evolve such that ultimately, its dynamics are described by one region where $\mathbf{A}$ is linear.

2.2.2.1 Stable charge-pumps

We define the *stable* subclass of charge-pump conditioning circuits as those for which the autonomous evolution of V_{L_n} and V_{R_n} over the cycles of variation of C_t is bounded, regardless of the initial state of the circuit or of the values of C_{max} or C_{min}. The conversion cycles therefore evolve over the cycles of variation of C_t in a similar way to what is depicted in Fig. 2.7a. It can be shown that such charge-pumps necessarily saturate, in the sense that the converted energy across the cycles of autonomous operation starting from any initial charge-pump state asymptotically approaches zero.

2.2.2.2 Unstable charge-pumps

Contrarily to stable charge-pumps, unstable charge-pumps, depending on the initial state of the circuit, C_{max}, and C_{min}, can show an unstable steady-state operation mode. This mode is characterized by an unbounded evolution of both V_L and V_R. In this context, the limit in the converted energy per cycle is only put by eventual constraints which are set, e.g., by the electronic components. Simple examples of such constraints will be studied in Sec. 4.1 of Chap. 4, where different conditioning schemes are compared.

All of the reported unstable conditioning circuits are such that, in their unstable steady-state

mode of operation, the ratio between $V_{\mathrm{R_n}}$ and $V_{\mathrm{L_n}}$ approaches some value γ:

$$\lim_{n\to\infty} \frac{V_{\mathrm{R_n}}}{V_{\mathrm{L_n}}} = \gamma > 1. \tag{2.43}$$

We shall hence characterize such circuits by the value of γ they implement. We will also consider that the equality holds and discard the fact that this ratio is asymptotically reached. In fact, among the reported unstable conditioning circuits, only our topology of series-parallel charge-pump (Chap. 3) shows a γ ratio that is asymptotically reached instead of being exactly reached. And in this case, it is possible to choose the values of the fixed capacitors so that the convergence of $V_{\mathrm{R_n}}/V_{\mathrm{L_n}}$ to γ is arbitrarily fast. Therefore, we will suppose that unstable charge-pumps are characterized by

$$\forall n_1, n_2 > n^*, \quad \frac{V_{\mathrm{R}_{n_1}}}{V_{\mathrm{L}_{n_1}}} = \frac{V_{\mathrm{R}_{n_2}}}{V_{\mathrm{L}_{n_2}}} \quad =: \gamma, \tag{2.44}$$

rather than (2.43).

In this view, considering the approximation of ideal charge-pump, (2.14) reduces to

$$\Delta W_\gamma(V_{\mathrm{L}}) = C_{\min} V_{\mathrm{L}}(\gamma - 1)(V_{\mathrm{L}}(\eta - \gamma) - E(\eta - 1)). \tag{2.45}$$

An example of several C_{t} biasing cycles for an unstable charge-pump is illustrated in the charge-voltage diagrams of Fig. 2.7b.

Finally, note that these notions of stability and unstability are given in rather informal terms. We did not yet have found a clear relation between the stability properties of a charge-pump and its topology. A path of research on this matter is to link the eigenvalues of $\mathbf{A}$ in each of its linear region of definition, to the topology of the charge-pump. This has to be the subject of future works geared towards a complete theory of charge-pump conditioning circuits, as we explain in the conclusion and future works section (Sec. 2.5).

2.2.3 Practical motivations for charge-pump conditioning circuits

Now that what is meant by a charge-pump conditioning circuits is clear, let us give some of the motivations as of why they are the subject of investigation in electrostatic vibration energy harvesting, based on the properties stated above.

Contrarily to the conditioning schemes described in Sec. 1.3.2.1 and Sec. 1.3.2.2 charge-pump conditioning circuits do not require active synchronization with the variation of the transducer's capacitance. The analysis of the idealized charge-pump in Sec. 2.1.2 on which charge-pumps are based on, shows that the reconfiguration of the topology, leading to energy conversion, is done without the need of an external command. It is done automatically thanks to the diodes D_1 and D_2. Also, the dynamics, in the electrical domain, of charge-pump conditioning circuits only depend on the extremal values of C_{t}, and not on the pointwise $C_{\mathrm{t}}(t)$ evolution. This is the same as for the circuits of Sec. 1.3.2.1 and Sec. 1.3.2.2, but contrarily to the primitive conditioning scheme presented in Sec. 1.3.2.3 for which the converted energy depends on $C_{\mathrm{t}}(t)$'s pointwise evolution.

At the same time, charge-pump conditioning circuits store the converted energy in a network of capacitors for further use or processing, a requirement that was highlighted in Sec. 1.3.2.1.

This property is shared with the circuit of Sec. 1.3.2.1 and 1.3.2.2. But contrarily to those circuits, charge-pump conditioning circuits do not include inductors. This can be advantageous, e.g., for size-constrained applications. However, note that an asynchronous control interface may be needed to sustain their maximum energy conversion point, and this interface includes an inductor (see Sec. 2.4.1 below).

Among the different charge-pump conditioning circuits, the unstable subclass is particularly appealing. Indeed, their unstable property means that cycles of high energy conversion can be attained by the charge-pump's autonomous operation starting from, in principle, arbitrarily low (but non-zero) initial energy. In fact, merely having $E > 0$ is sufficient as a source of this initial energy, as we have experimentally verified in [KBG15]. This will be further discussed in Sec. 4.1.3 of Chap. 4.

2.3 List of charge-pump conditioning circuits

We now list various charge-pumps that were either reported in the literature, our framework of charge-pump conditioning circuits. This means in particular the circuits are presented supposing that the fixed capacitors in the charge-pump network have large enough value so that we can identify them, at the scale of one cycle, to the idealized charge-pump of Fig. 2.2a. At this scale, they are hence characterized by the voltages V_{L} and V_{R}. In particular, the charge-voltage diagrams of each following circuits are presented under ideal rectangular approximation.

Note that the generalized series-parallel charge-pump presented below in Sec. 2.16a was proposed during this work. Its detailed presentation and analysis is the subject of Chap. 3.

2.3.1 Stable charge-pumps

2.3.1.1 Roundy's charge-pump revisited

With Roundy's charge-pump, the characteristic cycle voltages V_{L} and V_{R} voltages at any cycle simply map to the voltages across C_{L} and C_{R} capacitors.

$$\begin{cases} V_{\mathrm{L}} &= V_{\mathrm{CL}}, \\ V_{\mathrm{R}} &= V_{\mathrm{CR}}. \end{cases} \tag{2.46}$$

We remind that the discussion in Sec. 2.2.1 highlights that, as long as we are dealing with a small number of consecutive cycles of C_{t}'s variation, we can describe all such cycles by the same V_{L} and V_{R} characteristic voltages if the fixed capacitances values are chosen large enough. For Roundy's charge-pump, this means that $C_{\max} \ll \min(C_{\mathrm{L}}, C_{\mathrm{R}})$. This hypothesis will be supposed to be verified in all of the following of the manuscript, except in Chap. 5 where the deviation from the ideal charge-pump will have to be explicitly taken into account.

The analysis done in Sec. 2.1.3 shows that, even for the simplest charge-pump topology that is the Roundy's charge-pump, the detailed analysis can be somewhat tedious. The framework of charge-pump conditioning circuits allows us to resort to powerful simplification. For example, we want to find the cycle of maximum converted power that will be reached by Roundy's

charge-pump throughout its autonomous operation. Instead of computing the expression of $\Delta W_{n+1} - \Delta W_n$ explicitly from the formulas (2.41) and searching for its maximum, we can simplify the analysis using the approximations made to identify the Roundy's charge-pump to the ideal charge-pump of Sec. 2.2a. To do so, we suppose that C_L and C_R are initially charged with a voltage $V_0 > 0$. This means that C_t is charged with a voltage $V_0 + E$. The charge conservation principle enforces that

$$V_{\mathrm{CR}} C_\mathrm{R} + V_{\mathrm{CL}} C_\mathrm{L} + V_\mathrm{t} C_\mathrm{t} = V_0 (C_\mathrm{R} + C_\mathrm{L} + C_\mathrm{t}) + E C_\mathrm{t} \tag{2.47}$$

Now, in our approximation, we may neglect $V_\mathrm{t} C_\mathrm{t}$, and $C_\mathrm{t}(V_0 + E)$, so that we have

$$V_{\mathrm{CR}} = V_0 \left(1 + \frac{C_\mathrm{L}}{C_\mathrm{R}}\right) - V_{\mathrm{CL}} \frac{C_\mathrm{L}}{C_\mathrm{R}}. \tag{2.48}$$

This equation links the V_R and V_L characteristic voltages at any cycle of the charge-pump's operation, through the trivial relation (2.46). Injecting it in (2.14), which approximates the energy converted by the Roundy's charge-pump and searching its maximum in terms of V_{CR} yields

$$\Delta W_{\mathrm{opt}} = \frac{C_{\min}(C_\mathrm{L} + C_\mathrm{R})(E + V_0)^2(\eta - 1)^2}{4(C_\mathrm{L} + \eta C_\mathrm{R})} \tag{2.49}$$

attained at cycle voltages

$$\begin{cases} V_{\mathrm{Lopt}} &= \dfrac{1}{2}\left(V_0 + \dfrac{V_0(C_\mathrm{R} + C_\mathrm{L}) + E(\eta - 1)C_\mathrm{R}}{C_\mathrm{L} + \eta C_\mathrm{R}}\right) \\ V_{\mathrm{Ropt}} &= \dfrac{V_0(2\eta C_\mathrm{R} + (\eta + 1)C_\mathrm{L}) + E(\eta - 1)C_\mathrm{L}}{2(C_\mathrm{L} + \eta C_\mathrm{R})}. \end{cases} \tag{2.50}$$

2.3.1.2 Rectifier topology charge-pumps

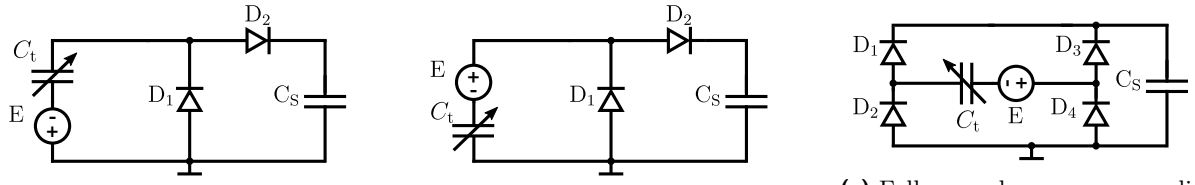

(a) Half-wave 1 charge-pump conditioning circuit

(b) Half-wave 2 charge-pump conditioning circuit

(c) Full-wave charge-pump conditioning circuit

Figure 2.8: Schematics of rectifiers charge-pumps

The three rectifier-topology charge-pumps whose schematic are depicted in Fig. 2.8 are used in electrostatic vibration energy harvesters that use of electret charging. If $E = 0$, then one can verify that none of these circuits satisfy the definition of charge-pump conditioning circuits given in Sec. 2.2.1. Besides, the only topological difference between the half-wave 1 and half-wave 2 charge-pumps are the polarity of the built-in voltage source. In fact, all the circuits presented in this section (Sec. 2.3) can be envisaged with a reversed-polarity electret, sometimes leading to different dynamics. We only explicitly present this transformation for the half-wave circuits, because the two circuits with opposite electret polarity are going to be used in Chap.5 for a method of electrostatic device characterization.

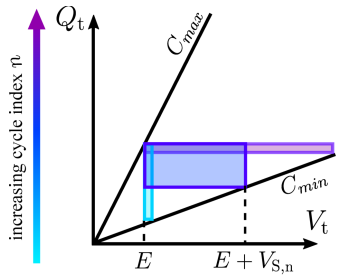

(a) Charge-voltage diagrams of the half-wave 1 (HW1) charge-pump, corresponding to different cycles in the autonomous evolution.

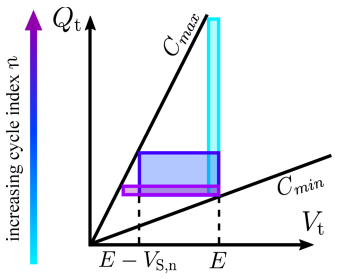

(b) Charge-voltage diagrams of the half-wave 2 (HW2) charge-pump, corresponding to different cycles in the autonomous evolution.

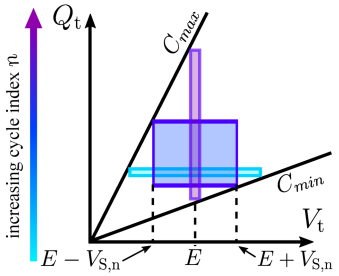

(c) Charge-voltage diagrams of the full-wave (FW) charge-pump, corresponding to different cycles in the autonomous evolution.

Figure 2.9: Idealized rectangular charge-voltage diagrams of rectifiers charge-pumps

In the literature, these three circuits are used as a modification of the primitive conditioning circuit presented in Sec. 1.3.2.3, in which the load is directly connected to the electret-charged transducer and experienced AC voltage. The reason invoked for using these rectifier topologies is to provide the load with rectified, DC voltage. For example, this is done by Miki *et al.* in [MSK09].

But as C_t is not a mere alternating voltage source, the rectifier topology changes the energy conversion scheme compared to what it is with the primitive conditioning circuit. This obviously results in different amounts of converted energy, let alone in different circuit dynamics, even for the same values of E and $C_{\max}, C_{\min}$. The fact that the transducer conditioning scheme implemented by any of the rectifier conditioning circuits is different from that implemented by the primitive conditioning circuit is necessarily verified at least for the following reason. These circuits being charge-pump conditioning circuits, their electrical dynamics are solely dependent on $C_{\max}$ and $C_{\min}$, with no dependence on the time evolution of C_t in between these extrema. On the contrary, as we have mentioned in Sec. 1.3.2.3, the energy converted by a primitive conditioning scheme depends on the pointwise time evolution of $C_t(t)$.

The full derivation of both the evolution law and the charge-voltage diagrams of these circuits is similar and simpler than the derivation of the evolution law for the Roundy's charge-pump done above (because there is only one fixed capacitor in the network). It has been done in this work, but we postpone it to Sec. 5.1 of Chap. 5 where these circuits are used for the characterization of e-VEHs, with a non-null diode threshold voltage taken into account to enhance precision. Here, we solely report the results of the analysis that are the explicit evolution laws of the voltage across C_S, at $C_t = C_{\max}$:

$$V_{S,\underline{n}}^{HW1} = \left(\frac{C_S}{C_{\min}+C_S}\right)^n \left(V_{S,\underline{n_0}}^{HW1} - \frac{C_{\max}-C_{\min}}{C_{\min}}E\right) + \frac{C_{\max}-C_{\min}}{C_{\min}}E, \tag{2.51}$$

$$V_{S,\overline{n}}^{HW2} = \left(\frac{C_S}{C_{\max}+C_S}\right)^n \left(V_{S,\overline{n_0}}^{HW2} - \frac{C_{\max}-C_{\min}}{C_{\max}}E\right) + \frac{C_{\max}-C_{\min}}{C_{\max}}E, \tag{2.52}$$

$$V_{S,\overline{n}}^{FW} = \left(\frac{(C_{\max}-C_S)(C_{\min}-C_S)}{(C_{\max}+C_S)(C_{\min}+Cs)}\right)^n \left(V_{S,\overline{n_0}}^{FW} - \frac{C_{\max}-C_{\min}}{C_{\max}+C_{\min}}E\right) + \frac{C_{\max}-C_{\min}}{C_{\max}+C_{\min}}E. \tag{2.53}$$

As their charge-voltage diagrams in Fig. 2.9 show, in the approximation of rectangular charge-voltage diagram, their respective characteristic voltages relate to the circuit's capacitors voltages

as

$$(HW1)\begin{cases} V_{\mathrm{L}} &= 0 \\ V_{\mathrm{R}} &= V_{\mathrm{S}} \end{cases} \qquad (HW2)\begin{cases} V_{\mathrm{L}} &= -V_{\mathrm{S}} \\ V_{\mathrm{R}} &= 0 \end{cases} \qquad (FW)\begin{cases} V_{\mathrm{L}} &= -V_{\mathrm{S}} \\ V_{\mathrm{R}} &= V_{\mathrm{S}} \end{cases} \tag{2.54}$$

The fact that rectifiers charge-pumps are stable charge-pumps is clear from (2.51)-(2.53), which clearly show that the charge-pump's state (which reduces to scalar $V_{\mathrm{S},\bar{\mathrm{n}}}$) is bounded.

The cycle maximizing the energy conversion can be easily found in the same way as for the Roundy's charge-pump, as (2.14) accurately approximates the converted energy per cycle in the case where $C_{\mathrm{S}} \gg C_{\max}$. Therefore, we search for the maximum of (2.14) over V_{S}, injecting each of (2.54) into (2.14). Doing so yields

$$\begin{aligned} \Delta W_{\mathrm{opt}}^{\mathrm{HW1}} &= \frac{1}{4} C_{\min} E^2 (\eta - 1)^2 \\ \Delta W_{\mathrm{opt}}^{\mathrm{HW2}} &= \frac{1}{4} C_{\min} E^2 \frac{(\eta - 1)^2}{\eta} \\ \Delta W_{\mathrm{opt}}^{\mathrm{FW}} &= \frac{1}{2} C_{\min} E^2 \frac{(\eta - 1)^2}{\eta + 1} \end{aligned} \tag{2.55}$$

reached for voltages across V_{S} that read

$$\begin{aligned} V_{\mathrm{S,opt}}^{\mathrm{HW1}} &= \frac{1}{2} C_{\min} E (\eta - 1), \\ V_{\mathrm{S,opt}}^{\mathrm{HW2}} &= \frac{1}{2} C_{\min} E \frac{(\eta - 1)}{\eta}, \\ V_{\mathrm{S,opt}}^{\mathrm{FW}} &= C_{\min} E \frac{(\eta - 1)}{\eta + 1}. \end{aligned} \tag{2.56}$$

2.3.2 Unstable charge-pumps

We now list the main reported unstable charge-pump conditioning circuits. In our framework for charge-pump conditioning circuits, we can characterize each of these circuits by their γ-ratio in their unstable mode of operation (see Sec. 2.2.2.2). Chap. 4 will show that having a wide range of selectable γ ratios for unstable charge-pumps can be useful in order to optimize the energy conversion. Let us hence list here some circuits that allow to implement such ratios.

2.3.2.1 Bennet's doubler

The Bennet's doubler is the first reported example of an unstable charge-pump. Its topology is depicted in Fig. 2.10a. All of the subsequently reported unstable charge-pumps are generalizations of its topology, as the next examples will show. This circuit is adapted from an electrostatic machine described by Bennet at the end of the 18^{th} century [BK87]. The first time it was reported for electrostatic vibration energy harvesting, it was with differential electrostatic transducers. Its analysis in this context has been done by De Queiroz in [DD11], for a simplified case using switches instead of diodes. The full analysis of the Bennet's doubler without simplification assumptions is contained in the analysis of the next chapter. Indeed, the analysis of a general topology of which the Bennet's doubler is a particular case is presented therein. Here, let us limit ourselves to an intuitive description of its operation that explains the unstable

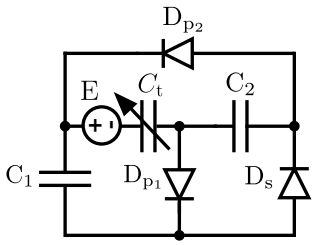

(a) The first example of an unstable charge-pump: the Bennet's doubler.

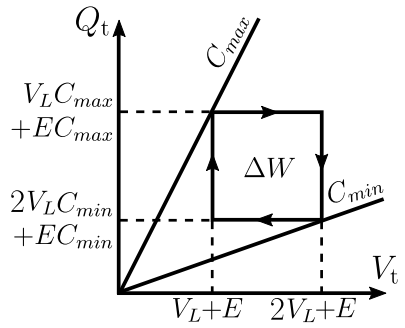

(b) Idealized charge-voltage diagram for one cycle of operation of the Bennet's doubler

Figure 2.10: The Bennet's doubler

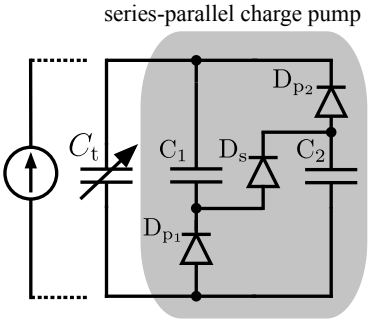

(a) View of the Bennet's doubler proposed in this work. (E removed for simplicity).

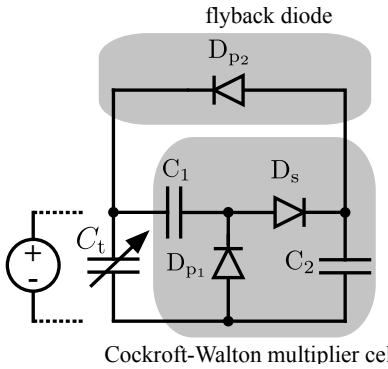

(b) View of the Bennet's doubler proposed by Lefeuvre *et al.* (E removed for simplicity).

Figure 2.11: Different ways to view the Bennet's doubler.

behavior of this circuit.

In its unstable mode of operation, the Bennet's doubler implements a ratio of $\gamma = 2$ between the cycle's characteristic voltages V_{L} and V_{R}. The unstable mode of operation is the Bennet's steady-state operation mode. It is reached from autonomous operation of the charge-pump, as long as $\eta > 2$ from any admissible initial state of the charge-pump.

To intuitively understand how the Bennet's doubler induces unstable behavior, we propose to consider the circuit as depicted in Fig. 2.11a. This circuit is exactly the same as the circuit of Fig. 2.10a but arranged slightly differently. Let us further consider C_{t} as an ideal, alternating current source (see the property (i) in Sec. 2.2.1). The circuit cyclically alternates between two

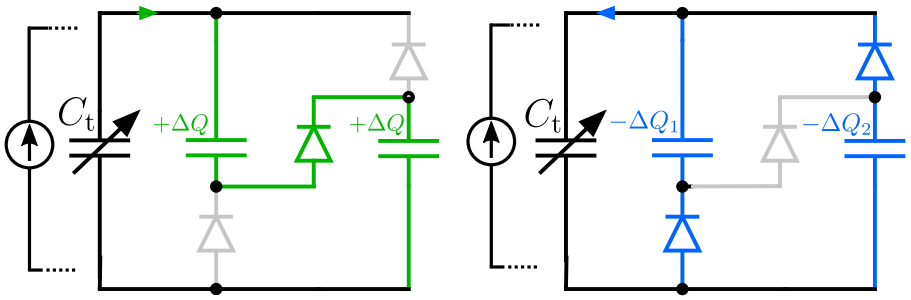

Figure 2.12: Intuitive explanation of the operation of the Bennet's doubler in unstable operation mode. Phase (i) on the left, phase (ii) on the right.

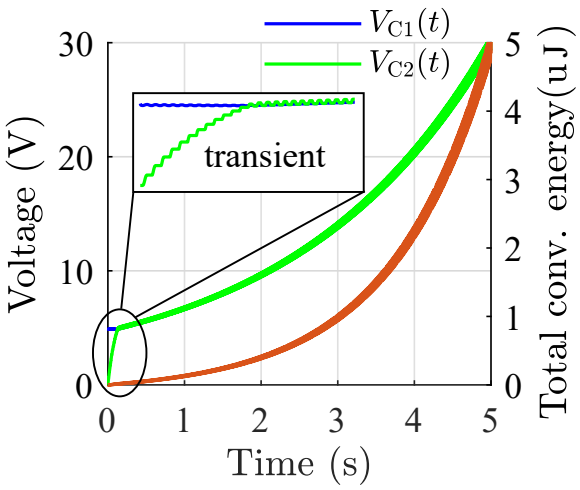

(a) Simulation of the Bennet's doubler: time-domain.

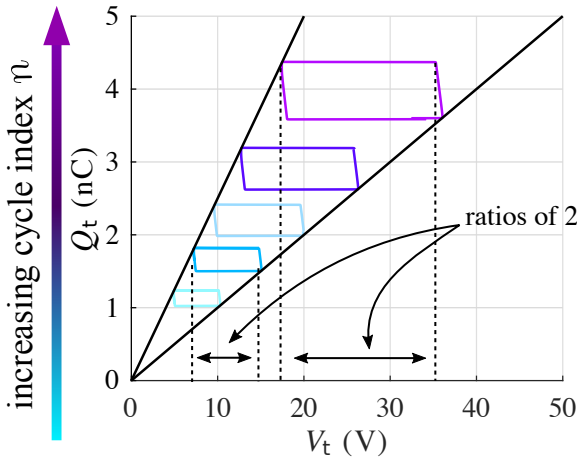

(b) Simulation of the Bennet's doubler: charge-voltage diagrams of some cycles.

Figure 2.13: Simulation of the Bennet's doubler.

phases of negative and positive current, depicted in Fig. 2.12. In phase (i), the current through C_t is negative and the fixed capacitors of the network are in series through D_s. At the end of this phase *each one* of the capacitors has received a positive charge amount of δQ. In phase (ii), the current through C_t is positive, and the fixed capacitors of the network are in parallel with the current source through D_{p_1} and D_{p_2}. The *total* positive charge given back to the current source amounts to δQ. Thus, at the end of the cycle, the total charge in the fixed capacitors C_1, C_2 has increased of $\delta Q > 0$. Consequently, the system's total energy has increased. The Bennet's doubler sets the ratio between δQ and the total charge in the circuit's capacitors at the beginning of the to a constant, for each cycle of variation C_t, when the circuit operates in its unstable operation mode. Therefore, the total charge in the circuit's fixed capacitors, and hence the total energy, increases exponentially.

In the phase (i) where the positive current flows from C_t to the fixed capacitors, the sum of the voltages across the two capacitors bias C_t. In phase (ii), the two capacitors are in parallel, so that they have the same voltage. This pattern cyclically takes places throughout the consecutive cycles of variation of C_t. Therefore, if the capacitances are of large value, then δQ does not induce a large voltage swing across C_1 and C_2 between phases (i) and (ii). Hence, the voltage of both capacitors can in fact be considered to be equal throughout all the operation of the charge-pump. As a result, for a cycle in unstable operation characterized by its V_L and V_R voltage

$$\begin{cases} V_L &= V_{C_1} = V_{C_2} \\ V_R &= V_{C_1} + V_{C_2} = 2V_{C_1} \end{cases} \tag{2.57}$$

which clearly shows the ratio of $\gamma = 2$.

The above interpretation of the Bennet's doubler operation has led us to the generic series-parallel topology of charge-pump conditioning circuits. This topology is briefly presented hereafter in Sec. 2.3.2.4, and is then extensively studied in the next chapter. The formal analysis of the Bennet's doubler is contained in that of our generic topology, as the latter is a generalization of the former.

To further illustrate the Bennet's doubler operation, we provide the simulation results de-

picted in Fig. 2.13a for the time domain evolution of the circuit's capacitors voltages. For this simulation, we have chosen $C_1 = 1\,\text{nF}$, $C_2 = 10\,\text{nF}$, $C_{\max} = 250\,\text{pF}$, $C_{\min} = 100\,\text{pF}$, and $E = 0$. The oscillating nature of the voltages across the fixed capacitors is visible, due to the fact that the capacitances receive the charge δQ in phase (i) when they are put in series, and lose part of δQ in phase (ii). The frequency of variation of C_t between $C_{\max}$ and $C_{\min}$ is of 100 Hz.

These results show that, in the unstable steady-state mode of operation, the voltages across the two fixed capacitors are roughly equal, as we have previously highlighted. Also, one notices that, contrarily to the Roundy charge-pump which reaches its steady-state operation mode after at most one cycle of variation of C_t, the transient operation mode of the Bennet's doubler lasts for several cycles before it reaches its (unstable) steady-state operation mode. Again, these different modes are thoroughly described in the analysis of the next chapter. Fig. 2.13b shows several charge-voltage diagrams for different conversion cycles, all in unstable mode of operation. As $E = 0$, we verify that the vertical sides of these cycles are located on the V-axis with a ratio of 2 in between them.

2.3.2.2 Lefeuvre's charge-pump

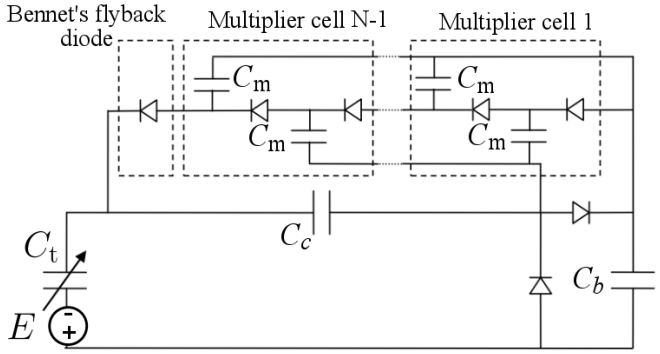

(a) Generic topology of the unstable charge-pump conditioning circuit proposed by Lefeuvre *et al.* (copied from [LRW14])

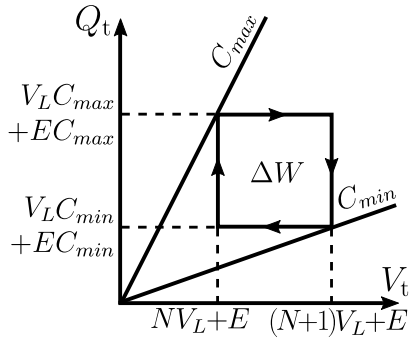

(b) Rectangular charge-voltage diagram implemented by Lefeuvre's charge-pump and Illenberger's charge-pump.

Figure 2.14: Lefeuvre's charge-pump.

Lefeuvre *et al.* reported on a generic unstable charge-pump topology generalizing the Bennet's doubler in [LRW14]. Their topology is depicted in Fig. 2.14a. A brief, intuitive explanation of its operation can be given as follows.

Lefeuvre *et al.* have proposed to view C_t in the Bennet's doubler topology as an alternating voltage source which is at the input of a Cockroft-Walton [KK00] multiplier cell. The output node of the multiplier is connected to C_t to provide a flyback mechanism. Therefore, in unstable mode of operation, the voltage across the fixed capacitor C_c is kept at a value that is equal to N times the voltage across the fixed capacitor C_b, in its unstable mode of operation. At $C_\text{t} = C_{\max}$, C_t is biased by C_c, while at $C_\text{t} = C_{\min}$, it is biased by C_b in series with C_c. THus, we can give the expression of the cycle characteristic voltages V_R and V_L as a function of the charge-pump's topology in unstable mode:

$$\begin{cases} V_\text{L} &= V_{C_\text{c}} = NV_{C_\text{b}}, \\ V_\text{R} &= V_{C_\text{c}} + V_{C_\text{b}} = (N+1)V_{C_\text{b}}, \end{cases} \tag{2.58}$$

from which a γ ratio of $1 + 1/N$ clearly ensues.

Note that no full formal analysis of such charge-pumps has been done yet, but we base our understanding of this topology on the reports of Lefeuvre *et al.* [LRW14]. In the following of the manuscript, we suppose that this topology satisfies our definition of charge-pumps conditioning circuits, and that they show a steady-state unstable behavior with ratios of the form $\gamma = 1 + 1/N$ ($N \in \mathbb{N}_*$). We also suppose this steady-state mode is attained from any initial state admissible by the topology, as long as $\eta > \gamma$. The charge-voltage diagram for a cycle in unstable operation mode is depicted in Fig. 2.14b.

2.3.2.3 Illenberger's charge-pump

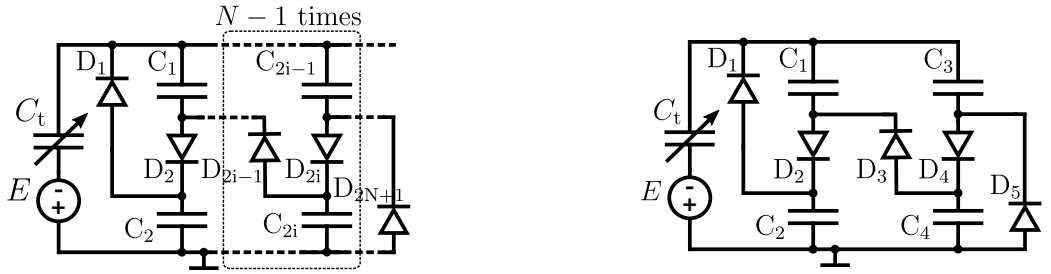

(a) Generic topology of the charge-pump conditioning circuit proposed by Illenberger *et al.*.

(b) Illenberger's charge-pump with $N = 3$.

Figure 2.15: Illenberger's charge-pump.

At about the same time as De Queiroz claimed that the Bennet's doubler and its variation may be suited for electrostatic vibration energy harvesting, McKay *et al.* and Illenberger *et al.* have reported on a topology of unstable charge-pump conditioning circuit initially destined to be used for dielastomer energy generators [MOC10; ITK17]. Still, this charge pump, depicted in Fig. 2.15a, is also suited for inertial e-VEHs that are studied in this document, as the electrical lumped-model of both devices is a variable capacitor.

In summary, Illenberger's circuit is another topology of unstable charge-pump topology that implements ratios of the form $\gamma = 1 + 1/N$ ($N \in \mathbb{N}_*$) in its unstable steady-state mode of operation, which is attained as long as $\eta > \gamma$. A quantitative analysis of the steady-state dynamics of this topology limited to the case $N = 2$ (depicted in Fig. 2.15b), but readily generalizable, has been done by Illenberger *et al.* in [ITK17].

2.3.2.4 Series-parallel charge-pumps

Series-parallel charge-pumps were proposed in this work. They are another generalization of the Bennet's doubler. They are obtained by adding capacitor branches, starting from the series-parallel view of the Bennet's doubler depicted above in Fig. 2.12. The generic topology of series-parallel charge-pumps is depicted in Fig. 2.16a, and the illustrating case of $N = 3$ is depicted in Fig. 2.16b.

Their thorough analysis verified and illustrated by simulations is the subject of Chap. 3. The reader can refer to the conclusion of Sec. 3.6 which summarizes the characteristics of this charge-pump in terms of its γ-ratio and how it relates to the circuit's fixed capacitors values.

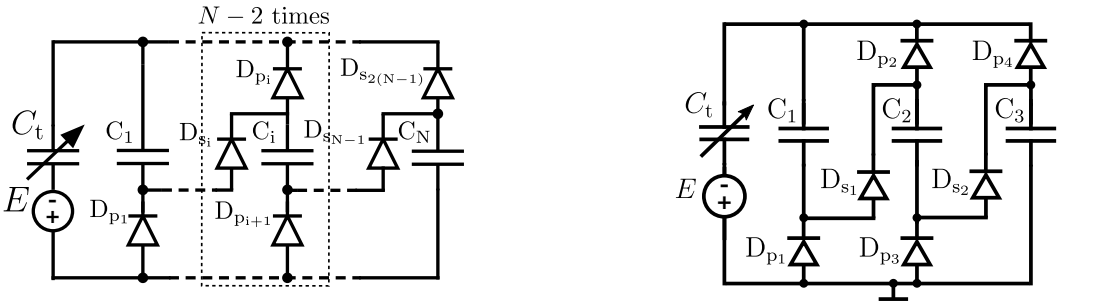

(a) Generic topology of the series-parallel charge-pump.

(b) Series-parallel charge-pump with $N = 3$.

Figure 2.16: Series-parallel charge-pump.

2.3.2.5 Other topologies

Other variations of the Bennet's doubler have been proposed in the literature. These circuits use of Zener diodes [DD13], or take advantage of multiple variable capacitances [Que14]. Therefore, we will not consider these topologies in this work, as they do not fit in our framework of charge-pump conditioning circuits. Notably, we will not consider them in the comparison between the different charge-pump conditioning schemes done in Chap. 4.

Note that all the cited unstable circuits can be considered by reversing the polarity of the transducer. Obviously, this does not change the circuit's operation in the case of $E = 0$. But for a transducer with a built-in voltage, the obtained behavior is different. For example, it can be proved that reversing the polarity of the transducer in the Bennet's doubler, when $E > 0$, turns it into a necessarily stable charge-pump. We will not consider the reversed polarity of transducer in the rest of this manuscript dealing with the unstable conditioning circuits.

2.4 Asynchronous control

As explained above in Sec. 2.2.2.1, the stable charge-pump conditioning circuits show a cycle of maximal energy conversion, but if the circuit continues its autonomous evolution under variation of C_t, it ends up in saturation and the converted energy per cycle asymptotically approaches zero. Consequently, to sustain the cycle of maximum energy conversion, an external control is needed. Such a control is also needed by unstable conditioning circuits, for example to satisfy a constraint of maximum voltage across the transducer (see Sec. 4.1). Plus, in Sec. 4.2, the electromechanical coupling effect will be shown to be responsible for the existence of maximum energy conversion cycles with unstable charge-pump conditioning circuits. In this condition, an external control is also needed to sustain this optimal cycle.

2.4.1 Yen's inductive flyback

Yen *et al.*, in [YL06], have proposed a way to have a control over the otherwise autonomous evolution of the Roundy's charge pump. Their architecture is depicted in Fig. 2.17a. It uses an inductive flyback mechanism. It allows to finely tune, through an asynchronous command of the switch SW, the values of both V_L and V_R. A an external control command activates the switch

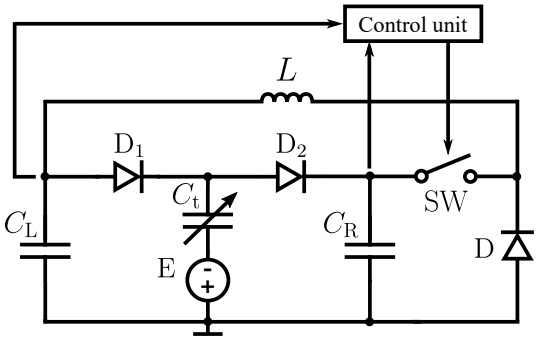

(a) Roundy's charge-pump with flyback control of the voltages V_L and V_R.

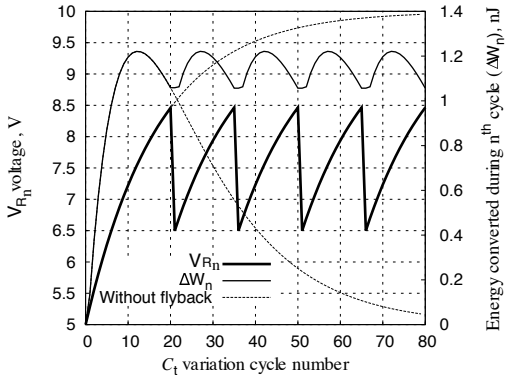

(b) Example of operation of the inductive flyback. V_L is not depicted as it merely changes from its initial value of 5 V, because C_L is chosen much larger than C_R. Taken from [Dud14].

Figure 2.17: Yen's inductive flyback.

SW when based on the sensed values of V_L and V_R. This transfers charges from C_L to C_R. A fine control of SW therefore allows for the sustaining of a chosen cycle, characterized in terms of targeted V_L and V_R voltages. The detailed operation of this circuit is thoroughly explained in [BBG16; Dud14; KBH12] and numerous implementations have been proposed so far [KBH13; Dud14].

The simulation example of Fig. 2.17b illustrates how it allows to sustain conversion cycle within specific limits for V_R. Note that in the depicted simulation, as C_L is very large compared to C_R, the V_L voltage merely changes within the duration of the simulation.

2.4.2 DC-DC converter energy-extracting interface

The presentation of the various conditioning circuits done in this chapter shows that the energy converted by an e-VEH is first stored in the fixed capacitors of the conditioning circuit. Because of the constraints on the form of the energy needed by the load (e.g., requirements on the load voltage), an intermediary interface circuit is needed between the conditioning circuit and the load. This interface circuit has to (i) extract the energy from the conditioning circuit and (ii) deliver it in a suitable form to the load (e.g., load's nominal voltage requirement). The task (ii) is relatively independent of the transducer's conditioning circuitry, and will not be discussed herein.

The circuit depicted in Fig. 2.18 is a simple candidate to fulfill the task (i). By a fine command of the switch and on how exactly it is connected to the conditioning circuit, the characteristic voltages V_L and V_R can be controlled by a proper discharge of the charge-pump's fixed capacitors. Specifically, the switch can be commanded so to sustain a cycle of maximum energy conversion as described above. However, this interface is not capable of setting V_L and V_R out of the ranges in which they can evolve from the conditioning circuit's autonomous operation, because it only removes energy from the capacitor network. The practical implementation of such energy-extracting interfaces for charge-pump conditioning circuits is studied, e.g., in [BKG17].

A simple example of a switch control policy for this interface will be presented Sec. 3.5.7, where the interface is associated in a simulation to a series-parallel charge-pump.

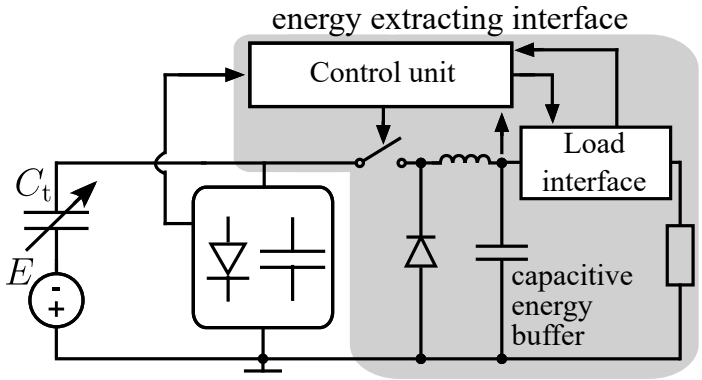

Figure 2.18: Energy extracting interface connected to a charge-pump conditioning circuit.

Finally, note that other means of asynchronous control of unstable charge-pump conditioning circuits have been proposed, e.g., by Wei *et al.* in [WLM16]. For the present manuscript, it suffices to acknowledge that there are reported mechanisms that allow to sustain the charge-pumps' autonomous operation at a particular energy conversion cycle.

2.5 Conclusion and future works

This section presented the charge-pump conditioning circuits in a unified way and gave a comprehensive list of reported topologies useful for electrostatic vibration energy harvesting. Among them, the series-parallel charge-pump conditioning circuits are thoroughly analyzed in the next chapter. The conditioning schemes corresponding to the different presented topologies will be compared in Chap. 4 in the electrical domain, and a method geared towards their comparison in the electromechanical domain will also be presented therein.

By giving a presentation of the existing charge-pump conditioning circuits starting from a general framework in which they fit, we attempted to pave the way for a complete theory of charge-pump conditioning circuits. Among the pressing questions that such a theory could help answering, one would be a criterion that could identify, from the topology of the circuit's diodes-capacitors network, whether it can exhibit unstable operation or not. This question has an obvious theoretical interest. But a complete theory of charge-pumps can also have very practical applications for e-VEH. For example, Chap. 4 highlights that different application cases can ask for different unstable charge-pumps, that is, different γ ratios. Once an optimal γ ratio is determined, it can be interesting to formally identify the charge-pump conditioning circuit with minimum amount of diodes that implements the determined γ ratio. In this example, minimizing the number of diodes is of interest as each diode is the source of energy dissipation. Besides, another important that such a theory can help is description of the dynamics of charge-pump conditioning circuits submitted to capacitance variation functions with multiple extremum values, and not just fixed $C_{\max}$ and $C_{\min}$ as it was considered in this chapter and in the next.

Chapter 3

Series-parallel charge-pump conditioning circuits

The previous chapter has defined the concept of unstable charge-pump conditioning circuit. State-of-the-art topologies of such circuits were presented, that allowed to implement unstable steady-state behavior of ratios of the form $1 + 1/N$, for positive integer N.

The charge-pump conditioning circuit that we propose in this chapter extends the family of unstable charge-pump conditioning circuits. This new generic topology is able to implement any rational ratio greater than 2 between the conversion cycle's characteristic voltages. The intuitive idea behind this generic topology is to increase the number of parallel branches in the Bennet's doubler, presented in Sec. 2.3.2.1. The obtained circuit is depicted in Fig. 3.1.

Intuitively, by resorting to the qualitative description of the Bennet's doubler that we gave in Sec. 2.3.2.1, one could expect that adding branches as in Fig. 3.1 would simply change the γ ratio to larger integer values. The reasoning is that C_t does not becomes in series with only 2 but N fixed capacitors, that are kept at the same voltage at each cycle of the capacitance variation. At the scale of one cycle, the biasing across C_t would then change from the equal voltage across all N capacitors when it is in parallel with them, to the sum of all N voltages, i.e., N times the voltage across each of the fixed capacitors. If one chooses V_L to be the voltage across any of those capacitors, then $V_\mathrm{R} = NV_\mathrm{L}$, or in other words, the γ ratio implemented by the circuit in its unstable operation mode, if it is attained, is such that $\gamma = N$.

However, the following analysis shows that the situation is slightly different. In fact, our analysis shows that the γ ratio between V_R and V_L is not necessarily equal to N, but can be tuned to take any real value between 2 and N. This is done by properly choosing the values of the fixed capacitors.

The essential part of this chapter is a formal proof of the unstable behavior of our new generic topology, which in the process yields the formula that links the value of γ to the value of the circuit's fixed capacitors. We also express the conditions under which this mode is attained. Simulation results are presented to support the analysis. Note that the analysis is done with a built-in voltage $E = 0$ for simplicity. Yet, the results are not qualitatively different if $E > 0$, as discussed in the end of the chapter. The role of parasitiac effects is also briefly discussed and illustrated in the simulations. Finally, note that this formal analysis contains that of the

Bennet's doubler, which is the particular case $N = 2$, including transient behavior. Such analysis has not been previously reported.

This work has led to the publication [KGB17b] on which the present chapter is largely based on.

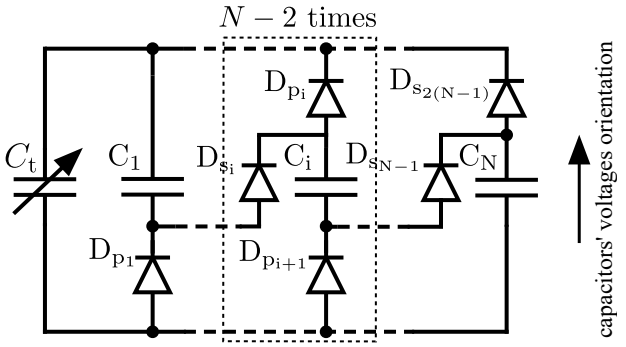

Figure 3.1: The proposed generic topology: series-parallel charge-pumps.

3.1 Local evolution laws

The notations and context of C_t variation are the same as those detailed in Sec. 2.1.1. We add here that the voltage across C_t at any time t is denoted by $V_\mathrm{t}(t)$. The voltage across a fixed capacitor $\mathrm{C_i}$ of the circuit, $i \in [\![1; N]\!]$, is denoted by $V_{i,\overline{n}}$ at a cycle n when $C_\mathrm{t} = C_\mathrm{max}$, $V_{i,\underline{n}}$ at a cycle n when $C_\mathrm{t} = C_\mathrm{min}$, and $V_i(t)$ at a any time t. The beginning of time is denoted by t_0.

All the circuit elements are considered ideal. In particular, the diode elements follow the ideal diode current-voltage law, with zero threshold voltage.

Let's immediately note that, from the circuit topology:

$$\forall t \geqslant t_0, \forall i \in [\![1; N]\!], V_i(t) \leqslant V_\mathrm{t}(t) \leqslant \sum_{j=1}^{N} V_j(t) \tag{3.1}$$

3.1.1 Half-cycle: decreasing variable capacitance

Let's consider an arbitrary cycle n, at the moment when C_t starts to decrease from C_max of the previous cycle n, to C_min of the cycle $n + 1$.

Suppose that;

$$V_{\mathrm{t},\overline{n}} > 0, \exists j \in [\![1; N]\!], V_{j,\overline{n}} > 0, \forall i \in [\![1; N]\!], V_{i,\overline{n}} \geqslant 0. \tag{3.2}$$

As no current flows until a subset of the $(\mathrm{D_{s_i}})_{1 \leqslant i \leqslant N-1}$ diodes conduct, the law for $V_\mathrm{t}(t)$, immediately after C_t starts to decrease, is, for a certain $t_{\overline{n},s} \in [t_{\overline{n}}; t_{\underline{n+1}}]$:

$$\forall t \in [t_{\overline{n}}; t_{\overline{n},s}], \qquad V_\mathrm{t}(t) = V_{\mathrm{t},\overline{n}} \frac{C_\mathrm{max}}{C_\mathrm{t}(t)}, \tag{3.3}$$

and the voltage across the fixed capacitors remains constant:

$$\forall i \in [\![1;N]\!], \forall t \in [t_{\overline{n}}; t_{\overline{n},s}], \qquad V_i(t) = V_{i,\overline{n}}. \tag{3.4}$$

3.1.1.1 No series switching

If the diodes $(\mathrm{D_{s_i}})_{1 \leqslant i \leqslant N-1}$ do not conduct for any $t \in [t_{\overline{n}}; t_{\underline{n+1}}[$ then $t_{\overline{n},s} = t_{\underline{n+1}}$, and the voltage across C_t at the end of the half-cycle is:

$$V_{\mathrm{t},\underline{n+1}} = \eta V_{\mathrm{t},\overline{n}}. \tag{3.5}$$

The voltage across the fixed capacitors at the end of the half-cycle is:

$$\forall i \in [\![1;N]\!], \qquad V_{i,\overline{n}} = V_{i,\underline{n+1}}. \tag{3.6}$$

3.1.1.2 Series switching

Otherwise, the circuit will switch to its series configuration when the voltage across C_t makes the $(\mathrm{D_{s_i}})_{1 \leqslant i \leqslant N-1}$ diodes conduct. This happens when:

$$V_\mathrm{t}(t =: t_{\overline{n},s}) = \sum_{i=1}^{N} V_{i,\overline{n}}, \tag{3.7}$$

and the corresponding value of C_t is:

$$C_\mathrm{t} = \frac{V_{\mathrm{t},\overline{n}}}{\sum_{i=1}^{N} V_{i,\overline{n}}} C_\mathrm{max}. \tag{3.8}$$

The circuit is then equivalent to C_t being in series with a capacitor of value $C = 1/(\sum_{i=1}^{N} {C_i}^{-1})$. The voltage variation law on C_t becomes:

$\forall t \in [t_{\overline{n},s}; t_{\underline{n+1}}]$,

$$V_\mathrm{t}(t) = \sum_{i=1}^{N} V_i(t) = \sum_{i=1}^{N} V_{i,\overline{n}} + \Delta Q_n(t) \sum_{i=1}^{N} {C_i}^{-1}, \tag{3.9}$$

where:

$$\forall t \in [t_{\overline{n},s}; t_{\underline{n+1}}], \qquad \Delta Q_n(t) = \frac{V_{\mathrm{t},\overline{n}} C_\mathrm{max} - C_\mathrm{t}(t) \sum_{i=1}^{N} V_{i,\overline{n}}}{1 + C_\mathrm{t}(t) \sum_{i=1}^{N} {C_i}^{-1}}. \tag{3.10}$$

If the circuit has entered its series configuration before $C_\mathrm{t} = C_\mathrm{min}$, the capacitors voltages when $C_\mathrm{t} = C_\mathrm{min}$ satisfy:

$$\forall i \in [\![1;N]\!], \qquad V_{i,\underline{n+1}} = V_{i,\overline{n}} + \frac{\Delta Q_n}{C_i}, \tag{3.11}$$

where ΔQ_n is the amount of charges given by C_t to the other capacitors, from $C_\mathrm{t} = C_\mathrm{max}$ to

$C_\mathrm{t} = C_\mathrm{min}$. For every capacitor of the loop, this amount is equal to:

$$\Delta Q_n = C_\mathrm{min} \frac{\eta V_{\mathrm{t},\overline{n}} - \sum_{i=1}^{N} V_{i,\overline{n}}}{1 + C_\mathrm{min} \sum_{i=1}^{N} {C_i}^{-1}}. \tag{3.12}$$

Note that $\Delta Q_n > 0$ as the quantity in (3.8) is larger than C_min by the series switching hypothesis.

The N capacitors being all in series, with the chosen voltage orientations:

$$V_{\mathrm{t},\underline{n+1}} = \sum_{i=1}^{N} V_{i,\underline{n+1}}. \tag{3.13}$$

Note that the voltages remained positive through the half cycle.

3.1.2 Half-cycle: increasing variable capacitance

Consider now an arbitrary cycle n, at the moment when $C_\mathrm{t} = C_\mathrm{min}$ starts to increase from C_min of the cycle n to C_max of the cycle n.

Suppose, without loss of generality, that the voltages are ordered as

$$V_{1,\underline{n}} \geqslant \ldots \geqslant V_{N,\underline{n}}. \tag{3.14}$$

Now, consider C_t increasing from C_min of the cycle n to C_max of the same cycle. As no current flows until the $(\mathrm{D_{p_i}})_{1 \leqslant i \leqslant 2(N-1)}$ diodes eventually start to conduct, the law for $V_\mathrm{t}(t)$, immediately after C_t starts to increase, is:

$$\forall t \in [t_{\underline{n}}; t_{\underline{n},1}], \qquad V_\mathrm{t}(t) = V_{\mathrm{t},\underline{n}} \frac{C_\mathrm{min}}{C_\mathrm{t}(t)}, \tag{3.15}$$

where, $t_{\underline{n},1} \in [t_{\underline{n}}; t_{\overline{n}}]$.

Consider a fixed capacitor $\mathrm{C_k}$. It will remain disconnected from C_t, until the diodes of its branch conduct. This eventually happens when $V_\mathrm{t}(t)$ becomes as:

$$V_\mathrm{t}(t =: t_{\underline{n},k}) = V_{k,\underline{n}}. \tag{3.16}$$

The corresponding value of C_t is given by:

$$C_{\mathrm{t}(k,n)} = \frac{V_{\mathrm{t},\underline{n}} C_\mathrm{min} + \sum_{i=1}^{k} V_{i,\underline{n}} C_i}{V_{k,\underline{n}}} - \sum_{i=1}^{k} C_i. \tag{3.17}$$

Then, when (3.16) is fulfilled, the voltage variation law on C_t (and for every capacitor in parallel with C_t) becomes:

$\forall t \in [t_{\underline{n},k}; t_{\underline{n},k+1}]$,

$$V_\mathrm{t}(t) = \frac{V_{\mathrm{t},\underline{n}} C_\mathrm{min} + \sum_{i=1}^{k} V_{i,\underline{n}} C_i}{C_\mathrm{t}(t) + \sum_{i=1}^{k} C_i}, \tag{3.18}$$

with $t_{\underline{n},N+1} = t_{\overline{n}}$. This holds until another capacitor is eventually connected in parallel with C_t, i.e., until $C_\mathrm{t} = C_{\mathrm{t}(k+1,n)}$.

At $C_\mathrm{t} = C_\mathrm{max}$ of a given cycle, considering N capacitors and defining $p \in [\![1;N]\!]$ as the number of capacitors in parallel with C_t at $C_\mathrm{t} = C_\mathrm{max}$:

$$C_{\mathrm{t}(p,n)} \leqslant C_\mathrm{max} < C_{\mathrm{t}(p+1,n)}. \tag{3.19}$$

Note that, as the voltages are supposed ordered as in (3.14), and as the voltages across the capacitors vary continuously:

$$t_{\underline{n}} \leqslant t_{\underline{n},1} \leqslant \ldots \leqslant t_{\underline{n},p} \leqslant t_{\overline{n}}. \tag{3.20}$$

At $C_\mathrm{t} = C_\mathrm{max}$ of the cycle n, the voltages across the fixed capacitors that are in parallel with C_t are as:

$\forall k \in [\![1;p]\!]$,

$$V_{k,\overline{n}} = V_{\mathrm{t},\overline{n}} = \frac{V_{\mathrm{t},\underline{n}} C_\mathrm{min} + \sum_{i=1}^{p} V_{i,\underline{n}} C_i}{C_\mathrm{max} + \sum_{i=1}^{p} C_i}, \tag{3.21}$$

and the voltages across the fixed capacitors that are not in parallel with C_t at $C_\mathrm{t} = C_\mathrm{max}$ of cycle n have not changed:

$$\forall k \in [\![p+1;N]\!], \qquad V_{k,\overline{n}} = V_{k,\underline{n}}. \tag{3.22}$$

The inequality $C_{\mathrm{t}(p,n)} < C_{\mathrm{t}(p+1,n)}$ comes from the hypothesis (3.14). Note that, under this hypothesis, at a given cycle at $C_\mathrm{t} = C_\mathrm{min}$, (3.19) is equivalent to, for the same cycle at $C_\mathrm{t} = C_\mathrm{max}$:

$$V_{\mathrm{t},\overline{n}} = \ldots = V_{p,\overline{n}} > V_{p+1,\overline{n}} > \ldots > V_{N,\overline{n}}. \tag{3.23}$$

Finally, note that the voltages remained positive during the whole half-cycle.

3.1.3 Evolution laws across a complete cycle

3.1.3.1 No series switching

At an arbitrary cycle n, if the half cycle of decreasing of C_t from C_max to C_min is such that no series switching occurs (see 3.1.1.1), then:

$$\forall i \in [\![1;N]\!], \qquad \begin{aligned} V_{\mathrm{t},\overline{n+1}} &= V_{\mathrm{t},\overline{n}} \\ V_{i,\overline{n+1}} &= V_{i,\overline{n}}. \end{aligned} \tag{3.24}$$

3.1.3.2 Series switching

The evolution law for the capacitors voltages at $C_\mathrm{t} = C_\mathrm{max}$ between two consecutive cycles n and $n+1$ can now be obtained for fixed p and given that (3.7) is fulfilled. Under these assumptions,

with $\mathbf{V}_{\overline{\mathbf{n}}} = (V_{\mathrm{t},\overline{n}}, V_{1,\overline{n}}, \ldots, V_{N,\overline{n}})^{\mathrm{T}}$, the system's evolution is given by:

$$\mathbf{V}_{\overline{\mathbf{n+1}}} = \mathbf{A_p}\mathbf{V}_{\overline{\mathbf{n}}}, \quad \text{if } V_{\mathrm{t},\overline{n}} = \ldots = V_{p,\overline{n}} > V_{p+1,\overline{n}} > \ldots > V_{N,\overline{n}}. \tag{3.25}$$

The matrix $\mathbf{A_p}$, for $0 \leqslant p \leqslant N$, is defined as:

$$\mathbf{A_p} = \begin{pmatrix} a_p & \ldots & a_p & b_p & \ldots & b_p \\ \vdots & \ddots & \vdots & \vdots & \ddots & \vdots \\ a_p & \ldots & a_p & b_p & \ldots & b_p \\ c_{p_{p+1}} & \ldots & c_{p_{p+1}} & d_{p_{p+1}} + 1 & \ldots & d_{p_{p+1}} \\ \vdots & \ddots & \vdots & \vdots & \ddots & \vdots \\ c_{p_N} & \ldots & c_{p_N} & d_{p_N} & \ldots & d_{p_N} + 1 \end{pmatrix}, \tag{3.26}$$

where the coefficients are

$$a_p = \frac{(C_{\max} + \sum_{i=1}^{p} C_i) C_{\min} \sum_{i=1}^{N} {C_i}^{-1} + \sum_{i=1}^{p} C_i + p(C_{\max} - (p-1)C_{\min})}{(C_{\max} + \sum_{i=1}^{p} C_i)(1 + C_{\min} \sum_{i=1}^{N} {C_i}^{-1})}, \tag{3.27}$$

$$b_p = -\frac{C_{\min}(p-1)}{(C_{\max} + \sum_{i=1}^{p} C_i)(1 + C_{\min} \sum_{i=1}^{N} {C_i}^{-1})}, \tag{3.28}$$

$$c_{p_k} = \frac{C_{\max} - pC_{\min}}{C_k(1 + C_{\min} \sum_{i=1}^{N} {C_i}^{-1})}, \tag{3.29}$$

$$d_{p_k} = -\frac{C_{\min}}{C_k(1 + C_{\min} \sum_{i=1}^{N} {C_i}^{-1})}. \tag{3.30}$$

As all the $(V_{i,\overline{n}})_{1 \leqslant i \leqslant p}$ are equal (to $V_{\mathrm{t},\overline{n}}$) and follow the same law at the scale of the cycle n, a reduced form of the matrix will be considered: $\tilde{\mathbf{A}}_{\mathbf{p}} \in \mathbb{R}^{(N-p+1)\times(N-p+1)}$.

$$\tilde{\mathbf{A}}_{\mathbf{p}} = \begin{pmatrix} a_p & b_p & \ldots & b_p \\ c_{p_{p+1}} & d_{p_{p+1}} + 1 & \ldots & d_{p_{p+1}} \\ \vdots & \vdots & \ddots & \vdots \\ c_{p_N} & d_{p_N} & \ldots & d_{p_N} + 1 \end{pmatrix}. \tag{3.31}$$

Thus, (3.25) becomes, with $\tilde{\mathbf{V}}_{\overline{\mathbf{n}}} = (V_{\mathrm{t},\overline{n}}, V_{p+1,\overline{n}}, \ldots, V_{N,\overline{n}})^{\mathrm{T}}$:

$$\tilde{\mathbf{V}}_{\overline{\mathbf{n+1}}} = \tilde{\mathbf{A}}_{\mathbf{p}}\tilde{\mathbf{V}}_{\overline{\mathbf{n}}}, \quad \text{if } V_{\mathrm{t},\overline{n}} = \ldots = V_{p,\overline{n}} > V_{p+1,\overline{n}} > \ldots > V_{N,\overline{n}}. \tag{3.32}$$

3.2 Steady-state dynamics of the circuit

From the local evolution laws, we now derive the global dynamics of the circuit. This is the evolution of the state of the conditioning circuit defined by $\mathbf{V_n} = (V_{\mathrm{t},\overline{n}}, V_{1,\overline{n}}, \ldots, V_{N,\overline{n}})^{\mathrm{T}} \in \mathbb{R}_+^{N+1}$,

starting from an initial state $\mathbf{V_0}$, for a periodic variation of C_t maximum and minimum C_max and C_min. We remind the reader that these two quantities are incorporated into the system's parameters, allowing to consider the system as autonomous. The coordinates of $\mathbf{V_0}$ are supposed to satisfy (3.1), as constrained by the circuit, and (3.2).

The goal of this analysis is to rigorously describe the different possible operation regimes of the circuit, and in particular, to quantitatively describe the steady-state modes of operation, as a function of the circuit's parameters. More precisely, the conditions for the circuit to show an exponential steady-state mode are derived, in the sense that the voltage across the circuit's fixed capacitors increase exponentially across the cycles of C_t's variation. This mode is an unstable mode according to the terminology of charge-pump conditioning circuits that was exposed in the previous chapter.

We divide the analysis into two cases: $\eta > N$ and $\eta < N$. The first case is such that the steady-state mode is attained irrespective of the values of the initial circuit's state. We make the analysis for the second case for a particular configuration of the circuit's initial state.

3.2.1 Case $\eta > N$

First, let's state the following lemma, that states that in steady-state mode, the order of the voltages across the circuit's capacitors, relative to their capacitance, does not depend on the initial voltages, given that $\eta > N$ and (3.1), (3.2), are fulfilled:

Lemma 1 (Order of voltages and capacitors)**.** *Consider the circuit topology in Fig. 3.1. For any values of the initial voltages fulfilling (3.1) and (3.2):*

$$\eta > N \Rightarrow (\exists n^* \in \mathbb{N}, \forall n \in \mathbb{N}, n \geqslant n^* \Rightarrow (V_{1,\overline{n}} \geqslant \ldots \geqslant V_{N,\overline{n}} \Leftrightarrow C_1 \leqslant \ldots \leqslant C_N)).$$

Proof. Consider two fixed capacitors of the network, C_1 and C_2. Let:

$$\begin{aligned} \mathcal{Q}_i^j &= \{n \in \mathbb{N} \mid n \geqslant i, V_{\mathrm{t},\overline{n}} = V_{j,\overline{n}}\}, \\ \mathcal{S}_i^j &= \{n \in \mathbb{N} \mid n \geqslant i, (V_{\mathrm{t},\overline{n-1}} = V_{j,\overline{n-1}}) \wedge (V_{\mathrm{t},\overline{n}} \neq V_{j,\overline{n}})\}. \end{aligned}$$

(a) Consider a cycle n_1 such that $\mathcal{Q}_{n_1}^1 \cup \mathcal{Q}_{n_1}^2 = \varnothing$. In this case, the evolution laws derived in section 3.1 predict an evolution of the circuit's state with no parallel configuration of C_1 and/or C_2 with C_t. As at each cycle, the switching in series will necessarily occur, since $\eta > N$:

$$\forall n \geqslant n_1, \qquad \begin{aligned} V_{1,\overline{n}} &= V_{1,\overline{n_1}} + \frac{1}{C_1} \sum_{k=n_1}^{n} \Delta Q_k, \\ V_{2,\overline{n}} &= V_{2,\overline{n_1}} + \frac{1}{C_2} \sum_{k=n_1}^{n} \Delta Q_k, \end{aligned} \tag{3.33}$$

with ΔQ_k defined in (3.12). Thus:

$$\forall n \geqslant n_1, \qquad \Delta_n = V_{1,\overline{n}} - V_{2,\overline{n}} = V_{1,\overline{n_1}} - V_{2,\overline{n_1}} + \frac{C_2 - C_1}{C_1 C_2} \sum_{k=n_1}^{n} \Delta Q_k, \tag{3.34}$$

where:

$$\sum_{k=n_1}^{n} \Delta Q_k = \sum_{k=n_1}^{n} \left(\frac{C_{\min}}{1 + C_{\min} \sum_{i=1}^{N} {C_i}^{-1}} (V_{\mathrm{t},\overline{k}}(\eta - \ p_k) - \sum_{i=p_k+1}^{N} V_{i,\overline{k}}) \right), \tag{3.35}$$

and where p_k is the number of capacitors in parallel with C_t in cycle k at $C_\mathrm{t} = C_{\max}$. Hence, since for any $(k, i) \in \mathbb{N} \times [\![1; N]\!]$, $V_{i,\overline{k}} \leqslant V_{\mathrm{t},\overline{k}}$, and under the condition $\eta > N$:

$$\frac{C_{\min}}{1 + C_{\min} \sum_{i=1}^{N} {C_i}^{-1}} (V_{\mathrm{t},\overline{k}}(\eta - p_k) \quad - \sum_{i=k_i+1}^{N} V_{i,\overline{k}}) \geqslant C_{\min} \frac{V_{\mathrm{t},\overline{n_1}}(\eta - N)}{1 + C_{\min} \sum_{i=1}^{N} {C_i}^{-1}} > 0. \tag{3.36}$$

Therefore, the sequence $(\Delta_n)_{n \geqslant n_1}$ diverges to $+\infty$ if and only if $C_1 < C_2$, to $-\infty$ if and only if $C_2 < C_1$. Consequently, eventually swapping the capacitors indexes in the case $C_1 = C_2$ so as to have $V_{1,\overline{n_1}} \geqslant V_{2,\overline{n_1}}$:

$$\exists n_1' \geqslant n_1, \, \forall n, \, n \geqslant n_1' \Rightarrow (V_{1,\overline{n}} \geqslant V_{2,\overline{n}} \Leftrightarrow C_1 \leqslant C_2). \tag{3.37}$$

(b) Consider a cycle $n_2(i)$ such that $\mathcal{Q}^1_{n_2(i)} \cup \mathcal{Q}^2_{n_2(i)} \neq \varnothing$. Suppose $V_{1,\overline{n_2(i)}} \geqslant V_{2,\overline{n_2(i)}}$.

(b.1) First, the case when $C_1 \leqslant C_2$ is investigated. From (3.33), with $n_1 = n_2(i)$, it follows that $\mathcal{Q}^1_{n_2(i)} \neq \varnothing$ and:

$$C_1 \leqslant C_2 \Rightarrow (\forall n \in [\![n_2(i); \min \mathcal{Q}^1_{n_2(i)}[\![, \, V_{1,\overline{n}} \geqslant V_{2,\overline{n}}). \tag{3.38}$$

(b.1.1) If $\mathcal{S}^1_{n_2(i)} = \varnothing$, (3.38) can be extended to any cycle after $n_2(i)$:

$$C_1 \leqslant C_2 \Rightarrow (\forall n, n \geqslant n_2(i) \Rightarrow V_{1,\overline{n}} \geqslant V_{2,\overline{n}}). \tag{3.39}$$

(b.1.2) Now, suppose $\mathcal{S}^1_{n_2(i)} \neq \varnothing$.

(b.1.2.1) On the one hand, note that:

$$\forall n \in [\![\min \mathcal{Q}^1_{n_2(i)}; \min \mathcal{S}^1_{n_2(i)}[\![, \qquad V_{1,\overline{n}} \geqslant V_{2,\overline{n}}. \tag{3.40}$$

(b.1.2.2) On the other hand, (see condition (3.16)):

$$\forall n \in \mathcal{S}_{n_2(i)}, \qquad V_{1,\underline{n}} < V_{\mathrm{t},\overline{n}}, \tag{3.41}$$

with, from (3.11), and with ΔQ_n defined in (3.12):

$$\forall n, \qquad \begin{aligned} V_{1,\overline{n}} &= V_{1,\overline{n-1}} + \frac{\Delta Q_{n-1}}{C_1}, \\ V_{2,\overline{n}} &= V_{2,\overline{n-1}} + \frac{\Delta Q_{n-1}}{C_2}. \end{aligned} \tag{3.42}$$

Hence:

$$\begin{aligned}&((C_1 \leqslant C_2) \wedge (\forall k \in \mathcal{S}_{n_2(i)},\, V_{1,\overline{k-1}} \geqslant V_{2,\overline{k-1}})),\\ &\Rightarrow \forall n \in \mathcal{S}_{n_2(i)},\, V_{2,\underline{n}} \leqslant V_{1,\underline{n}} < V_{\mathrm{t},\overline{n}},\\ &\Rightarrow \forall n \in \mathcal{S}_{n_2(i)},\, V_{2,\overline{n}} = V_{2,\underline{n}} \leqslant V_{1,\overline{n}} = V_{1,\underline{n}}.\end{aligned} \tag{3.43}$$

Putting it all together, from (3.38) and (3.39) comes:

$$C_1 \leqslant C_2 \Rightarrow (\forall n \in [\![n_2(i); \min \mathcal{S}^1_{n_2(i)}[\![,\, V_{1,\overline{n}} \geqslant V_{2,\overline{n}}), \tag{3.44}$$

and from (3.43), the above reasoning starting from ***(b.1)*** can then be inductively repeated choosing $n_2(i+1) = \min \mathcal{S}^1_{n_2(i)}$: if $\mathcal{Q}^1_{n_2(i)} \cup \mathcal{Q}^2_{n_2(i)}$ is not a finite set, then inductively:

$$C_1 \leqslant C_2 \Rightarrow (\forall n,\, n \geqslant n_2 \Rightarrow V_{1,\overline{n}} \geqslant V_{2,\overline{n}}). \tag{3.45}$$

Otherwise, if there exists $n_2(j) \in \mathcal{S}^1_{n_2(j-1)}$ such that $\mathcal{Q}^1_{n_2(j)} \cup \mathcal{Q}^2_{n_2(j)} = \varnothing$, then ***(a)*** can be applied, choosing $n_1 = n_2(j)$, and the same conclusion, i.e. (3.45), holds.

(b.2) Consider now $C_2 < C_1$. Let $\mathcal{T}^{a,b}_i$ be the set such that:

$$\mathcal{T}^{a,b}_i = \{n \in \mathbb{N} \mid (V_{a,\overline{n}} \geqslant V_{b,\overline{n}}) \wedge (n \geqslant i)\}.$$

Suppose $\mathcal{T}^{2,1}_{n_2(i)} = \varnothing$. Then, the laws of variation of voltages on both capacitors are:

$\forall n \geqslant n_2(i)$,

$$\begin{aligned}V_{1,\overline{n}} &= V_{1,\overline{n_2(i)}} + \frac{1}{C_1} \sum_{k=n_2(i)}^{n} \Delta Q_k - \Delta V_n,\\ V_{2,\overline{n}} &= V_{2,\overline{n_2(i)}} + \frac{1}{C_2} \sum_{k=n_2(i)}^{n} \Delta Q_k,\end{aligned} \tag{3.46}$$

where the term ΔV_n represents decrease of the voltage across C_1 when it is in parallel with C_t. As $\forall n$, $\Delta V_n \geqslant 0$, it comes, with (Δ_n) defined in (3.34):

$$V_{1,\overline{n}} - V_{2,\overline{n}} \leqslant \Delta_n, \tag{3.47}$$

and as $C_2 < C_1$ implies that $(\Delta_n)_{n \geqslant n_2(i)}$ diverges to $-\infty$, $(V_{1,\overline{n}} - V_{2,\overline{n}})_{n \geqslant n_2(i)}$ diverges to $-\infty$, and hence a contradiction since it would therefore exist $n \geqslant n_2(i)$ such that $V_{1,\overline{n}} \leqslant V_{2,\overline{n}}$. Thus, $\mathcal{T}^{2,1}_{n_2(i)} \neq \varnothing$ and, applying ***(b.1)*** with initial cycle $n_2(j) = \min \mathcal{T}^{2,1}_{n_2(i)}$ and swapping the capacitors indexes, all the cases are covered. Applying the proof to every couple of fixed capacitors in the network, the implication part of the proof is concluded for the voltages at $C_\mathrm{t} = C_\mathrm{max}$. From (3.11) and the capacitance values order, it is clear that the conclusion also holds for $C_\mathrm{t} = C_\mathrm{min}$.

The proof of the converse, which is not useful in our application of the lemma, easily follows by *reductio ad absurdum*. □

Let us now define the condition $\Omega(k)$:

$$\Omega(k) \coloneqq \text{“}C_{\max} + \sum_{i=1}^{k} C_i - (k-1)C_k > 0''. \tag{3.48}$$

Its negation will be denoted $\overline{\Omega(k)}$.

Note that the circuit switches in its series configuration for any configuration of the voltages, if and only if $\eta > N$: under the topology constraints over the voltages (3.1), and from (3.8), the condition is necessary and sufficient (necessary because of the case $\forall i \in [\![1; N]\!], V_{\mathrm{t},\overline{n}} = V_{i,\overline{n}}$).

Consider a cycle $n > n^*$, where n^* is given by lemma 1, and a capacitor $\mathrm{C_k}$. Suppose that, at $C_\mathrm{t} = C_{\max}$ of this cycle, the capacitors $\mathrm{C}_1, \ldots, \mathrm{C_k}$ are in parallel with C_t. As it is ensured from lemma 1 that the order of the voltages do not change for every cycle $n \geqslant n^*$, (3.17) can be used to ensure that a capacitor in parallel with C_t at a cycle $n \geqslant n^*$ will also be in parallel with C_t at the following cycle. Indeed, it is ensured that each capacitor label corresponds to the same capacitor for any two different cycles following n^*, as this depends on the order of the circuit's capacitors voltages because of the local hypothesis in (3.14). Some algebra yields:

$$C_{\mathrm{t}(k,n+1)} < C_{\max} \Leftrightarrow \Omega(k). \tag{3.49}$$

Therefore, for any capacitor $\mathrm{C_k}$, if there exists a cycle $n_k \geqslant n^*$ such that $V_{\mathrm{t},\overline{n_k}} = V_{k,\overline{n_k}}$ and the condition in (3.49) holds, then for every $n \geqslant n_k$, $V_{\mathrm{t},\overline{n_k}} = V_{k,\overline{n_k}}$. Note that this implies that $\mathrm{C}_1, \ldots, \mathrm{C}_{\mathrm{k}-1}$ are also in parallel with C_t at $C_\mathrm{t} = C_{\max}$ of every cycle $n \geqslant n_k$, by the property of n^* given by lemma 1.

Now, consider $p \geqslant 1$ capacitors in parallel with C_t when $C_\mathrm{t} = C_{\max}$, at a cycle $n_p \geqslant n^*$, where n^* is given by lemma 1. The case $p = 0$ is impossible because of the circuit topology, $\max_{1 \geqslant i \geqslant N} V_i \geqslant V_\mathrm{t}/N$.

Also, suppose that $\Omega(p)$. Thus, because of (3.49), for all $n \geqslant n_p$, $V_{1,\overline{n}} = V_{\mathrm{t},\overline{n}} = \ldots = V_{p,\overline{n}}$. Consequently, we can define a cycle interval I_p in which the voltages evolution are given by the linear map:

$$\begin{aligned} &\exists n_{p+1} \in \mathbb{N} \cup \{+\infty\}, n_{p+1} > n_p, I_p \coloneqq [\![n_p; n_{p+1}[\![\\ &\forall n \in I_p \qquad \tilde{\mathbf{V}}_{\overline{\mathbf{n}}} = (\tilde{\mathbf{A}_\mathbf{p}})^n \, \tilde{\mathbf{V}}_{\overline{\mathbf{0_p}}}, \\ &\qquad\qquad \tilde{\mathbf{V}}_{\overline{\mathbf{0_p}}} = \tilde{\mathbf{V}}_{\overline{\mathbf{n_p - 1}}} \end{aligned} \tag{3.50}$$

where $\tilde{\mathbf{A}_\mathbf{p}}$ is given in (3.31), and $\tilde{\mathbf{V}}_{\mathbf{0_p}} \in \mathbb{R}^{N-p+1}$.

We now need some explicit information about the evolution of the voltage across the circuit's fixed capacitors, for each region I_p.

For all $N, p, 1 \leqslant p \leqslant N$, the matrix $\tilde{\mathbf{A}_\mathbf{p}}$ has 1 of algebraic multiplicity $N - p$ and $r_p \in \mathbb{R}$ of algebraic multiplicity 1 as eigenvalues. The following assumes that $r_p \neq 1$. The eigenvalue 1 has

a geometric multiplicity of $N-p$. Subsequently, $\tilde{\mathbf{A_p}}$ is diagonalizable over $\mathbb{R}$, and it comes that:

$$\mathbf{V_{\overline{n}}} = \mathbf{P_p} \begin{pmatrix} 1 & & & \\ & \ddots & & \\ & & 1 & \\ & & & {r_p}^n \end{pmatrix} {\mathbf{P_p}}^{-1} \mathbf{V_{\overline{0_p}}}, \tag{3.51}$$

$$r_p = \frac{C_{\min}((C_{\max} + \sum_{i=1}^{p} C_i) \sum_{i=1}^{p} {C_i}^{-1} + p(\eta - p + 1)) + \sum_{i=1}^{p} C_i}{(1 + C_{\min} \sum_{i=1}^{N} {C_i}^{-1})(C_{\max} + \sum_{i=1}^{p} C_i)}, \tag{3.52}$$

and where $(\mathbf{P_p}, {\mathbf{P_p}}^{-1}, \mathbf{V_{\overline{0_p}}}) \in (\mathbb{R}^{(N-p+1)^2})^2 \times \mathbb{R}^{(N-p+1)}$. Hence:

$$\begin{aligned} V_{\mathrm{t},\overline{n}} &= \alpha_{\mathrm{t},p}\ {r_p}^n + \beta_{\mathrm{t},p}, \\ V_{k,\overline{n}} &= \alpha_{k,p}\ {r_p}^n + \beta_{k,p}, \end{aligned} \tag{3.53}$$

with $(\alpha_{\mathrm{t},p}, \beta_{\mathrm{t},p}, \alpha_{k,p}, \beta_{k,p}) \in \mathbb{R}^4$, and $k \in [\![p+1; N]\!]$. A simple study of the $\tilde{\mathbf{A_p}}$ map allows the derivation of the coefficients' expressions; the vectors $(\mathbf{v_i}^1)_{1 \leqslant i \leqslant N-p}$, where $\mathbf{v_i}^1 = (v^1_{i_1}, .., v^1_{i_{N-p+1}})^{\mathrm{T}} \in \mathbb{R}^{N-p+1}$, are eigenvectors of $\tilde{\mathbf{A_p}}$ associated to the eigenvalue 1:

$$\begin{aligned} v_{i_1} &= \frac{1}{\eta - p}, \\ v_{i_j} &= \delta_{i(j-1)},\ 1 < j \leqslant N, \end{aligned} \tag{3.54}$$

where δ_{ij} is the Kronecker symbol. An eigenvector $\mathbf{v}^{r_p} = (v_1^{r_p}, \ldots, v_{N-p+1}^{r_p})^{\mathrm{T}} \in \mathbb{R}^{N-p+1}$ associated to the eigenvalue r_p is:

$$\begin{aligned} v_1^{r_p} &= \frac{(p-1)C_N}{C_{\max} + \sum_{i=1}^{p} C_i}, \\ v_i^{r_p} &= \frac{C_N}{p - 1 + i},\ \ 1 < i \leqslant N - p + 1. \end{aligned} \tag{3.55}$$

Finally, it comes:

$$\alpha_{\mathrm{t},p} = \frac{(p-1)(\sum_{i=p+1}^{N} V_{i,\overline{0_p}} - V_{\mathrm{t},\overline{0_p}}(\eta - p))}{(C_{\max} + \sum_{i=1}^{p} C_i) \sum_{i=p+1}^{N} {C_i}^{-1} - (p-1)(\eta - p)}, \tag{3.56}$$

$$\alpha_{k,p} = \frac{(C_{\max} + \sum_{i=1}^{p} C_i)(\sum_{i=p+1}^{N} V_{i,\overline{0_p}} - V_{\mathrm{t},\overline{0_p}}(\eta - p))}{C_k((C_{\max} + \sum_{i=1}^{p} C_i) \sum_{i=p+1}^{N} {C_i}^{-1} - (p-1)(\eta - p))}, \tag{3.57}$$

$$\beta_{\mathrm{t},p} = \frac{(C_{\max} + \sum_{i=1}^{p} C_i) \sum_{i=p+1}^{N} {C_i}^{-1} V_{\mathrm{t},\overline{0_p}} - \quad (p-1) \sum_{i=p+1}^{N} V_{i,\overline{0_p}}}{(C_{\max} + \sum_{i=1}^{p} C_i) \sum_{i=p+1}^{N} {C_i}^{-1} - \quad (p-1)(\eta - p)}, \tag{3.58}$$

$$\beta_{k,p} = V_{k,\overline{0_p}} + \frac{(C_{\max} + \sum_{i=1}^{p} C_i)(V_{\mathrm{t},\overline{0_p}}(\eta - p) - \quad \sum_{i=p+1}^{N} V_{i,\overline{0_p}})}{C_k((C_{\max} + \sum_{i=1}^{p} C_i) \sum_{i=p+1}^{N} {C_i}^{-1} - \quad (p-1)(\eta - p))}. \tag{3.59}$$

The steady-state behavior of the circuit can now readily be described, that is, the value of p for which $I_p = [\![n; +\infty[\![$, and the long-term voltage evolution laws in this interval. Given the p previously fixed, three cases are discriminated:

3.2.1.1 Case $r_p > 1$

The variations of $(V_{\mathrm{t},\overline{n}} - V_{p+1,\overline{n}})_{n \geqslant n_p}$, using the evolution laws of in (3.51), are such that

$$(V_{\mathrm{t},\overline{n+1}} - V_{p+1,\overline{n+1}}) - (V_{\mathrm{t},\overline{n}} - V_{p+1,\overline{n}}) < 0 \Leftrightarrow \Omega(p+1). \tag{3.60}$$

Also, by virtually fixing the law (3.50) for fixed p, and from (3.56) and (3.57):

$$\lim_{n \to +\infty} \frac{V_{\mathrm{t},\overline{n}}}{V_{p+1,\overline{n}}} = \frac{\alpha_{\mathrm{t},p}}{\alpha_{p+1,p}} = \frac{(p-1)\, C_{p+1}}{C_{\max} + \sum_{i=1}^{p} C_i}. \tag{3.61}$$

In the case $\Omega(p+1)$, the limit in (3.61) being then strictly less than 1, $n_{p+1} < +\infty$ and $V_{p+1,\overline{n_{p+1}}} = V_{\mathrm{t},\overline{n_{p+1}}}$. Because of (3.49), $\forall n, n \geqslant n_{p+1} \Rightarrow V_{\mathrm{t},\overline{n}} = V_{p+1,\overline{n}}$. In the case $\overline{\Omega(p+1)}$, $n_{p+1} = +\infty$ as the sequence $(V_{\mathrm{t},\overline{n}} - V_{p+1,\overline{n}})_{n \geqslant n_p}$is strictly increasing. For all $k \in [\![p+1; N]\!]$, the asymptotic value of the ratio $V_{\mathrm{t},\overline{n}}/V_{k,\overline{n}}$ is given by:

$\forall k \in [\![p+1; N]\!]$,

$$\lim_{n \to +\infty} \frac{V_{\mathrm{t},\overline{n}}}{V_{k,\overline{n}}} = \frac{\alpha_{\mathrm{t},p}}{\alpha_{k,p}} = \frac{(p-1)\, C_k}{C_{\max} + \sum_{i=1}^{p} C_i}. \tag{3.62}$$

3.2.1.2 Case $r_p < 1$

From (3.52), this case happens only if $\Omega(p+1)$. By virtually fixing the law (3.50):

$$\lim_{n \to +\infty} V_{\mathrm{t},\overline{n}} = \beta_{\mathrm{t},p}, \text{ and } \lim_{n \to +\infty} V_{p+1,\overline{n}} = \beta_{p+1,p}. \tag{3.63}$$

From (3.58) and (3.59), some algebra leads to:

$$\beta_{p+1,p} > \beta_{\mathrm{t},p} \Leftrightarrow \Omega(p+1). \tag{3.64}$$

Subsequently, $n_{p+1} < +\infty$ and $V_{p+1,\overline{n_{p+1}}} = V_{\mathrm{t},\overline{n_{p+1}}}$. In other words, a cycle interval I_p such that $r_p < 1$ cannot be the steady-state regime of the circuit.

3.2.1.3 Case $r_p = 1$

In this case, the reduction done in (3.51) no longer holds, as the linear map $\tilde{\mathbf{A_p}}$ is no longer diagonalizable. The voltages increase in this case is linear. This can be seen from the Jordan reduction of $\tilde{\mathbf{A_p}}$, that leads to $\tilde{\mathbf{A_p}}^n = \mathbf{P_p}'(\mathbf{I_{N-P+1}} + \mathbf{N})\mathbf{P_p}'^{-1}\tilde{\mathbf{V}_{\overline{\mathbf{0_p}}}}$, where $\mathbf{I_{N-P+1}} \in \mathbb{R}^{(N-P+1)^2}$ is the identity matrix, $\mathbf{P_p}' \in \mathbb{R}^{(N-P+1)^2}$ is invertible and $\mathbf{N}$ has all its coefficients equal to zero except for $\mathbf{N}_{2,1} = n$. This case is supposed to not happen in the rest of the analysis, as $r_p = 1$ will never be exactly reached in practice.

3.2.1.4 Summary

The steady-state mode of operation in the case $\eta > N$ can now be described. This is done by inductively applying the previous reasoning to $p+1$ parallel capacitors with $\Omega(p)$ fulfilled. We start from the smallest p such that there exists a cycle following n^* (the cycle given by lemma 1) where p capacitors are in parallel at the same cycle, and $\Omega(p+1)$ is fulfilled ($\Omega(2)$ is always fulfilled and $p \geqslant 1$). Defining Π as:

$$\Pi := \min(\{p \ \in]\!]1; N[\![\mid \overline{\Omega(p+1)}\} \cup \{N\}), \tag{3.65}$$

the biasing of C_t in the steady-state mode is implemented in the following fashion:

- C_t is in parallel with the capacitors $\mathrm{C}_1, \ldots, \mathrm{C}_\Pi$ at $C_\mathrm{t} = C_\mathrm{max}$ of every cycle, i.e., $V_{\mathrm{t},\overline{n}} = V_{1,\overline{n}} = \ldots = V_{\Pi,\overline{n}}$.
- The voltage across the capacitor $\mathrm{C_i}, i \in]\!]\Pi+1; N]\!]$ at $C_\mathrm{t} = C_\mathrm{max}$ is such that the ratio $V_{\mathrm{t},\overline{n}}/V_{i,\overline{n}}$ tends to $(\Pi-1)C_i/(C_\mathrm{max} + \sum_{j=1}^{\Pi} C_j)$.
- C_t is in series with all the fixed capacitors $C_1, \ldots, C_N$ at $C_\mathrm{t} = C_\mathrm{min}$. Hence, C_t is biased by the sum of voltages across the fixed capacitors at $C_\mathrm{t} = C_\mathrm{min}$.

The time evolution of the voltages across the fixed capacitors C_t exhibits an exponential increase in this mode. Indeed, the voltages follow an arithmetico geometric progression with common ratio $r_\Pi > 1$ in the steady-state mode.

The ratio γ between the voltages at $C_\mathrm{t} = C_\mathrm{max}$ of cycle n and $C_\mathrm{t} = C_\mathrm{min}$ of cycle $n+1$ in the steady-state mode of operation is given by:

$$\gamma = \frac{\Pi + \frac{C_\mathrm{max} + \sum_{i=1}^{\Pi} C_i}{\Pi - 1} \sum_{i=\Pi+1}^{N} {C_i}^{-1} + C_\mathrm{max} \sum_{i=1}^{N} {C_i}^{-1}}{1 + C_\mathrm{min} \sum_{i=1}^{N} {C_i}^{-1}} \tag{3.66}$$

Note that, in the case $\Pi \neq N$, this ratio is attained asymptotically as it is the result of the limit process (3.62).

The simplified version of this expression in the case that $C_{\max} \ll \left(\sum_{i=1}^{N} {C_i}^{-1}\right)^{-1}$ (see (3.79) below) corresponds to the γ ratio of unstable charge-pumps as presented in Sec 2.2.2.2. In fact, once we will have sketched the charge-voltage diagram in Sec. 3.3, the series-parallel charge-pump will be described in terms of the γ parameter for unstable charge-pumps, presented in the last chapter. We saw in Sec. 2.2.1 that this holds if $C_{\max}$ is sufficiently small compared to the smallest fixed equivalent capacitance that C_{t} is connected to. For our series-parallel unstable conditioning circuit topology, this means that $C_{\max} \ll (\sum_{i=1}^{N} 1/C_i)^{-1}$.

The converted energy during a cycle n of the steady-state operation defined above is given by:

$$\Delta W_n = \frac{1}{2}\left(C_{\max}({V_{\mathrm{t},\overline{n+1}}}^2 - {V_{\mathrm{t},\overline{n}}}^2) + \sum_{i=1}^{N} C_i({V_{i,\overline{n+1}}}^2 - {V_{i,\overline{n}}}^2)\right). \tag{3.67}$$

an expression that will be greatly simplified by resorting to the presentation of the circuit as implementing the ideal charge-pump behavior, i.e., a rectangular charge voltage diagram, at each cycle of the capacitance variation.

Remark 1. *The circuit's dynamics were derived for the steady-state operation mode, irrespective of the initial configuration (this is the purpose of lemma 1). In this process, the piecewise defined transient mode is described: for each region of the definition, the explicit evolution follows the laws given in (3.53), with proper corresponding values of coefficients $\alpha_{i,j}$ and $\beta_{i,j}$ (see (3.56)-(3.59)). However, because of this piecewise definition, there is no simple way to derive the* explicit *evolution laws starting from initial voltage values that do not necessarily fulfill the order in (3.14), other than applying the evolution law that apply in each region, and checking for the intersections of voltage in the time domain that lead to a change of the definition region.*

3.2.2 Case $\eta \leqslant N$

In this case, depending on the initial state of the circuit, the condition of series switching at every cycle of the autonomous evolution is not necessarily verified. As a consequence, the lemma 1 does not necessarily hold, and the long-term evolution of the circuit's state depends not only on the values of the capacitors, but also on their initial voltages.

Because of that, to simplify the analysis, only the dynamics starting from a particular order of the circuit's capacitors voltages at the initial cycle will be considered. This particular configuration is the same as in the conclusion of lemma 1. It is described as follows.

Consider an arbitrary cycle n_0, chosen as the initial cycle. The conditions (3.1), (3.2) are set by the circuit topology and hence still hold. The capacitors are labeled such that $C_1 \leqslant \ldots \leqslant C_N$. The circuit's capacitors voltages are supposed to verify:

$$V_{\mathrm{t},\overline{n_0}} = V_{1,\overline{n_0}} \geqslant \ldots \geqslant V_{N,\overline{n_0}}. \tag{3.68}$$

Now, if the initial voltages on the capacitors verify:

$$\eta V_{\mathrm{t},\overline{n_0}} > \sum_{i=1}^{N} V_{i,\overline{n_0}}, \tag{3.69}$$

then it can be verified by induction, using local laws of section 3.1, that the circuit switches in series for all cycles following n_0. Otherwise, the circuit shows the trivial dynamics of (3.24). The following supposes that (3.69) is fulfilled. By a variation of the lemma 1, and given the supposed order of the capacitors, the voltage ordering in (3.14) does not change for any $n \geqslant n_0$. Indeed, this is the case ***(b.1)*** in the proof of the foregoing lemma, using the positivity of the expression (3.34).,

We also define the logical proposition $\Psi(k)$ as :

$$\Psi(k) \coloneqq \text{“}\eta - (k-1) - C_k \sum_{i=k}^{N} {C_i}^{-1} > 0''. \tag{3.70}$$

Its negation will be denoted $\overline{\Psi(k)}$.

Consider $p \geqslant 1$ capacitors in parallel at cycle $n_p > n_0$, and $\Omega(p)$ is fulfilled. As (3.69) guarantees series switching at all cycles, and similarly to the case $\eta > N$ (see (3.49)):

$$\begin{aligned} &\exists n_{p+1} \in \mathbb{N} \cup \{+\infty\}, n_{p+1} > n_p, I_p \coloneqq [\![n_p; n_{p+1} [\![\\ &\forall n \in I_p \qquad \tilde{\mathbf{V}_{\overline{\mathbf{n}}}} = (\tilde{\mathbf{A}_{\mathbf{p}}})^n \, \tilde{\mathbf{V}_{\overline{\mathbf{0_p}}}}, \\ &\qquad\qquad \tilde{\mathbf{V}_{\overline{\mathbf{0_p}}}} = \tilde{\mathbf{V}_{\overline{\mathbf{n_p - 1}}}} \end{aligned} \tag{3.71}$$

i.e., the evolution laws derived in section 3.2.1 given in (3.53) can be used in this interval.

3.2.2.1 Case $r_p > 1$

In this case, the conclusion is the same as in the $r_p > 1$ case of the analysis for $\eta > N$, in section 3.2.1. We make the additional remark that if $\Omega(p+1)$ holds in addition to $r_p > 1$, then working out through some algebra, one deduces that $r_{p+1} > 1$.

3.2.2.2 Case $r_p < 1$

By virtually fixing the law (3.71):

$$\lim_{n \to +\infty} V_{\mathrm{t},\overline{n}} = \beta_{\mathrm{t},p}, \text{ and } \lim_{n \to +\infty} V_{p+1,\overline{n}} = \beta_{p+1,p}. \tag{3.72}$$

Also, some algebra yields:

$$\forall i, p \in [\![1; N]\!], \qquad \beta_{\mathrm{t},p} < \beta_{p+1,p} \Leftrightarrow \Psi(p+1). \tag{3.73}$$

Thus, if $\overline{\Psi(p+1)}$, then $n_{p+1} = +\infty$ and the voltages saturate following (3.72). Otherwise, $n_{p+1} < +\infty$, and $\Omega(p+1)$ holds, as it is implied by $r_p < 1$ and $\Psi(p+1)$ as one can easily show by elementary calculations.

3.2.2.3 Summary

As for the case $\eta > N$ in section 3.2.1, inductively, the steady-state regime of the circuit can be characterized. As $\forall k \geqslant 1, \Psi(k+1) \Rightarrow \Psi(k)$, then if there exists $p \in]\!]1; \lfloor \eta^- \rfloor]\!]$ such that $r_p >$

1, and $\Psi(p)$ is verified ($\lfloor \eta^- \rfloor = \eta - 1$ if $\eta \in \mathbb{N}, \lfloor \eta \rfloor$ otherwise), then the steady-state mode is an exponential mode. In fact, some algebra yields that these conditions are fulfilled and only if $\eta > \gamma$, where γ is defined as in (3.66) and Π as

$$\Pi := \min(\{t \ \in [\![p; \lfloor \eta^- \rfloor [\![\mid \overline{\Omega(t+1)}\}). \tag{3.74}$$

Hence, the condition for an exponential steady-state mode to be reached is, as for the case $\eta > N$, that $\eta > \gamma$, to which we shall add the initial state hypothesis (3.69) and (3.68). This mode is described as for the case $\eta > N$ (see the summary in section 3.2.1.4). In particular, if operating in the exponential mode, the γ ratio between the transducer's extreme voltages across one cycle of operation is given by (3.66), with the parameter Π computed from (3.74).

Otherwise, if $\eta < \gamma$, then the steady-state mode is a saturation regime.

Remark 2. *This analysis refines the case $\eta > N$, as $\eta > N \Rightarrow \forall p, \Psi(p)$.*

Example 1 (Bennet's doubler)**.** *Let us investigate the particular case of the Bennet's doubler ($N = 2$), when $\eta \leqslant 2$, with $V_{\mathrm{t},\overline{n_0}} = V_{1,\overline{n_0}} > V_{2,\overline{n_0}}$, and supposing that (3.69) is fulfilled. The evolution of $V_{1,\overline{n}}$ and $V_{2,\overline{n}}$ is given by (3.53). We have that $\forall n \geqslant n_0, V_{1,\overline{n}} = V_{1,\overline{n_0}}$. Besides, as $r_1 < 1$, we have that $\lim_{n\to+\infty} V_{2,\overline{n}} = \beta_{2,1}$. Defining σ as:*

$$\sigma := \frac{V_{\mathrm{t},\overline{n_0}}(\eta - 1)}{V_{\mathrm{t},\overline{n_0}}(\eta - 1) - V_{2,\overline{n_0}}}, \tag{3.75}$$

if $\sigma < 1 + r_1$, then an optimal cycle of index $n_{opt} > n_0$ exists:

$$n_{opt_0} = n_0 + \left\lfloor \frac{\log(\sigma) - \log(1 + r_1)}{\log(r_1)} \right\rfloor. \tag{3.76}$$

Otherwise, $n_{opt_0} = n_0$. These are simply found by solving for n the equation $\partial \Delta W_n / \partial n = 0$ with ΔW_n computed as in (3.67). Note that the transient process leading to the exponential steady-state mode of the Bennet's doubler circuit, when $\eta > 2$, can be characterized in a similar way to this example. For instance, to assess the duration of the transient process before the exponential steady-state mode, one has to solve $V_{2,\overline{n}} \geqslant V_{1,\overline{n_0}}$ for n, which will necessarily have a solution if $\eta > 2$.

3.3 Derivation of the rectangular charge-voltage diagram

In the present subsection, the exact charge-voltage diagram implemented by the circuits using the topology in Fig. 3.1 is sketched first. Then, the approximations that allow the diagram to be assimilated to a rectangular charge-voltage diagram are highlighted. We hence make the link with the formalism developed in Chap. 2. This allows to characterize the series-parallel charge-pumps in terms of their γ ratio between characteristic voltages V_{R} and V_{L} of a given cycle of C_{t}, following the presentations of the unstable charge-pump conditioning circuits of Chap. 2.

We will sketch the charge-voltage diagram for an arbitrary cycle of an exponential steady-state mode, defined in Sec. 3.2.1.4. We remind the reader that, as a result of the analysis of Sec. 3.2, such an exponential steady-state mode is always reached under the condition $\eta > \gamma$ (where γ is defined in (3.66)), with the initial state fulfilling (3.68) and (3.69) in the case $\eta < N$. Also, we will suppose that for any fixed capacitor C_{i}, $V_{\mathrm{t},\overline{n}}/V_{i,\overline{n}}$ is considered equal to its limit

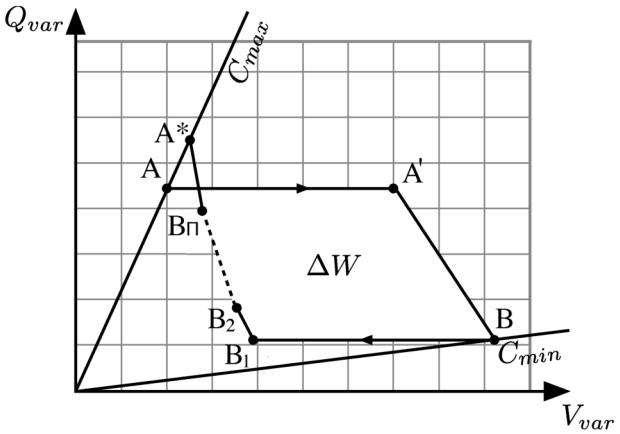

Figure 3.2: The charge-voltage diagram, for the generic circuit topology depicted in Fig. 3.1, as derived in Sec. 3.3.1.

$(\Pi - 1)C_i/(C_{\max} + \sum_{i=1}^{\Pi} C_i))$, for $i \in]\!]\Pi; N]\!]$. The constant Π is defined as in (3.65).

3.3.1 Exact derivation

Starting from the point A (see Fig. 3.2), with C_t decreasing from $C_\mathrm{t} = C_{\max}$, no current is flowing, and V_t increases as stated in (3.3), hence the horizontal segment [AA'] in the charge-voltage plane.

When, at each cycle, $V_\mathrm{t}(t)$ reaches the sum of the voltages across all the fixed capacitors, a current flows and the variation law of V_t changes accordingly to (3.9). The equation of the corresponding segment [A'B] in the charge-voltage plane is given by:

$$Q_\mathrm{t}(t) = -V_\mathrm{t}(t)\left(\sum_{i=1}^{N} {C_i}^{-1}\right)^{-1} + \left(\sum_{i=1}^{N} {C_i}^{-1}\right)^{-1}\left(\Pi + \frac{C_{\max} + \sum_{i=1}^{k} C_i}{\Pi - 1}\sum_{i=\Pi+1}^{N} {C_i}^{-1}\right) V_{\mathrm{t},\overline{n}}. \quad (3.77)$$

Now, starting from the point B, with C_t increasing from $C_{\min}$, no current is flowing, and V_t decreases as stated in (3.15), hence the horizontal segment [$\mathrm{BB_1}$] in the charge-voltage plane.

When, at each cycle, $V_\mathrm{t}(t)$ reaches the voltage of the smallest capacitor, a current flows and the law of variation of V_t changes, as given in (3.18). This repeatedly occurs with the other fixed capacitors, until $C_\mathrm{t} = C_{\max}$.

The equations of the corresponding segments [$\mathrm{B_jB_{j+1}}$] in the charge-voltage plane are given by, with $j \in [\![1; k[\![$:

$$Q_{\mathrm{t}_j}(t) = -V_\mathrm{t}(t)\sum_{i=1}^{j} C_i + V_{\mathrm{t},\overline{n}}\left[C_{\max} + \sum_{i=1}^{j} C_i + \left(j-1\right)\times \left(C_{\max} - C_{\min}\left(\Pi + \frac{C_{\max} + \sum_{i=1}^{k} C_i}{\Pi - 1}\sum_{i=\Pi+1}^{N} {C_i}^{-1}\right)\right)\right] \quad (3.78)$$

When $C_\mathrm{t} = C_{\max}$ at the cycle $n+1$, the voltage and charge coordinates of the point have increased compared to $C_\mathrm{t} = C_{\max}$ at the cycle n ($V_{\mathrm{t},\overline{n+1}} = r_\Pi V_{\mathrm{t},\overline{n}}$, $r_\Pi > 1$).

3.3.2 Approximation to a rectangular charge-voltage diagram: connection to the unified presentation of charge-pump conditioning circuits

The equation (3.77) shows that if $C_{\min} < C_{\max} \ll \min_{1 \leqslant i \leqslant N} C_i$, then the segment [A'B] can be considered as vertical going through A'. Also, under the same condition, equation (3.78) allows the segment [B_1A*] to be considered vertical, and going through A* $\approx$ A as $r_\Pi \approx 1^+$.

In light of these considerations, when $C_{\max}$ is sufficiently small compared to the values of the fixed capacitors, the cycle can be approximated by an ideal rectangular charge-voltage diagram, and the series-parallel charge-pump can be described by the ideal charge-pump of Sec. 2.1.2. In this view, γ is the ratio between characteristic voltages V_{L} and V_{R} at each cycle of variation of C_{t}, following the formalism presented in the last chapter. For the series-parallel topology, the characteristic voltage V_{L} is equal to the voltage of the fixed capacitance(s) that has or have the highest voltage. The characteristic cycle voltage V_{R} is measured between the two nodes of the dipole constituted by all of the circuit's fixed capacitances put in series: it is equal to the sum of voltages of all fixed capacitances in the circuit. This also holds for the Bennet's doubler as it is the case $N = 2$ of this topology. Remember that, even if our detailed analysis show that these voltages are not constant during the variation cycle of C_{t}, their evolution can be made arbitrarily small for large enough values of the fixed capacitor, so that V_{L} and V_{R} can be considered constant. This is a general result that is applicable to all charge-pump conditioning circuits, as we have exposed in Sec. 2.2 of the previous chapter.

By simplifying (3.66) with $C_{\max}$, $C_{\min}$ small compared to the C_i's, it comes that

$$\gamma = \Pi + \frac{1}{\Pi - 1} \sum_{i=1}^{\Pi} C_i \sum_{i=\Pi+1}^{N} {C_i}^{-1}. \tag{3.79}$$

The converted energy for a cycle n in the steady-state exponential mode can then be approximated by the area of the obtained rectangle:

$$\Delta W_n = C_{\min} {V_{\mathrm{L}_n}}^2 (\gamma - 1)(\eta - \gamma), \tag{3.80}$$

where V_{L_n} is the n-th cycle caracteristic voltage V_{L}. Note that, as we emphasized during the analysis above, this ratio is attained asymptotically if $\gamma < N$. One can assess the speed of convergence from (3.62). In particular, it can be shown that the values of the fixed capacitors can be chosen to achieve arbitrarily fast convergence up to a given error, without changing the value of the implemented ratio γ.

In the remaining of this manuscript, we shall adopt the point of view of Chap. 2, and hence not make a distinction between the exact value of γ and its approximated value (for all other unstable charge-pump conditioning circuits). In particular, the energy converted by the series parallel charge-pump at each cycle of the capacitance variation is supposed to be given by (3.80) when operating in unstable operation mode.

3.4 Discussion on the built-in voltage and on components non-idealities

The analysis carried out in sections 3.1 and 3.2 does not include parasitic effects of the electrical components, and supposed that the built-in voltage $E = 0$. In particular, the diodes are considered ideal, i.e., zero-current for reverse bias and ideal zero-voltage source for forward bias, with zero threshold voltage. These non-idealities have an impact on the circuit dynamics. However, these effects are of higher order, and do not qualitatively change the results of the analysis carried out in the rest of the paper. In this subsection, the effect of these model changes are qualitatively discussed. As a side note, in e-VEHs studied accounting for the electromechanical coupling, the effect of the latter on the system's dynamics will probably be prominent over the modifications of the evolution laws consecutive to the circuit's non-idealities. The effect of the electromechanical coupling will be discussed in detail in Chap. 4.

3.4.1 Non-null diodes forward voltage drop

Considering an ideal diode model with a non-null forward voltage drop has an effect on the explicit voltages evolution over time (this can be seen in the simulations results below in Sec. 3.5, by comparing Fig. 3.5a and Fig. 3.7a). Interestingly, it is worth noting that introducing this non-ideality does not change the obtained conditions to be satisfied, nor the asymptotically reached value of the γ biasing ratio. A proof of that fact and the modified evolution laws can be found analytically by changing the local evolution laws of section 3.1, so to take in account a constant threshold V_{T}. The rest of the analysis is very similar to what is done in sections 3.1 and 3.2, except that the the piecewise linear maps turn into piecewise affine maps (or the charge-pump state can be augmented by a dummy V_{T} variable, as we did in Sec. 2.3.1.1 to account for E). The coefficient in r_p in (3.52) is not altered, but the expressions for coefficients $\alpha_{i,j}$ and $\beta_{i,j}$ in (3.56)-(3.59) are affected. However, their expressions become heavier and uncomfortable to work with to derive the steady-state characteristics as done in section 3.2. The fact that r_p is not modified implies that for large time scales in the steady-state mode, the ratio between the explicit evolution laws with and without taking in account a constant threshold voltage is constant. Note that in practice, taking in account this non-ideality suffices to give very accurate results on the explicit long term dynamics, provided that V_{T} is chosen accordingly to the average currents that flow through the diodes.

3.4.2 Diodes' reverse parasitic capacitance

The diodes' reverse capacitances are responsible for a small change of the conditions for the different operation modes. Again, it is possible to quantify this effect by rewriting the laws in section 3.1 so to take in account the charge exchange between the transducer and the diodes' capacitances, when the transducer's capacitance is varying. However, this results in mathematically cumbersome evolution laws. Still, this effect can be estimated by a modification of the charge-voltage diagram derived in section 3.3. To do so, it suffices to turn the horizontal segments into segments with a negative slope, whose value is dictated by the value of the equivalent capacitance seen by the transducer, when the diodes are not conducting (see simulation result in

Fig. 3.7b). In practical cases, the transducer's capacitance is such that this effect is negligible. For example, JPAD5 didoes have a 2pF reverse capacitance value at zero voltage biasing. The induced negative slope in the charge-voltage diagram is negligible provided that the transducer's capacitance values are typically an order of magnitude above.

3.4.3 Reverse currents, capacitors leakages

Other non-idealities include the capacitors leakages and the diodes reverse currents. If the diodes' breakdown voltage is not reached, these leakages are usually so low that their effect on the circuit's dynamics is negligible. However, they can become important at high time scales during which the system is not submitted to input excitations.

3.4.4 Non-null built-in voltage

The foregoing analysis was made supposing that the value of the built-in voltage source E, presented in the two last chapters, is equal to zero. In fact, it is easily understandable that adding this source changes the quantitative dynamics in terms of the circuit state as an explicit function of the cycle index. An analysis taking it into account would change the linear mappings (3.25) to affine mappings, much like the effect of a constant threshold voltage V_{T} discussed above in Sec. 3.4.1. Yet, interestingly, the analysis done in the particular cases of $N = 3$ and that we do not report here, shows that the ratio γ between extreme biasing voltages of the transducer from which E is subtracted. Equivalently, the conditions derived in Sec. 3.2 for the existence of an unstable exponential steady-state are not altered by $E > 0$. This is illustrated in the charge-voltage diagrams in Fig. 2.7b in the previous chapter: the ratio (γ) is fixed in steady-state operation between V_{R} and V_{L}, and E is a mere offset on the transducer biasing. This is supported by a simulation below in Sec. 3.5.5.

Hence, at each cycle of the capacitance variation, and as for the other unstable charge-pumps encountered in this work, the converted energy per cycle reads

$$\Delta W = C_{\min} V_{\mathrm{L}} (V_{\mathrm{L}}(\eta - \gamma) - E(\eta - 1))(\gamma - 1) \tag{3.81}$$

when operating in the exponential mode, which coincides with (3.80) when $E = 0$.

3.5 Simulations

In the following, we show examples of simulations to both validate the analysis, and to illustrate the effects of some of the effects qualitatively discussed in Sec. 3.4. The simulated topologies in the following simulations are the case $N = 3$ (depicted in Fig. 3.3.a), $N = 2$ (Bennet's doubler, depicted in Fig. 3.3.b), and the addition of an energy-extracting interface to the series-parallel topology with $N = 3$. The simulations are done with Linear Technology's LTSpice IV.In all the following simulations, the transducer's variable capacitance C_{t} is varying sinusoidally between its extremum values $C_{\max}$ and $C_{\min}$ with a frequency of 100Hz.

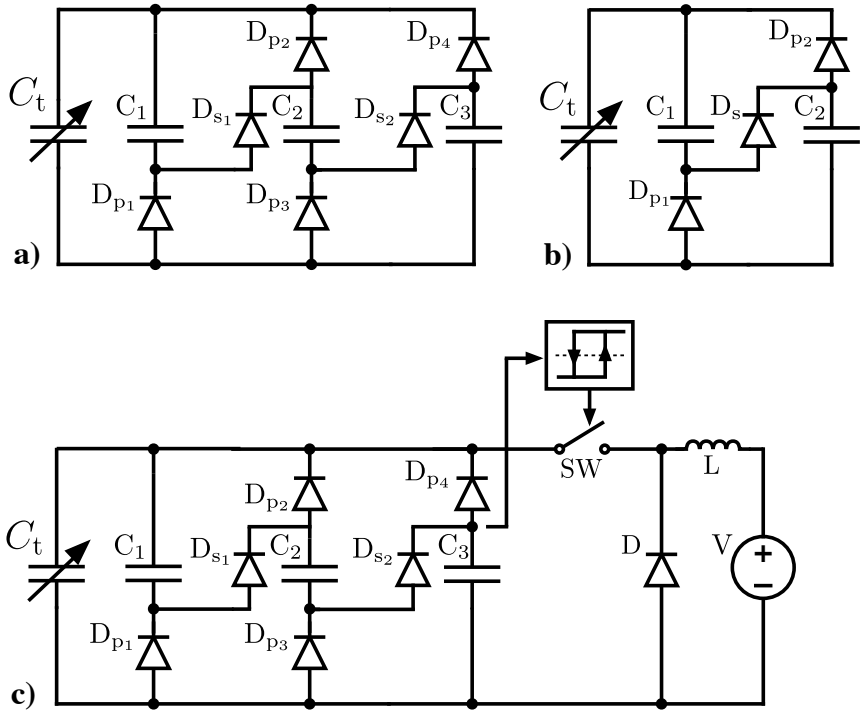

Figure 3.3: The three circuits simulated in this section.

3.5.1 $N = 3$, $\eta > N$, $\Omega(3)$ is fulfilled, exponential steady-state

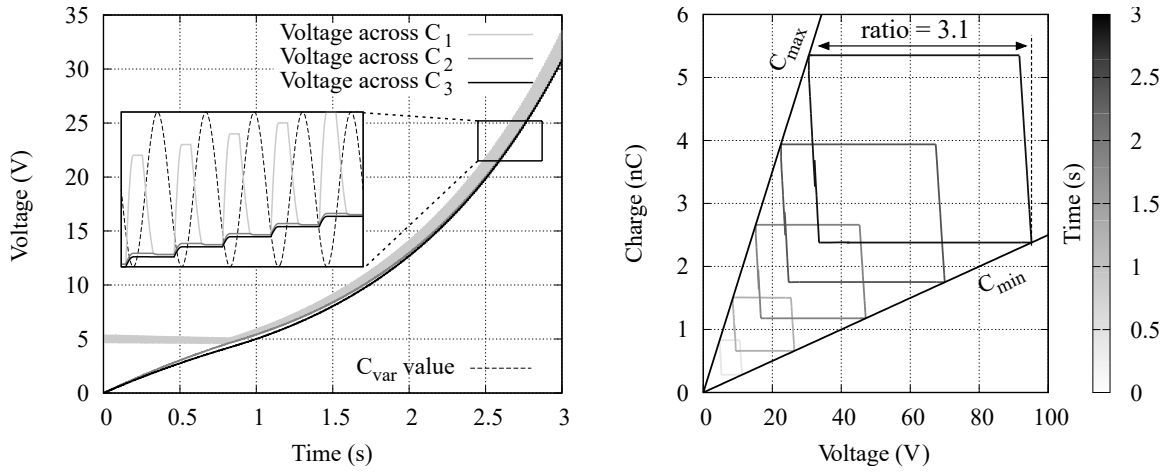

(a) Time evolution

(b) Charge-voltage diagrams at different cycles.

Figure 3.4: Results of the simulation of the series-parallel charge-pump with $N = 3$.

For the first simulation, the parameters were chosen such that $\Omega(3)$ is fulfilled, and thus, the circuit reaches a steady-state mode during which all the capacitors of the network are in parallel at $C_\mathrm{t} = C_\mathrm{max}$.

The exact values of the parameters are: $C_{min} = 25\mathrm{pF}$, $C_{max} = 175\mathrm{pF}$, $C_1 = 1\mathrm{nF}$, $C_2 = 10\mathrm{nF}$ and $C_3 = 11\mathrm{nF}$. The initial voltages are $V_{\mathrm{t},\bar{0}} = V_{1,\bar{0}} = 5\mathrm{V}$, $V_{2,\bar{0}} = V_{3,\bar{0}} = 0\mathrm{V}$.

The time-domain simulation results are depicted in Fig. 3.4a, showing the exponential unstable steady-state mode. The charge-voltage diagram for one cycle, at different instants, is depicted in Fig. 3.4b. The γ-ratio is measured as 3.1 in the simulations, which agrees with the

application of (3.66). In the approximation of the ideal charge-pump circuit (or, equivalently, rectangular charge-voltage diagram), (3.79) yields a γ ratio of 3 between characteristic cycle voltages V_{R} and V_{L} at all cycles of the steady state operation mode.

3.5.2 $N = 3$, $\eta > N$, $\Omega(3)$ is not fulfilled, exponential steady-state

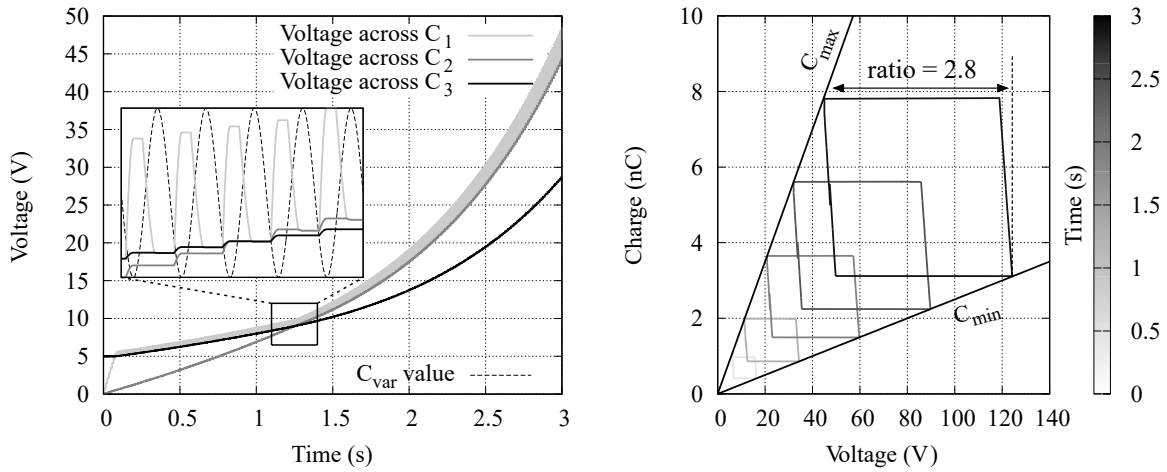

(a) Times-evolution

(b) Charge-voltage diagrams at different cycles.

Figure 3.5: Results of the simulation of the series-parallel charge-pump with $N = 3$.

For the second simulation, the parameters were chosen such that $\Omega(3)$ is not fulfilled. The steady-state mode of operation begins at the time which is zoomed in the figure. At every cycle in this mode of operation, C_1 and C_2 are in parallel at $C_{\mathrm{t}} = C_{\max}$. The voltage across C_3 is lower, and C_3 is never in parallel with C_1 and C_2 in the steady-state.

The exact values of the parameters are: $C_{min} = 25\mathrm{pF}$, $C_{max} = 175\mathrm{pF}$, $C_1 = 1\mathrm{nF}$, $C_2 = 10\mathrm{nF}$ and $C_3 = 20\mathrm{nF}$. The initial voltages are $V_{\mathrm{t},\overline{0}} = V_{3,\overline{0}} = 5\mathrm{V}$, $V_{1,\overline{0}} = V_{2,\overline{0}} = 0\mathrm{V}$.

The time-domain simulation results are depicted in Fig. 3.5a, showing the exponential unstable steady-state mode. The charge-voltage diagram for one cycle, at different instants, is depicted in Fig. 3.5b. The γ-ratio is measured as 2.8 in the simulations, which again is close to the application of (3.66) that yields 2.7. The slight difference is due to the fact that the ratio of 2.7 computed from (3.66) is reached asymptotically. Using (3.79), the approximation to a rectangular charge-voltage diagram of (3.79) yields a ratio of 2.6 between the characteristic voltages V_{R} and V_{L}.

3.5.3 $N = 3$, $\eta < N$, exponential steady-state

The simulation results in Fig. 3.6a and Fig. 3.6b show examples of the circuit working with $\eta \leqslant N$, exhibiting an exponential steady-state regime, with $\eta \leqslant N = 3$. The exact values of the parameters are: $C_{min} = 120\mathrm{pF}$, $C_{max} = 280\mathrm{pF}$, $C_1 = 1\mathrm{nF}$, $C_2 = 5\mathrm{nF}$ and $C_3 = 25\mathrm{nF}$. The initial voltages are $V_{\mathrm{t},\overline{0}} = V_{1,\overline{0}} = 5\mathrm{V}$, $V_{2,\overline{0}} = V_{3,\overline{0}} = 0\mathrm{V}$.

The measured γ-ratio is of 2.3, which is in agreement with (3.66). The approximated γ ratio between characteristic cycle voltage V_{R} and V_{L} yields a value of 2.2 (see (3.79)).

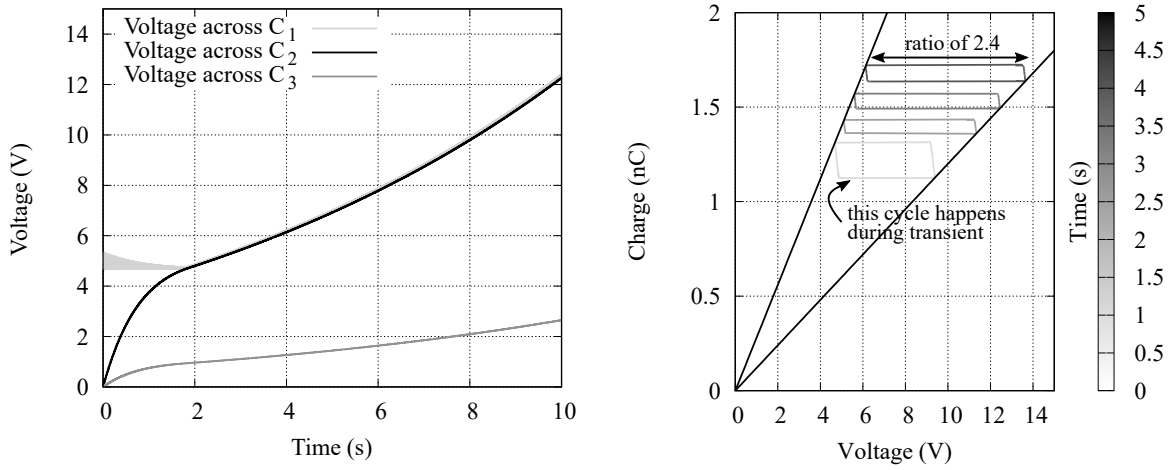

(a) Time evolution

(b) Charge-voltage diagrams at different cycles.

Figure 3.6: Results of the simulation of the series-parallel charge-pump with $N = 3$ and $\gamma < \eta < N$. An exponential steady-state mode is reached.

3.5.4 $N = 3$, $\eta > N$, $\Omega(3)$ is fulfilled, exponential steady-state, level 1 diode model

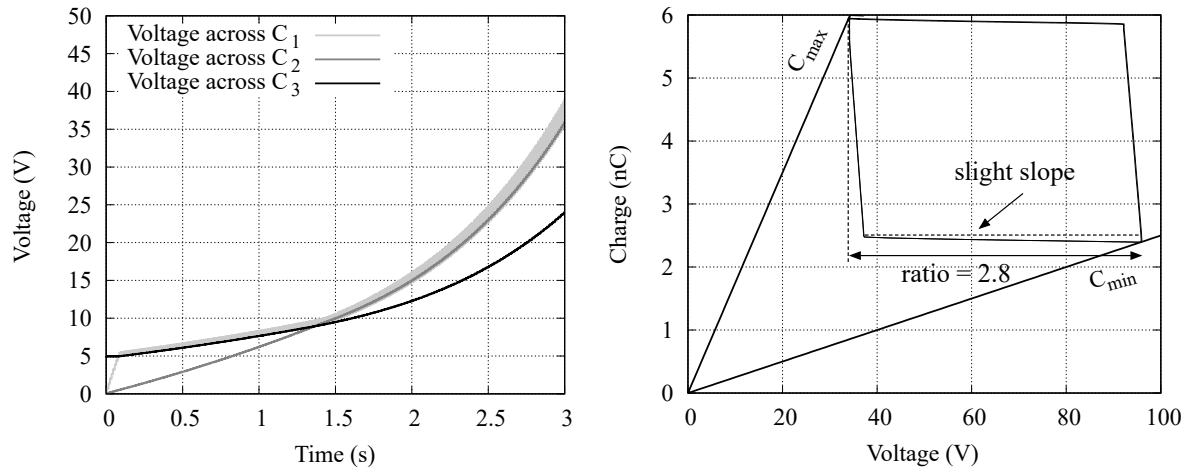

(a) Time evolution

(b) Charge-voltage diagram

Figure 3.7: Results of the simulation of the series-parallel charge-pump with the same parameters as in Sec. 3.5.2, but using a more realistic model for the diodes.

We now present the results of the same simulation as in Sec. 3.5.2, but using a more accurate model of the diodes. The used model is an exponential level 1 model, with default SPICE parameter values (saturation current of 1pA), and a parasitic capacitance of 2pF (corresponding for example to the JPAD5 diode capacitance at zero voltage). The results are depicted in Fig. 3.7a for the time evoltion of the voltages, and in Fig. 3.7b for the charge-voltage diagram corresponding to one cycle of C_t. Note that although the long term voltage evolution is quantitatively different compared to Fig. 3.5a, locally, the charge-voltage diagram is almost unaltered: the extreme voltage biasing ratio γ of the capacitor is not changed, as was discussed in Sec. 3.4.1. The effect of the diodes' parasitic capacitances is visible by the slight modification of the slopes of the segments of the charge-voltage diagram. The deviation from the time-domain results in Fig. 3.5a can be predicted with great accuracy, by using the ideal diode model with constant

voltage threshold, discussed in 3.4.1: the other non-idealities (parasitic capacitance and use of an exponential diode model instead of an ideal diode model) are of much more difficult to take into account in the analysis done above, but are of higher order and do not change the results qualitatively and quantitatively.

3.5.5 $N = 3$, $\eta > N$, $E > 0$, exponential steady-state

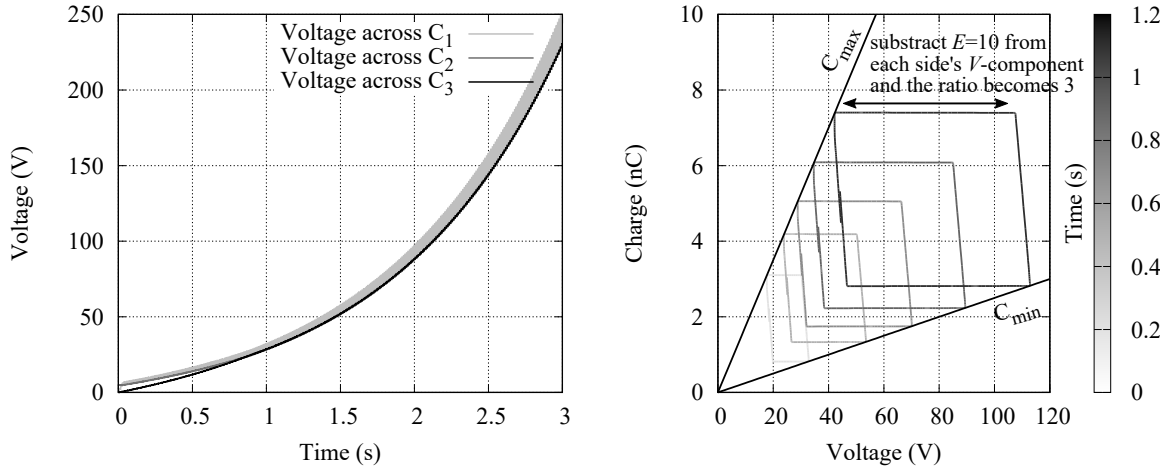

(a) Time evolution **(b)** Charge-voltage diagram

Figure 3.8: Results of the simulation of the series-parallel charge-pump with $N = 3$ and a non-null built-in voltage $E = 10\,\mathrm{V}$.

The simulations are now carried out with the same parameter values as the simulation in Sec. 3.5.1, but using a built-in voltage source $E = 10\mathrm{V}$ in series with C_t, as was considered in the previous chapters. The time-domain results are depicted in Fig. 3.8a, and the charge-voltage diagram in Fig. 3.8b. The time-domain results differ from Fig. 3.4a, as energy is converted at a higher rate. However, as we pointed out in Sec. 3.4.4, the ratio between the extreme voltage biasing the capacitance from which we subtract E is unaltered compared to Fig. 3.4b ($\gamma = 3.1$). In other words, this means that in the formalism of charge-pump conditioning circuits of previous chapter, the γ ratio that is implemented by an unstable charge-pump circuit between characteristic cycle voltages V_R and V_L is not affected by $E > 0$, but only depends on the topology of the diodes-capacitances network. The conversion rate is higher with $E > 0$ as one easily infers from the charge-voltage diagram that for equal voltages across the circuit's fixed capacitors (i.e., equal V_L and V_R) for a given cycle, the area of the corresponding rectangle increases with the offset E.

3.5.6 $N = 2$, $\eta < N$, saturating steady-state

We also simulated the case $N = 2$ (Bennet's doubler), with $\eta < 2$. The time domain results are depicted if Fig. 3.9a. The charge-voltage diagrams for different cycles selected throughout the circuit's autonomous evolution are depicted in Fig. 3.9b. A maximal power point (inflexion point on the energy over time graph) is highlighted. This point exists accordingly to the discussion in 3.2.2. The initial conditions are chosen such that the cycle n for this maximal power point is strictly positive (0 being the cycle at $t = 0$). The exact value of the parameters are: $C_{min} = 100\mathrm{pF}$, $C_{max} = 180\mathrm{pF}$, $C_1 = 1\mathrm{nF}$ and $C_2 = 10\mathrm{nF}$. The initial voltages are

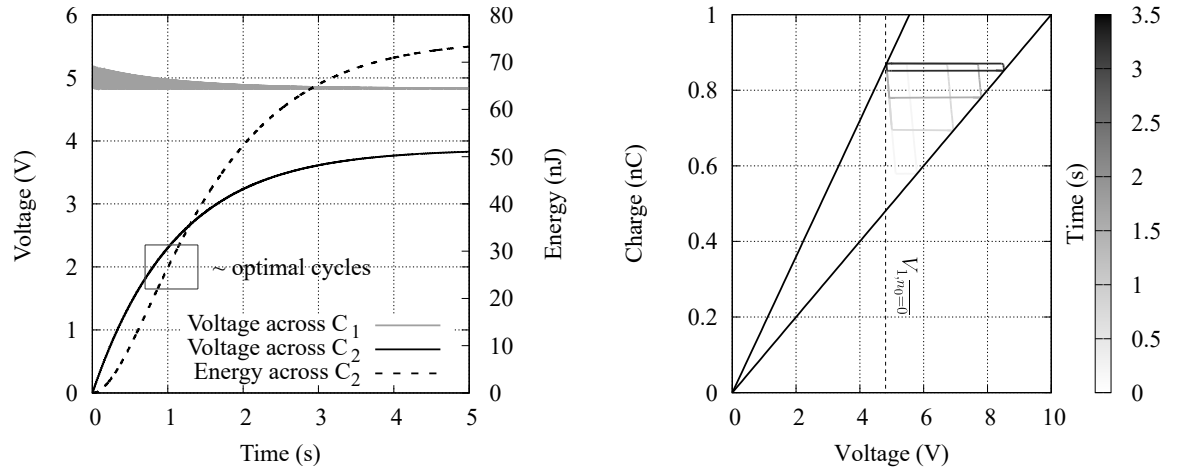

(a) Time evolution

(b) Charge-voltage diagrams at different cycles.

Figure 3.9: Results of the simulation of the series-parallel charge-pump in the case $N = 2$ (Bennet's doubler), with $\eta < 2$.

$V_{\mathrm{t},\bar{0}} = V_{1,\bar{0}} = 5\mathrm{V}$, $V_{2,\bar{0}} = 0\mathrm{V}$. The voltage saturates at around 4 V, which is the value predicted by (3.59). Also, (3.76) indicates that the optimal cycle is attained at $n = 76$.

3.5.7 Energy extracting interface

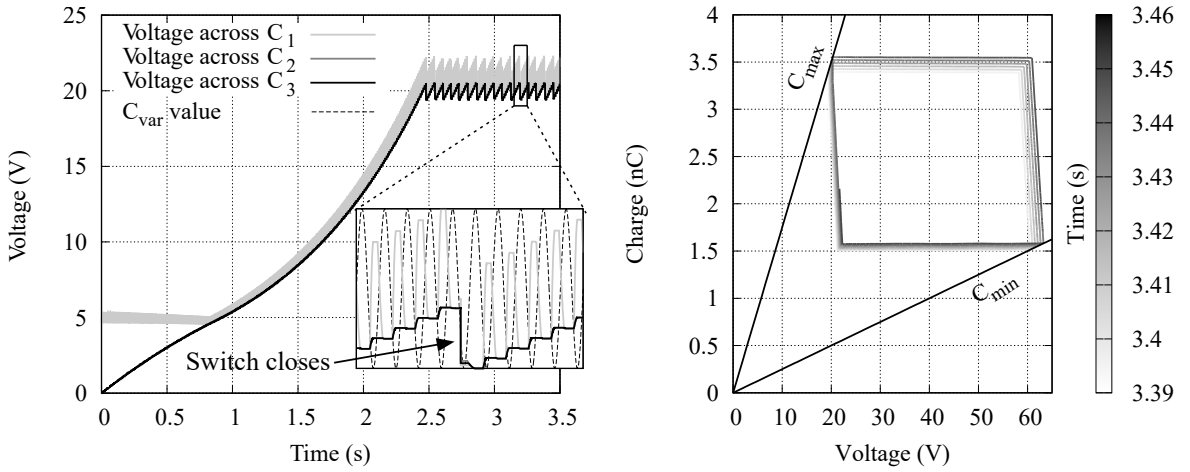

(a) Time evolution

(b) Charge-voltage diagram

Figure 3.10: Results of the simulation of the series-parallel charge-pump connected to an energy extracting interface.

The last simulation features the series-parallel topology with $N = 3$, joined to an energy-extracting interface whose role was introduced in the Sec. 2.4.2 of the previous chapter. We take this opportunity to illustrate the operation of an example of such energy-extracting interface. To discard any consideration about the regulation of voltage at the load (task (ii) in Sec. 2.4.2), the output capacitor and load are modeled as a voltage source of 5V. This can also model a practical case where the output capacitor is replaced by a battery.

In our example, the switch control works in the following way: the voltage across C_3 is sensed. When it exceeds a given value $V_{\mathrm{comp}} + V_{\mathrm{h}}$, the switch is closed, thus discharging the circuit's

fixed capacitors in the inductor and the output voltage source. The switch remains closed until the voltage across C_3 falls below a given value $V_{\text{comp}} - V_{\text{h}}$ (comparison with hysteresis). In this simulation example, $V_{\text{comp}} = 20\text{V}$ with an hysteresis of $V_{\text{h}} = 0.5\text{V}$. Note that we have supposed that this voltage is lower than the voltage V_{comp}. The simulation is carried out with $C_{min} = 25\text{pF}$, $C_{max} = 175\text{pF}$, $C_1 = 1\text{nF}$, $C_2 = 10\text{nF}$, $C_3 = 10\text{nF}$, and $L = 100\mu\text{H}$.

This example with hysteresis comparison constrains the voltage evolution in a way that a desired cycle of conversion is sustained, whilst the converted energy is supplied to the load. In this simulated example, we know from the circuit's topology that $V_{\text{R}} = 3V_{\text{L}}$ in the steady-state regime. Also, at each cycle of this mode, each of the circuit's fixed capacitors is biased by V_{L}. Hence, the cycle $(V_{\text{L}} = 20\,\text{V} \pm 0.5\,\text{V}, V_{\text{R}} = 60\,\text{V} \pm 1.5\,\text{V})$ is sustained by the energy-extracting interface. The charge-voltage diagram depicted in Fig. 3.10b shows the successive energy conversion cycles between two closing events of the switch.

It should be noted that V_{comp} and V_{h} have to be computed depending conversion cycle that maximizes the converted energy. In the approximation of a rectangular charge-voltage diagram, this is allows to sustain an energy converison cycle such that its characteristic voltages V_{L} and V_{R} maximize the converted energy. The determination of such an optimum cycle is the subject of the next chapter.

3.6 Conclusion and future works

This chapter presented a rigorous analysis of the new generic topology of series-parallel charge-pumps in the electrical domain. The main result of the analysis is a formal proof that these conditioning circuits are unstable charge-pump conditioning circuits that, in their steady-state mode of operation, implement the ratio γ between V_{L} and V_{R} characteristic voltages. The value of γdefined by

$$\gamma := \Pi + \frac{1}{\Pi - 1} \sum_{i=1}^{\Pi} C_i \sum_{i=\Pi+1}^{N} {C_i}^{-1} \tag{3.82}$$

where

$$\begin{aligned} \Pi &:= \min(\{p \ \in]\!]1; N[\![\text{ such that } \overline{\Omega(p+1)}\} \cup \{N\}), \\ \Omega(p) &:= \text{“} \sum_{i=1}^{p} C_i - (p-1)C_p > 0'' \end{aligned} \tag{3.83}$$

and where the C_i denote the circuit's N fixed capacitors ordered as $C_1 \leqslant \cdots \leqslant C_{\text{N}}$. This steady-state mode is attained from any initial condition if $\eta > N$. If $\eta < N$, then this steady state-mode of operation is attained if $\eta > \gamma$ and if the initial voltages across the circuit's fixed capacitors verify

$$\begin{aligned} V_{\text{t},\overline{n_0}} = V_{1,\overline{n_0}} \geqslant \ldots \geqslant V_{N,\overline{n_0}}, \\ \eta V_{\text{t},\overline{n_0}} > \sum_{i=1}^{N} V_{i,\overline{n_0}}. \end{aligned} \tag{3.84}$$

This generic topology hence extends the range of ratios γ of unstable charge-pump conditioning circuits to values greater than 2. We can further explicitely characterize a cycle in unstable mode operation by relating the values of the V_{L} and V_{R} voltages to the circuit topology. With

$C_1 \leqslant \cdots \leqslant C_\mathrm{N}$, we have that

$$\begin{cases} V_\mathrm{L} &= V_1, \\ V_\mathrm{R} &= \sum_{i=1}^{N} V_i. \end{cases} \tag{3.85}$$

The analysis is somewhat intricated and resorts to details that are specific to the studied topology. This intrication is linked to the existence of multiple operation modes that can be encountered before the steady-state operation mode is reached. Also, the implemented ratio in steady-state mode γ is a nontrivial function of the circuit's fixed capacitors. A complete theory of charge-pump conditioning circuit as discussed in the conclusion of the previous chapter may result in finding at least part of the results of this analysis using a systematic method, without resorting to the level of details considered in this chapter.

Chapter 4

Comparison and electromechanical study of electrostatic vibration energy harvesters using charge-pump conditioning circuits

The first part of this chapter is concerned with the comparison of the different charge-pump conditioning circuits in the electrical domain. This comparison is done under the simple constraint of maximum voltage across the transducer. It is done supposing idealized electrical components. It confirms the advantage of unstable charge-pump conditioning circuits over their stable counterparts, in that they can implement cycles of maximal energy conversion starting from a low pre-charge energy in the circuit.

Then, the second part of the chapter discusses the role of the electromechanical coupling in e-VEHs using unstable charge-pump conditioning circuits, on the basis of experiments. These experiments feature an electrostatic transducer fabricated in MEMS technology, electrically conditioned by the Bennet's doubler. The obtained results are qualitatively different from the behavior predicted by the study in the electrical domain, and demonstrate the role of the electromechanical coupling on the system's dynamics.

Thus, the third and last part of the chapter presents an electromechanical domain study of e-VEHs using unstable conditioning circuits. This study serves as the basis of a semi-analytical method geared towards the comparison of different unstable charge-pump conditioning schemes in the electromechanical domain, as a function of the system and input parameters. Some early results of the application of the method under different input and system parameters are presented. These results support that the γ ratio of the used unstable charge-pump, but also the pre-charge voltage are important design parameters. They also show for the example of the symmetrical gap-closing geometry, that unstable charge-pump are advantageous when targeting harmonic inputs of lower frequency than the natural frequency of the e-VEH's mechanical resonator.

The work related to the comparison in the electrical domain was published in [KGB17c], whereas a part of the experimental work below was published in [DKB15; DKB14]. The work

related to the semi-analytical analysis of e-VEHs using charge-pump conditioning circuits is being drafted for a future publication at the time of writing of this manuscript. Note that we do not discuss here the results of the experimental comparison between the primitive conditioning circuit and the Bennet's doubler, which we have published in in [KBG15].

4.1 Comparison in the electrical domain

This section presents a comparison, in the electrical domain, of the charge-pump conditioning circuits presented in the two previous chapters. This comparison is made supposing idealized circuit components as in the presentation of the charge-pump conditioning circuits of previous chapters. We also make the same hypothesis that C_t monotonically varies between C_max and C_min and between C_min and C_max, both of which are supposed to be constant. We remind that $\eta := C_\mathrm{max}/C_\mathrm{min}$. All of the charge-pumps below are supposed to fulfill the hypothesis that the fixed capacitors are large compared to C_max, so that we may use our framework of charge-pump conditioning circuit of Chap. 2. In particular, each conversion cycle is specified in terms of V_L and V_R characteristic voltages, except for the rectifier charge-pumps, which nonetheless can be supposed to implement rectangular charge-voltage diagrams. We remind the energy converted per cycle formula for a cycle characterized by V_L and V_R voltages:

$$\Delta W(V_\mathrm{L}, V_\mathrm{R}) = C_\mathrm{min}(V_\mathrm{R} - V_\mathrm{L})(\eta V_\mathrm{L} - V_\mathrm{R} + E(\eta - 1)) \tag{4.1}$$

This electrical domain comparison starts by determining which of the rectifier charge-pumps is optimal among the three presented in Sec. 2.3.1.2. That is, we determine which one of the three can implement a C_t variation cycle of maximum converted energy, for η and E supposed to be given parameters, and under a maximum voltage constraint across the transducer. We then show that Roundy's charge-pump is preferable over rectifier charge-pumps, thanks to the additional parameter V_0 that allows adequate tuning of the energy conversion cycle. Then, we determine the cycle of maximal energy conversion for unstable charge-pumps under the maximal transducer voltage constraint. The optimal γ ratio is determined, and hence this determines the optimal topology of unstable charge-pump for given η and E. It is also shown that the Roundy charge-pump, by adequate charging of its fixed capacitors, can implement the same maximal energy conversion cycle. However, the unstable charge-pumps have the important advantage that this maximum energy conversion cycle can be reached by autonomous operation from arbitrarily low initial energy in the system. On the contrary, pre-charging C_L and C_R of Roundy's charge-pump to the right values requires a possibly high amount of pre-charge energy in the circuit.

This comparison in the electrical domain is useful in cases where the electromechanical coupling is negligible, or in cases where the displacement of the transducer's mobile electrode is imposed by the external mechanical action. We will see starting Sec. 4.8 that the results of this electrical comparison, as far as unstable charge-pumps are concerned, can be mitigated by the electromechanical coupling. We will hence have to resort to a completely different study.

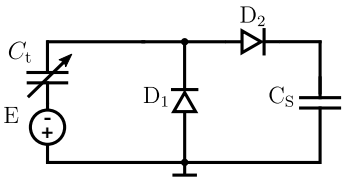

(a) Half-wave 1 charge-pump conditioning circuit

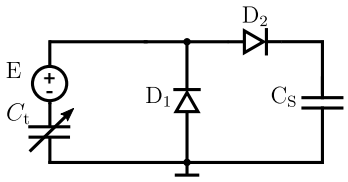

(b) Half-wave 2 charge-pump conditioning circuit

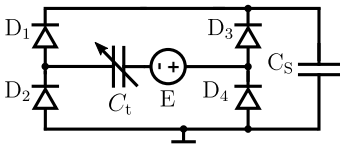

(c) Full-wave charge-pump conditioning circuit

Figure 4.1: Schematics of rectifiers charge-pumps

4.1.1 Comparison between the three rectifier topologies

First, we compare the maximum energy conversion cycles of the rectifier charge-pump topologies, which are all depicted in Fig. 4.1. In this subsection, we are dealing with a transducer such that $E > 0$.

The C_t variation cycles showing maximum energy conversion with these circuits were derived and given in Chap. 2. We report them here again:

$$\Delta W_{\text{opt}}^{\text{HW1}} = \frac{1}{4} C_{\min} E^2 (\eta - 1)^2, \tag{4.2}$$

$$\Delta W_{\text{opt}}^{\text{HW2}} = \frac{1}{4} C_{\min} E^2 \frac{(\eta - 1)^2}{\eta}, \tag{4.3}$$

$$\Delta W_{\text{opt}}^{\text{FW}} = \frac{1}{2} C_{\min} E^2 \frac{(\eta - 1)^2}{\eta + 1}. \tag{4.4}$$

It is straightforward that, in the absence of any constraint, we have

$$\Delta W_{\text{opt}}^{\text{HW1}} > \Delta W_{\text{opt}}^{\text{FW}} > \Delta W_{\text{opt}}^{\text{HW2}}. \tag{4.5}$$

Let us now consider a constraint on the maximum voltage that the transducer can support. This is the absolute value of the voltage across the $\{C_t + E\}$ dipole. Given the topology of the rectifier charge-pumps depicted in Fig. 2.8, this voltage also corresponds to the maximum blocking voltage that the circuits diodes can support. The voltages that bias the transducer corresponding to each of the optimal energy cycles were also derived in Chap. 2 and read:

$$V_{\text{S,opt}}^{\text{HW1}} = \frac{1}{2} C_{\min} E (\eta - 1), \tag{4.6}$$

$$V_{\text{S,opt}}^{\text{HW2}} = \frac{1}{2} C_{\min} E \frac{(\eta - 1)}{\eta}, \tag{4.7}$$

$$V_{\text{S,opt}}^{\text{FW}} = C_{\min} E \frac{(\eta - 1)}{\eta + 1}. \tag{4.8}$$

Note that these voltages designate the voltage V_S across the C_S capacitor of each circuit, rather than using the V_R, V_L formalism. Indeed, the comparison is easier by resorting to the description of the rectifiers charge-pump state in terms of V_S, because in this case the $V_{\max}$ constraint can be uniquely written $V_S < V_{\max}$ across all three configurations. If we had used the V_L, V_R description of these charge-pumps states at each cycle, then for each charge-pump, the $V_{\max}$ constraint would have read differently. For example, for HW1 it is $V_R \leqslant V_{\max}$, whereas for HW2 it is $V_L \leqslant V_{\max}$ (see the V_L and V_R definition of each of these circuits in Sec. 2.3.1.2). Hence, in the rest of this

subsection dealing with the charge-pump rectifiers, the voltage V_S across C_S of each circuit is chosen as the characteristic cycle voltage.

The energies converted per cycle as a function of V_S can be found in the rectangular charge-voltage diagram approximation. For this, it suffices to consider (4.1) and (2.54). As a result, we find for the expressions of the energy converted per cycle for a given value of the V_S voltage:

$$\Delta W^{\mathrm{HW1}}(V_S) = V_S C_{\min}(E(\eta-1) - V_S), \tag{4.9}$$

$$\Delta W^{\mathrm{HW2}}(V_S) = V_S C_{\min}(E(\eta-1) - \eta V_S), \tag{4.10}$$

$$\Delta W^{\mathrm{FW}}(V_S) = 2V_S C_{\min}(E(\eta-1) + V_S(\eta+1)). \tag{4.11}$$

We will need these expressions of the energy converted per cycle for general V_S, in order to account for the $V_{\max}$ constraint. We remind that the maximum power points in (4.2)-(4.4) were simply found by maximizing (4.9)-(4.11) for V_S, as we did in Sec. 2.3.1.2.

From (4.6)-(4.8), one immediately notices that

$$V_{S,\mathrm{opt}}^{\mathrm{HW1}} > V_{S,\mathrm{opt}}^{\mathrm{HW2}} > V_{S,\mathrm{opt}}^{\mathrm{FW}} \tag{4.12}$$

Hence, the comparison under the $V_{\max}$ maximum voltage constraint is as follows.

If $V_{\max} \geqslant V_{S,\mathrm{opt}}^{\mathrm{HW1}}$, then the HW1 is the optimal circuit, as (4.5) applies. If $V_{S,\mathrm{opt}}^{\mathrm{FW}} < V_{\max} < V_{S,\mathrm{opt}}^{\mathrm{HW1}}$, then first note that $\Delta W^{\mathrm{HW1}}(V_S)$ is an increasing function of V_S for $V_S \leqslant V_{S,\mathrm{opt}}^{\mathrm{HW1}}$. Then, comparing (4.9) evaluated at $V_{\max}$ and (4.4) yields that HW1 is optimal over FW in this region of definition of $V_{\max}$ if and only if

$$V_{\max} \geqslant \frac{1}{2}E(\eta-1)\left(1-\sqrt{\frac{\eta-1}{\eta+1}}\right). \tag{4.13}$$

. In this same region of $V_{S,\mathrm{opt}}^{\mathrm{FW}} < V_{\max} < V_{S,\mathrm{opt}}^{\mathrm{HW1}}$, HW2 cannot be optimal because its optimal voltage is higher than that of FW and its converted power is lower.

The only case where the HW2 circuit could potentially be optimal is then when $V_{\max} < V_{S,\mathrm{opt}}^{\mathrm{FW}}$. But then again, comparing the general energy per cycle formula in (4.3) with that of the HW1 circuit (4.2) shows that the HW1 circuit has always a better figure of converted energy per cycle, regardless of η and E. Hence, the HW2 circuit is never optimal. Note that this is also easily seen geometrically by a quick glance at the charge-voltage diagrams of HW1 and HW2.

In this same region where $V_{\max} < V_{S,\mathrm{opt}}^{\mathrm{FW}}$, we still have to compare HW1 and FW circuits. The comparison relies on the general energy per cycle formula evaluated at $V_{\max}$, as they are increasing functions of V_S for $V_S < V_{S,\mathrm{opt}}^{\mathrm{FW}}$. We easily determine that HW1 is optimal over FW if and only if

$$V_{\max} \geqslant \frac{1}{2}E\frac{\eta-1}{\eta+1}. \tag{4.14}$$

which concludes the comparison of the three circuits. The fact that HW2 is never optimal is generalizable to all the other charge-pump conditioning circuits presented in the previous chapters with reversed electret polarity. This is the reason why we do not consider these versions of the charge-pump conditioning circuits in the present manuscript.

Up to this point, we have merely determined the V_S that maximizes the converted energy per

cycle ΔW in the setting of the ideal charge-pump approximation. In fact, the cycles of maximal energy conversion determined above can be reached by autonomous charge-pump operation, from any initial voltage across C_S fulfilling $V_\mathrm{S} \leqslant V_\mathrm{S,opt}$. In a practical operation setting, the circuits have to be kept at this maximum power point by controlling the voltage across C_S so for it to stay around $V_\mathrm{S,opt}$. This is done using an energy-extracting interface, as we discussed in Sec. 2.4.2, and as was illustrated in the simulations of Sec. 3.5.7 with the example of the series-parallel charge-pump.

4.1.2 Comparing Roundy's charge-pump with the rectifiers

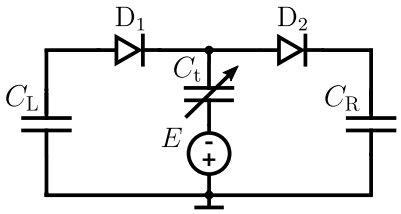

Figure 4.2: Schematic of the charge-pump conditioning circuit proposed by Roundy *et al.*

Roundy's charge-pump is classed as a stable charge-pump in Chap. 2. Its schematic is reported again in Fig. 4.2. Let us recall here the simplified formula for the maximum converted energy per cycle by Roundy's charge-pump, derived at the end of Sec. 2.3.1.1:

$$\Delta W_\mathrm{opt}^\mathrm{ROU} = \frac{C_\mathrm{min}(C_\mathrm{L}+C_\mathrm{R})(E+V_0)^2(\eta-1)^2}{4(C_\mathrm{L}+\eta C_\mathrm{R})} \tag{4.15}$$

where V_0 denotes the initial voltage across C_L and C_R. This cycle is attained at the cycle voltages

$$\begin{cases} V_\mathrm{L,opt}^\mathrm{ROU} &= \dfrac{1}{2}\left(V_0 + \dfrac{V_0(C_\mathrm{R}+C_\mathrm{L}) - E(\eta-1)C_\mathrm{R}}{C_\mathrm{L}+\eta C_\mathrm{R}}\right) \\ V_\mathrm{R,opt}^\mathrm{ROU} &= \dfrac{V_0(2\eta C_\mathrm{R} + (\eta+1)C_\mathrm{L}) + E(\eta-1)C_\mathrm{L}}{2(C_\mathrm{L}+\eta C_\mathrm{R})} \end{cases}. \tag{4.16}$$

From this equation, one notices that Roundy's charge-pump is different from the rectifier charge-pump operations in two aspects. Firstly, the expression of the maximum converted energy per cycle (4.15) that we had derived in Chap. 2 depends on the values of the fixed capacitors. It is straightforward to show that it increases as $C_\mathrm{L}/C_\mathrm{R} \to \infty$. Hence, the formula (4.15) reduces, in this limit, to

$$\Delta W_\mathrm{opt}^\mathrm{ROU} = \frac{1}{4}C_\mathrm{min}(E+V_0)^2(\eta-1)^2, \tag{4.17}$$

and the voltages in (4.16) reduce to

$$\begin{cases} V_\mathrm{L,opt}^\mathrm{ROU} &= V_0 \\ V_\mathrm{R,opt}^\mathrm{ROU} &= \dfrac{1}{2}(E(\eta-1)+V_0(\eta+1)) \end{cases} \tag{4.18}$$

In fact, with $C_\mathrm{L} \gg C_\mathrm{R}$, the Roundy's charge-pump is equivalent to the HW1 rectifier, where E is substituted as $E \leftarrow E + V_0$, V_0 being the voltage across C_L.

Therefore, we can mention the second important difference with the rectifiers charge-pumps: the value of the maximum converted energy per cycle depends on another parameter, namely V_0.

This parameter is the initial voltage across C_L and C_R of the circuit, and the corresponding total initial energy reads $1/2 \cdot {V_0}^2(C_\mathrm{L} + C_\mathrm{R})$. Increasing this initial energy increases the maximum converted energy per cycle that the charge-pump can reach through autonomous operation.

The comparison in the cases where $E = 0$ is not meaningful as rectifier charge-pumps cannot operate under this hypothesis. In the cases where $E > 0$, and with the maximum voltage constraint of V_max across the $\{C_\mathrm{t} + E\}$ dipole, then Roundy's charge-pump always performs at least as good as the HW1 rectifier. The V_max constraint translates to $V_\mathrm{R} \leqslant V_\mathrm{max}$ for Roundy's charge-pump. To show Roundy's charge-pump optimality, remark that (4.17) and (4.18) matches the maximum converted energy per cycle and voltage of the HW1 circuit when $V_0 = 0$. Therefore, if $V_\mathrm{max} \geqslant V_\mathrm{S,opt}^\mathrm{HW1}$, then V_0 can be chosen such that $0 < V_\mathrm{R,opt}^\mathrm{ROU} = V_\mathrm{max}$ and the converted power will necessarily be larger than with the half-wave charge-pumps. If $V_\mathrm{max} < V_\mathrm{S,opt}^\mathrm{HW1}$, then the Roundy's charge-pump with $V_0 = 0$ performs equally good as the HW1 charge-pump.

In conclusion, using Roundy's charge-pump is necessarily the optimal choice over any of the rectifiers conditioning circuits for given E, η and V_max across the transducer. Here we have determined a non-degenerated cycle characterized in terms of V_L and V_R that will be reached throughout Roundy's charge-pump autonomous operation, from the state where $V_\mathrm{R} = V_\mathrm{L} = V_0$. An energy-extracting interface has to discharge C_L and C_R so to sustain the charge-pump's state corresponding to $V_\mathrm{L,opt}^\mathrm{ROU}$ and $V_\mathrm{R,opt}^\mathrm{ROU}$ (see Sec. 2.4.2).

Now that we have established the optimality of Roundy's charge-pump compared to rectifier charge-pumps, let us see how it compares to the unstable charge-pumps.

4.1.3 Comparing stable and unstable charge-pumps

We now determine the optimal unstable conditioning circuit for given E and η parameters. To do so, we use the characterization of these circuits in terms of their γ ratio, and we set a constraint on V_R. The maximization procedure reduces to a simple geometrical problem, which is solved in terms of optimal values of γ and V_L. Again, the effects of electrical non-idealities are neglected here.

For all charge-pump conditioning circuits, the abrupt limitation on V_R corresponds to a maximum voltage constraint across the transducer, that is, the maximum allowable voltage across the $\{C_\mathrm{t}+E\}$ dipole. In Fig. 4.6 are depicted some charge-voltage diagrams that correspond to a charge-pump biasing where this constraint is fulfilled. Note that in the absence of such a constraint, there is no limit to the converted energy per cycle, as the energy converted per cycle for an unstable charge-pump in unstable mode reads

$$\Delta W(V_\mathrm{L}) = C_\mathrm{min} V_\mathrm{L}(\gamma - 1)(V_\mathrm{L}(\eta - \gamma) + E(\eta - 1)) \tag{4.19}$$

which has no upper-bound for positive V_L provided that $\eta > \gamma > 1$.

Let us geometrically derive the rectangular charge-voltage diagram that maximizes the converted energy per cycle, in terms of (V_L, γ). We remind that $\gamma := V_\mathrm{R}/V_\mathrm{L}$ is the unstable charge-pump's characteristic ratio. This translates to the following constrained maximization problem

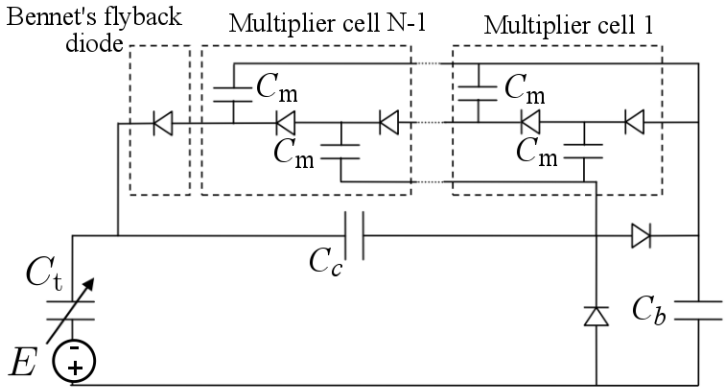

Figure 4.3: Generic topology for Lefeuvre's charge-pump [LRW14].

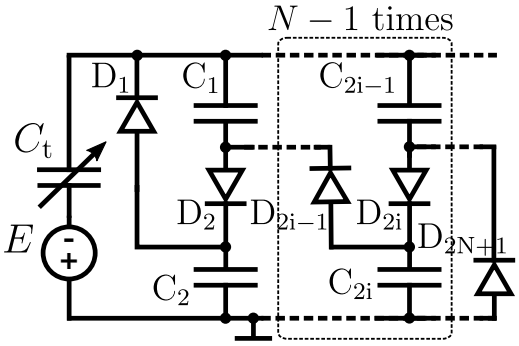

Figure 4.4: Generic topology for Illenberger's charge-pump [ITK17].

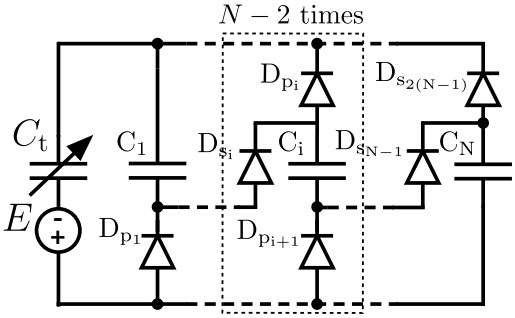

Figure 4.5: Generic topology for series-parallel charge-pump.

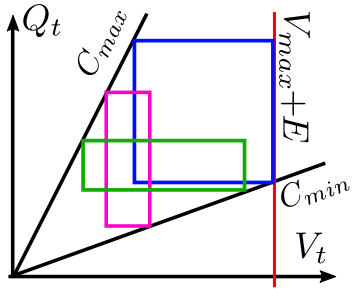

Figure 4.6: A bunch of charge-voltage diagrams that fulfill the condition $V_R \leqslant V_{max}$. Equivalently, V_{max} is the maximum allowable voltage across the $\{C_t + E\}$ dipole.

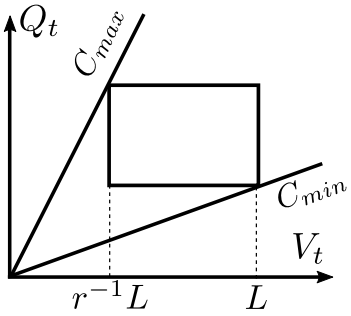

Figure 4.7: Illustration of the simple geometrical situation of Sec. 4.1.3.

that has to be solved for (γ, V_{L})

$$\max_{\substack{\gamma>1 \\ \gamma V_{\mathrm{L}} \leqslant V_{\max}}} \Delta W(V_{\mathrm{L}}, \gamma V_{\mathrm{L}}) = C_{\min} V_{\mathrm{L}} (\gamma - 1)(V_{\mathrm{L}}(\eta - \gamma) + E(\eta - 1)). \tag{4.20}$$

This problem has a straightforward geometrical solution. Consider a rectangular charge-voltage diagram whose left side vertical side is at the $r^{-1}L$ coordinate on the V-axis ($r > 1$), while its right vertical side lies at the L coordinate. This situation is depicted in Fig. 4.7 for clarity. Such a rectangle has an area of

$$\mathcal{A} = C_{\min} L^2 (\eta r^{-1} - 1)(1 - r^{-1}) \tag{4.21}$$

which attains its maximum, for fixed L, for r chosen such that

$$r = \frac{2\eta}{\eta + 1} \tag{4.22}$$

Also, the rectangle's area is an increasing function of L. The solution to the problem (4.20) above therefore corresponds to a conditioning circuit that implements a charge voltage diagram such that: (i) the ratio between the V coordinate of right and left side is of r, that is, $(E + \gamma_{\mathrm{opt}} V_{\mathrm{L}})/(E + V_{\mathrm{L}}) = r$, (ii) its right side is at maximum allowable voltage, that is $V_{\mathrm{Ropt}} = \gamma_{\mathrm{opt}} V_{\mathrm{Lopt}} = V_{\max}$. Thence, replacing r by (4.22), we have that

$$\begin{cases} V_{\mathrm{Lopt}} & = \gamma_{\mathrm{opt}}^{-1} V_{\max} \\ \gamma_{\mathrm{opt}} & = \dfrac{2\eta V_{\max}}{V_{\max}(\eta + 1) - E(\eta - 1)}. \end{cases} \tag{4.23}$$

The corresponding maximum converted energy reads

$$W_{\mathrm{opt}}^{\mathrm{UNS}} = C_{\min} \frac{(\eta - 1)^2 (E + V_{\max})^2}{4\eta}. \tag{4.24}$$

One remarks that this solution is not valid when $V_{\max} \leqslant E(\eta - 1)/(\eta + 1)$. This can be seen geometrically on the charge-voltage diagram: in this case, the left vertical side of the rectangle is required to be at a V-coordinate that is less than E, which is not possible as unstable charge-pumps are such that $0 < V_{\mathrm{L}} < V_{\mathrm{R}}$. In fact, in this case, we have that $\Delta W(\gamma^{-1} V_{\max}, V_{\max})$ is a strictly increasing function of γ for fixed $V_{\max}$. We will not further discuss this case here. Let us therefore only consider the case where $V_{\max} > E \geqslant 0$, so that γ_{opt} necessarily satisfies $\gamma_{\mathrm{opt}} > 1$.

If we find that $\gamma_{\mathrm{opt}} \geqslant 2$, then an appropriate series-parallel topology (including the Bennet's doubler) can implement this cycle in its unstable operation mode. The series-parallel topology is depicted again in Fig. 4.5. One has merely to choose the values of the fixed capacitors so that (3.83) yields γ_{opt} determined above. If, on the other hand, we obtain γ_{opt} such that $2 > \eta > \gamma_{\mathrm{opt}}$, then Lefeuvre's (Fig. 4.3) or, equivalently, Illenberger's (Fig. 4.4) charge-pump topology is optimal. As only γ of the form $1 + 1/N$ are implementable using these two topologies, then one of N_1 and N_2 such that $1 + 1/N_1 \leqslant \gamma_{\mathrm{opt}} \leqslant 1 + 1/N_2$ has to be chosen. Which one is simply determined by comparing $\Delta W((1 + 1/N_1)^{-1} V_{\max}, V_{\max})$ and $\Delta W((1 + 1/N_2)^{-1} V_{\max}, V_{\max})$ and choosing the N_i that yields the largest of these two quantities.

Now, let us come to the main conclusion of this section on electrical comparison: the ad-

vantage of unstable charge-pumps over the stable charge-pumps. First, for this comparison, the stable charge-pumps reduce to the Roundy circuit because of the optimality of the latter over rectifier charge-pumps, as determined above in Sec. 4.1.2.

It is clear that the Roundy's charge-pump can be set in the electrical state corresponding to the conversion cycle characterized by (4.23). Indeed, it suffices to set the voltages across C_L and C_R to ${\gamma_\mathrm{opt}}^{-1}V_\mathrm{max}$ and V_max, respectively. In this case, this cycle of Roundy's charge-pump will be the same as if it was implemented by an unstable charge-pump. However, this requires to use a mechanism external to the charge-pump in order to charge C_L and C_R to these two voltages. This requires transfers of large energy amounts, from a separate electrical energy tank to the capacitors C_R and C_L to charge them to the voltages ${\gamma_\mathrm{opt}}^{-1}V_\mathrm{max}$ and V_max. Indeed, the energy is the square of these voltages weighted by C_L and C_R respectively, which are chosen large to fulfill the ideal charge-pump approximation. Because of the necessarily limited efficiency of such energy transfer circuits, this would result in possibly large amounts of dissipated energy.

On the contrary, unstable charge-pumps can reach the cycle characterized by (4.23) from their autonomous operation starting from arbitrarily low initial energy in the charge-pump's fixed capacitors, provided that: (i) $\gamma_\mathrm{opt} < \eta$, (ii) the initial state of the charge-pump is such that it is in unstable mode, or in other words, there is no transient before the unstable steady-state mode of operation. One can check using (4.23) that the point (i) is always verified under our assumption that $V_\mathrm{max} > E$. The point (ii) depends on the used topology of unstable charge-pump. For the series-parallel charge-pumps including the Bennet's doubler, the analysis of Chap. 3 shows that it is always possible to choose such an initial charge-pump state. For example, for the Bennet's doubler, it suffices to charge both fixed capacitors with the same, arbitrarily small voltage. More generally, for any series-parallel charge-pump, it suffices to charge the capacitors following (3.68) and (3.69). It turns out that, for these topologies, merely having $E > 0$ arbitrarily small suffices to initiate the unstable operation, as we have shown experimentally in [KBG15]. For Lefeuvre's charge-pump, the initial state must be as: C_b is charged to an arbitrarily low voltage V_b, while C_c is charged to NV_b. In addition, the capacitors in the multiplier branches (C_m) should be chosen small compared to both C_b and C_c. For Illenberger's charge-pump, we refer the reader to the initial voltage configuration given by Illenberger's *et al.* in [ITK17]. Note however that the energy extracting interface must be connected to the circuit in a way that each event of energy extraction leaves the charge-pump in a state satisfying the requirement (ii) above. For example, this is the case in the simulated example of Sec. 3.5.7, as one can infer from the (admittedly short) exponential voltage increases in between switch closing events.

Let us however mention that Roundy's charge-pump, combined with Yen's inductive flyback discussed in Sec. 2.4.1, allows increasing the value of V_0 subsequently to the charge-pump's operation and from arbitrarily low pre-charge. However, this requires an asynchronously controlled switch, additionally to that used by the energy-extracting interface that sustains the maximum power point.

4.1.4 Some additional comments

It should be stressed that the comparison and determination of the optimal charge-pump to use in the different cases above do not take into account the necessarily non-ideal nature of each circuit's components. This can have a non-negligible impact on the conclusions. For example,

for small timescales of the conditioning circuit's operation (i.e., small number of consecutive cycles of C_t), the influence of the diodes forward voltage can slightly change the value of the γ ratio effectively implemented by an unstable charge-pump conditioning circuit compared to its theoretical value determined by the choice of the circuit topology. This has already been highlighted in Sec. 3.4.1 supported by the simulations of Sec. 3.5.4.

Also, an important dimension that was not taken into account is the number of cycles it takes, from a given initial state of the charge-pump, for each circuit to reach the determined optimal conversion cycles from autonomous operation. Some authors have given more importance to this figure in other works, such as the work by Kempityia on the Roundy's circuit in [KBH12] or the work by De Queiroz on the Bennet's doubler in [DD11]. In the point of view adopted in this section and the rest of the chapter, we do not consider this settling time as a meaningful parameter. Yet, note that determining this settling time can be done for circuits like the rectifiers circuits or the Roundy's charge-pump in a straightforward manner by using the explicit discrete evolution relations given in Chap 2. However, doing the same from arbitrary initial states is much more difficult for unstable charge-pumps. We did so for the Bennet's doubler in the example at the end of Sec. 3.2, but adding branches to the series-parallel charge-pump makes the task cumbersome. This is related to the multiple regions of the piecewise-affine maps that govern the dynamics of the charge-pump conditioning circuits. This is also the case for the Lefeuvre's charge-pump, for which the transient dynamics have not been characterized yet. For the unstable charge-pumps, at most, it should be possible to find an upper bound for the transient process duration, using arguments that do not rely on the explicit evolution laws of each circuit. We won't further investigate this question here.

4.2 Experimental evidence of the electromechanical coupling and impact on the comparison

The study done in Chap. 2, Chap. 3 and in Sec. 4.1 above were made in the electrical domain, that is, considering $C_\mathrm{t}(t)$ as the system's unalterable input. As pointed out in Sec. 1.2.2, in inertial e-VEHs, C_t's variation is the result of the dynamics of the system, that encompass the input vibration, the forces generated by the system, and the dynamics of the electrical circuit that biases the transducer.

The previous electrical domain study of unstable charge-pump conditioning circuits shows an unlimited increase of the converted energy from arbitrary non-zero initial states of the charge-pump, as long as $\eta > \gamma$. Physically, this behavior is of course prohibited, at least by the fundamental energy conservation principle. In fact, the upper-bound for harmonic vibrations inputs that is presented later in Chap. 6 (see (6.5)) has at least to be enforced. It is hence expected that some mechanism mitigates the unstable charge-pump behavior, setting a limit to this seemingly unlimited increase of the converted energy.

This limit can result, for instance, from the breakdown voltage of the dielectric in between the transducer's electrodes, or the breakdown voltage of the electrical components. As an example, the experiments by De Queiroz *et al.* in [DD11] with the Bennet's doubler show an exponential increase, up to a point where the voltages biasing the transducer (i.e., V_L and V_R) saturate abruptly. De Queiroz *et al.* identify this saturation as a result of the breakdown of the electrical

mass m	60.5 mg
linear spring stiffness k	68.1 N m^{-1}
resulting resonant frequency f_0	168.9 Hz
finger length L_f	2000 µm
finger height h_f	380 µm
number of fingers N_f	130
resulting transducer half-area S	1 cm^2
transducer gap at rest d_0	46.7 µm
maximum displacement x_M	43.8 µm
resulting capacitance at x_M $C_\mathrm{t}(x_\mathrm{M})$	311.5 pF
resulting capacitance at rest $C_\mathrm{t}(d_0)$	37.5 pF
complete device dimensions	$12 \times 10 \times 0.4$ mm^3

Table 4.1: Main device parameters as extracted from the device's layout file.

measured resonant frequency f_0	160 Hz
measured capacitance at rest $C_\mathrm{t}(d_0)$	59 pF $\pm$ 2 pF
resulting parasitic capacitance C_p	21.5 pF $\pm$ 2 pF

Table 4.2: Some measured device parameters.

components.

As we now will see by experiments, the electromechanical coupling is also responsible for a qualitative change of the behavior of electrostatic vibration energy harvesters. In fact, at least for the micro-scale devices that we use in our experiments, the electromechanical coupling is the sole responsible for the qualitative change in the e-VEH's dynamics.

4.2.1 Description of the device

The electrostatic transducer device used for the experiment is a resonant MEMS designed and fabricated at ESIEE Paris, and is based on the mechanical structure presented in Sec. 1.4.3.1. Some of the important lumped parameters of the device used for this experiment are summarized in Table 4.1, extracted from the device's layout file (the file containing the description of the photomask for lithography, see Sec. 1.4.1). Note that the used device was devoid of electret charging.

Using the setup of Sec. 1.5.2, the natural resonant frequency of the mechanical resonator composed of the lumped spring and mass is experimentally measured as $f_0 = 160$ Hz, which is 10 Hz below the resonant frequency computed from the mass and stiffness given in the layout (see Table 4.1). The obtained swept waveform is depicted in Fig. 1.33 of Chap. 1, where it served as an illustration of the frequency sweep experiment. We also measured the device's parasitic capacitance, that is, the difference between the capacitance at rest in Table 4.1, and that measured when the device is in the setting of the experiments described below (see Fig. 4.8). We found a value of $C_\mathrm{p} = 21.5$ pF. These results are summarized in Table 4.2.

The capacitance variation was measured at zero biasing for different inputs corresponding to those used in the experiments below. This measurement was done by the synchronous detection technique described in Sec. 1.5.1. The results are summarized in Table 4.3 and Table 4.4. Note

Input amplitude	1.3 g	1.5 g	1.7 g	2 g
η	2.1 ± 0.09	2.31 ± 0.07	2.45 ± 0.07	2.5 ± 0.06

Table 4.3: Values of $\eta \coloneqq C_{\max}/C_{\min}$ measured by synchronous detection on the device used for the experiments, for different amplitudes of the harmonic input excitation. For all of these measurements, the frequency of the harmonic input is of 150 Hz. These measurements correspond to an unbiased transducer (apart from the very low amplitude carrier signal used for synchronous detection, that can be supposed to have no impact on the dynamics). Note: we did not account for the error on $C_{\min}$, which is the capacitance at rest, to compute the given error margins.

Input frequency	140 Hz	150 Hz	160 Hz	170 Hz
η	2.04 ± 0.1	2.31 ± 0.07	2.51 ± 0.06	2.56 ± 0.05

Table 4.4: Values of $\eta \coloneqq C_{\max}/C_{\min}$ measured by synchronous detection on the device used for the experiments, for different frequencies of the harmonic input excitations. For all of these measurements, the amplitude of the harmonic input is of 1.5 g. These measurements correspond to an unbiased transducer (apart from the very low amplitude carrier signal used for synchronous detection, that can be supposed to have no impact on the dynamics). Note: we did not account for the error on $C_{\min}$, which is the capacitance at rest, to compute the given error margins.

that η is larger at 170 Hz than at the resonant frequency, a phenomenon that can be attributed to the hardening behavior of the structure's spring. Indeed, the frequency sweep used to determine the resonant frequency of the device was of low amplitude (0.3 g), so the peak at resonance looked sharp (see Fig. 1.33). However the frequency sweep was also done at 1.5 g corresponding to the conditions of Table 4.4, and showed comparable levels of voltage swing across the primitive circuit's resistance at both 160 Hz and 170 Hz.

4.2.2 Experimental set-up

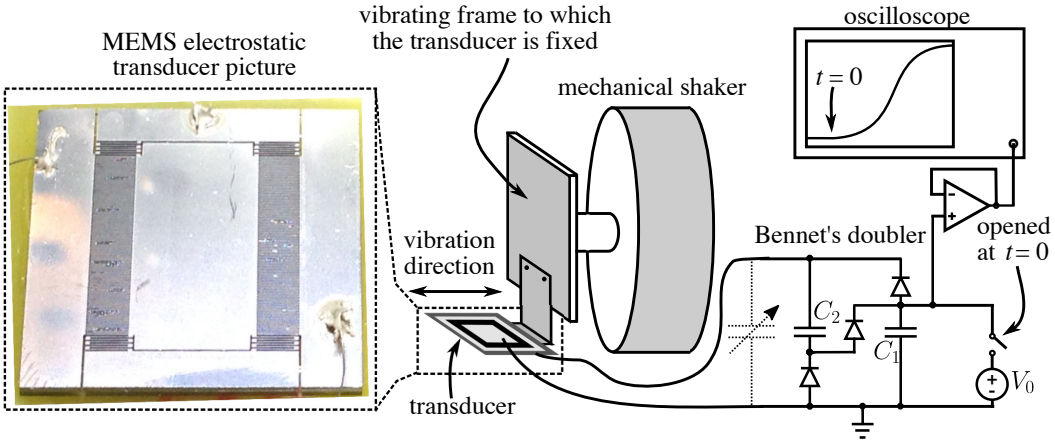

Figure 4.8: Setup used for the measurement of the electret potential, with a top-view picture of the electret MEMS transducer. The device dimensions are 1.5cm × 1.6cm × 380µm. This illustration features the transducer connected to the HW1 circuit to get (V_1, Δ_1). For the measurement method, the same setup has to be used afterwards with the HW2 circuit, that is, with the polarity of the transducer reversed, to get (V_2, Δ_2).

The Bennet's doubler capacitors were manually pre-charged to 5 V at the beginning of the experiment. The fixed capacitors were chosen as $C_1 = 1.5$ nF, $C_2 = 100$ nF. The amplifier used for the reading is an OPA454 and the diodes in the circuit are JPAD5 diodes. A schematic of the set-up for the experiment is depicted in Fig. 4.8.

Our experiment consisted in submitting the device to mechanical vibrations, while the trans-

ducer is electrically conditioned by the Bennet's doubler. The measured quantity is the time-evolution of the voltage across the Bennet's doubler largest capacitor. From this quantity, the energy in this capacitor is readily computed, and so is the converted power, which is found as the slope of the energy variation in C_1. As $C_1 \gg C_2$, C_1 receives the major part of the converted energy. This is because we know from the Bennet's doubler analysis that the two capacitors are approximately biased by the same voltage throughout the circuit's operation. We hence consider the derivative of its energy to amount to the converted power. Also recall that monitoring the voltage across C_1 is equivalent, with the Bennet's doubler, to monitoring the V_L characteristic cycle voltage (see Sec. 2.3.2.1).

4.2.3 Results and discussion

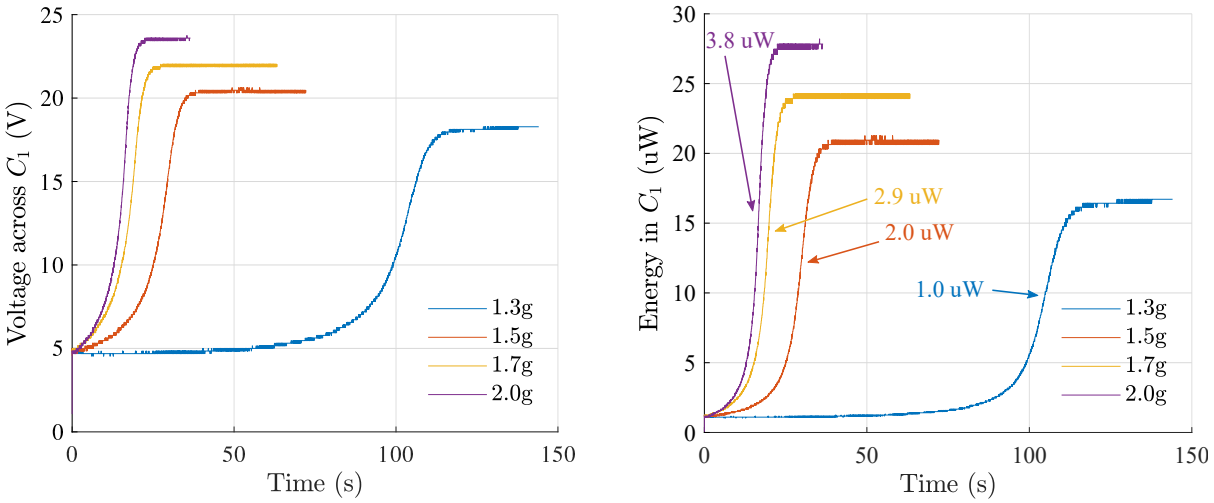

(a) Results obtained with inputs of different amplitudes, in terms of voltage across C_1.

(b) Results obtained with inputs of different amplitudes, in terms of energy in C_1.

Figure 4.9: Results of experiments for a MEMS transducer biased by the Bennet's doubler conditioning circuit, for inputs of the same frequency but of different amplitudes.

The results of the experiment where the e-VEH is submitted to harmonic inputs of different amplitudes, with fixed frequency of 160 Hz (the resonance frequency of the mechanical resonator) are depicted in Fig. 4.9. These results show that the Bennet's doubler starts by operating in an unstable exponential voltage increase mode from its pre-charge, as predicted from the electrical domain study. Note that there is no transient operation of the Bennet's doubler, because both capacitors were pre-charged. Then for each input, at some point in the evolution, the rate of the voltage evolution goes through a maximum and then starts to decrease. It finally becomes null: a saturation voltage is reached. Equivalently, the rate of energy conversion, i.e., the converted power, first increases exponentially, then reaches a maximum, and then decreases, asymptotically becoming null.

The input excitations of higher amplitude lead to higher saturation voltages as well as to higher values of maximum converted power. The measured values of maximum converted power, range from 1.0 µW with the input of lowest amplitude, to 3.8 µW with the input of highest amplitude. As is, it is not possible to exclude that the saturation phenomenon that is shown it these experiments is of electrical origin. This is because larger harmonic excitation amplitudes lead to larger displacement amplitudes, so larger $\eta = C_{max}/C_{min}$ and hence larger converted

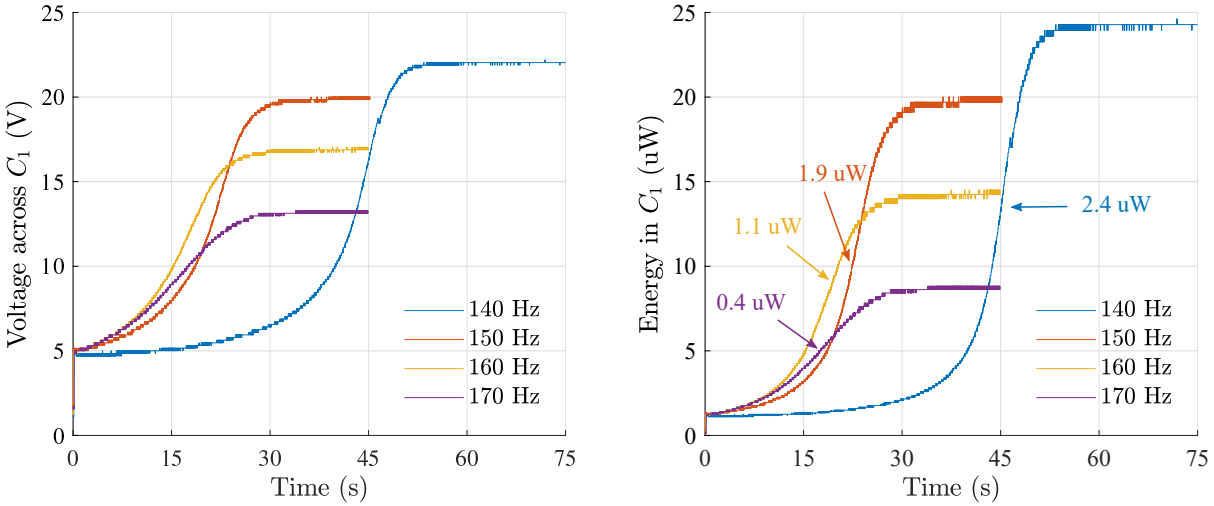

(a) Results obtained with inputs of different frequencies, in terms of voltage across C_1.

(b) Results obtained with inputs of different frequencies, in terms of energy in C_1.

Figure 4.10: Results of experiments for a MEMS transducer biased by the Bennet's doubler conditioning circuit, for inputs of the same amplitude but of different frequencies.

power. This is clear from the electrical analysis of the Bennet's doubler, according to which the converted energy per cycle in unstable operation mode is given by

$$\Delta W = C_{\min} {V_{\mathrm{L}}}^2 (\eta - 2). \tag{4.25}$$

where V_{L} is the cycle characteristic voltage, which is here equal to the voltage across C_1. The converted power is equal to this quantity times the frequency of the capacitance variation subsequent to the input vibration. This frequency (150 Hz) is the same across all of the four measurements done at different amplitudes.

So at any given value of the voltage V_{L} (corresponding for the Bennet's doubler to the voltage across C_1), a larger η yields a larger converted power. Hence, the saturation in this case may as well happen because some electrical saturation phenomenon occurs, which is compensated up to higher voltages across the transducer for inputs of larger amplitude. However, this remains unlikely as the used JPAD5 diodes have a breakdown voltage of at least 45 V, and the saturation shown in the results is not the typical abrupt saturation phenomenon usually exhibited by diodes in breakdown or amplifiers in saturation. For this reason, it is very likely that the electromechanical coupling effect on the device's dynamics is responsible for the observed saturations. A saturating behavior due to the breakdown of the electrical components has been observed in [DD11], where the Bennet's doubler is used with a macroscopic variable capacitor. To leave no room for doubt on the role of the electromechanical coupling on the observed behavior, let us study the results depicted in Fig. 4.10.

The results depicted in Fig. 4.10 are obtained with harmonic inputs of the same amplitude and different frequencies. At first, the voltage increase is faster with the input at 160 Hz (or at 170 Hz), which is the device's resonant frequency, and hence, the converted power is larger. This is expected as this frequency of the input results in larger displacement – if one views the resonator simply in the mechanical domain – which in turn results in larger converted energy per cycle of the capacitance variation. However, at some point, the converted power goes through a maximum, and then starts to decrease, eventually leading to voltage saturation. The results

with the inputs of lower frequencies translate to a converted power that is first lower than with the input at resonant frequency. However, the maximum converted power is higher than with the input at resonant frequency, and so is the saturation voltage. In fact, the lower the input frequency, the larger is the maximum converted power (reaching 2.4 µW for an input frequency of 140 Hz).

This time, the obtained results can be attributed without a doubt to the electromechanical coupling effect, because the conjunction of a lower frequency input and a lower capacitance variation cannot possibly yield a higher converted power accounting for the sole electrical domain study. Again, this is simply inferred from (4.25), that has additionally to be weighted by the capacitance variation frequency to get the converted power.

In fact, the observed results are compatible with an interpretation based on the effects of the electromechanical coupling briefly discussed in Sec. 1.3.4. We remind that in that section, the results depicted in Fig. 1.18 showed that the frequency response, in terms of the e-VEH's inertial mass' displacement amplitude, was modulated by the V_0 voltage in the primitive conditioning circuit (see the "symmetrical gap closing" case in Fig. 1.17b). If we transpose this behavior to our experiment with the Bennet's doubler, then the experimental results of Fig. 4.10 can be qualitatively understood as follows.

For the input at resonant frequency, as the voltage across C_1 increases over time subsequently to the Bennet's doubler operation, the transducer is biased by increasing V_L and V_R characteristic voltages, with V_L equal to the voltage across C_1 and $V_\mathrm{R} = 2V_\mathrm{L}$ as the Bennet's doubler imposes. Subsequently, the amplitude of the mass movement decreases, because the amplitude vs. frequency response gradually shifts to the lower frequencies (see Fig. 1.18), and becomes out-of-tune with the fixed frequency of the input. As a result, the value of η cannot be considered constant from cycle to cycle anymore: it decreases from cycle to cycle as the voltage increases. Thus, the converted power increases up to a point where the V_L increase does not compensate the subsequent decrease of η anymore. After this point, the amplitude continues to decrease, and thus so does the converted power.

With inputs of lower frequency, the amplitude of the movement of the mass is first lower than with the input at the resonant frequency, because the input is out-of-tune compared to the peak in the frequency response of the resonator. Hence, it is also the case for the capacitance variation. However, if yet the capacitance variation is high enough so that $\eta > 2$, then the Bennet's doubler operates in its unstable mode and the e-VEH converts energy. As a result, the voltage across C_1 increases as the energy accumulates. As the voltage increases, the amplitude also increases because the frequency response gradually shifts to the left, towards the frequency of the input. Consequently, the converted power also increases. When the amplitude starts to decrease, for some range of the increasing voltage the converted power still increases. Next, when the voltage increase does not compensate the decrease in the capacitance variation subsequent to the decreasing mass displacement amplitude, the maximum power point is reached. If we further assume intuitively that the frequency shift resulted in the e-VEH to reach higher voltages at the same amplitude with the input below resonant frequency than with the input at resonant frequency, the maximum converted power is larger from the former than from the latter.

Finally, with all inputs, the saturation happens as η asymptotically approaches 2, as we know from the electrical domain study of the Bennet's doubler that this is a necessary condition

for energy conversion, when all the capacitors are charged to the same voltage (see Sec. 3.2.2).

These experimental results are an evidence of the impact of the electromechanical coupling on e-VEHs using the Bennet's doubler. As a consequence, a quantitative study is necessary in order to assess the dynamics of e-VEHs using these circuits when accounting for the electromechanical effects. In particular, a quantitative argument has to be given so as to transpose the shift in the amplitude vs. frequency response presented in Fig. 1.18 to the case of the Bennet's doubler. Also, on a practical and e-VEH optimization level, our results show the existence of a maximum power point which depends on the characteristics of the input. A deeper study is hence needed in order to explore the dependency of this maximum power point to the circuit parameters (mainly, the parameter γ), as well as to the input characteristics and to the transducer's geometrical parameters. This study is the subject of the next section.

4.3 Electromechanical study towards the comparison of electrostatic vibration energy harvesters using unstable charge-pump conditioning circuits

The previous experimental results reinforced the insight gained from the electrical analysis that unstable charge-pumps can bring the e-VEH to reasonable levels of converted power from a low pre-charge. Yet, the results highlighted the existence of a limit on the converted power. In Sec. 4.1 that dealt with the electrical domain, we saw that depending on the constraint and on the device's parameters E and η, an optimal choice of charge-pump conditioning, in terms of γ, maximizes the converted power. It is now legitimate to consider this same question accounting for the electromechanical coupling, and quantify the maximum converted power at the limit shown in the experiments above. However, the study becomes more difficult because of the nested electromechanical dynamics, and the fact that there are more parameters than in the electrical domain study, in which merely E, η and a voltage constraint appeared. For example, one may want to predict the maximum converted power for different characteristics of the input, for other choices of unstable charge-pumps than the Bennet's doubler, or even for different geometrical and mechanical parameters of the transducer.

Instead of relying upon multiple simulations, having a method that eases the computational procedures needed to carry out such predictions is of primary importance. This method has to account for the impact of the electromechanical coupling on the harvester's dynamics to yield accurate predictions. In this section, we report the draft of such a method, based on a semi-analytical procedure, that addresses this question. More precisely, this method provides the evolution of the converted power by an e-VEH submitted to a harmonic input force and using an unstable charge-pump conditioning circuit operating in unstable mode. With this tool, one can estimate the influence of the different parameters mentioned above on the system, at a much lower computational cost than multiple simulations. In particular, the influence of the γ parameter of the unstable charge-pump can be assessed.

Before proceeding to the presentation of our method, let us first give some results of the electromechanical simulation of an e-VEH using the Bennet's doubler. In all of the following, we consider e-VEHs devoid of electret charging, that is, $E = 0$.

4.3.1 Simulations illustrating the electromechanical dynamics of an e-VEH using the Bennet's doubler

The simulations are carried out with VHDL-AMS, allowing for the co-simulation of both the mechanical part of the e-VEH and of its electrical part, that is, the Bennet's doubler. We can therefore assess the evolution of the complete electrical and mechanical state through the e-VEH's operation, and have a better grasp of the system's behavior. The procedure of modeling and co-domain simulation of an e-VEH with VHDL-AMS is further explained in [GPB07].

We also stress on the fact that the goal here is not to try to quantitatively obtain the exact same results as in the experiments. Doing so would require a meticulous study of the device, and a subsequent fitting of the model. Here, we rather employ simulations in order to get insights on the dynamics of the e-VEH using the Bennet's doubler. Later in Sec. 4.3.3.2, we will use simulations in order to validate our method presented in Sec. 4.3.2. Finally, we will again resort to simulations in Sec. 4.18 to highlight some nonlinearities effects that are not predicted by our method.

4.3.1.1 Modeling

On the mechanical side, we use the VHDL-AMS language to model the system described by the ODE

$$m\ddot{x} = -kx - c(x,\dot{x})\dot{x} - k_{\mathrm{st}}(x) - c_{\mathrm{st}}(x,\dot{x}) + \frac{1}{2}V_{\mathrm{t}}^2\frac{\partial C}{\partial x}(x) + \xi_0\sin(\omega_{\mathrm{ext}}t + \phi) \tag{4.26}$$

where the capacitance $C(x)$ is of symmetrical gap-closing geometry (see Sec. 1.2.2.1)

$$C(x) = \varepsilon_0\frac{2Sd_0}{{d_0}^2 - x^2} \tag{4.27}$$

and where

$$c(x,\dot{x}) = B\left((1-\alpha) + \frac{\alpha}{2}\left(\frac{{d_0}^3}{(d_0-x)^3} + \frac{{d_0}^3}{(d_0+x)^3}\right)\right). \tag{4.28}$$

where [Bao05]

$$B = N_{\mathrm{f}}L_{\mathrm{f}}\frac{{h_{\mathrm{f}}}^3}{{d_0}^3}\mu_{\mathrm{air}}. \tag{4.29}$$

Here, μ_{air} is the air's coefficient of viscosity that we take equal to $18\,\mu\mathrm{Pa\,s^{-1}}$, corresponding to room temperature conditions. The signification of the other symbols are reminded in Table 4.1, and one may refer to Fig. 1.25 for further clarification. This term accounts for frictional effects due to the air in between the device's fingers. It is the superposition of a linear damping term and a term accounting for the squeeze-film damping effect. A weight $\alpha \in [0\,;1]$ is added, where $\alpha = 0$ accounts for purely linear damping whereas $\alpha = 1$ models a damping that is purely due to squeeze-film damping effect. This latter nonlinear damping effect arises from the pinching of air in between the transducer's facing fingers. This term for the squeeze-film damping is inspired from [Bao05], Chap. 3: we have dropped the distributed nature of the squeeze-film damping force given in this reference, and we consider the force as a lumped force acting on the mass seen as a point mass.

Without the nonlinear damping term, the simulations give results that are qualitatively

much different from the measurements. In fact, in the following, we have set $\alpha = 1$ for all simulations and numerical calculations. Yet, we keep the linear term in the presentation so as to not lose generality. Also, notice that we used a linear model of a spring, although the device used in the experiments exhibited a spring hardening behavior, as we have pointed out in in Sec. 4.2.1. Typically, this can be modeled by a stiffness term proportional to the third power of the displacement, that we did not add to our model.

Our model of the stoppers is as was presented in Sec. 1.2.2.3 of the introduction chapter. Compared to (1.15), here in (4.26) we have separated the terms of the resonator spring and of the air damping from the terms related to the stoppers. Hence we have that

$$k_{\mathrm{st}} = \begin{cases} 0 & \text{if } |x(t)| \leqslant x_{\mathrm{M}} \\ -k_{\mathrm{s}}|x(t) - x_{\mathrm{M}}| & \text{otherwise} \end{cases} \tag{4.30}$$

and

$$c_{\mathrm{st}} = \begin{cases} 0 & \text{if } |x(t)| \leqslant x_{\mathrm{M}} \\ -c_{\mathrm{s}}\dot{x}(t) & \text{otherwise} \end{cases} \tag{4.31}$$

We have loosely based the values of the end-stops parameters on those reported in [KHS15], that is, we used the same orders of magnitude. We chose $k_{\mathrm{st}} = 1\,\mathrm{MN\,m^{-1}}$ and $c_{\mathrm{st}} = 10\,\mathrm{N\,s\,m^{-1}}$. However, note that all of the simulations done in this section barely show mechanical contact between the mass and the end-stops, except at the mechanical transient process and with the dynamic pull-in phenomenon highlighted below in Sec. 4.3.4.2. Therefore, the influence of the stoppers model in the rest of the study of this chapter can be considered to be negligible.

The electrical side is modeled as a SPICE netlist, that the simulator represents as a $\mathbf{\Psi}$ map describing a set of differential algebraic equations, the $V_{\mathrm{t}}, i_{\mathrm{t}}$ variables making the connection between electrical and mechanical domains. For the diode, we used level 1 exponential model, that is, $i(V_{\mathrm{D}}) = I_{\mathrm{s}}(\exp(V_{\mathrm{D}}/V_{\mathrm{T}}) - 1)$. Our model uses a saturation current value of $I_{\mathrm{s}} = 1\,\mathrm{pA}$. Here, V_{D} denotes the voltage across the diode and $V_{\mathrm{T}} \approx 26\,\mathrm{mV}$ is the thermal voltage. Note in particular that the used diode model is devoid of parasitic capacitance effects or series resistance.

The fixed capacitors were both pre-charged to 5 V. Furthermore, the transducer is electrically disconnected from the circuit for the first 500 ms in order to let any possible mechanical transient behavior end before the beginning of the coupled simulation. Finally, note that we did not add any parasitic capacitance value to the transducer's capacitance.

The parameters used for the device are that of Table 4.1.

4.3.1.2 Simulation results and discussion

The results of the simulation for one input at 160 Hz (the resonator's resonant frequency) and one input at $7/8 \cdot 170 = 148.75\,\mathrm{Hz}$ are presented in Fig. 4.11 and Fig. 4.12, respectively. The frequency factor of 7/8 for the out-of-resonance input is chosen to be the same as between the 140 Hz and the 160 Hz inputs in the experiments above.

The behavior that was described in the discussion on the experiments results in Sec. 4.2.3 is clearly visible here. For the input at the resonant frequency, the amplitude decreases with the voltage increase, resulting in the decrease of the capacitance variation amplitude. At about

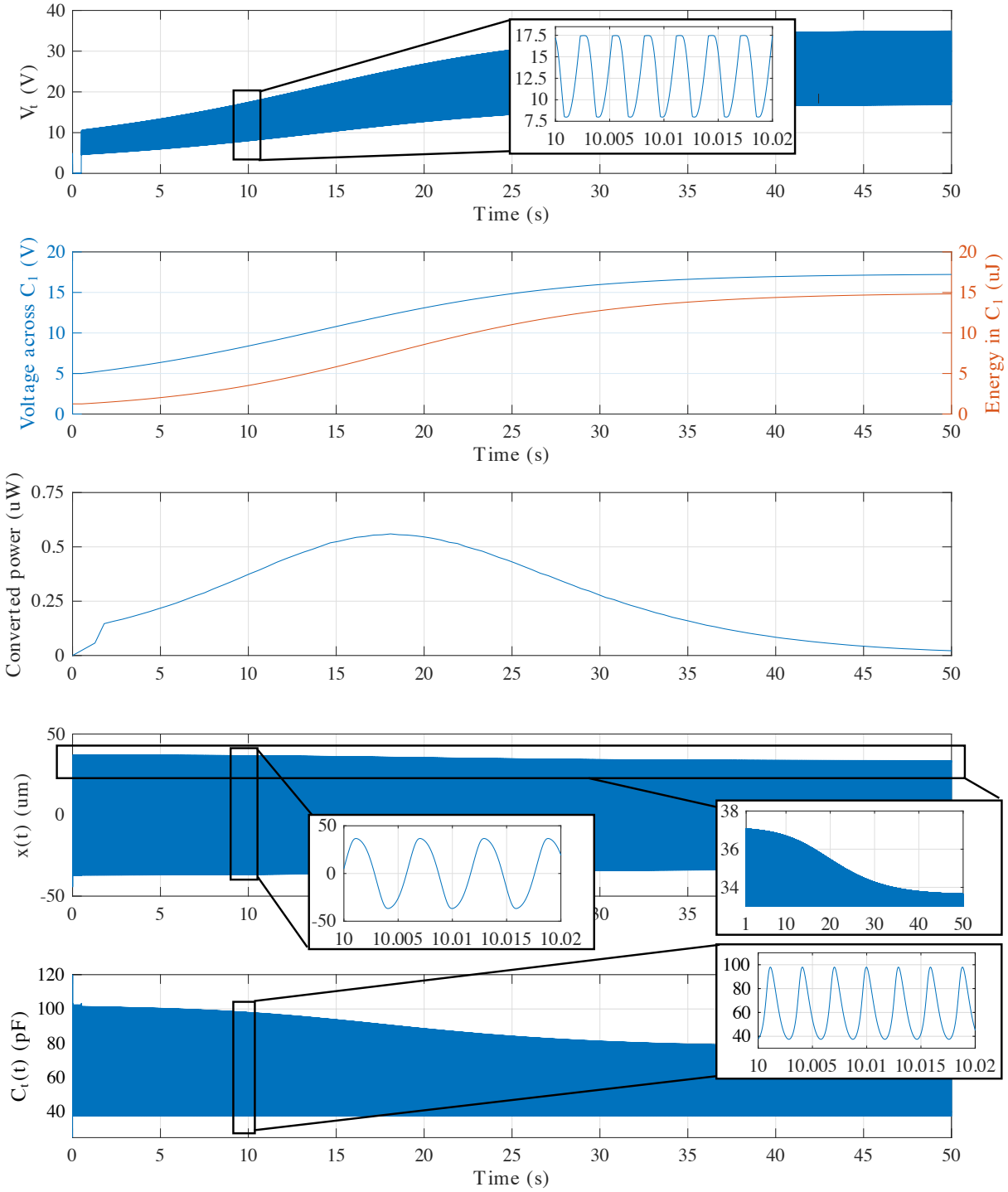

Figure 4.11: Simulation results for an e-VEH connected to the Bennet's doubler. The input is of 1.5 g amplitude, at the device's resonant frequency f_0. The system's parameters are listed in Table. 4.1.

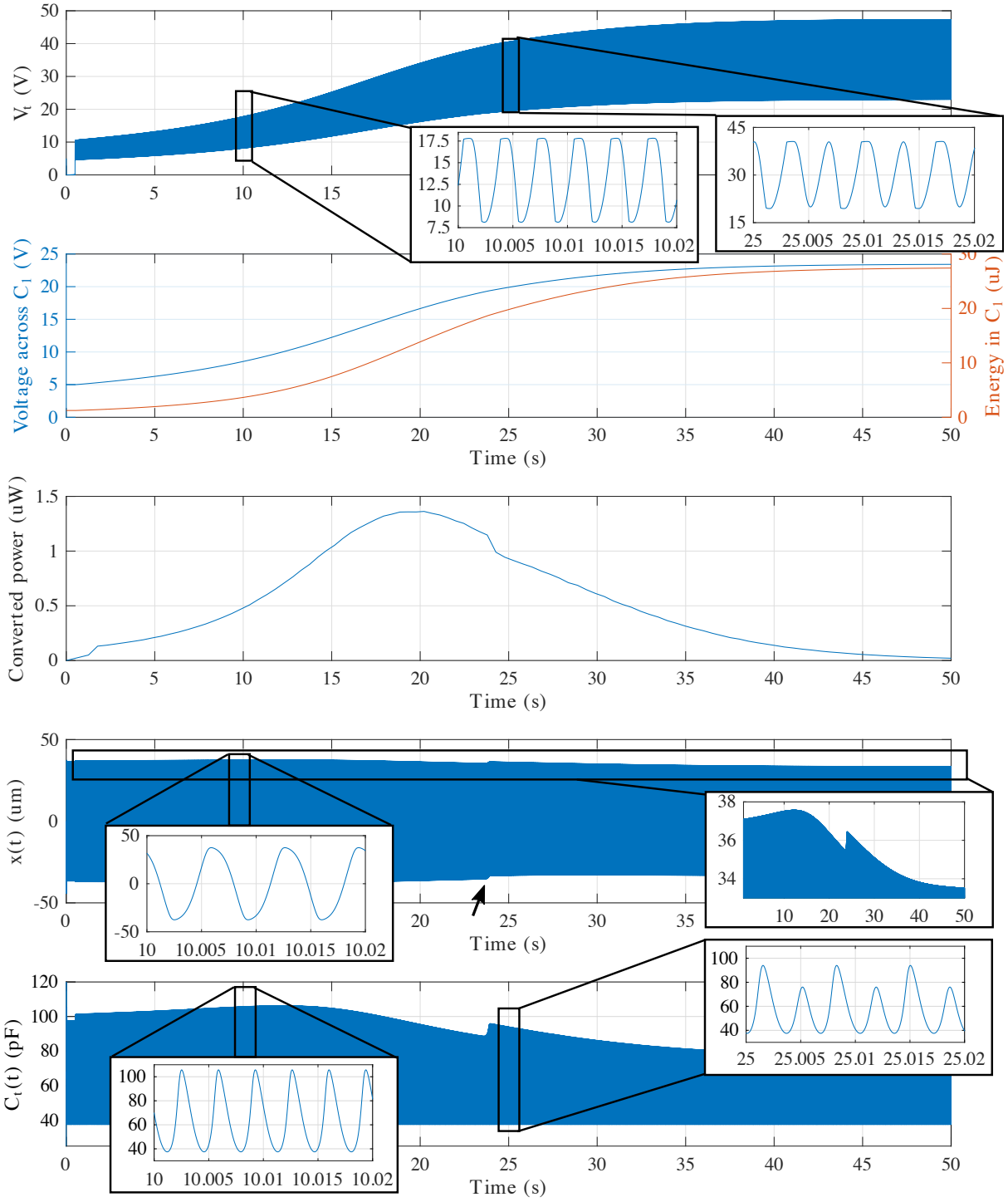

Figure 4.12: Simulation results for an e-VEH connected to the Bennet's doubler. The input is of 1.5 g amplitude, at a frequency of $7/8 \cdot f_0$. The system's parameters are listed in Table. 4.1.

17.5 s, for a voltage V_L of 12.5 V, the converted power reaches a maximum, of 0.6 µW. Note that this is different from the value of the maximum converted power obtained in the corresponding experiment, which was of 1.1 µW. This is due to discrepancies between the modeled transducer and the transducer used in the experiments. After this maximum power point, the converted power asymptotically reaches zero, and V_L evolution from cycle to cycle saturates, while $x(t)$ becomes such that the capacitance variation ratio asymptotically approaches 2. Note that the evolution of V_t shows that the voltage across V_t keeps alternating between V_L and $2V_L$, since the capacitance variation is still slightly superior to 2. But the exchanged charge becomes zero, so that the charge-voltage diagram at saturation would correspond to a degenerated, horizontal line.

For the input at 148.75 Hz, when V_L is still close to 5 V, the capacitance variation amplitude is slightly lower than for the input at the resonant frequency. As the voltage V_L increases, this time the capacitance variation first increases as well. On the magnified portion of the capacitance variation happening at 10 s, one clearly sees that the capacitance variation is higher with the input at 148.75 Hz than with the input at the resonant frequency, although the V_L voltages are approximately the same at this time in both simulations. The voltage keeps increasing, and eventually, the amplitude of capacitance variation starts to decrease. Soon after this point of maximum capacitance is reached, a maximum power point of 1.4 µW is reached, for a V_L voltage of 16.5 V.

Note that for this simulation with input at 148.75 Hz, as the circuit saturates, a qualitative change in the dynamics happens at about 23.5 s (see the black arrow in Fig. 4.12). The average position of the mobile mass switches from being about zero to a positive value. The effect on the capacitance variation is clearly shown on the magnified portion of the capacitance variation at 25 s: at each period of $x(t)$ (we loosely suppose here that $x(t)$ is periodic for a given V_L), C_t reaches its maximum value twice.

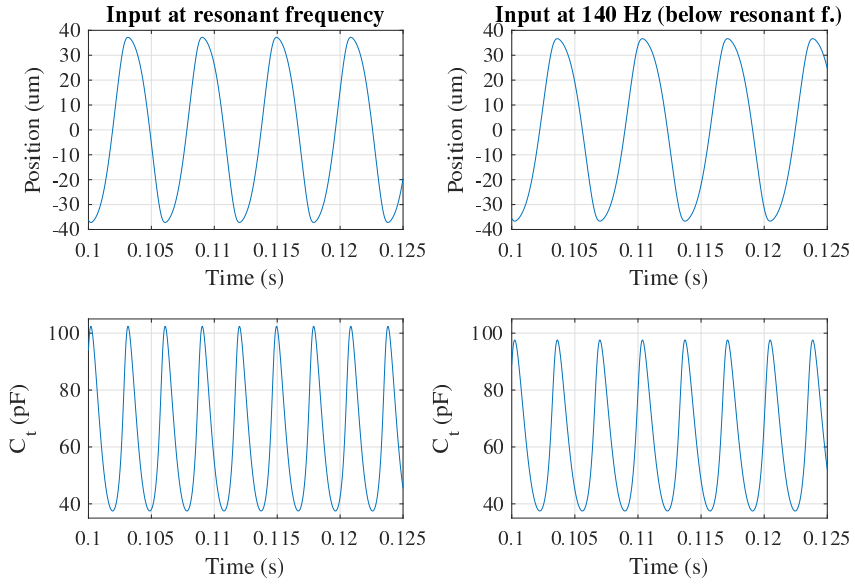

Figure 4.13: Simulations of the sole mechanical structure dynamics, without any electrical conditioning. The figure depicts the position and capacitance variation when the structure is submitted to inputs at the resonant frequency (and 1.5 g amplitude) on the left, and at 148.75 Hz on the right.

The simulation results in Fig. 4.13 show that in the absence of any bias, the excitation at the

resonator's natural frequency gives indeed a (slightly) larger capacitance variation (ratio of 2.73) than for the input at lower frequency (2.58), as expected. The difference in terms of the mass displacement amplitude are almost indistinguishable, but the small difference is magnified by the hyperbolic capacitance-versus-displacement function of the symmetrical gap-closing transducer. The difference in the capacitance variation ratios in the unbiased simulations is not as dramatic as in the experiments above (see Table 4.10), due to parameter value and modeling differences.

Finally, let us mention that each of these simulations, even after a careful choice of the numerical solver parameters, take about 500 s to complete on a relatively powerful computation server. Therefore, it is quite inefficient to rely on such simulations as a mean to explore the parameter space. However, we shall resort to simulations again in the rest of this chapter, in order to validate the results we obtain with the method that we now present.

4.3.2 Description of the method

We now give a general description of the method that is the subject of the remaining of this chapter. We remind that this method is a mean to predict the converted power by an e-VEH using an unstable conditioning circuit in unstable mode, throughout its autonomous operation subsequent to a harmonic input excitation. Let us start by presenting the model of the e-VEH we are studying in this section. Firstly, the input force reads $\xi(t) = \xi_0 \sin(\omega_{ext} t + \phi)$. The generic VEH model is

$$\begin{cases} m\ddot{x} & = -k(x)x - c(x,\dot{x})\dot{x} + \underbrace{\frac{1}{2}V_{\mathrm{t}}^2 \frac{\partial C}{\partial x}(x)}_{u(t)} + \xi_0 \sin(\omega_{\mathrm{ext}} t + \phi) \\ \boldsymbol{\Psi}_\gamma(\dot{\mathbf{V}}, \dot{\mathbf{I}}, \mathbf{V}, \mathbf{I}, \dot{x}, x) & = 0, \end{cases} \tag{4.32}$$

to which we may add the dynamics in the end-stops region when $|x(t)| > x_{\mathrm{M}}$. We will suppose in the following that $|x(t)| \leqslant x_{\mathrm{M}}$, and we set $x_{\mathrm{M}} = d_0$. Here, $\boldsymbol{\Psi}_\gamma$ represents the a set of differential-algebraic equations that govern the evolution the electrical state of the unstable charge-pump conditioning circuit, which we defined in Sec. 2.2. In particular, V_{t} is a component of $\mathbf{V}$. The used unstable charge-pump conditioning circuit is characterized by its γ-ratio, as presented in Sec. 2.2.2.2. Note that compared to (1.13), we have removed the t dependence in $\boldsymbol{\Psi}_\gamma$, reflecting the fact that charge-pump conditioning circuits do not need an external synchronization command with the mechanical state of the e-VEH.

As is, we can barely get any insight from the model in (4.32). The reason is that the generally nonlinear mechanical part is coupled with the nonlinear electrical part, which is represented by the map $\boldsymbol{\Psi}_\gamma$. The resulting model is highly impractical to work with in order to capture the essence of the system's dynamics. We hence have to resort to our understanding of the charge-pump conditioning circuits gained from the electrical domain analysis, where we have considered the circuit in the context of a time-varying capacitor whose value was given as an input of the system. In particular, we know that at the scale of one cycle of the capacitance variation, the unstable charge-pump conditioning circuits operating in unstable mode impose a biasing scheme of the transducer represented by a rectangular charge-voltage diagram characterized by the voltage V_{L} and the ratio γ.

The first step in our analysis of the e-VEH's dynamics is to find a quantitative link be-

tween the e-VEH's mechanical state and the electrostatic force as imposed by a charge-pump conditioning.

4.3.2.1 Steady-state dynamics at fixed V_{L}

Let us hence consider a cycle of the capacitance variation, starting from $C_{\mathrm{t}} = C_{\max}$. For now, we suppose that V_{L} is fixed. We consider here the transducer's capacitance as a function of the displacement $x(t)$, but to describe the energy conversion cycle as we did in the electrical domain, we have to somehow impose $x(t)$. Therefore, let us impose that $x(t)$ is such that, at the beginning of our cycle, (i) C_{t} first strictly monotonically decreases to $C_{\min}$, and then (ii) C_{t} strictly monotonically increases again until it reaches $C_{\max}$. Let us further suppose that $C_{\max}/C_{\min} > \gamma > 1$, and that the cycle takes place in the unstable operation mode of the charge-pump. As a result, for our cycle of interest, the characteristic cycle voltage V_{R} is such that $V_{\mathrm{R}} = \gamma V_{\mathrm{L}}$.

For the part (i), the transducer is first operating at constant charge, and the voltage across it evolves as

$$V_{\mathrm{t}}(t) = \frac{C_{\max} V_{\mathrm{L}}}{C_{\mathrm{t}}(x(t))}, \quad C_{\mathrm{t}}(x(t)) \in [C_1 \,; C_{\max}] \tag{4.33}$$

until, as inferred by the ideal charge-pump approximation, $V_{\mathrm{t}} = \gamma V_{\mathrm{L}}$. This happens for a capacitance value of $C_1 = \gamma^{-1} C_{\max}$. The segment at constant voltage ensures

$$V_{\mathrm{t}}(t) = \gamma V_{\mathrm{L}}, \quad C_{\mathrm{t}}(x(t)) \in [C_{\min} \,; C_1]. \tag{4.34}$$

The part (ii) is similar: the transducer first operates at constant charge, its voltage reads

$$V_{\mathrm{t}}(t) = \frac{\gamma C_{\min} V_{\mathrm{L}}}{C_{\mathrm{t}}(x(t))}, \quad C_{\mathrm{t}}(x(t)) \in [C_{\min} \,; C_2] \tag{4.35}$$

until $V_{\mathrm{t}} = V_{\mathrm{L}}$, which happens for a capacitance of value of $C_2 = \gamma C_{\min}$. The segment at constant voltage ensues;

$$V_{\mathrm{t}}(t) = V_{\mathrm{L}}, \quad C_{\mathrm{t}}(x(t)) \in [C_2 \,; C_{\max}]. \tag{4.36}$$

As a matter of fact, we merely described the ideal charge-pump conditioning at the scale of one cycle of the capacitance variation. This was already done in Sec. 2.1.2. Here we have simply added explicitly the dependence of C_{t} on the position variable, as well as $V_{\mathrm{R}} = \gamma V_{\mathrm{L}}$ for $\gamma > 1$.

We can hence describe the evolution of the transducer force across such a cycle of the capacitance variation. As above, we suppose that the condition $C_{\max}/C_{\min} > \gamma$ is fulfilled. In these conditions, the force evolution throughout the cycle of capacitance variation described above

reads

$$u(t) = \begin{cases} \frac{1}{2}\frac{{V_\mathrm{L}}^2 {C_\mathrm{max}}^2}{{C_\mathrm{t}}^2(x(t))}\frac{\partial C_\mathrm{t}}{\partial x}(x(t)) & \text{if } C_\mathrm{t}(x(t)) \in [C_\mathrm{max}\,;\gamma^{-1}C_\mathrm{min}] \text{ and } \frac{\partial C_\mathrm{t}}{\partial x}(x(t))\dot{x}(t) < 0 \\ \frac{1}{2}\gamma^2 {V_\mathrm{L}}^2\frac{\partial C_\mathrm{t}}{\partial x}(x(t)), & \text{if } C_\mathrm{t}(x(t)) \in [\gamma^{-1}C_\mathrm{max}\,;C_\mathrm{min}] \text{ and } \frac{\partial C_\mathrm{t}}{\partial x}(x(t))\dot{x}(t) < 0 \\ \frac{1}{2}\frac{\gamma^2 {V_\mathrm{L}}^2 {C_\mathrm{min}}^2}{{C_\mathrm{t}}^2(x(t))}\frac{\partial C_\mathrm{t}}{\partial x}(x(t)), & \text{if } C_\mathrm{t}(x(t)) \in [C_\mathrm{min}\,;\gamma C_\mathrm{min}] \text{ and } \frac{\partial C_\mathrm{t}}{\partial x}(x(t))\dot{x}(t) > 0 \\ \frac{1}{2}V_\mathrm{R}^2\frac{\partial C_\mathrm{t}}{\partial x}(x(t)), & \text{if } C_\mathrm{t}(x(t)) \in [\gamma C_\mathrm{min}\,;C_\mathrm{max}] \text{ and } \frac{\partial C_\mathrm{t}}{\partial x}(x(t))\dot{x}(t) > 0 \end{cases} \tag{4.37}$$

where we have highlighted the dependencies on x and t for clarity. The second condition on each line merely translates to the direction of variation of C_t (it is the time derivative of C_t).

For a given charge-pump conditioning scheme (i.e., given γ) and for a particular cycle (i.e., given V_L), the expression of the force (4.37) is convenient because it allows us to decouple the mechanical dynamics from the full dynamics of the electrical circuit. This means that we can reduce (4.32) to merely the first mechanical equation, considering u to be as given in (4.37). This is made possible at the price of an hypothesis on the capacitance variation $C_\mathrm{t}(t)$, through an hypothesis on the system's state variable $x(t)$.

To precise the matter, we start by making the ansatz that the e-VEH submitted to the charge-pump biasing given in terms of γ and V_L, attains a steady-state mode in which the position variable reads

$$x(t) = \overline{x} + x_0\cos(\omega_\mathrm{ext}t) \tag{4.38}$$

where $\overline{x}$ and x_0 are in $[0\,;1]$, and where ω_ext is the normalized frequency of the external forcing. That is to say, (4.38) is the hypothesized form of the steady-state oscillations of the mobile mass for the system (4.32), in which we have replaced the dependence (through V_t) on the electrical dynamics by (4.37).

Here and for the rest of this chapter, the qualifier "steady-state" refers to the oscillations of the inertial mass, i.e., the "mechanical" steady-state, reached by our system (4.58) in which the dependence on the electrical interface $\mathbf{\Psi}_\gamma$ is replaced with the *a priori* knowledge of the transducer force, of the form (4.37). It shall not to be confused with the "electrical" steady-state operation mode of a charge-pump, such that was defined in Sec. 2.2.2. In the context of the present analysis, the unstable charge-pump is implicitly supposed to operate in an unstable steady-state mode, because we supposed that $V_\mathrm{R} = \gamma V_\mathrm{L}$, and because we will assume below that $C_\mathrm{max}/C_\mathrm{min} > \gamma$.

In the following, we will denote by $\tau \coloneqq 2\pi/\omega_\mathrm{ext}$ the period of $x(t)$. Notice that we have reported the information on the phase shift between the input forcing $\xi(t)$ and the displacement $x(t)$ in the ϕ term of the input's phase, so that we further can suppose without loss of generality that $x_0 \geqslant 0$. Our goal now is to link $\overline{x}$ and x_0 to the electrical conditioning of the transducer: that is, to the V_L voltage and the γ ratio of the charge pump.

Let us study the dynamics of the electrostatic force at the scale of one period $[0\,;\tau]$ of $x(t)$ in steady-state operation, in order to particularize (1.6) for our hypothesized displacement of (4.38). In the light of (4.38), as C_t is a function of x, the capacitance-versus-time function is therefore also a periodic function, of period of at most τ. Moreover, as it is continuous, it attains

at least one pair of extrema for each period of $x(t)$. As we may as well do a time-translation, let us suppose without loss of generality that the period $[0\,;\tau]$ of $x(t)$ that we study starts with a maximum of C_t.

Now, in all generality, $C_\mathrm{t}(x)$ may reach any finite number of extrema in a period of $x(t)$. However, let us here restrict ourselves to the three geometries of electrostatic transducers presented in Sec. 1.2.2. We lose very little generality by doing so because the vast majority of inertial e-VEHs are based on these three geometries. For the area-overlap and non-symmetrical gap-closing geometries, C_t reaches one pair on extrema per period $[0\,;\tau]$ of $x(t)$. Hence, a period of $x(t)$ corresponds to one cycle of the capacitance variation given in terms of C_max, C_min, for a unstable charge-pump cycle of ratio γ and voltage V_L. The matter is slightly different for the symmetrical gap-closing geometry, as (1.9) shows that in all generality, C_t can reach one or pairs of extrema per period of $x(t)$ depending on the relative values of $\overline{x}$ and x_0. More precisely, C_t reaches two different local maxima per period of $x(t)$ if $|\overline{x}| < x_0$ and only one otherwise. In both cases, there is only one value of local minima per period of $x(t)$ (but reached twice if $|\overline{x}| < x_0$). In this document we will avoid obnoxious technicalities and suppose that $\overline{x} = 0$ when dealing with the symmetrical gap-closing geometry, as in the example of application below in Sec. 4.3.3. This hypothesis allows us to avoid dealing with the behavior of charge-pumps in the electrical domain for C_t inputs that have successive local maxima and minima of different values. Indeed, we did not characterize the charge-pump dynamics in that setting, as we have always supposed in the previous chapters that C_max and C_min are fixed throughout the charge-pump's autonomous operation.

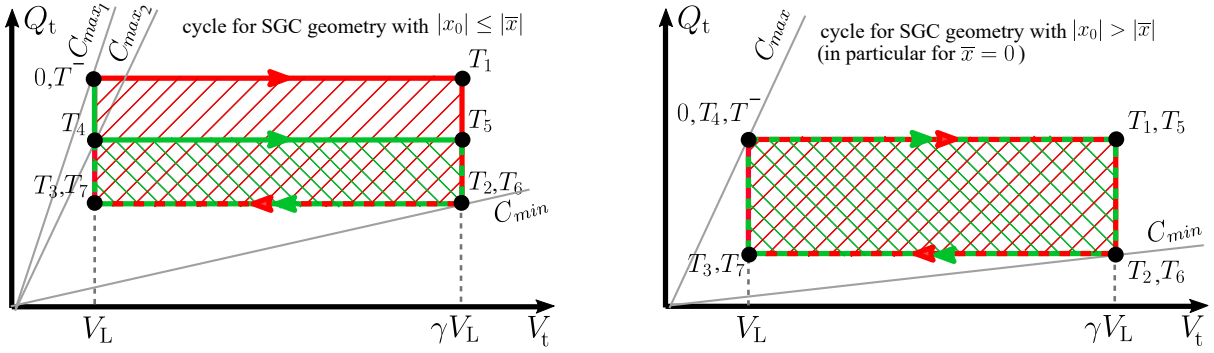

Figure 4.14: The charge-voltage diagram for two consecutive cycles of operation of an unstable charge-pump conditioning circuit that occur in one period of $x(t)$. The diagram on the left presents a situation where the two cycles are different because the C_t exhibits two distinct pairs of extrema in one period of $x(t)$ (but we kept the C_min to be the same). This corresponds to the case of the symmetrical gap-closing geometry where $\overline{x} \geqslant x_0$. The diagram on the right shows the two cycles being superposed, because the two pairs of extrema of C_t are of same values. This corresponds to the case of the symmetrical gap-closing geometry where $\overline{x} < x_0$. This latter case, more precisely $\overline{x} = 0$, is further investigated in Sec. 4.3.3. In all cases, it is supposed that the voltage V_L is the same for the two cycles of capacitance variation. Note that here, we have that $C_{\mathrm{max}1}/C_\mathrm{min} > \gamma$ and $C_{\mathrm{max}2}/C_\mathrm{min} > \gamma$. These twofold conditions suggest that there are additional considerations that arise from a study involving nested cycles like on the left diagram, which is why all our analysis will suppose that the two cycles are alike. We also have $C_\mathrm{max}/C_\mathrm{min} > \gamma$ for the diagram on the right.

Indeed, by supposing $\overline{x} = 0$ in (4.38), the capacitance variation for the symmetrical gap-closing geometry is periodic with period $\tau/2$. Therefore at each period of the capacitance variation, only one pair of capacitance extrema occurs. Furthermore, these two contiguous cycles of variation of C_t happening in one period of $x(t)$ can be supposed to have the same V_L cycle voltage. This is because, the charge-pump theory based on rectangular charge-voltage diagrams implies that C_t is small compared to the circuit's fixed capacitors, so that their voltage

can be supposed to be invariant across a finite number of contiguous cycles. Thus, because V_{L} is a function of the voltages across the fixed capacitors of the circuit, it can therefore also be considered to be invariant during one period of $x(t)$. Charge-voltage diagrams summarizing the evolution of C_{t}'s for a period of $x(t)$ in both cases $|\overline{x}| < x_0$ and $|\overline{x}| \geqslant x_0$ are depicted in Fig. 4.14.

From now on, $C_{\max}$ and $C_{\min}$ will denote the values of the extrema of C_{t} for the capacitance variation steady state. Given the form of $x(t)$ in (4.38), for a given ω_{ext}, then $\overline{x}$ and x_0 are sufficient to unambiguously define $x(t)$. Hence the values of $C_{\max}$ and $C_{\min}$ are completely characterized in terms of $\overline{x}$ and x_0, provided that a capacitance geometry $C_{\mathrm{t}}(x)$ has been specified. Note however that we do not explicitly make the dependence always appear in order to keep notations simple. If we suppose that $C_{\max}/C_{\min} \geqslant \gamma$, then the description of a cycle done at the beginning of the section holds. This hypothesis has to be post-checked once $\overline{x}$ and x_0 are identified. The force $u(t)$ is given for t in one period $[0\,;\tau]$ of $x(t)$ by

$$u(t) = \begin{cases} \dfrac{1}{2}\dfrac{{V_{\mathrm{L}}}^2 {C_{\max i}}^2}{{C_{\mathrm{t}}}^2(x(t))}\dfrac{\partial C_{\mathrm{t}}}{\partial x}(x(t)), & \text{if } t \in [0\,;T_1[, \\ \dfrac{1}{2}\gamma^2 {V_{\mathrm{L}}}^2\dfrac{\partial C_{\mathrm{t}}}{\partial x}(x(t)), & \text{if } t \in [T_1\,;T_2[, \\ \dfrac{1}{2}\dfrac{\gamma^2 {V_{\mathrm{L}}}^2 {C_{\min i}}^2}{{C_{\mathrm{t}}}^2(x(t))}\dfrac{\partial C_{\mathrm{t}}}{\partial x}(x(t)), & \text{if } t \in [T_2\,;T_3[, \\ \dfrac{1}{2}V_{\mathrm{R}}^2\dfrac{\partial C_{\mathrm{t}}}{\partial x}(x(t)) & \text{if } t \in [T_3\,;\tau[. \end{cases} \tag{4.39}$$

for the case of the area-overlap and non-symmetrical gap-closing geometries (note that the consecutive intervals have a common point but the force is continuous). The T_i are given by

$$\begin{aligned} T_1 &= \min\{t \in [0\,;\tau] \quad | \, C(x(t)) = \gamma^{-1} C_{\max}\} \\ T_2 &= \min\{t \in [T_1\,;\tau] \quad | \, C(x(t)) = C_{\min}\}, \\ T_3 &= \min\{t \in [T_2\,;\tau] \quad | \, C(x(t)) = \gamma C_{\min}\}. \end{aligned} \tag{4.40}$$

These times are well-defined because of our hypothesis that $C_{\max}/C_{\min} > \gamma$. For the symmetrical gap-closing geometry with $\overline{x} = 0$, $u(t)$ reads for t in $[0\,;\tau]$:

$$u(t) = \begin{cases} \dfrac{1}{2}\dfrac{{V_{\mathrm{L}}}^2 {C_{\max i}}^2}{{C_{\mathrm{t}}}^2(x(t))}\dfrac{\partial C_{\mathrm{t}}}{\partial x}(x(t)), & \text{if } t \in [0\,;T_1[\cup [T_4\,;T_5[, \\ \dfrac{1}{2}\gamma^2 {V_{\mathrm{L}}}^2\dfrac{\partial C_{\mathrm{t}}}{\partial x}(x(t)), & \text{if } t \in [T_1\,;T_2[\cup [T_5\,;T_6[, \\ \dfrac{1}{2}\dfrac{\gamma^2 {V_{\mathrm{L}}}^2 {C_{\min i}}^2}{{C_{\mathrm{t}}}^2(x(t))}\dfrac{\partial C_{\mathrm{t}}}{\partial x}(x(t)), & \text{if } t \in [T_2\,;T_3[\cup [T_6\,;T_7[, \\ \dfrac{1}{2}V_{\mathrm{R}}^2\dfrac{\partial C_{\mathrm{t}}}{\partial x}(x(t)) & \text{if } t \in [T_3\,;T_4[\cup [T_7\,;\tau[. \end{cases} \tag{4.41}$$

and the T_i are given by

$$\begin{aligned} &T_1 = \min\{t \in [0\,;\tau] \,|\, C(x(t)) = \gamma^{-1} C_{\max}\} \\ &T_2 = \min\{t \in [T_1\,;\tau] \,|\, C(x(t)) = C_{\min}\}, \\ &T_3 = \min\{t \in [T_2\,;\tau] \,|\, C(x(t)) = \gamma C_{\min}\}, \\ &T_4 = \tau/2, \quad T_5 = T_1 + \tau/2, \quad T_6 = T_2 + \tau/2, \quad T_6 = T_3 + \tau/2. \end{aligned} \tag{4.42}$$

Again, all these minima exist because of our hypothesis that $C_{\max}/C_{\min} > \gamma$.

Under the hypothesis (4.38), $u(t)$ in the steady-state of system (4.32) must then be periodic with a period of at most τ, as are all other force terms of (4.32). In particular, they can be approached by the partial sum of their Fourier series. We restrict this approximation to the average and first harmonic of each force. We hence project the first equation of (4.32) on 1, $\sin_1$ and $\cos_1$ and equate the 1, $\cos_1$ and $\sin_1$ coordinate of each terms. Defining, for all periodic f

$$\begin{aligned}
\langle f, 1\rangle &:= \frac{\omega_{\text{ext}}}{2\pi}\int_0^{2\pi/\omega_{\text{ext}}} f(t)\,\mathrm{d}t,\\
\langle f, \cos_1\rangle &:= \frac{\omega_{\text{ext}}}{\pi}\int_0^{2\pi/\omega_{\text{ext}}} f(t)\cos(\omega_{\text{ext}}t)\,\mathrm{d}t,\\
\langle f, \sin_1\rangle &:= \frac{\omega_{\text{ext}}}{\pi}\int_0^{2\pi/\omega_{\text{ext}}} f(t)\sin(\omega_{\text{ext}}t)\,\mathrm{d}t.
\end{aligned} \tag{4.43}$$

this yields the following relations, where $x = \overline{x} + x_0\cos(\omega_{\text{ext}}t)$

$$\begin{cases}
\langle m\ddot{x}, 1\rangle + \langle u, 1\rangle + \langle k(x)x, 1\rangle + \langle c(x,\dot{x})\dot{x}, 1\rangle & = 0,\\
\langle m\ddot{x}, \sin_1\rangle + \langle u, \sin_1\rangle + \langle k(x)x, \sin_1\rangle + \langle c(x,\dot{x})\dot{x}, \sin_1\rangle & = \xi_0\cos\phi,\\
\langle m\ddot{x}, \cos_1\rangle + \langle u, \cos_1\rangle\ + \langle k(x)x, \cos_1\rangle\ + \langle c(x,\dot{x})\dot{x}, \cos_1\rangle & = \xi_0\sin\phi.
\end{cases} \tag{4.44}$$

We also introduce the quantities

$$u_1(\overline{x}, x_0) := \frac{\langle u, 1\rangle}{{V_{\text{L}}}^2}, \quad u_{\text{c}}(\overline{x}, x_0) := \frac{\langle u, \cos_1\rangle}{{V_{\text{L}}}^2}, \quad u_{\text{s}}(\overline{x}, x_0) := \frac{\langle u, \sin_1\rangle}{{V_{\text{L}}}^2}. \tag{4.45}$$

which do not depend on V_{L}, and for which we explicitly make the dependence on $\overline{x}$ and x_0 appear. Let us also introduce the notations

$$\begin{aligned}
&k_1(\overline{x}, x_0) := \langle k(x)x, 1\rangle, && k_{\text{c}}(\overline{x}, x_0) := \langle k(x)x, \cos_1\rangle, && k_{\text{s}}(\overline{x}, x_0) := \langle k(x)x, \sin_1\rangle,\\
&c_1(\overline{x}, x_0) := \langle c(x,\dot{x})\dot{x}, 1\rangle, && c_{\text{c}}(\overline{x}, x_0) := \langle c(x,\dot{x})\dot{x}, \cos_1\rangle, && c_{\text{s}}(\overline{x}, x_0) := \langle c(x,\dot{x})\dot{x}, \sin_1\rangle,\\
&m_1(\overline{x}, x_0) := \langle m\ddot{x}, 1\rangle, && m_{\text{c}}(\overline{x}, x_0) := \langle m\ddot{x}, \cos_1\rangle, && m_{\text{s}}(\overline{x}, x_0) := \langle m\ddot{x}, \sin_1\rangle.
\end{aligned} \tag{4.46}$$

We square and add the two last equations of (4.44) to eliminate the $\cos(\phi)$ and $\sin(\phi)$ terms. In fact, we don't need to solve this system for the phase shift between the input and $x(t)$, as it is not needed for the calculation of any of the forces (however, expressing the phase shift is needed to apply a stability criterion, see Sec. 4.3.4.2). This is because at each cycle of capacitance variation, the charge-pump conditioning circuits are only sensitive to the value of $C_{\max}$ and $C_{\min}$. We hence find an implicit relation linking the steady state oscillation amplitude x_0 and average $\overline{x}$ to the cycle's V_{L} voltage. By defining $\mathbf{\Phi} = (\Phi_1, \Phi_2)^{\text{T}}$;

$$\Phi_1(V_{\text{L}}, \overline{x}, x_0) := {V_{\text{L}}}^2 u_1 + k_1 + c_1 + m_1, \tag{4.47}$$

and

$$\begin{aligned}
\Phi_2(V_{\text{L}}, \overline{x}, x_0) :=& {V_{\text{L}}}^4({u_{\text{c}}}^2 + {u_{\text{s}}}^2) +\\
&+2{V_{\text{L}}}^2(u_{\text{c}}(k_{\text{c}} + c_{\text{c}} + m_{\text{c}}) + u_{\text{s}}(k_{\text{s}} + c_{\text{s}} + m_{\text{s}}))\\
&+ (k_{\text{c}} + c_{\text{c}} + m_{\text{c}})^2 + (k_{\text{s}} + c_{\text{s}} + m_{\text{s}})^2 - {\xi_0}^2
\end{aligned} \tag{4.48}$$

we obtain that

$$\mathbf{\Phi}(V_{\mathrm{L}}, \overline{x}, x_0) = (0\,,\,0)^{\mathrm{T}} \tag{4.49}$$

is a necessary condition that must be verified by the steady-state oscillation characteristics $\overline{x}$, x_0, for given V_{L}. The usefulness of the method is essentially enclosed in this relation: the initial ODE problem has been translated to a mere algebraic problem. The only solutions (V_{L}, x_0, x) that make physical sense are those such that the two following hypotheses are satisfied:

$$C_{\max}(\overline{x}, x_0)/C_{\min}(\overline{x}, x_0) > \gamma \tag{4.50}$$

because this hypothesis was used in the characterization of the transducer force (4.39), and

$$|\overline{x}| + x_0 \leqslant d_0 \tag{4.51}$$

because otherwise the mass position becomes larger than the transducer gap (as we have supposed in our model that the displacement limits are situated at d_0).

In summary, we have built an implicit relation linking the mass oscillation amplitude x_0 and average $\overline{x}$ to the electrostatic force arising from the charge-pump biasing, with characteristic voltages V_{L} and $V_{\mathrm{R}} = \gamma V_{\mathrm{R}}$ where γ is a parameter set by the unstable charge-pump that is considered. It is possible that (4.49) yields multiples values of x_0 for a given V_{L}. In this situation, only one of these oscillation amplitudes will be observed in practice. Which one depends on the stability properties of the solutions corresponding to each amplitude. This will be witnessed in the results of Sec. 4.3.3.3, and further discussed in Sec. 4.3.4.2. Until then, let us suppose that (4.49) uniquely defines an average $\overline{x}(V_{\mathrm{L}})$ and an amplitude $x_0(V_{\mathrm{L}})$ corresponding to the charge-pump cycle $(V_{\mathrm{L}}, \gamma V_{\mathrm{L}})$ biasing the transducer, and fulfilling the conditions (4.50) and (4.51).

The converted power is the energy converted in one period of $x(t)$ times $\omega_{\mathrm{ext}}/(2\pi)$. In the case that we have one pair of extrema of C_{t} per period of $x(t)$ (area-overlap, gap-closing, symmetrical gap-closing with $|\overline{x} \geqslant x_0|$, the (dimensionalized) converted power reads

$$P = \frac{\omega_{\mathrm{ext}}}{2\pi} {V_{\mathrm{L}}}^2 (\gamma - 1)(C_{\max}(\overline{x}(V_{\mathrm{L}}), x_0(V_{\mathrm{L}})) - \gamma C_{\min}(\overline{x}(V_{\mathrm{L}}), x_0(V_{\mathrm{L}}))) \tag{4.52}$$

In the case of symmetrical gap-closing geometry with $|\overline{x}| < x_0$ (and in particular, $\overline{x} = 0$), this figure has simply to be multiplied by two. This is because there are two identical periods of variation of C_{t} per period of $x(t)$, each cycle of variation of C_{t} having one pair of extrema and being characterized by supposedly unchanged V_{L}. Hence in this case:

$$P = \frac{\omega_{\mathrm{ext}}}{\pi} {V_{\mathrm{L}}}^2 (\gamma - 1)(C_{\max}(\overline{x}(V_{\mathrm{L}}), x_0(V_{\mathrm{L}})) - \gamma C_{\min}(\overline{x}(V_{\mathrm{L}}), x_0(V_{\mathrm{L}}))) \tag{4.53}$$

4.3.2.2 V_{L} evolution and the quasi-static hypothesis

What we merely did up to this point is to characterize the average and first harmonic components of the steady-state oscillations of the inertial mass when the electrical conditioning follows a fixed charge-pump conditioning scheme $(V_{\mathrm{L}}, \gamma V_{\mathrm{L}})$. To do so, we have eluded the full electrical dynamics of our unstable charge-pump conditioning circuit, which are described by $\mathbf{\Psi}_\gamma$ in (4.32).

However, we know that the energy accumulation property of charge-pumps implies an evolution of the cycle's voltages V_{L} and $V_{\mathrm{R}} = \gamma V_{\mathrm{L}}$ throughout C_{t}'s cycles of variation. Our description of the e-VEH's dynamics for V_{L} cannot by definition account for this long-term evolution of the e-VEH's electrical state. Yet, we can use our derivation of the electromechanical dynamics done at fixed V_{L} in order to describe V_{L}'s evolution. To do so, we have to resort to two additional hypotheses.

The first hypothesis we make is that the increase of V_{L} subsequent to the e-VEH's dynamics submitted to the input is a quasi-static process. More precisely, we suppose that the evolution of V_{L} from cycle-to-cycle does not induce mechanical transient behavior. This hypothesis holds because, roughly speaking, the mechanical transient processes subsequent to the change of value of V_{L} are very brief compared to rate of increase of V_{L} over the cycles of C_{t}'s variation. This hypothesis tends to be verified with charge-pump conditioning circuits as we presented them. This is because the values of the fixed capacitors are supposed to be large compared to C_{t}, an assumption that is implicit in this analysis, as the charge-pumps are characterized in terms of their γ ratio. We also used this assumption above when we supposed that multiple variation cycles of C_{t} happening in one period of $x(t)$ have the same characteristic V_{L} voltage.

We also make the hypothesis that the system has no memory. In other words, the steady-state mass oscillation for given V_{L} does not depend on how the e-VEH has arrived to the corresponding electrical state that maps to this V_{L}. This argument is supported by the experimental results in depicted Fig. 4.15, obtained with the same device and same experimental conditions as in Sec. 4.2. These experiments show the superposition of voltage evolution across C_1 of the Bennet's doubler, for different pre-charge voltages. The charge-pump's evolution from a given voltage is unchanged whether this voltage was reached by direct pre-charge or by autonomous charge-pump evolution.

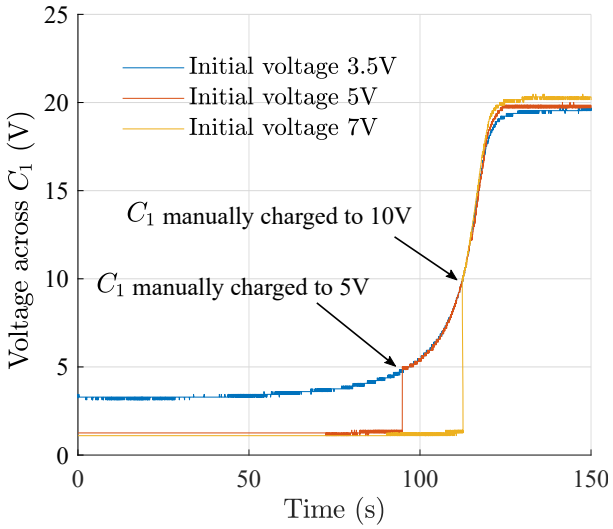

Figure 4.15: Results of some experiments with the same setup as in Sec. 4.2, with different initial voltages across the Bennet's doubler capacitors. The dynamics of the system in the long time scale are independent of the value of the pre-charge.

By applying these working hypotheses, we can construct the evolution of the converted power throughout the charge-pump's evolution, subsequent to the e-VEH being submitted to the harmonic input force. To do so, it suffices to solve (4.49) for a range of values of positive V_{L}, $[V_{\mathrm{Ls}}\,; V_{\mathrm{Le}}]$. For any given V_{L0} in this interval such that $x_0(V_{\mathrm{L0}})$ and $\overline{x}(V_{\mathrm{L0}})$ fulfill the

conditions (4.50) and (4.51), the charge-pump will necessarily evolve through all V_{L} such that $V_{\mathrm{L}0} < V_{\mathrm{L}} < V_{\mathrm{L}1}$. Here, $V_{\mathrm{L}1}$ denotes the smallest $V_{\mathrm{L}} > V_{\mathrm{L}0}$ such that (4.50) and (4.51) are not verified. In fact, $V_{\mathrm{L}1}$ corresponds to the C_{t} variation cycle at which the unstable charge-pump saturates, that is, $C_{\max}(\overline{x}(V_{\mathrm{L}1}), x_0(V_{\mathrm{L}1}))/C_{\min}(\overline{x}(V_{\mathrm{L}1}), x_0(V_{\mathrm{L}1})) = \gamma$.

This evolution of V_{L} across the cycles is monotonic, as we infer from the electrical analysis of unstable charge-pumps. Also, the electrical analysis of unstable charge-pumps indicates that, for all V_{L} in the interval $]V_{\mathrm{L}1}\,;V_{\mathrm{L}2}[$, the successive biasing cycles of C_{t} are all characterized by $(V_{\mathrm{L}}, V_{\mathrm{R}} = \gamma V_{\mathrm{L}})$. The quasi-static hypothesis ensures that for each $V_{\mathrm{L}} \in [V_{\mathrm{L}0}\,;V_{\mathrm{L}1}]$, the values of $\overline{x}(V_{\mathrm{L}}), x_0(V_{\mathrm{L}})$ obtained from solving (4.49) effectively correspond to that that are observed when this value of V_{L} is reached subsequently to the charge-pump's autonomous evolution.

In summary, the interval $]V_{\mathrm{L}0}\,;V_{\mathrm{L}1}[$ can be interpreted as a re-parametrization of time, because V_{L} can be supposed to vary continuously if the fixed capacitors of the circuit are large enough. Any value of V_{L} in this interval will necessarily be attained for a sufficiently long operation time of the e-VEH submitted to the harmonic input. The mass oscillation characteristics for this V_{L} are obtained by solving (4.49) for x_0 and $\overline{x}$ at this V_{L}. From this, the converted power throughout the e-VEH's operation that describes the interval $]V_{\mathrm{L}0}\,;V_{\mathrm{L}1}[$ can readily be computed from (4.52) or (4.53) depending on the transducer's geometry (symmetrical gap-closing or not).

4.3.3 Example of application to a symmetrical gap-closing configuration

Let us apply the foregoing method to the case of an e-VEH based on a transducer of symmetrical gap-closing geometry. The parameters of the device that we study in this section are given in Table 4.1. The mechanical subsystem, namely the model of the spring and of the damping, follow that of Sec. 4.3.1.

Recall the capacitance versus mass displacement function for the symmetrical gap-closing geometry, where we define $C_0 := 2\varepsilon_0 S/d_0$, and we substitute for normalization: $x \leftarrow x/d_0$:

$$C(x) = \frac{C_0}{1 - x^2}. \tag{4.54}$$

As stated above in Sec. 4.3.2, we make here the hypothesis that $\overline{x} = 0$ for all V_{L}, which greatly simplifies the forthcoming computations. With

$$x(t) = x_0 \cos(\omega_{\mathrm{ext}} t), \tag{4.55}$$

the symmetrical gap-closing capacitance $C_{\mathrm{t}}(t)$ has then a period of $\tau/2$. Also, now that we have particularized a $C_{\mathrm{t}}(x)$ function, we additionally require that $x_0 < 1$ (i.e., $x_{\mathrm{M}} = d_0$ in the presentation of Sec. 4.3.2). The maximum capacitance is reached at each period of $x(t)$ when $x(t) = \pm x_0$ and reads

$$C_{\max} = \frac{C_0}{1 - {x_0}^2} \tag{4.56}$$

and the minimum capacitance is independent of the oscillation amplitude x_0, as it is reached at $x(t) = 0$. It reads

$$C_{\min} = C_0. \tag{4.57}$$

Of course, we can immediately see on the simulations results of Fig. 4.12 that this hypothesis

will prevent our method from predicting the average position shift that is depicted there. Yet, in this particular case, the position shift happens after the maximum converted power point, so our method would in principle not fail to predict its value.

Particularizing our model for the linear spring and nonlinear damping function we specified in Sec. 4.3.1, and by normalizing the mechanical part of our model equation as is customary in the study of dynamical systems arising from mechanics oscillators, the model becomes:

$$\begin{cases} \ddot{x} + x + \dfrac{\dot{x}}{Q}\left(1 - \alpha + \dfrac{\alpha}{2}\left(\dfrac{1}{(1-x)^3} + \dfrac{1}{(1+x)^3}\right)\right) & = \dfrac{1}{2}{V_\mathrm{t}}^2 \dfrac{\partial \mathcal{C}}{\partial x}(x) + \xi_0 \sin(\omega_\mathrm{ext} t + \phi) \\ \boldsymbol{\Psi}_\gamma(\dot{\mathbf{V}}, \dot{\mathbf{I}}, \mathbf{V}, \mathbf{I}, \dot{x}, x) & = 0 \end{cases} \tag{4.58}$$

where ω_0 is the resonator's natural frequency

$$\omega_0 = \sqrt{k/m}. \tag{4.59}$$

In particular, V_t is a component of $\mathbf{V}$. and where the quality factor Q is expressed as:

$$Q = \frac{k}{B\omega_0} \tag{4.60}$$

The system (4.58) is obtained by substituting $t \leftarrow t\omega_0$, $\xi_0 \leftarrow \xi_0/(kd_0)$, $u(t) \leftarrow u(t)/(kd_0)$, $\omega_\mathrm{ext} \leftarrow \omega_\mathrm{ext}/\omega_0$. The overdot now denotes differentiation with respect to the new time. We have also defined $\mathcal{C}(x) \coloneqq C(x)/(k{d_0}^2)$. The position variable was already substituted in the beginning of the subsection, and the $\partial/\partial x$ operator denotes differentiation with respect to this new position variable. Note that the results of the simulations presented in this section will be given as dimensionalized variables. This is also the case for figures of converted power obtained by the application of our method.

4.3.3.1 Expressions

As presented in the general description of Sec. 4.3.2, we start by using our ansatz (4.55) to get rid of the dependence on the electrical dynamics. We first express the force for the considered geometry, in one period of $x(t)$ given as in 4.55. The adimensionalized force reads

$$u(t) = \frac{1}{2}{V_\mathrm{t}}^2(t) \frac{\partial \mathcal{C}}{\partial x}(x(t)) \tag{4.61}$$

where $\mathcal{C}_0 \coloneqq \mathcal{C}(0)$. The expression force in (4.41) can be further particularized for symmetrical gap-closing transducers in one period $[0\,;\tau]$ of $x(t)$ in the steady-state regime. By replacing $V_\mathrm{t}(t)$ with $V_\mathrm{L} C_\mathrm{max}/C_\mathrm{t}(t)$ (C_t from maximum to minimum) or with $\gamma V_\mathrm{L} C_\mathrm{min}/C_\mathrm{t}(t)$ (C_t from minimum to maximum), one easily derives that

$$u(t) = \begin{cases} \mathcal{C}_0 {V_\mathrm{L}}^2 \dfrac{x_0}{1 - {x_0}^2} x(t) & \text{if } t \in [0\,;T_1] \cup [T_4\,;T_5], \\ \mathcal{C}_0 \gamma^2 {V_\mathrm{L}}^2 \dfrac{x(t)}{(1 - x^2(t))^2} & \text{if } t \in [T_1\,;T_2] \cup [T_5\,;T_6], \\ \mathcal{C}_0 \gamma^2 {V_\mathrm{L}}^2 x(t) & \text{if } t \in [T_2\,;T_3] \cup [T_6\,;T_7], \\ \mathcal{C}_0 {V_\mathrm{L}}^2 \dfrac{x(t)}{(1 - x^2(t))^2} & \text{if } t \in [T_3\,;T_4] \cup [T_7\,;\tau]. \end{cases} \tag{4.62}$$

where the times T_i are found following (4.42) and read

$$T_1 = {\omega_{\text{ext}}}^{-1} \arccos({x_0}^{-1}\sqrt{1-\gamma(1-{x_0}^2)}) \tag{4.63}$$
$$T_2 = {\omega_{\text{ext}}}^{-1}\pi/2 \tag{4.64}$$
$$T_4 = {\omega_{\text{ext}}}^{-1} \arccos(-{x_0}^{-1}\sqrt{1-\gamma^{-1}}) \tag{4.65}$$
$$T_4 = {\omega_{\text{ext}}}^{-1}\pi \tag{4.66}$$

and T_5, T_6, T_7 are obtained by adding π/ω_{ext} to T_1, T_2, T_3, respectively. The T_i are well defined provided that $1/(1-{x_0}^2) > \gamma$, or equivalently, $C_{\max}/C_{\min} > \gamma$, an hypothesis that we suppose fulfilled for now.

We next compute the relevant Fourier coefficients of the force. Thanks to the symmetry of the capacitance variation between the two half-periods $[0\,;\tau/2]$ and $[\tau/2\,;\tau]$, we get:

$$\langle u, \sin_1\rangle = 2\mathcal{C}_0 {V_{\text{L}}}^2 \frac{\omega_{\text{ext}}}{\pi}\left(\frac{1}{(1-{x_0}^2)^2}\int_0^{T_1} x(t)\sin(\omega_{\text{ext}}t)\,\mathrm{d}t + \gamma^2\int_{T_1}^{T_2}\frac{x(t)}{(1-x^2(t))^2}\sin(\omega_{\text{ext}}t)\,\mathrm{d}t + \right.$$
$$\left. +\gamma^2\int_{T_2}^{T_3} x(t)\sin(\omega_{\text{ext}}t)\,\mathrm{d}t + \int_{T_3}^{T_4}\frac{x(t)}{(1-x^2(t))^2}\sin(\omega_{\text{ext}}t)\,\mathrm{d}t\right) \tag{4.67}$$

$$\langle u, \cos_1\rangle = 2\mathcal{C}_0 {V_{\text{L}}}^2 \frac{\omega_{\text{ext}}}{\pi}\left(\frac{1}{(1-{x_0}^2)^2}\int_0^{T_1} x(t)\cos(\omega_{\text{ext}}t)\,\mathrm{d}t + {V_{\text{L}}}^2\gamma^2\int_{T_1}^{T_2}\frac{x(t)}{(1-x^2(t))^2}\cos(\omega_{\text{ext}}t)\,\mathrm{d}t + \right.$$
$$\left. +\gamma^2\int_{T_2}^{T_3} x(t)\cos(\omega_{\text{ext}}t)\,\mathrm{d}t + \int_{T_3}^{T_4}\frac{x(t)}{(1-x^2(t))^2}\cos(\omega_{\text{ext}}t)\,\mathrm{d}t\right) \tag{4.68}$$

All of these integrals can be readily put into closed-form, being rational functions of trigonometric functions. For the sake of completeness, we give here the expressions of the various Fourier coefficients as well as the final expression of Φ. The projection of u on $\sin_1$ has a relatively simple closed-form expression

$$\langle u, \sin_1\rangle = \mathcal{C}_0 {V_{\text{L}}}^2 \frac{2}{\pi}\frac{(\gamma-1)(1-\gamma(1-{x_0}^2))}{x_0(1-{x_0}^2)} \tag{4.69}$$

but the closed-form expression of the $\cos_1$ component of u is rather obnoxious. Nevertheless, one can show that is has a simple asymptotic behavior

$$\langle u, \cos_1\rangle \underset{x_0\to 1}{\sim} \mathcal{C}_0 {V_{\text{L}}}^2\sqrt{\gamma}\frac{x_0}{(1-{x_0}^2)^{3/2}}. \tag{4.70}$$

We also easily compute

$$\begin{aligned}
&\langle \ddot{x}, \sin_1\rangle = 0 = \langle x, \sin_1\rangle = \langle \frac{\dot{x}}{Q}\left(1-\alpha+\frac{\alpha}{2}\left(\frac{1}{1-x^3}+\frac{1}{1+x^3}\right)\right), \cos_1\rangle,\\
&\langle x, \cos_1\rangle = x_0,\\
&\langle \ddot{x}, \cos_1\rangle = -{\omega_{\text{ext}}}^2 x_0,\\
&\langle \frac{\dot{x}}{Q}\left(1-\alpha+\frac{\alpha}{2}\left(\frac{1}{1-x^3}+\frac{1}{1+x^3}\right)\right), \sin_1\rangle = \frac{\omega_{\text{ext}} x_0}{Q}\left(1-\alpha+\frac{\alpha}{(1-{x_0}^2)^{3/2}}\right)
\end{aligned} \tag{4.71}$$

so that we gave the projections of all terms appearing in (4.58). The system resulting from

coordinate identification reads

$$\begin{cases} \theta_1(x_0,\phi) \coloneqq x_0\left(1-{\omega_{\text{ext}}}^2-\mathcal{C}_0{V_{\text{L}}}^2\sqrt{\gamma}\dfrac{1}{(1-{x_0}^2)^{3/2}}\right)-\xi_0\sin(\phi) & =0 \\ \theta_2(x_0,\phi) \coloneqq x_0\left(\dfrac{\omega_{\text{ext}}}{Q}\left(1-\alpha+\dfrac{\alpha}{(1-{x_0}^2)^{3/2}}\right)-\mathcal{C}_0{V_{\text{L}}}^2\dfrac{2}{\pi}\dfrac{(\gamma-1)(1-\gamma(1-{x_0}^2))}{{x_0}^2(1-{x_0}^2)}\right)-\xi_0\cos(\phi) & =0 \end{cases} \tag{4.72}$$

Note that we have defined two new functions θ_1 and θ_2 that will be useful for stability assessment in Sec. 4.3.4.2. Squaring and adding yields *in fine* for Φ, which is scalar because we have no average component:

$$\begin{aligned} \Phi(V_{\text{L}},x_0) = {x_0}^2\Bigg(&{V_{\text{L}}}^4{\mathcal{C}_0}^2\left(\frac{4}{\pi^2}\frac{(\gamma-1)^2(1-\gamma(1-{x_0}^2))^2}{{x_0}^4(1-{x_0}^2)^2}+\frac{\gamma}{(1-{x_0}^2)^3}\right)+ \\ +2{V_{\text{L}}}^2\mathcal{C}_0\Bigg(&(1-{\omega_{\text{ext}}}^2)\frac{\sqrt{\gamma}}{(1-{x_0}^2)^{3/2}}-\frac{2}{\pi}\frac{\omega_{\text{ext}}}{Q}\left(1-\alpha+\frac{\alpha}{(1-{x_0}^2)^{3/2}}\right)\frac{(\gamma-1)(1-\gamma(1-{x_0}^2))}{{x_0}^2(1-{x_0}^2)} \\ &+\left((1-{\omega_{\text{ext}}}^2)^2+\frac{{\omega_{\text{ext}}}^2}{Q^2}\left(1-\alpha+\frac{\alpha}{(1-{x_0}^2)^{3/2}}\right)^2\right)\Bigg)-{\xi_0}^2 \end{aligned} \tag{4.73}$$

The dimensionalized converted power is obtained from (4.53) that we further particularize for our case of symmetrical gap-closing geometry:

$$P=\frac{\omega_{\text{ext}}\omega_0}{\pi}C_0{V_{\text{L}}}^2(\gamma-1)\left(\frac{1}{1-{x_0}^2}-\gamma\right). \tag{4.74}$$

We can now proceed to solve (4.73) for ranges of V_{L} of interest and $x_0\in\left]\sqrt{1-1/\gamma}\,;1\right[$. For each admissible couple (V_{L},x_0), the converted power is readily determined by (4.53). As stated in the general presentation of the method, the results are given in terms of the evolution of the amplitude and of the converted power throughout the evolution of V_{L} subsequent to the e-VEH's evolution under harmonic input.

4.3.3.2 First application and validation of the method

The fact that we used several approximating hypotheses to build our semi-analytical tool requires a validation of the method. To do so, we resort to the comparison against some results of electromechanical simulations, for the symmetrical gap-closing geometry. We remind that the device model is parametrized as in Table. 4.1, and that the stiffness, damping and end-stop functions are modeled as in Sec. 4.3.1.1.

The results of both the application of the method and of the simulations, in terms of converted power, are depicted in Fig. 4.16. Starting from any V_{L} such that (4.73) has a solution fulfilling (4.50) and (4.51) – which reduces here to the condition that the solution x_0 belongs to $\left]\sqrt{1-1/\gamma}\,;1\right[$ because $\overline{x}=0$ – the evolution of the converted power throughout the e-VEH's electrical state evolution subsequent to the external input is found by following the solution curve in increasing voltages. In particular, the maximum power point is of particular interest and is simply found as the peak of each curve. This is the power point that an asynchronous energy extracting interface would have to sustain in practice.

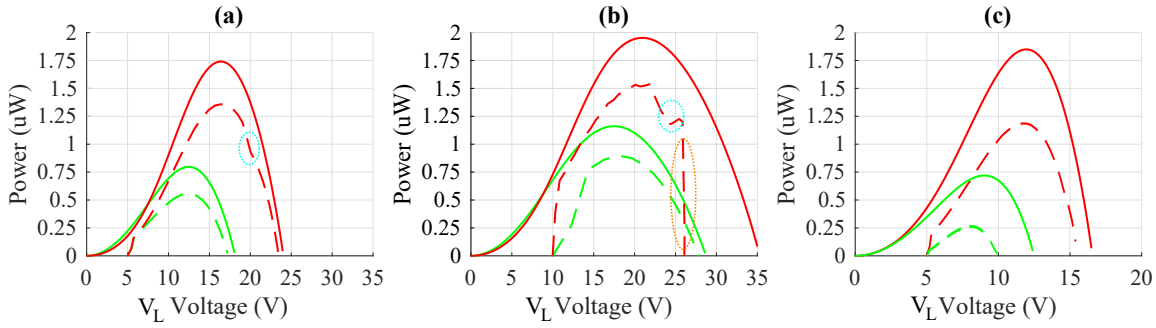

Figure 4.16: Results of application of our method that show the evolution of the converted power versus the evolving V_{L} voltage, for three circuits and the corresponding value of γ used in the method (a) The Bennet's doubler ($\gamma = 2$), (b) Lefeuvre's circuit with $N = 2$ ($\gamma = 3/2$), (c) Series-parallel charge-pump with $N = 3$ ($\gamma = 3$) For each case, the results are given for two different input excitations: (a) 1.5 g at 140 Hz ($\omega_{\mathrm{ext}} = 0.875$) in red, 1.5 g at 160 Hz ($\omega_{\mathrm{ext}} = 1$) in green. (b) 1.5 g at 140 Hz ($\omega_{\mathrm{ext}} = 0.875$) in red, 1.5 g at 160 Hz ($\omega_{\mathrm{ext}} = 1$) in green. (c) 3 g at 140 Hz ($\omega_{\mathrm{ext}} = 0.875$) in red, 3 g at 160 Hz ($\omega_{\mathrm{ext}} = 1$) in green.
The dashed curve represent the results extracted from simulations whereas the plain curves results are provided by the application of the method presented in this section. Note that the values of the input amplitudes ξ_0 are given dimensionalized.

Note that the curves obtained in simulation start from the value of V_{L} that corresponds to the initial charging of the circuit's capacitors. For the Bennet's doubler (a) and the series-parallel charge-pump (c), V_{L} is the voltage across the circuit's capacitor with the highest voltage (in fact, across any of the capacitors for the Bennet's doubler). For Lefeuvre's charge-pump (b) with $N = 2$, V_{L} is twice the voltage across the highest-voltage capacitor, so that V_{L}'s evolution starts at 10 V with this circuit.

The first remark that one can make from these results is that there is a relatively significant discrepancy between the predicted values of converted power and the values obtained by simulation. The discrepancy can be mainly attributed to three reasons, that we list here in increasing order of importance.

- The diodes are the source of losses, even though we modeled them with the simple exponential model. These losses are due to the subsequent forward voltage drop, that dissipates a power of qV_{T} for each amount of charge q that passes through the diode. In our case, we computed the converted power from the energies added to the fixed capacitors at each cycle of the capacitance variation. Thus, the figures of converted power obtained in simulations are decreased by the amount lost in the diodes, compared to the power effectively converted from the mechanical to the electrical domains. In our simulations, V_{T} is about 0.6 V. We have estimated that the losses in the diodes account for up to 15% of the energy converted by the transducer. Our method does not account for these losses.

- The γ ratio implemented by each circuit in simulation is not exactly of the value that is predicted by the charge-pump theory and used for the application of the method (we used $\gamma = 3/2$ for Lefeuvre's circuit with $N = 2$, $\gamma = 2$ with the Bennet's doubler, $\gamma = 3$ with the series-parallel charge-pump with $N = 3$). This is because the diodes forward voltage drop have a slight influence on the value of the γ ratio until higher transducer bias values are reached. This is true at least for the Bennet's and series-parallel charge-pump as we discussed in last chapter's Sec. 3.4.1. But this slight modification of γ, especially when coupled to the point above and the point below, adds to the inaccuracy.

- The most important source of inaccuracy is the error in the amplitude of the capacitance

variation. We remind that we compute the converted power at each value of V_{L} by injecting the displacement corresponding oscillation amplitude x_0 found through (4.73), in (4.53). The hyperbolic symmetrical gap-closing capacitance variation is very sensitive to variations in the computed mass oscillation amplitude x_0, which in turn is predicted with a slight inaccuracy using our method. The cause of this inaccuracy is that our hypothesis of harmonic displacement (4.55), and hence of harmonic force (the 1^{st} harmonic approximation) is a generally valid assumption as long as the system shows a narrow bandwidth in the input and outputs of interest (see, e.g., [Van68]). However, our choice of the nonlinear damping greatly mitigates the validity of this hypothesis. We remind that we have used the model of squeeze-film damping presented in Sec. 4.3.1, with a choice of $\alpha = 1$. We have plotted the frequency response of an otherwise linear resonator that uses this model of the nonlinear damping in Fig. 4.17. This figure shows that the requirement of high frequency selectivity is quite obviously not met in our case. This explains why the results in (c) are so much apart compared to the curves in (a) and (b): the input is larger than in these cases, which results in a dramatic decrease in the resonator's frequency selectivity, according to Fig. 4.16.

Other than using another model of the damping (which could nonetheless be physically accurate, for example for vacuum-packaged devices), one could think that a workaround to this last point would simply be to increase the number harmonics of the dynamical variables that we take into account. This is the generalized harmonic balance method, that in some cases allows to analytically derive the response of forced nonlinear oscillators in exact form [Lev60]. In our case, resorting to the generalized harmonic balance would make the algebra further cumbersome, but there is another technical reason that prevents an easy implementation of this workaround. It is the fact that, if one is to consider higher harmonics of the displacement and of the force, then the transducer force is not uniquely defined without any additional hypothesis on the amplitude of each of these harmonics. To clarify on an example, one can consider to hypothesize the displacement function as $x(t) = x_0 \cos(t) + x_1 \cos(2t)$ (let us drop the sin components for simplicity). Now, $x(t)$ has one pair of extrema per period iff $|x_0/x_1| \geqslant 4$, or two iff $|x_0/x_1| < 4$. Across those two cases, the capacitance will not vary in the same way and so the forces will be different depending on the values of x_0 and x_1. But the equations linking the coefficients x_0 and x_1 to the first two harmonics of the force cannot be determined if the number of extrema of the transducer force per period of the capacitance variation is not known *a priori*. Hence, to resort to this workaround consisting in taking into account higher harmonics of the dynamical variables, the computations of the force projections on the trigonometric functions have to be done carefully by a trial and-error process, resulting in an adequate partitioning into different regions in terms of V_{L}. We have not proceeded to this modification, but we can add it to the (long) list of possible improvements of our method.

The error in the amplitude can also come from the fact that the average components of displacement and transducer force were neglected. The blue dotted circles in Fig. 4.16 correspond to voltages for which a major shift in this average component was observed, similarly to what is shown in the time-domain results of Fig. 4.12. We will briefly elaborate on that point in Sec. 4.3.4.1 below. The orange dotted circle in Fig. 4.16 corresponds to the manifestation of a dynamic pull-in phenomenon (see Sec. 4.3.4.2 below).

Finally, it shall be noted that the error due to the misprediction of the oscillation amplitude

is less critical for the area-overlap transducer geometry, because then the dependence of the capacitance on the displacement becomes linear.

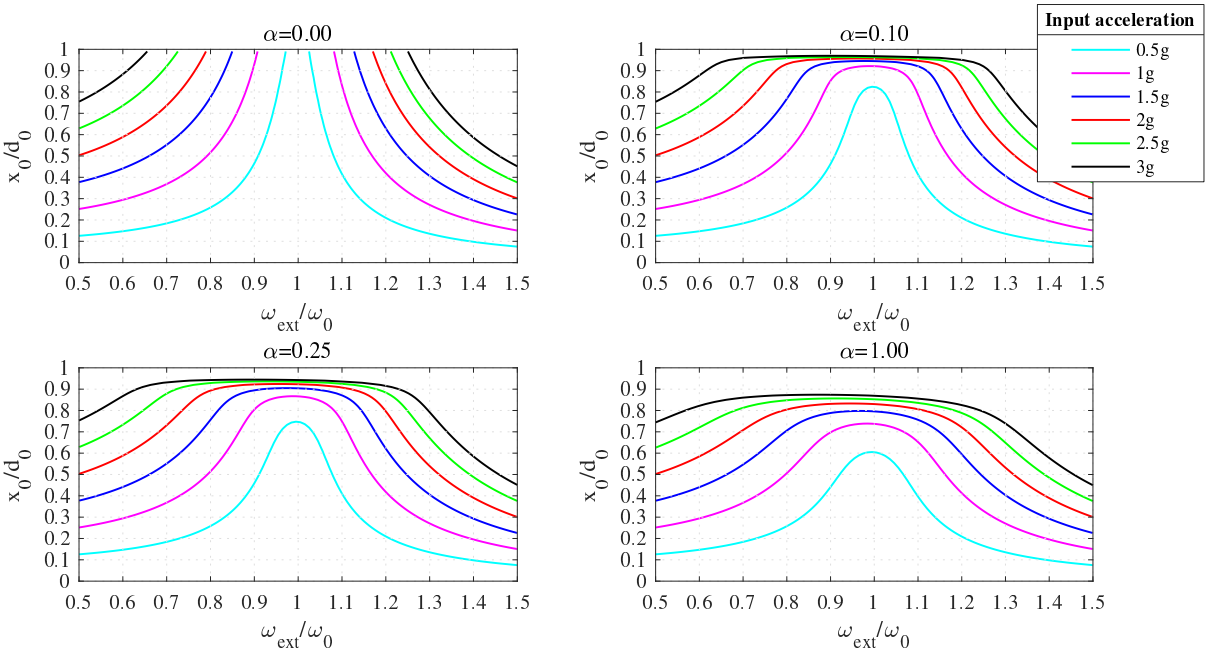

Figure 4.17: Amplitude vs. frequency response of the mechanical resonator obtained by a first-harmonic approximation, showing the effect of the nonlinear squeeze-film damping that we used in the applications of our method, for the quality factor Q computed as in (4.60) and the mechanical parameters of Table 4.1. The $\alpha = 0$ corresponds to a purely linear damping. We used $\alpha = 1$ in all of the simulations and the computations done by the method. The input amplitudes are given as dimensionalized quantities ($1\,\mathrm{g} \approx 10\,\mathrm{m\,s^{-1}}$).

Notwithstanding these issues, the trend seen in the results yielded by our method follows that of the relative values of converted power obtained by simulations and experiments across the different application cases. In particular, the results show that larger values of converted power are obtained for lower input frequencies. They also predict how the converted power compares across the different conditioning circuit.

4.3.3.3 Some results of application to different cases and practical implications on optimization and design

We now apply the method to several cases of inputs and mechanical parameters, for the symmetrical gap-closing electrostatic transducer geometry of Table 4.1. For each case, we apply it to several values of γ that can be, in principle, obtained using the unstable charge-pump conditioning circuits presented in Chap. 2-3. The computations are done and the plots are generated by a MATLAB program. Each figure is obtained almost instantaneously on a standard office computer, highlighting the practicality of this approach in order to explore the parameter space – but at the cost of some inaccuracy as we have previously seen in Sec. 4.3.3.2.

The results for these various cases are depicted in Fig. 4.19-4.30 that are put at the end of the chapter. Each pair of figure gives the results in terms of converted power versus increasing V_L voltages, and corresponding evolution of the amplitude versus increasing V_L voltages. The different cases are described in the figure's captions.

One immediately notes that several of these plots show that the amplitude is a multivalued

function of the V_{L} voltage, and thus so are the corresponding converted power as functions of V_{L}. This corresponds to multi-modality as we discussed in Sec. 1.3.4 of the introduction chapter, although now it is encountered with voltage as an input rather than frequency. This means that for some values of voltages, multiple oscillation amplitudes x_0 are admissible in the light of (4.73). No matter which one of these amplitudes is selected by the system's dynamics, as they have to fulfill $x_0 \in]\sqrt{1-1/\gamma}\,;1[$, energy is still being converted and the voltage V_{L} therefore necessarily increases. Discriminating between the multiple solutions can be done by applying a stability criterion that we give below in Sec. 4.3.4.2. For now, it suffices to acknowledge that this criterion was applied to the obtained solutions. From its application, it results that when the maximum converted power point is in a range of V_{L} of multi modality (for example, see Fig. 4.25 with $\gamma = 1.5$ and at $w_{\mathrm{ext}} = 0.5$), the other admissible amplitudes never happened to satisfy the stability criterion, whereas the amplitude corresponding to the maximum converted power point always did. In all, it means that the maximum converted power obtained in each case depicted in Fig. 4.19-4.30 corresponds to the peak of the curve of converted power versus V_{L}.

We saw in Sec. 4.3.3.2 that our method, as presented, seems to overestimate the value of converted power. Yet, we can still extract some insight from the results, about the operation of e-VEHs using unstable charge-pump in the electromechanical domain. Specifically, at least three interesting facts can be noted from these results.

- There is clearly a trend of the maximum converted power to increase as input frequencies are lower compared to the device's resonant frequency. This validates the insight that we used in the discussion of Sec. 4.2.3 about the shifting to the left of the frequency response with increasing V_{L} voltage. Note that another geometry of the transducer can give another behavior in this respect.

- Depending on system's and input parameters, different values of γ are optimal for different situations. This justifies the need for various unstable charge-pump conditioning circuits, in order to wide ranges of γ ratios. For example, the situation simulated in Fig. 4.19 advocate for smaller values of γ, whereas the results in Fig. 4.29 show that larger γ are better. In the first case, using a charge-pump based on Lefeuvre's or Illenberger's topology to implement $\gamma < 2$ would be advantageous. In the second case, a topology based on the series parallel charge-pump to implement $\gamma > 2$ would be preferred. Still, we lack an analytical criterion to determine the optimal γ, and hence further ease the comparison of the different unstable charge-pumps in the electromechanical domain. We give some future developments of our method that may yield such a criterion in Sec. 4.4 below.

- In the case that the oscillation amplitude is large enough ($x_0(V_{\mathrm{L}}) > \sqrt{1+1/\gamma}$) for small values of V_{L} to initiate energy conversion in unstable mode, the converted power gradually increases up to the optimal power point, that has then to be sustained. This is the case for excitations inputs that are near resonance. However, in the case of input excitations of lower frequencies, a larger pre-charge can be initially needed in order to bootstrap the energy conversion in the charge-pump's unstable operation mode. See for example the case in Fig. 4.19-4.20 for low values of ω_{ext}, for which pre-charge voltages in the range of 10 V to 20 V are needed depending on the value of γ. These cases may be interpreted as needing a larger shift in the frequency response of the resonator ensuing from the electromechanical effects, in order to tune it with the input excitation. Hence, V_{L} and therefore the pre-charge

must initially be large enough so to allow this frequency response shift. This frequency response shift results, in turn, in large enough oscillations allowing for unstable operation and power conversion. At the cost of this higher needed initial pre-charge, the maximum power point yielded by low-frequency inputs is of larger value than that obtained by inputs closer to or above the resonant frequency of the device.

These results have practical implications in the design of e-VEHs using unstable charge-pump conditioning circuits. A first implication is that the pre-charge voltage is an important design variable even in the case of e-VEHs using unstable charge-pump conditioning circuits. This observation is an important difference with the results of analysis of unstable charge-pumps in the electrical domain. A second implication is that the unstable charge-pump conditioning circuits (at least based on symmetrical gap-closing geometries) have desirable properties with respect to low-frequency inputs. This is because our results show that the resonant frequency of the device benefits from being chosen larger than the application's targeted frequency. Considering the challenge of building spring-mass based devices of low resonant frequency (we mentioned this in Sec. 1.6.1), this is a welcomed property of the e-VEHs using unstable charge-pump conditioning circuits.

It is also worth noting that, as highlighted for the electrical domain comparison in Sec. 4.1.4, the time taken to reach the maximum power point is absent of the considerations, as we have re-parametrized time in terms of the V_{L} cycle voltage. The time taken to reach a maximum converted power point can be long (for example, see the blue curve in the experimental result of Fig. 4.10), so a trade-off has to be found if the settling time is an important parameter, e.g., in cases where the system is often to be discharged completely.

Finally, note that all we gave here were insights based on the numerically solving the algebraic relation (4.49) for specific cases. The way we applied the semi-analytical tool in this section ultimately relies in numerical computations to solve $\Phi = 0$. We did not base our study on an analytical resolution that would allow a parameter sensitivity analysis of the maximum converted power point over the system's parameters. Modifying our method so as to enable such a procedure is the subject of ongoing work. Its outline will be given in the future works section.

4.3.4 Some comments and limitations of the method

In this section, we make some brief comments about our method. We also highlight some of the limitations of our tool as applied above in Sec. 4.3.3 that were not discussed in Sec. 4.3.3.2.

4.3.4.1 Shifting in the mass average position

Above in Sec. 4.3.3, we have made the hypothesis that the mass position has no average component, that is, $\overline{x} = 0$. However, the simulations in Sec. 4.3.1 clearly show that at some points in the evolution of V_{L}, this hypothesis is no longer verified. As a result, the capacitance variation changes compared to V_{L}s for which $\overline{x} = 0$. Indeed, while $C_{\min}$ remains unchanged (because the position still crosses $x = 0$), and $C_{\max}$ alternates between two values per period of $x(t)$. This situation is depicted in Fig. 4.14. This effect can be taken into account by resorting to the ansatz made in the general presentation of the method, that is, $x(t) = \overline{x} + x_0 \cos(\omega_{\mathrm{ext}} t)$ with $\overline{x} \neq 0$.

Note that in the case of the simulations of Sec. 4.3.1, the average component appears after the maximum power point is reached.

4.3.4.2 Stability of the solutions and justification of the method

In general, solving (4.49) can yield two or more solutions $(V_\mathrm{L}, \overline{x}, x_0)$ and $(V_\mathrm{L}, \overline{x}', x_0')$ such that $\overline{x} \neq \overline{x}'$ and/or $x_0 \neq x_0'$. We have seen it in the results of Sec. 4.3.3.3. Some of these results showed that there exists ranges of values of V_L for which multiple values of the mass oscillation amplitude x_0 are admissible. This is a phenomenon that is often seen in nonlinear resonators, and that we refer to as multi-modality. In practice, only one of these solutions is going to be observed. Which one depends on the initial conditions, but also on the stability properties of the periodic orbits of the vector field associated with our system. Means of analysis of periodic orbits stability properties include the introduction of a suited change of coordinates that sends the periodic orbit to the stationary point of a conjugated vector field. The stability properties of this equilibrium point are then linked to that of the periodic orbit [GH13].

In our case, the matter of stability assessment is even more complicated as the solutions we hypothesize are not *stricto sensu* periodic orbits of the system (4.58) but rather approximations relying on simplifying assumptions. On a more general note, we did not give any theoretical foundation as of why our method described should accurately describe the behavior of the system. In particular, we did not rigorously motivate and bound the difference between the actual system's solution and that given by (4.38) and satisfying (4.49). Instead, we followed more of a heuristic approach. As a matter of fact, our approach is essentially equivalent to the so-called describing function procedure, a basic tool in the analysis of nonlinear systems, albeit it is usually formulated in the frequency domain. More information and some justification for this procedure can be found in the authoritative reference [Van68].

We shall not pretend to have such theoretical concerns here, which are well beyond the scope of our study. Instead, we loosely assume that the oscillations satisfying (4.49) are acceptable approximations of the system's dynamics. Also, let us explicitly state the stability criterion that we have used in Sec. 4.3.3.3 to determine that in regions of multi-modality, the sole solution of (4.73) corresponding to a stable periodic orbit is the one which yields the highest converted power. Applied to our case study of the symmetrical gap-closing geometry, this criterion reduces to the following algebraic relation, where θ_1 and θ_2 were defined in (4.72):

$$\frac{\partial \theta_2}{\partial x_0}(x_0, \phi)\frac{\partial \theta_1}{\partial \phi}(x_0, \phi) - \frac{\partial \theta_1}{\partial x_0}(x_0, \phi)\frac{\partial \theta_2}{\partial \phi}(x_0, \phi) > 0. \tag{4.75}$$

This criterion is obtained using a procedure that is thoroughly explained in [Van68] and applied to a practical case in detail in [Jui15].

Let us end this discussion by mentioning that a nonlinear system such as our e-VEH leaves the door open for a rich variety of dynamic behavior. As an example, the simulation result depicted in Fig. 4.18 shows dramatic qualitative changes in the dynamics of the e-VEH as V_L increases. This simulation is carried out with the same device as above and conditioned by Lefeuvre's circuit with $N = 2$ ($\gamma = 3/2$). It shows that after some time, $x(t)$ becomes somewhat erratic, and finally it ends up remaining constant at $+x_\mathrm{M}$. This behavior cannot be quantitatively predicted by our method, but the solutions for $V_\mathrm{L} > 11.5\,\mathrm{V}$ do not fulfill our stability criterion

above, and the observed change in dynamics happens starting from $V_{\mathrm{L}} = 12.6\,\mathrm{V}$.

Incidentally, this simulation shows a transient operation mode of the Lefeuvre's charge-pump from 500 ms to 1 s. This transient mode is not characterized yet, as no work have yet reported a comprehensive and quantitative study of the dynamics of this circuit in the electrical domain.

4.3.4.3 Parasitic capacitances and electret charging

Finally, some other limitations of our method as presented above include the fact that we do not take into account the parasitic capacitance that superposes to that of the transducer, or a possible electret charging. As a crossed comparison of Table 4.1 and Table 4.2 shows, the value of the parasitic capacitance can be of same order of magnitude of the transducer's capacitance.

Taking into account the effect of the electret is not difficult in principle. Technically, this only changes (4.45) and the subsequent steps, because V_{L} cannot longer be factored. Indeed, V_{L} and $V_{\mathrm{R}} = \gamma V_{\mathrm{L}}$ have to be changed to $E + V_{\mathrm{L}}$ and $E + \gamma V_{\mathrm{L}}$ in (4.37), and the times interval for the piecewise definition of the force also have to be changed accordingly. This modification brings an additional algebraic burden, particularly if one anticipates future improvements of our tool so as to enable parameter sensitivity analysis. This modification is succinctly explained below in the future works section.

4.4 Conclusion and future works

This chapter presented an electrical domain comparison of several charge-pump conditioning circuits, as well as an study geared towards their comparison in the electromechanical domain. We first carried out an electrical domain comparison, when meaningful, between stable charge-pumps. Then, we carried out the same comparison among unstable charge-pumps. Setting some simple constraints, we determined which charge-pump is optimal among the unstable subfamily, given the η and E parameters. It was shown that a great advantage of unstable conditioning circuits is that the maximum energy conversion cycle can be reached by their autonomous operation, from arbitrarily low levels of initial energy in the circuit.

Then, we carried out a study in the electromechanical domain, first on the basis of experiments. These experiments showed that the unstable behavior is mitigated and that a maximum power conversion point exists and is reached under the charge-pump's autonomous operation. The value of this maximum power point depends on the characteristics of the input. In order to study how this maximum power point is influenced by the γ ratio of the unstable conditioning circuit, as well as by the input excitation and the transducer's geometrical parameters, we presented a semi-analytical tool allowing for a fast estimation of the maximum power point in these various situations.

The results yielded by this tool have been checked against electromechanical simulations. They show that our method, as we applied it, correctly predicts the trends of the converted power variation as a function of the input and system parameters, even if it suffers some pitfalls in its exact quantitative prediction. We have listed the reasons for this discrepancy, and future works will have to be geared towards the improvement of these matters.

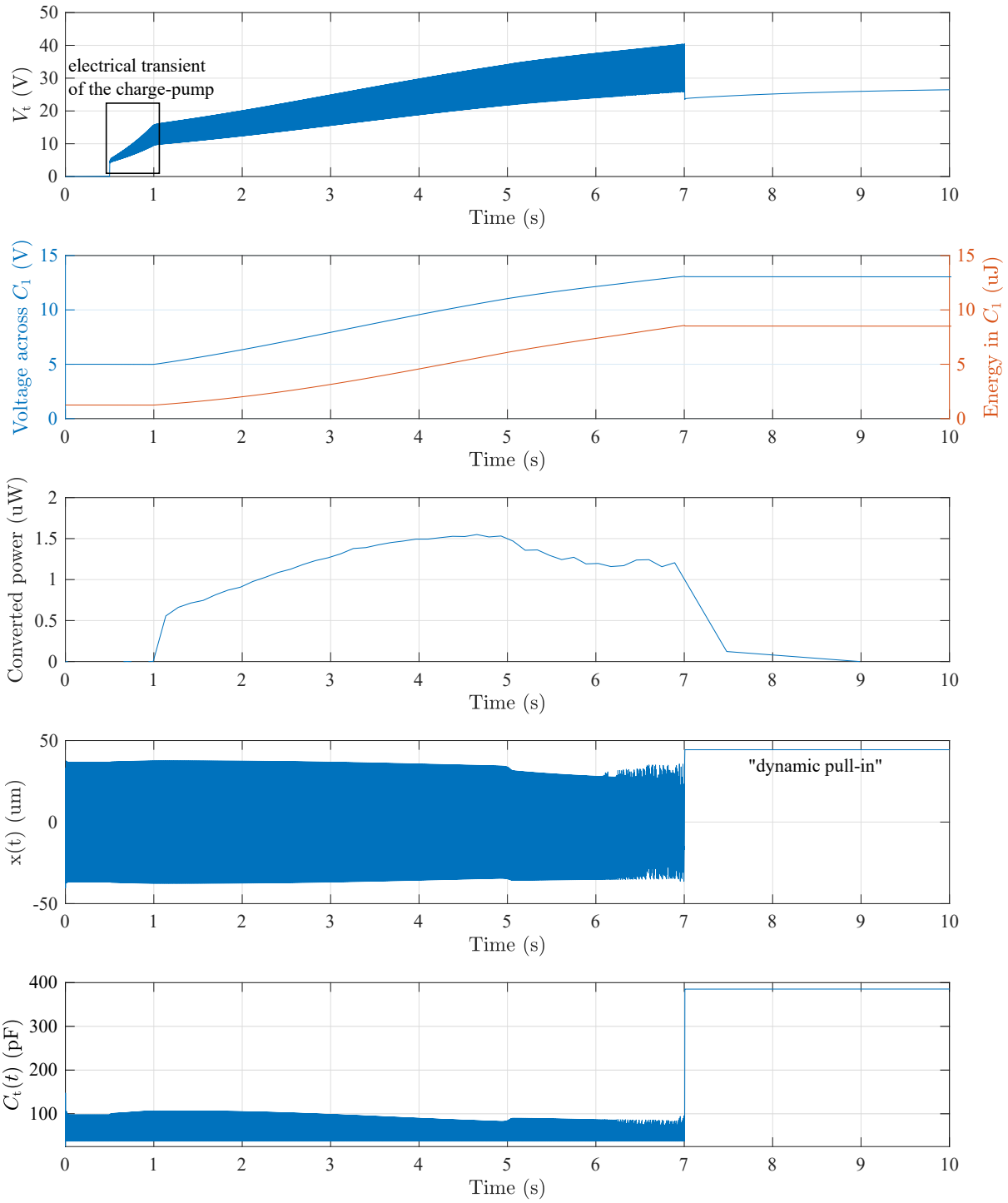

Figure 4.18: Simulation results for an e-VEH connected to Lefeuvre's charge-pump with $N = 2$, showing the manifestation of an instability followed by a pull-in phenomenon. The input is of 1.5 g dimensionalized, at a frequency of $\omega_{\text{ext}} = 7/8$. The system's parameters are listed in Table. 4.1. Note the transient behavior from 500 ms to 1 s that is due to the electrical dynamics of Lefeuvre's charge-pump.

We have nevertheless gathered some results from the application of our method. These results support that the γ ratio, and therefore, the choice of the unstable charge-pump, is a decisive parameter in optimizing the power yield of the e-VEH. This was somehow already clear from the electrical analysis. However, the electromechanical analysis shows that the charge-pump's pre-charge is also as an important design parameter. Moreover, in our application case to a symmetrical gap-closing transducer, the results show that resonant e-VEHs using unstable-charge pumps yield better power conversion figures for inputs of low frequencies compared to the resonator's natural frequency. This is an advantage in the context of small-scale e-VEHs for which mechanical resonant structures with low resonant frequencies can be difficult to fabricate.

As applied above, our method relies on a numerical part, and hence so does an eventual parameter sensitivity analysis in the view of optimized design. To overcome this limitation, one possible improvement is to have an estimate of the maximum power point for each value of the γ ratio, by merely evaluating the stationary points of $\partial P/\partial V_{\mathrm{L}}$ instead of evaluating the whole power versus V_{L} characteristic. For instance, for the symmetrical gap-closing geometry where P is as in (4.53):

$$\frac{\partial P}{\partial V_{\mathrm{L}}} = 0 \iff \underbrace{1-\gamma(1-{x_0}^2) - V_{\mathrm{L}}\frac{x_0}{1-{x_0}^2}\frac{\mathrm{d}\Phi(V_{\mathrm{L}},x_0)/\,\mathrm{d}V_{\mathrm{L}}}{\mathrm{d}\Phi(V_{\mathrm{L}},x_0)/\,\mathrm{d}x_0}}_{:=\chi(x_0,V_{\mathrm{L}})} = 0 \tag{4.76}$$

where Φ is the map defined in (4.73), and the rightmost term in $\chi(x_0, V_{\mathrm{L}})$ is obtained by evaluating $\partial x_0/\partial V_{\mathrm{L}}$ appearing in $\partial P/\partial V_{\mathrm{L}}$ by an application of the implicit functions theorem. Therefore, solving

$$\begin{cases} \Phi(x_0, V_{\mathrm{L}}) &= 0 \\ \chi(x_0, V_{\mathrm{L}}) &= 0 \end{cases} \tag{4.77}$$

directly gives a candidate point for the maximum power point. In principle, a parameter optimization can be done on the various parameters appearing in the expression of the solution to this set of equations, for example to determine the optimal value of γ and therefore proceed to the analytical comparison of different unstable charge-pumps. However, the solution is not associated to any dynamical context, in the sense that there is no history of how the system can arrive to this point and which initial condition allows it to do so. This is unlike the results of the method in Sec. 4.3 that show the evolution of the converted power with that of V_{L}. Plus, the stability of the corresponding solution has also to be checked. Also in practice, one of the main reasons why this approach could fail in giving useful insights is simply the algebraic complexity of the maps Φ and χ. But the use of symbolic computation software along with carrying out the right simplifications can in principle make this task easier.

Finally, we would like to emphasize that despite the fact that our experiments demonstrated the major impact of the electromechanical coupling on the e-VEHs' operation and performances, the results obtained for the electrical domain are still useful in some situations. This would be the case, for instance, for inertial e-VEHs of larger scales, where the breakdown of the components may happen before any significant impact of the electromechanical coupling on the dynamics. This is also the case for the family of direct force e-VEHs, e.g., triboelectric VEHs. Notably, unstable charge-pumps were reported in triboelectric VEHs in [Gei17; LHG17], where the constraints on the electrical components are prominent over any manifestation of the electromechanical coupling. In this context, future works may investigate the role of the

components parasitics on the comparison between conditioning circuits done in the electrical domain.

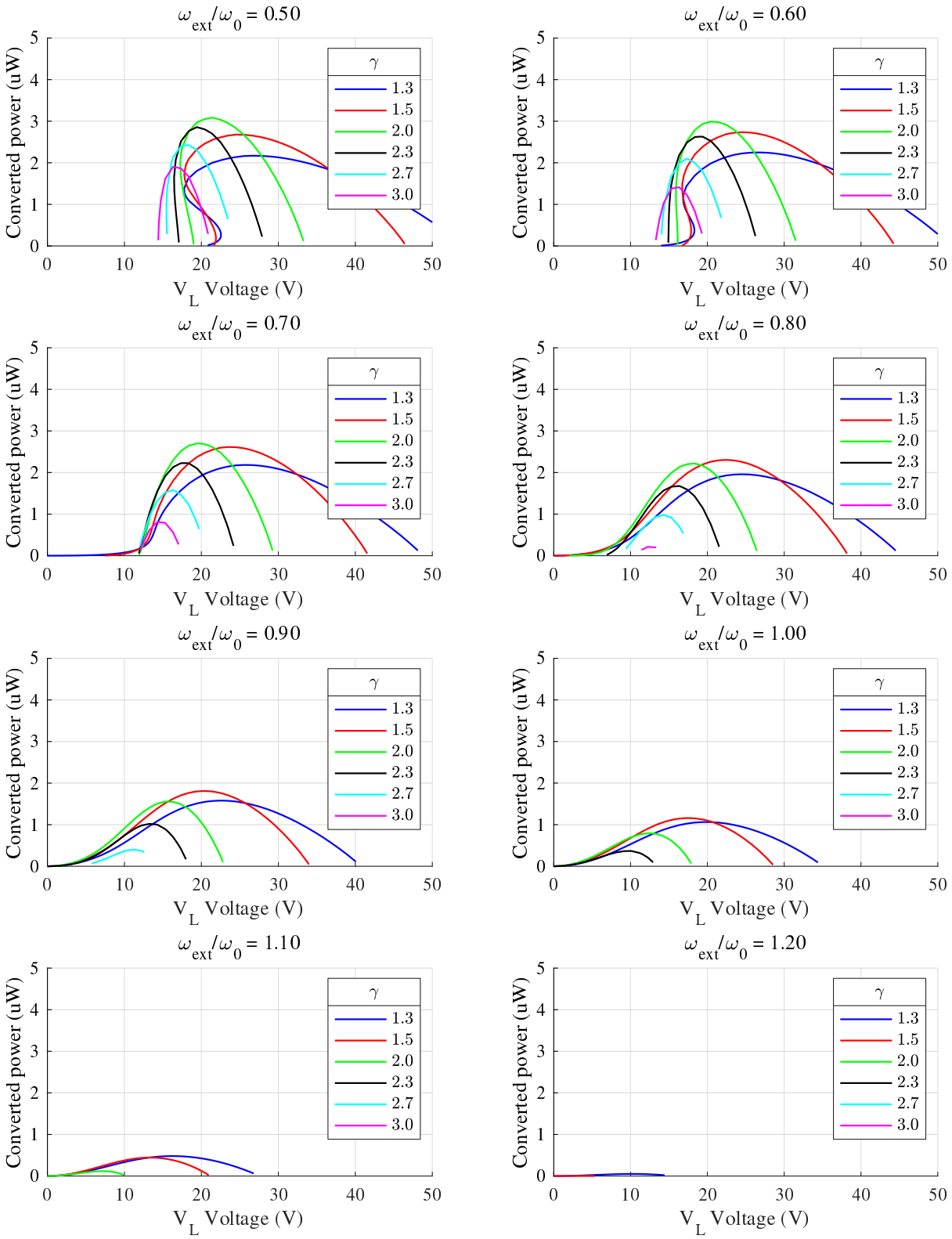

Figure 4.19: Results of converted power versus the charge-pump's evolving V_L voltage, obtained by applying the method to a transducer with the parameters in Table 4.1. The dimensionalized excitation amplitude is of 1.5 g.

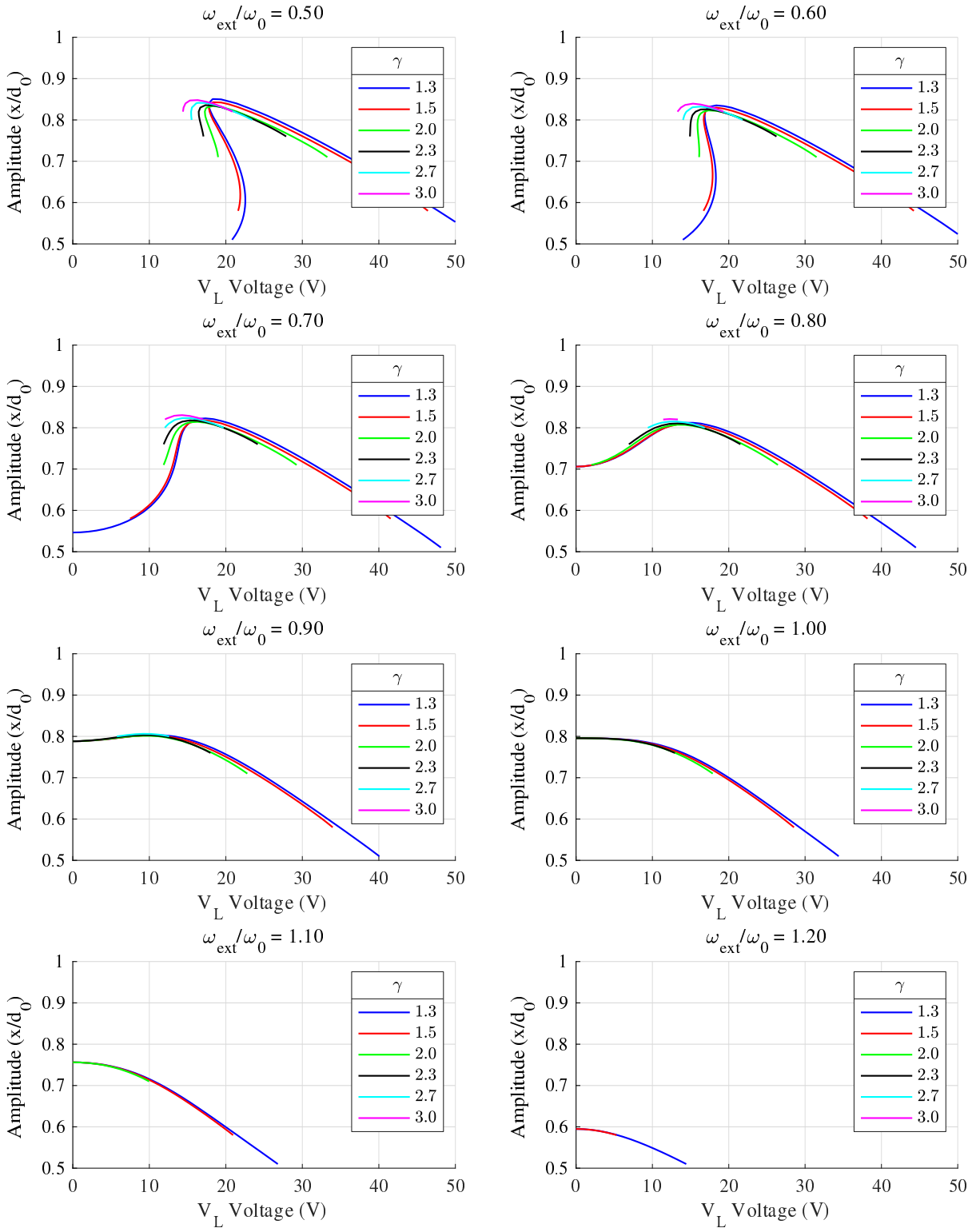

Figure 4.20: Results of the mass oscillation amplitude versus the charge-pump's evolving V_L voltage, obtained by applying the method to a transducer with the parameters in Table 4.1. The dimensionalized excitation amplitude is of 1.5 g.

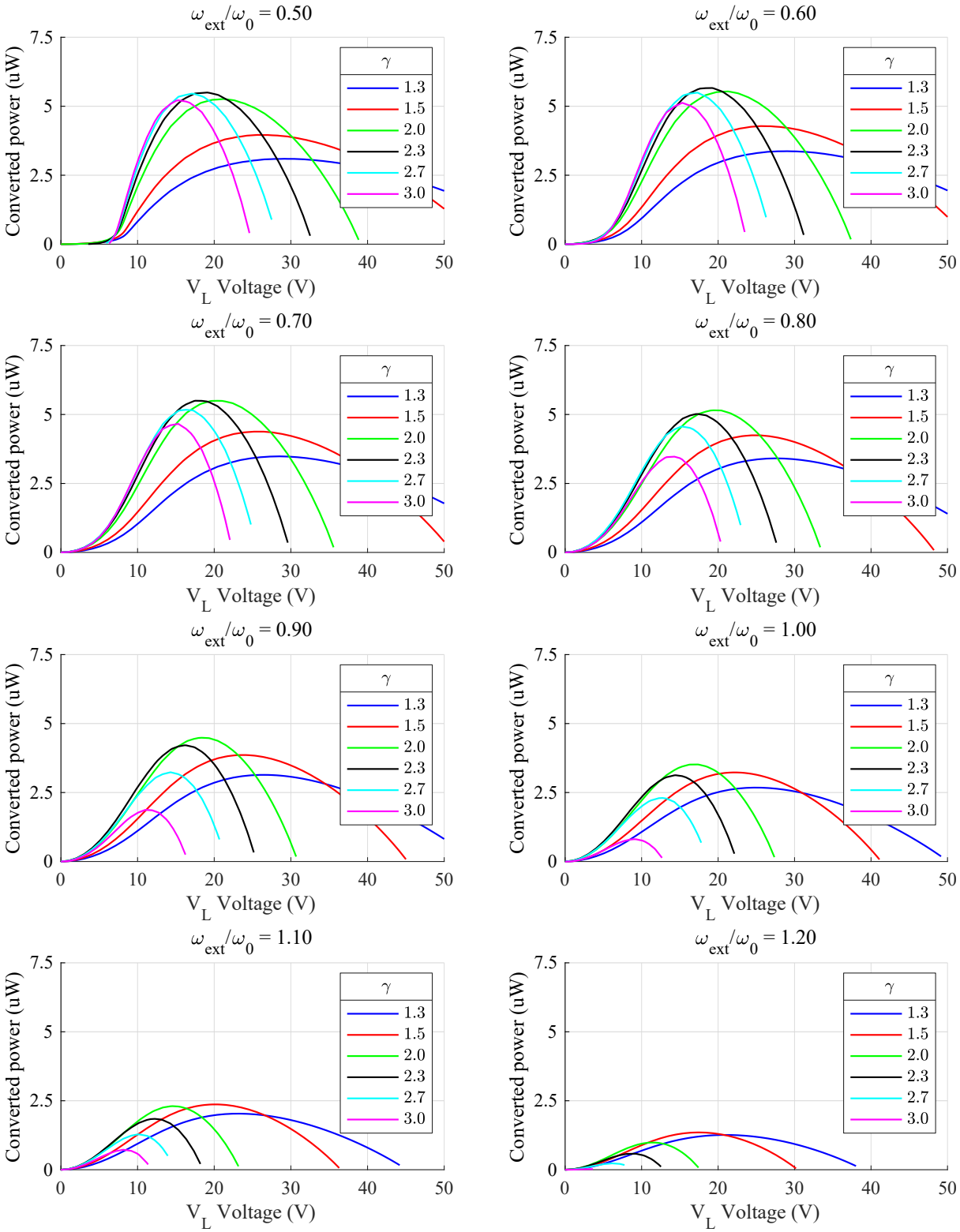

Figure 4.21: Results of converted power versus the charge-pump's evolving V_L voltage, obtained by applying the semi-analytical method to a transducer with the parameters in Table 4.1. The dimensionalized excitation amplitude is of 3 g.

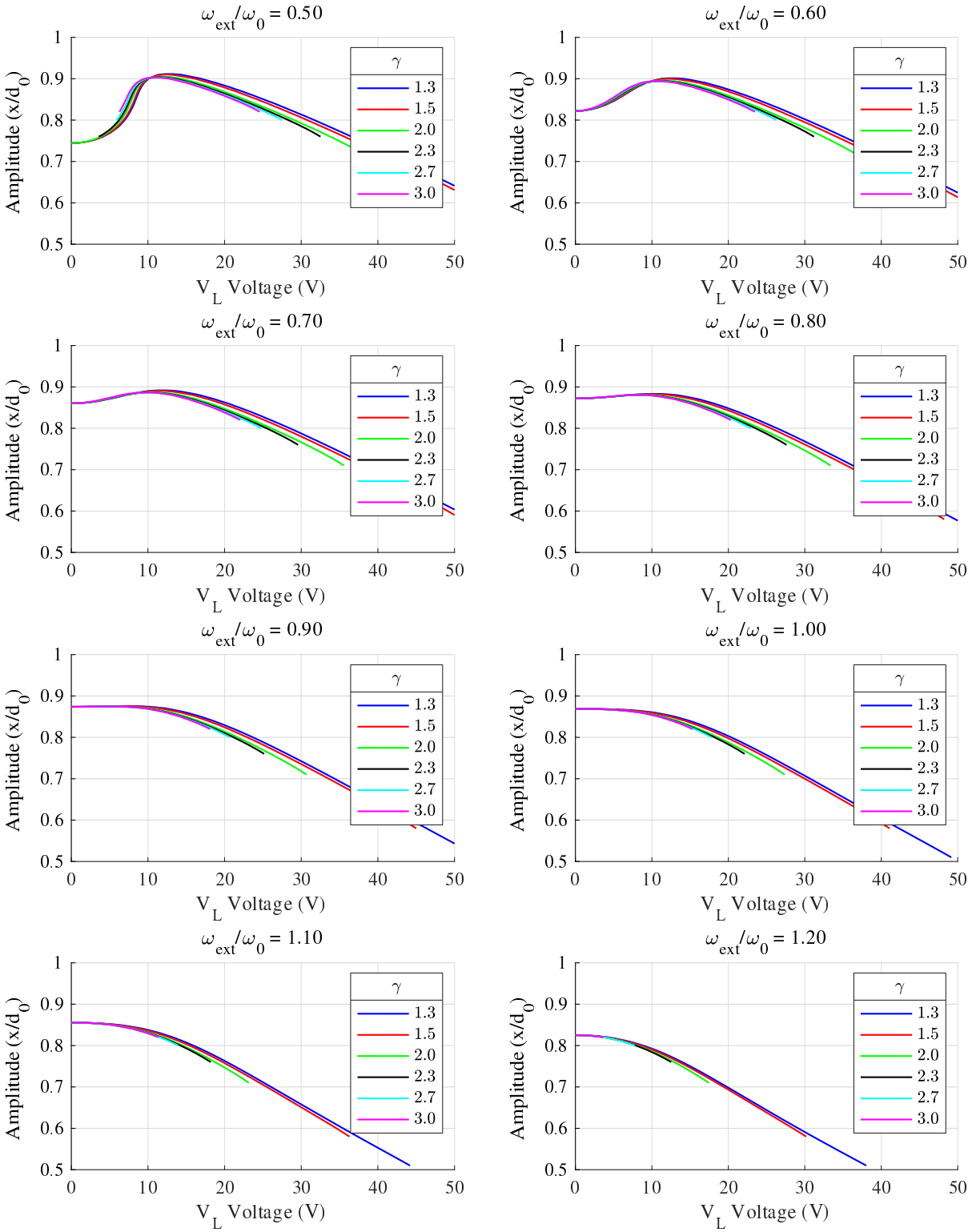

Figure 4.22: Results of the mass oscillation amplitude versus the charge-pump's evolving V_{L} voltage, obtained by applying the semi-analytical method to a transducer with the parameters in Table 4.1. The dimensionalized excitation amplitude is of 3 g.

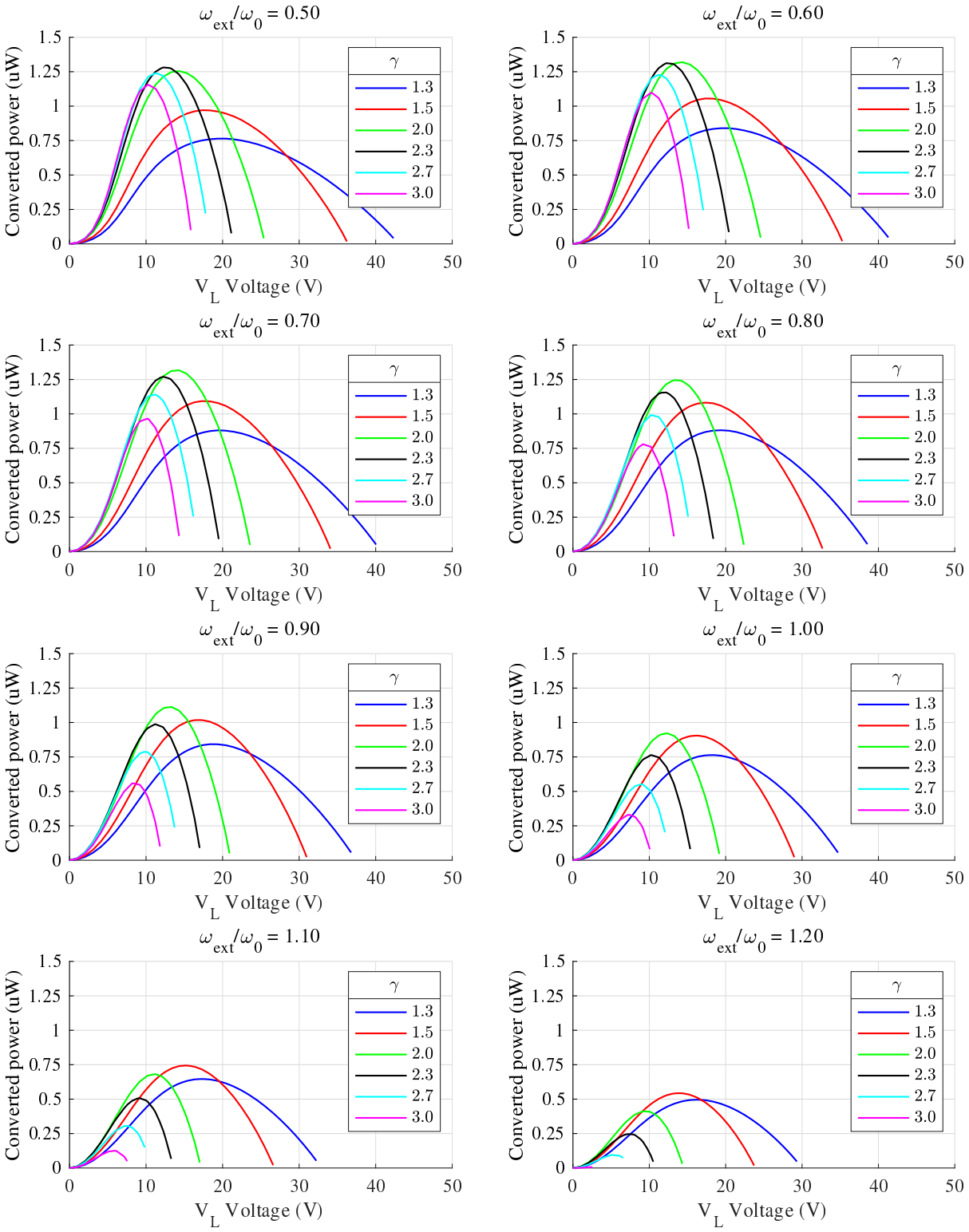

Figure 4.23: Results of converted power versus the charge-pump's evolving V_L voltage, obtained by applying the semi-analytical method to a transducer with the parameters in Table 4.1, except for $k = 24\,N\,m^{-1}$, corresponding to a mechanical resonator of 100 Hz dimensionalized resonant frequency. The dimensionalized excitation amplitude is of 1.5 g.

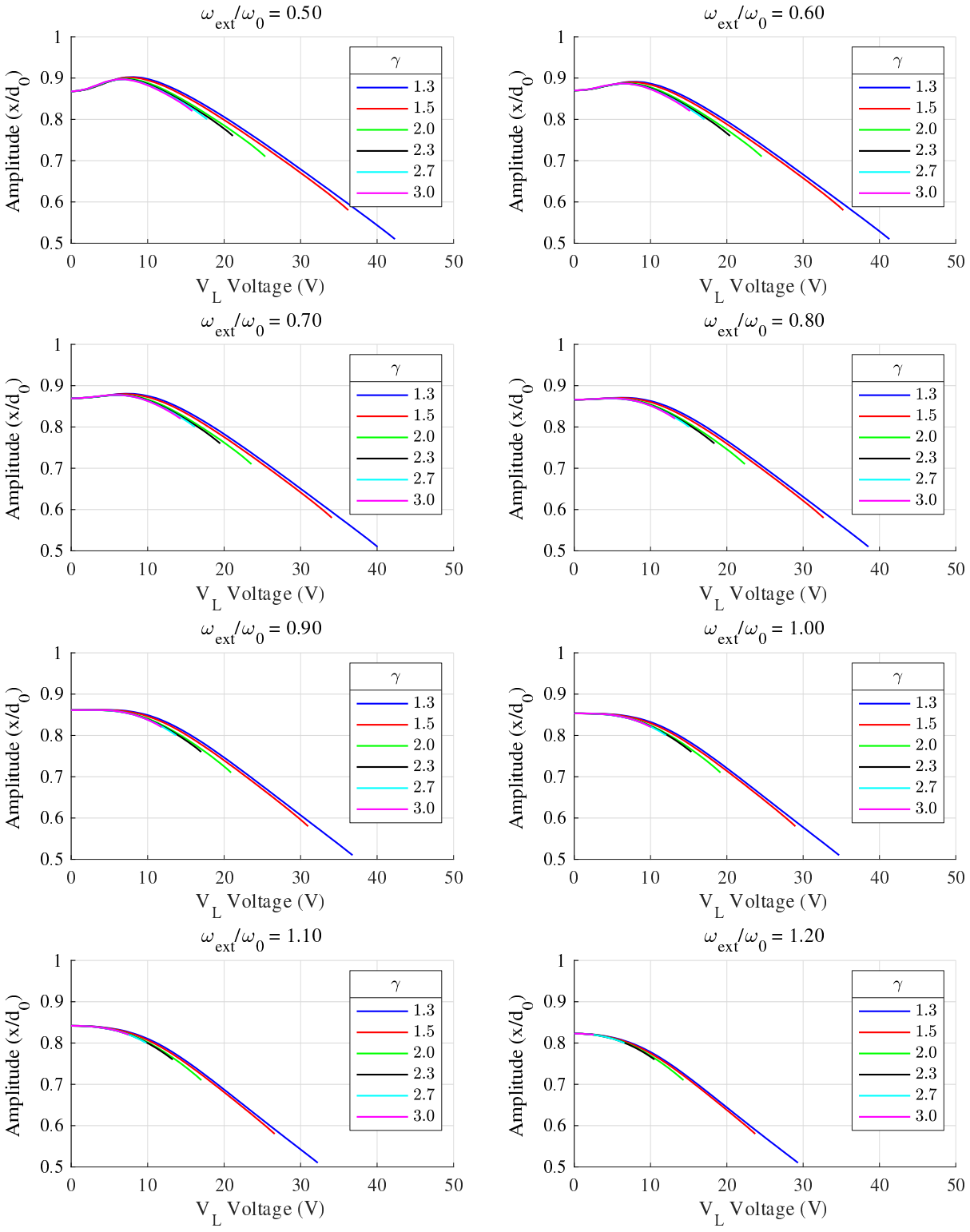

Figure 4.24: Results of the mass oscillation amplitude versus the charge-pump's evolving V_L voltage, obtained by applying the semi-analytical method to a transducer with the parameters in Table 4.1, except for $k = 24\,N\,m^{-1}$, corresponding to a mechanical resonator of 100 Hz dimensionalized resonant frequency. The dimensionalized excitation amplitude is of 1.5 g.

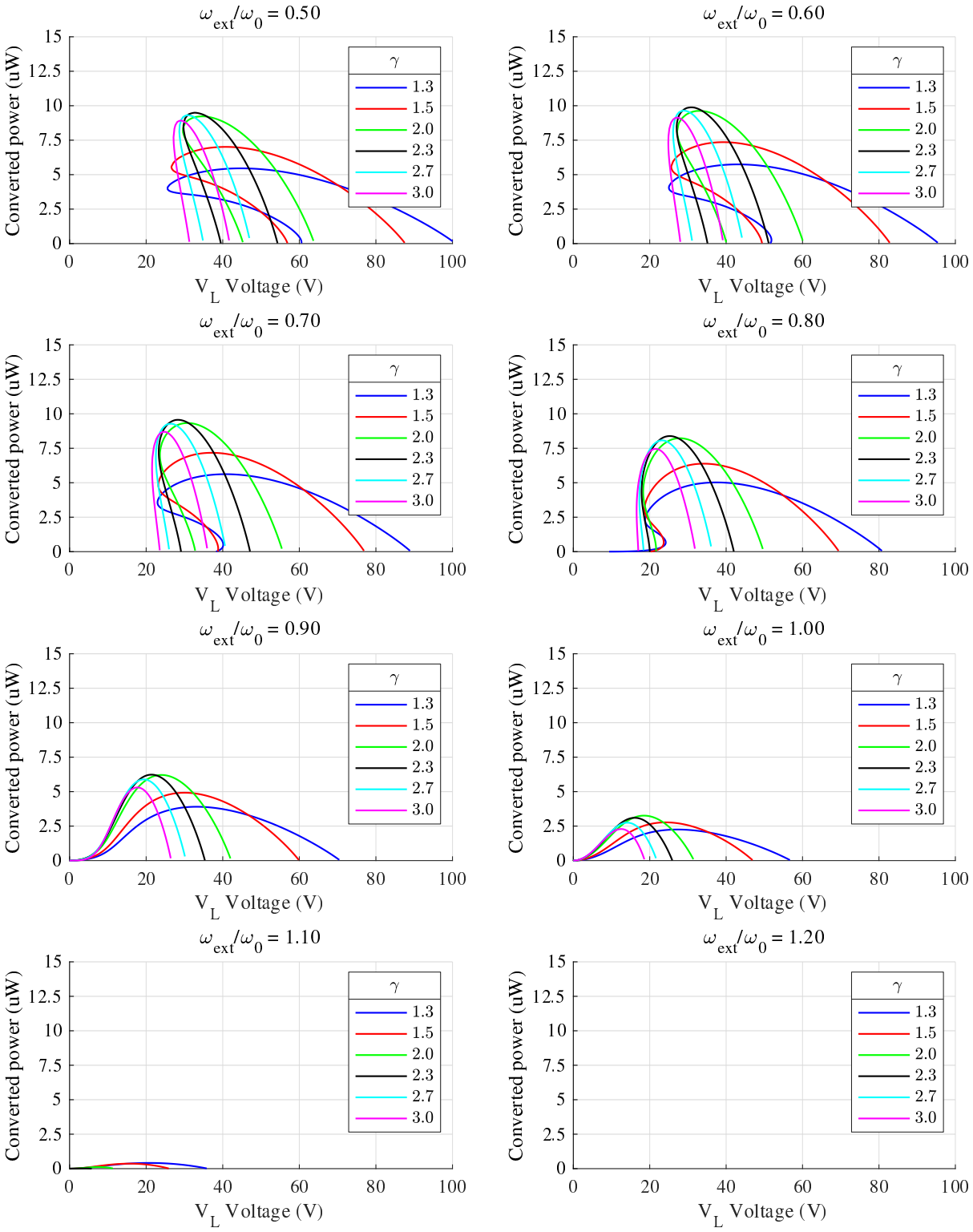

Figure 4.25: Results of converted power versus the charge-pump's evolving V_L voltage, obtained by applying the semi-analytical method to a transducer with the parameters in Table 4.1, except for $d_0 = 75\,\mu m$. The dimensionalized excitation amplitude is of 1.5 g.

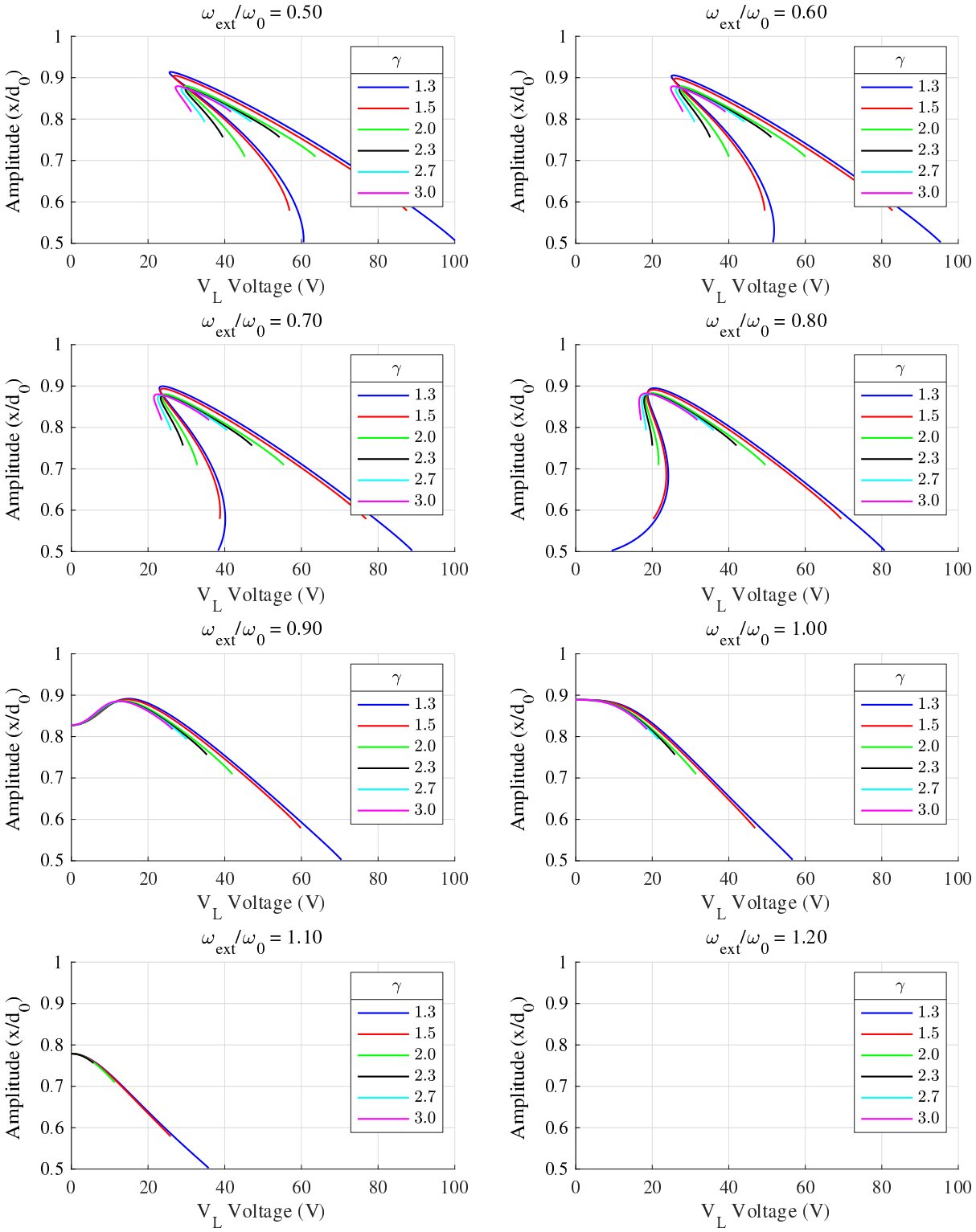

Figure 4.26: Results of the mass oscillation amplitude versus the charge-pump's evolving V_L voltage, obtained by applying the semi-analytical method to a transducer with the parameters in Table 4.1, except for $d_0 = 75\,\mu m$. The dimensionalized excitation amplitude is of 1.5 g.

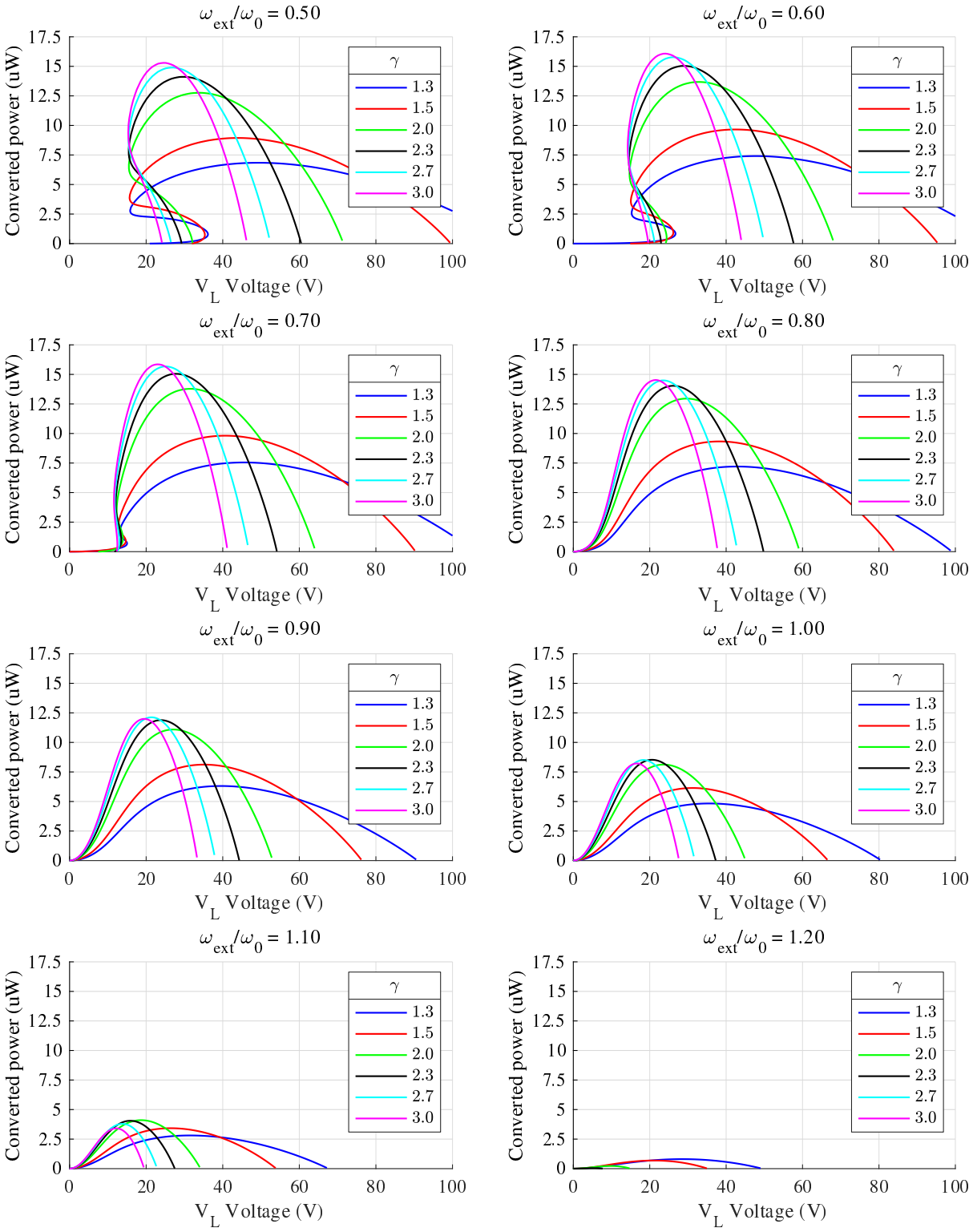

Figure 4.27: Results of converted power versus the charge-pump's evolving V_{L} voltage, obtained by applying the semi-analytical method to a transducer with the parameters in Table 4.1, except for $d_0 = 75\,\mu\mathrm{m}$. The dimensionalized excitation amplitude is of 3 g.

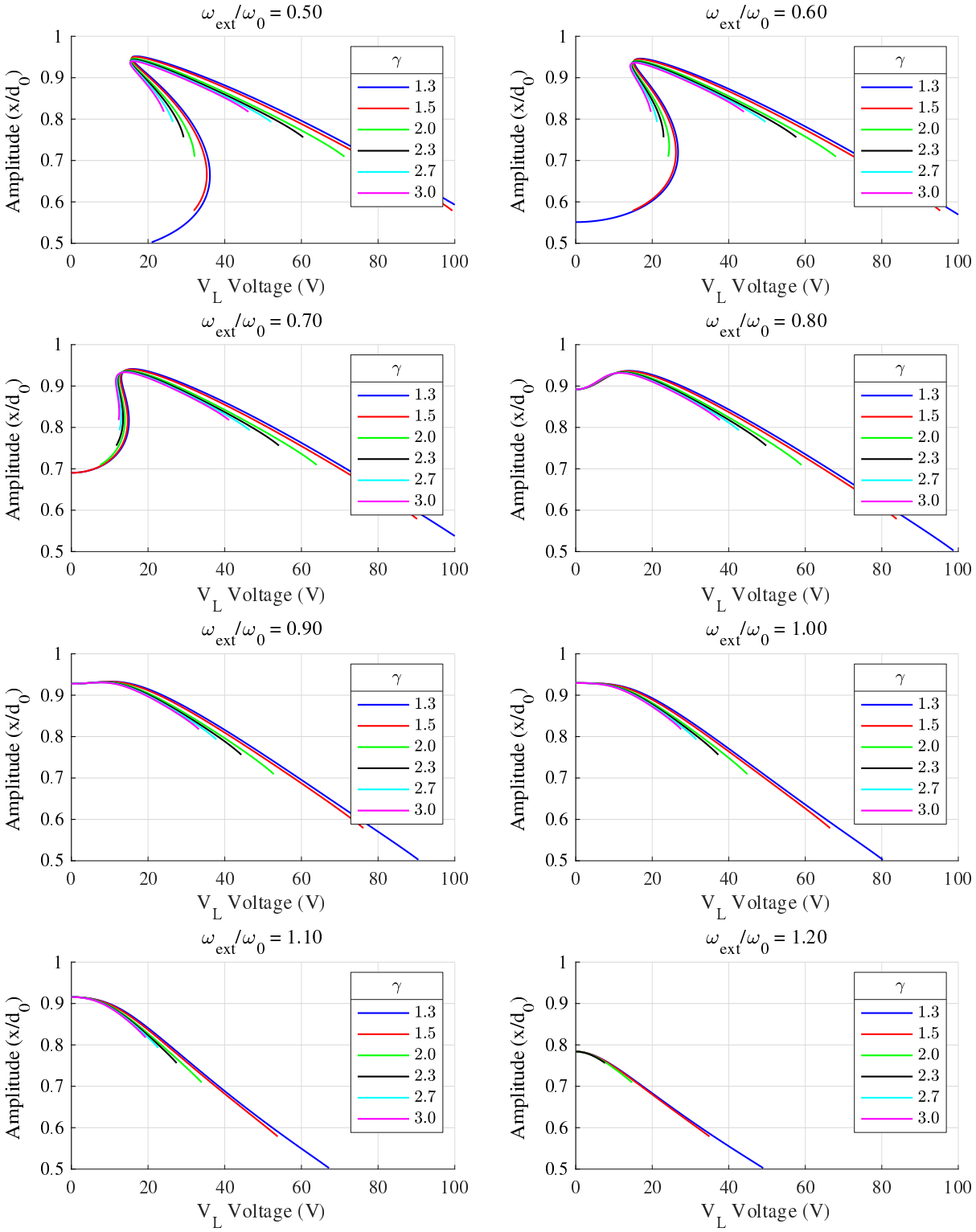

Figure 4.28: Results of the mass oscillation amplitude versus the charge-pump's evolving V_L voltage, obtained by applying the semi-analytical method to a transducer with the parameters in Table 4.1, except for $d_0 = 75\,\mu m$. The dimensionalized excitation amplitude is of 3 g.

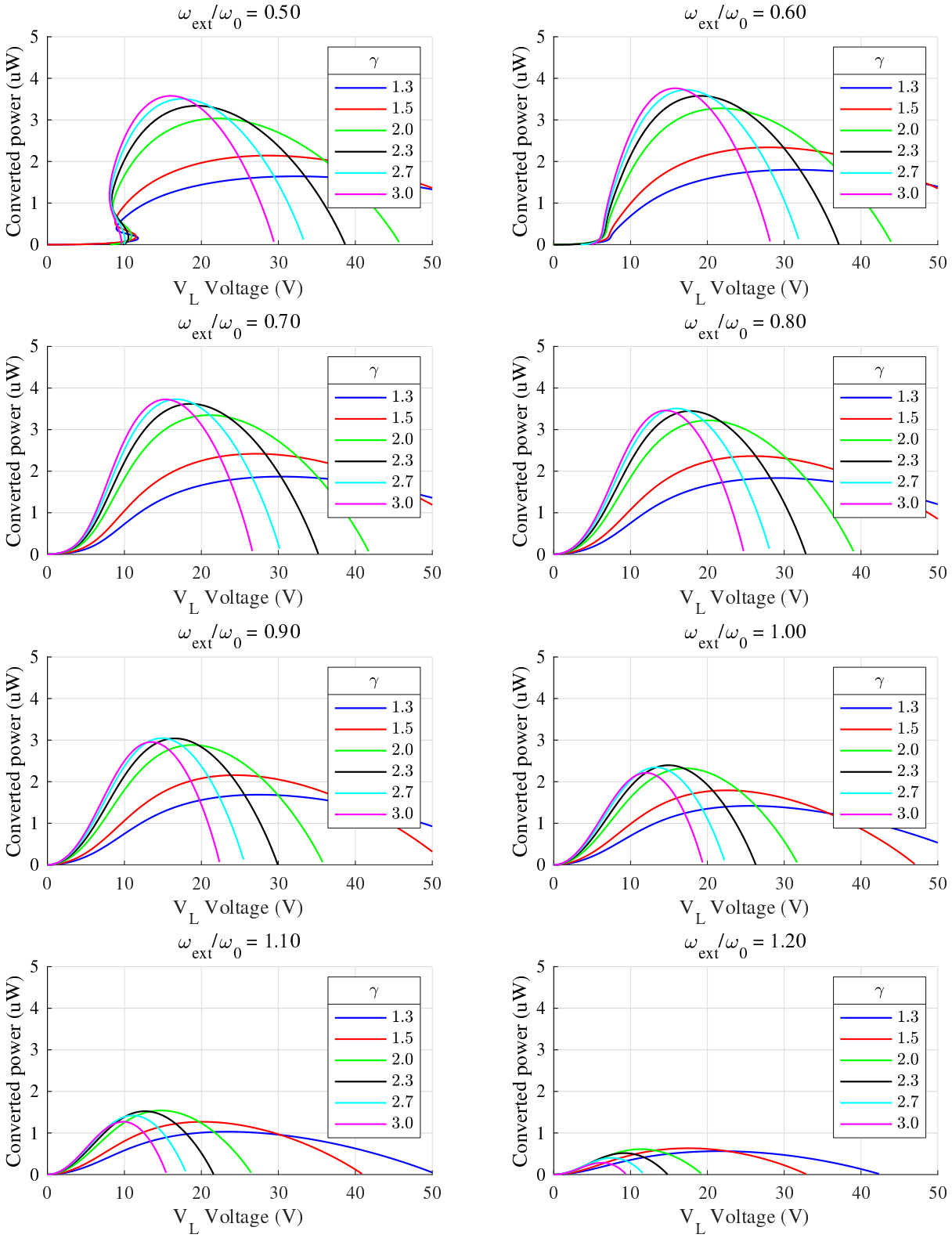

Figure 4.29: Results of converted power versus the charge-pump's evolving V_L voltage, obtained by applying the semi-analytical method to a transducer with the parameters in Table 4.1, except for $d_0 = 75\,\mu m$ and $k = 24\,N\,m^{-1}$. The dimensionalized excitation amplitude is of 3 g.

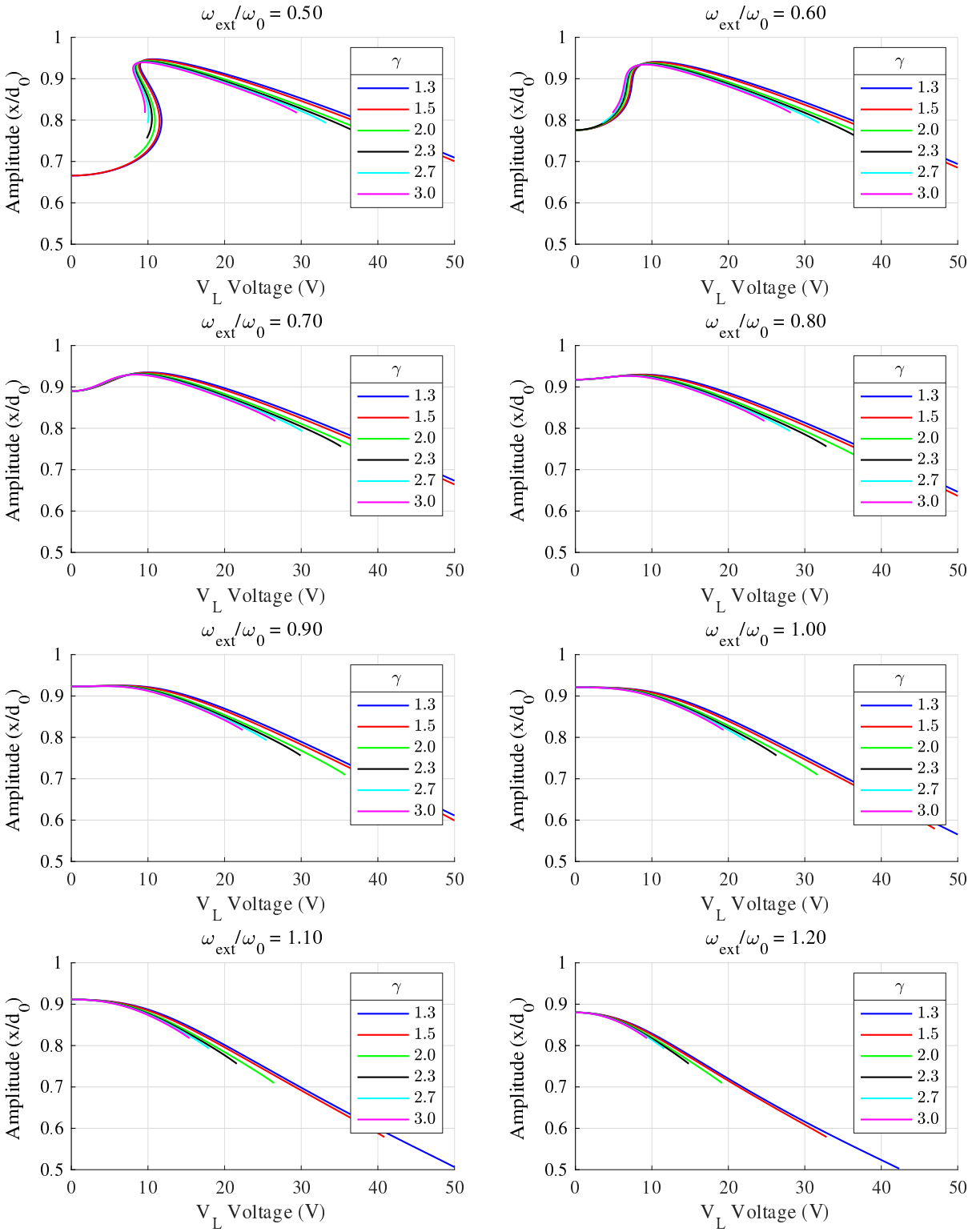

Figure 4.30: Results of the mass oscillation amplitude versus the charge-pump's evolving V_{L} voltage, obtained by applying the semi-analytical method to a transducer with the parameters in Table 4.1, except for $d_0 = 75\,\mu\mathrm{m}$ and $k = 24\,\mathrm{N\,m^{-1}}$. The dimensionalized excitation amplitude is of 3 g.

Chapter 5

Characterization methods for electrostatic vibration energy harvesters

This chapter presents a new method for the experimental characterization of electrostatic vibration energy harvesters. The method allows the characterization of the value of the lumped parameter E that models the built-in voltage of a transducer charged with an electret. The previous chapters have shown that this lumped parameter can have a tremendous impact on the system's performances, particularly when used in stable charge-pumps. Existing methods for such a characterization are either difficult to carry out with some transducer geometries, or can result in the degradation of the electret layer.

A modified version of this method is then presented. It allows the evaluation of the variation of the transducer's capacitance under the harvester's operation, when the transducer is biased by a charge-pump conditioning circuit. This can be of help in laboratory settings where advanced measurement instruments (e.g., laser measurement) are not available to precisely track the mechanical motion of the mass.

The work in this chapter has led to publications [KGB17a] and [KGB16].

5.1 Dynamics of the rectifier charge-pump conditioning circuits

The half-wave 1 (HW1) and half-wave 2 (HW2) conditioning circuits were briefly presented in Sec. 2.3.1.2. We also considered them in Sec. 4.1 when we compared different stable charge-pump conditioning circuits. Their schematic is depicted again here in Fig. 5.1a and Fig. 5.1b to ease the reading. In the present chapter, we will use these circuits to characterize electrostatic transducers. Let us start by deriving the cycle-to-cycle state evolution of HW1 circuit. We suppose that the diodes follow the ideal diode current-law voltage with a $V_{\mathrm{T}} > 0$ threshold. This supplementary precaution is needed to enhance the precision of the measurements. This derivation is very similar and simpler than for the Roundy's charge-pump. The derivation of the evolution law for the HW2 circuit is similar.

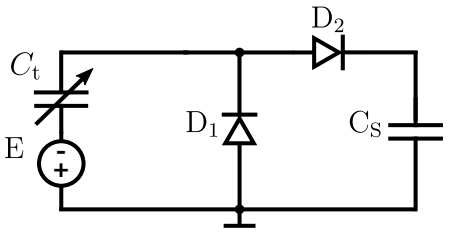

(a) Half-wave 1 charge-pump conditioning circuit

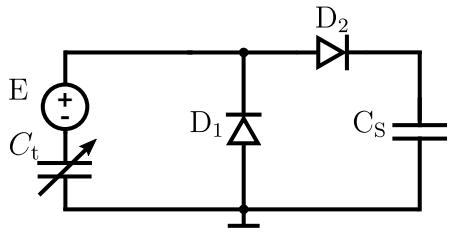

(b) Half-wave 2 charge-pump conditioning circuit

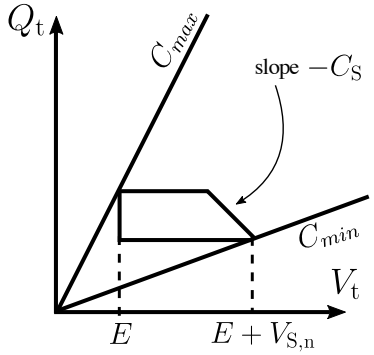

(c) Exact charge-voltage diagram for one cycle of variation of C_t with the HW1 charge-pump conditioning circuit

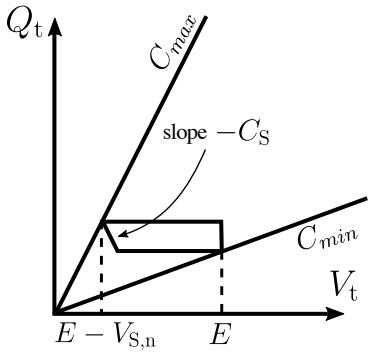

(d) Exact charge-voltage diagram for one cycle of variation of C_t with the HW2 charge-pump conditioning circuit

Figure 5.1: Schematics and charge-voltage diagrams of HW1 and HW2 rectifiers charge-pumps

Let C_t vary as in the context exposed in Sec. 2.1.1. The notations are also kept the same. Suppose that we are at a cycle n of C_t's variation, and at $C_t = C_{max}$, we have that $V_{t,=}V_{S,\overline{n}} + V_T$. As for the generic circuit and for Roundy's charge pump in Chap. 2 this will necessarily happen in at most one cycle of variation of C_t.

When C_t goes from C_{max} to C_{min}, it first remains at constant charge and its voltage increases, until $C_t = C_1$ where we define

$$C_1 \coloneqq \frac{E - V_T}{V_{S,\overline{n}} + E + V_T} C_{max}, \tag{5.1}$$

that is reached if

$$\eta > \frac{V_{S,\overline{n}} + E + V_T}{E - V_T} \tag{5.2}$$

is fulfilled, which we suppose true in the rest of this section. Otherwise, V_t merely oscillates between two values and no charge ever flows in the circuit, as explained for the generic circuit in Sec. 2.1.2. Note that $V_T > 0$ increases the requirement on η. Then, the diode D_2 connects C_t and C_S and the charge conservation equation yields

$$C_t \in [C_1\,; C_{max}], \quad V_t C_t + V_S C_S = V_{t,\overline{n}} C_{max} + V_{S,\overline{n}} C_S. \tag{5.3}$$

The mesh rule gives

$$C_t \in [C_1\,; C_{max}], \quad V_S = V_t - E - V_T \tag{5.4}$$

Thus, at $C_t = C_{min}$, and by combining (5.3) and (5.5, we have that

$$V_{S,\underline{n+1}} = \frac{C_S}{C_{min} + C_S} V_{S,\overline{n}} + E\frac{C_{max} - C_{min}}{C_{min} + C_S} - V_T \frac{C_{max} + C_{min}}{C_{min} + C_S}. \tag{5.5}$$

Then, when C_t goes from C_max to C_min, as the diode D_1 blocks any charge flowing through C_S, we just have

$$V_{\mathrm{S},\overline{\mathrm{n+1}}} = V_{\mathrm{S},\underline{\mathrm{n+1}}}, \tag{5.6}$$

and C_t's voltage decreases, until it reaches C_2 which is defined as

$$C_2 \coloneqq \frac{C_\mathrm{min} V_{\mathrm{t},\underline{\mathrm{n+1}}}}{E - V_\mathrm{T}}. \tag{5.7}$$

Because of the diode D_1 which ensures that at all times, $V_\mathrm{t} < E - V_\mathrm{T}$, C_2 is necessarily reached by C_t. The biasing cycle of C_t hence finishes by

$$C_\mathrm{t} \in [C_2\,; C_\mathrm{max}], \quad V_\mathrm{t} = E - V_\mathrm{T}, \tag{5.8}$$

as diode D_2 conducts.

The non-idealized (non-rectangular) charge-voltage diagram is immediately found. The slope at V_L is vertical. The slope corresponding to the segment where charges are exchanged between C_t and C_S is of $-C_\mathrm{S}$. The charge-voltage diagram for HW2 is symmetrical to that of HW1 with respect to $V_\mathrm{t} = E$, and both are depicted in Fig. 5.1d and Fig. 5.1d.

All we need for this measurement method are these local cycle-to-cycle evolution laws. The reader may verify that, for $V_\mathrm{T} = 0$, the explicit solution for all n is given by the relations presented in Sec. 2.3.1.2.

The equation (5.5) gives the evolution of the voltage across C_S, which does not depend on whether $C_\mathrm{t} = C_\mathrm{max}$ or $C_\mathrm{t} = C_\mathrm{min}$ because of (5.6). Thus, to lighten notations for the present chapter, instead of using the notations of Chap. 2, we will denote by V_1 and V_2 the voltage across the fixed capacitor C_S at $C_\mathrm{t} = C_\mathrm{max}$ of a given variation cycle of C_t, for the HW1 and HW2 circuits respectively. The labels V_1' and V_2' denote the voltage across the fixed capacitor C_S at $C_\mathrm{t} = C_\mathrm{max}$ of the following cycle, for the HW1 and HW2 circuits respectively. We also define $\Delta_1 \coloneqq V_1' - V_1$ and $\Delta_2 \coloneqq V_2' - V_2$. We keep the notation $\eta \coloneqq C_\mathrm{max}/C_\mathrm{min}$.

Under these conditions, the evolution law of the voltage across C_S from a cycle of variation of C_t to the next (either at $C_\mathrm{t} = C_\mathrm{max}$ or $C_\mathrm{t} = C_\mathrm{min}$), reads

$$V_1' = \frac{C_\mathrm{S} V_1 + (C_\mathrm{max} - C_\mathrm{min})E - (C_\mathrm{max} + C_\mathrm{min})V_\mathrm{T}}{C_\mathrm{min} + C_\mathrm{S}}, \tag{5.9}$$

$$V_2' = \frac{C_\mathrm{S} V_2 + (C_\mathrm{max} - C_\mathrm{min})E - (C_\mathrm{max} + C_\mathrm{min})V_\mathrm{T}}{C_\mathrm{max} + C_\mathrm{S}}, \tag{5.10}$$

$$\tag{5.11}$$

so that

$$\Delta_1 = \frac{(C_\mathrm{max} - C_\mathrm{min})E - (C_\mathrm{max} + C_\mathrm{min})V_\mathrm{T} - C_\mathrm{min} V_1}{C_\mathrm{min} + C_\mathrm{S}}, \tag{5.12}$$

$$\Delta_2 = \frac{(C_\mathrm{max} - C_\mathrm{min})E - (C_\mathrm{max} + C_\mathrm{min})V_\mathrm{T} - C_\mathrm{max} V_2}{C_\mathrm{max} + C_\mathrm{S}},. \tag{5.13}$$

We now describe the methods for characterizing respectively E and η as affected by the electromechanical coupling, based on these local dynamics.

5.2 Characterization method for the lumped-model parameter E

5.2.1 Motivation

In the previous chapters, we used the convenient lumped representation of electret-charged transducers as an equivalent constant voltage source in series with a variable capacitance. Such lumped-parameter models are expected to yield accurate predictions on the e-VEH dynamics, and to guide optimization choices in the conditioning circuit design. To do this, these models have to be parametrized accurately. For instance, the electrical domain comparisons done in the previous chapter have shown the importance of the value of E in deciding which charge-pump has the best performances under the given constraints.

The issue is that value of this important parameter is difficult to define precisely at the fabrication stage. Plus, it may decrease with time [BCD13], so it is necessary to be able to measure it after fabrication.

Until now, different techniques were used to do so. A first technique consists in measuring the device's surface potential, with a contact-less electrostatic voltmeter. Ideally, this measurement has to be done on top of the electret-charged plate of the transducer. However, this is difficult to perform on a wide range of e-VEHs because of the geometry of their transducer. For example, it is difficult to insert the needle of an electrostatic voltmeter in between the electrodes of an interdigitated gap-closing transducer such as in Fig. 1.24 which has a separating gap of about 50 µm between the fingers. Also, this technique gives a measure of a potential which is hard to accurately relate to the value of the lumped parameter E. Indeed, our derivation in Sec. 1.4.2.2 is based on the hypothesis of an uniform charge distribution across the dielectric layer. This hypothesis is not always verified, depending on both the employed charging technique and the transducer geometry [LOC16; RAE15].

Another technique consisted in manually adding a reverse voltage source in series with the transducer, so as to cancel out the electret's effect. To do so, the transducer is submitted to vibrations, and is put in the primitive conditioning circuit configuration as for the measurement described in Sec. 1.5.2. The voltage swing across the load resistance is then measured for different values of the reverse voltage source, until finding the reverse voltage value that results in a null voltage swing across the resistor. At this value of the source, its voltage cancels out the effect of the electret and can be considered equal to $-E$. The problem here with this procedure is that the nullification of the voltage swing across the resistor can be due to the fact that, for each different value of the manually added reverse voltage, the loading resistance, if unchanged, is not optimal anymore, rather than because we have found the exact opposite value of E. Also, it is not exactly clear how the effect of adding a reverse bias affects the electret layer, but it seems that it contributes to its depolarization.

The method proposed hereafter is non-destructive and allows to measure the value of E for a given transducer of, in principle, arbitrary geometry and charged with any technique. This is done indirectly by measuring the direct effect of E on the dynamics of charge-pump conditioning circuits, so the effective value of the lumped parameter can be estimated.

5.2.2 Description of the method

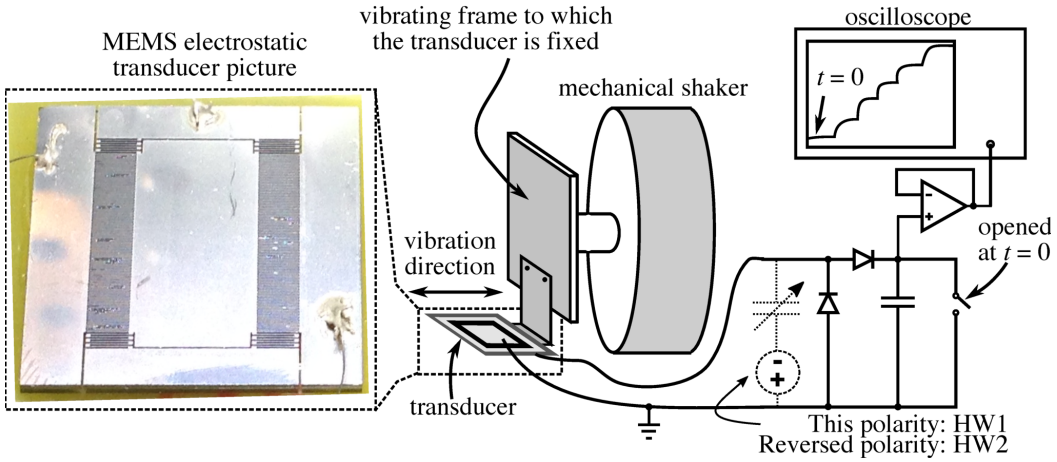

Figure 5.2: Setup used for the measurement of the electret potential, with a top-view picture of the electret MEMS transducer. The device dimensions are 1.5cm × 1.6cm × 380µm. This illustration features the transducer connected to the HW1 circuit to get (V_1, Δ_1). For the measurement method, the same setup has to be used afterwards with the HW2 circuit, that is, with the polarity of the transducer reversed, to get (V_2, Δ_2).

The measurement method is based on the dynamics of the half-wave circuits HW1 and HW2, depicted in Fig. 5.1a and 2.8b, respectively. Consider the transducer as a part of the circuit configurations HW1 or HW2, with C_t cyclically time-varying between maximum and minimum values (C_max, C_min), subsequently to a mechanical input excitation of the e-VEH (the same input for both circuit configurations). The choice of the input vibrations is not important as long as it results in the same values C_max and C_min at each cycle. Let us suppose that we use a harmonic input in the following.

In these conditions, when the transducer is connected to HW1 or HW2 charge-pump, the voltage across C_S evolves. This experimental setup is depicted in Fig. 5.2.

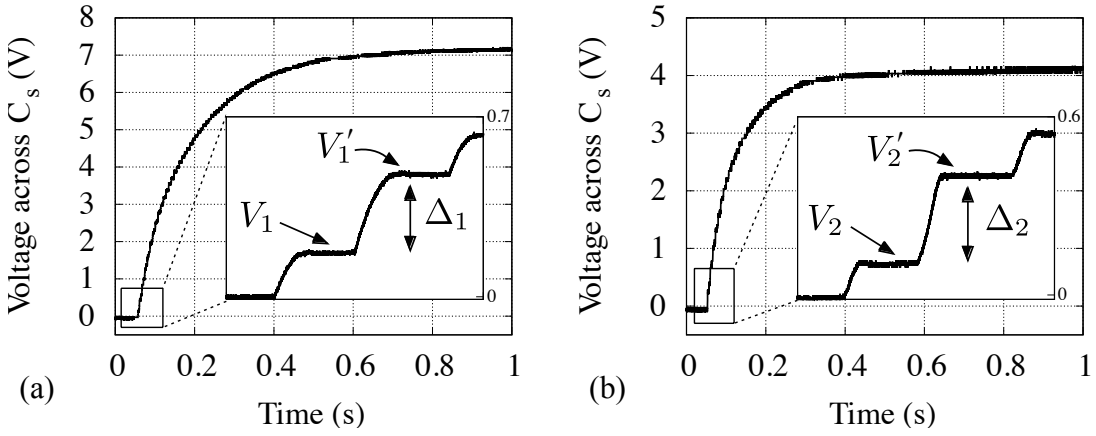

Figure 5.3: Example of measurements of $(\Delta_1, \Delta_2, V_1, V_2)$, measured on the MEMS electret transducer characterized in Sec. 5.2.4 below.
(a) Measured voltage across C_S with HW1 circuit.
(b) Measured voltage across C_S with HW2 circuit.

By monitoring the time-evolution of the voltages across C_S when the transducer is biased by HW1, the quantities (Δ_1, V_1) can be measured. Then, the circuit is changed to HW2 (i.e., the transducer is reversed polarity) and, similarly, (Δ_2, V_2) can be measured. To illustrate these

measurements, an experimental example of measurement of $(\Delta_1, \Delta_2, V_1, V_2)$ is shown in Fig. 5.3. These measurements are obtained with the device presented hereafter in the results of Sec. 5.2.4.

From (5.9) and (5.10), it comes that the measured $(\Delta_1, \Delta_2, V_1, V_2)$ can be linked to E and $C_{\max}$ by:

$$C_{\max} = \frac{C_S(\Delta_1 - \Delta_2) + C_{\min}(\Delta_1 + V_1)}{\Delta_2 + V_2}, \tag{5.14}$$

$$E = \frac{(C_{\min} + C_S)\Delta_1 + C_{\min}V_1 + (C_{\max} + C_{\min})V_T}{C_{\max} - C_{\min}}. \tag{5.15}$$

The value of $C_{\min}$ can be measured by a synchronous detection method [BGP09]. Note that in the case of interdigitated-combs transducer geometries, $C_{\min}$ is fixed independently of the harmonic input acceleration. Hence, it can be measured even more simply by traditional means of measurement of fixed capacitances, e.g., using a capacitance meter.

5.2.3 Measurement errors and choice of the circuit's parameters

5.2.3.1 On the reason for using two different circuits

In the measurement method as explained above, one could argue that if both $C_{\max}$ and $C_{\min}$ can be measured by synchronous detection, then (5.15) suffices, and measurements using HW1 suffice. In fact, the circuit HW2 has to be used in addition to the circuit HW1 as a mean to quantify the systematic error due to the electromechanical coupling. Let us explain this in more detail.

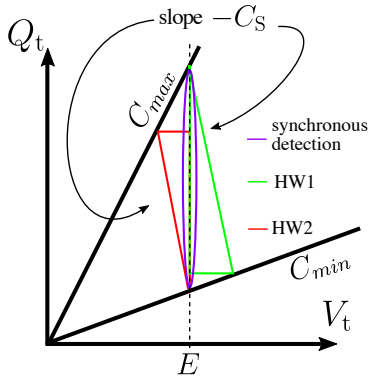

Figure 5.4: Comparison of the different biasing schemes between the circuit used for synchronous detection, HW1 and HW2 circuits. The width are exaggerated in order to make the figure clearer.

Suppose that we have measured $C_{\max}$ and $C_{\min}$ using synchronous detection. Their values depend on how the transducer was biased by the primitive conditioning circuit used for this measurement, because of the effect of the electromechanical coupling, as highlighted in Sec. 1.3.4. The electrostatic forces that are generated on the e-VEH's mobile mass throughout each cycle of C_t's variation are not the same with the HW1 circuit and the primitive conditioning circuit. This affects the dynamics of the mobile mass in different ways with each circuit, and as a result, the values of $C_{\max}$ and $C_{\min}$ are not necessarily the same depending on whether the transducer is in the HW1 circuit configuration or in the primitive conditioning circuit (for synchronous detection) configuration.

Hence, it has to be ensured that the values of $(C_{\max}, C_{\min})$ are the same in between its measurement by synchronous detection and when HW1 was used to get Δ_1. This is possible, as the synchronous detection method basically implements the primitive conditioning scheme presented in Sec. 1.3.2.3, and depicted again here as a violet contour in Fig. 5.4. If the resistance used for the measurement is low enough, which is the case in practice and can always be achieved by tuning the frequency of the carrier, then the implemented biasing will be a constant voltage. If we choose V_1 and V_2 close to zero with HW1 circuit, and if C_{S} is large enough, then the HW1 circuit will tend to implement the same biasing of the transducer. This is visible in Fig. 5.4: when V_1 and V_2 are small, when C_{S} is large, and when the violet contour degenerates into a line, then the violet and green contours become the same. But then, the uncertainty on E due to random error increases. This is inferred from the fact that, if we neglect all uncertainties except that on the voltage measurement, and defining

$$\zeta := \frac{C_{\mathrm{S}}}{C_{\min}}, \tag{5.16}$$

then the relative uncertainty on E due to random error sources in a broad sense (e.g., thermal, reading amplifier, and quantization noises) can be found, as a function of the effective value of the measurand E. Since

$$\frac{\delta_E}{E} = \frac{\delta_V}{E}\frac{\partial E}{\partial \Delta_1} \tag{5.17}$$

it comes, using (5.12), that

$$\frac{\delta_E}{E} = \frac{\delta_V}{E - V_{\mathrm{T}}}\frac{1+\zeta}{\eta}, \tag{5.18}$$

where we have denoted by δ_V the uncertainty on the measured voltage across C_{S} that is due to the superposition of these random error sources. We now see that this error increases with C_{S}.

Subsequently, a small enough value of C_{S} has to be chosen, resulting in an acceptable random-error uncertainty. At the same time, the chosen value of C_{S} should be large so that the electromechanical coupling effect does not result in different $(C_{\max}, C_{\min})$ between their values as measured by synchronous detection, and the measurement using HW1 that yielded Δ_1. This is hardly guaranteed without having another measurement reference. In our method, this is done by using the additional charge-pump HW2. We now explain the procedure allowing to select the optimum value of C_{S} in order to guarantee that the electromechanical error does not induce a systematic error on the measurement, whilst reducing the uncertainty due to random error sources.

5.2.3.2 Choice of the parameters and error minimization procedure

To accurately measure E for a given transducer using (5.15), it is necessary to wisely choose C_{S}, V_1, V_2, and the input acceleration. We now propose a procedure to do so.

Using the two charge-pump circuits HW1 and HW2, and still supposing that the uncertainty on V_{T} and $C_{\min}$ can be neglected, as well as $V_1 = V_2 = 0$, the relative uncertainties on $C_{\max}$ and

E due to random error sources are found by computing

$$\frac{\delta_{C_{\max}}}{C_{\max}} = \frac{\delta_V}{C_{\max}}\sqrt{\left(\frac{\partial C_{\max}}{\partial \Delta_1}\right)^2 + \left(\frac{\partial C_{\max}}{\partial \Delta_2}\right)^2}, \tag{5.19}$$

$$\frac{\delta_E}{E} = \frac{\delta_V}{E}\sqrt{\left(\frac{\partial E}{\partial \Delta_1}\right)^2 + \left(\frac{\partial E}{\partial \Delta_2}\right)^2} \tag{5.20}$$

which yields, using (5.12) and (5.13),

$$\frac{\delta_{C_{\max}}}{C_{\max}} = \delta_V \frac{(\eta+\zeta)\sqrt{(1+\zeta)^2+(\eta+\zeta)^2}}{\eta(E(\eta-1)-V_{\mathrm{T}}(\eta+1))} \tag{5.21}$$

$$\frac{\delta_E}{E} = \delta_V \frac{\sqrt{(\eta+\zeta)^4(E-V_{\mathrm{T}})^2+(1+\zeta)^2(E(1+\zeta)-V_{\mathrm{T}}(\zeta-1))^2}}{E(E(\eta-1)^2-V_{\mathrm{T}}(\eta^2-1))} \tag{5.22}$$

From (5.21) and (5.22), it comes that the measurement uncertainty due to random error sources decreases by decreasing C_{S}, as was inferred above in Sec. 5.2.3.1 when considering the sole measurement of E.

However, decreasing C_{S} increases the differential effect of the electromechanical coupling on the e-VEH's dynamics between the biasing done with HW1 and with HW2. This can be inferred by comparing the charge-voltage diagrams for both circuit configurations, in Fig. 5.4: as C_{S} becomes small, the biasing of the transducer tends to differ from HW1 to HW2 (remember that $V_1 = V_2 \approx 0$).

The different impacts of the electromechanical coupling in between the two circuit configurations induces a systematic measurement error on $C_{\max}$ and E. This is because equations (5.14) and (5.15) are derived from (5.9) and (5.10) assuming that $(C_{\max}, C_{\min})$ with circuit HW1 (in (5.9)) are equal to $(C_{\max}, C_{\min})$ with circuit HW2 (in (5.10)). But as we said, the evolution of the biasing of the transducer using the two circuits are different. In general, $(C_{\max}, C_{\min})$ with circuit HW1 cannot be considered equal to $(C_{\max}, C_{\min})$ with circuit HW2.

On the other hand, the charge-voltage diagrams depicted in Fig. 5.4 show that, by choosing C_{S} large and $V_1 = V_2 \approx 0$, the conditioning scheme of both HW1 and HW2 at the scale of one cycle of C_{t} tend to become alike. Therefore, increasing C_{S} reduces the systematic measurement error due to the differential impact of the electromechanical coupling.

In summary, there is a principle of uncertainty at work here, and a trade-off has to be found. Smaller C_{S} increases the systematic error due to the electromechanical coupling, but too large C_{S} increases the effect of random error sources on the measurement.

Hence, the following procedure is proposed to choose C_{S} so as to reduce the measurement uncertainty due to random error sources, whilst ensuring that the systematic error due to the electromechanical coupling remains negligible. An admissible value for δ_E/E is decided a priori, and solving (5.22) for ζ gives the corresponding C_{S}. Note that this supposes an a priori estimation of η and E. The former can be measured by synchronous detection [BGP09]. The latter can be estimated by one or several first inaccurate measurements (i.e., using an arbitrary value for C_{S} for the first measurement).

The measurements are then carried out with this value of C_{S}. If $C_{\max}$ obtained from (5.14) is

consistent with its value measured by synchronous detection, then E obtained from (5.15) using the same measured $(\Delta_1, \Delta_2, V_1, V_2)$ can be considered accurate. Indeed, this means that the biasing schemes across the three circuits are alike such that the value of $C_{\max}$ can be considered to be the same across all three circuits.Otherwise, C_S that satisfies the desired relative uncertainty δ_E/E results in a large systematic error on $C_{\max}$, and hence on E: it cannot be guaranteed that $C_{\max}$ and $C_{\min}$ had the same value during both measurements of Δ_1 (with HW1) and Δ_2 (with HW2). In this case, the measurement has to be carried out again with a larger C_S. The systematic error due to the electromechanical coupling will decrease, but the admissible uncertainties on E and $C_{\max}$ due to random error sources will increase.

Finally, the measurement uncertainty can also be decreased by increasing η as (5.21) and (5.22) show. This is done by increasing the amplitude of the mechanical harmonic input. But as η results from the dynamics of the e-VEH's mechanical part, it is harder to use the input amplitude as a control parameter on the error.

Note that a technique employing the HW1 circuit has been used for electret potential measurement in [LOC16], similar to the method presented in this chapter, but using saturation voltages instead of local evolution voltages. Because of this, the method in [LOC16] only holds if both $C_{\max}$ and $C_{\min}$ are fixed throughout the voltage evolution until saturation. In the presence of electromechanical coupling, this hypothesis is not fulfilled and hence, this method gives inaccurate results.

5.2.4 Application of the method: experimental results

In this section, the method is applied to a micro-scale electrostatic transducer realized in MEMS technology. The same device as used for these measurements is presented in [LOC16]. As the transducer has a symmetrical gap-closing, interdigitated-combs geometry, $C_{\min}$ is fixed. For the same reason, at each period of each harmonic input, C_t reaches its maximum and its minimum twice: the frequency of C_t variation is twice the frequency of the input. This was already discussed in Sec. 4.3. It is important to note that with the present device, the two maximum of C_t that are reached at each period of the input excitation are not the same. In other words, there exists two values of $C_{\max}$ for each harmonic mechanical input excitation the device is submitted to[LOC16]. This is likely due to slight fabrication asymmetry, which because of the hyperbolic capacitance versus displacement function (see (1.9)) translates to several picofarads of difference between the two values of $C_{\max}$. The electrostatic force due to the electret may also be responsible for this phenomenon (wee have seen in the simulations of Chap 4 that the effects of the electrical biasing can induce such behavior).

For the measurement, two inputs are chosen: 1.5g and 2g amplitude, both of 150Hz frequency. Our experimental setup is such that the device is continuously submitted to the input vibrations, and C_S is first short circuited. Then, the short circuit is opened and the voltage evolution across C_S starts. But the time at which the short circuit is opened cannot be exactly chosen as corresponding to an extrema of C_t. To ensure that the measured values of Δ_1 and Δ_2 results from a complete cycle of variation of C_t, the first cycle of voltage evolution across C_S is ignored with both circuits. Hence, V_1, V_2 are slightly above zero (see Fig. 5.3). Note that this fact makes the uncertainty on V_1 and V_2 non negligible anymore – terms $\partial/\partial V_1$ and $\partial/\partial V_2$ have to be added in (5.19) and (5.20) – but we nevertheless carry on the method with this slight inaccuracy in the

uncertainties express in (5.19) and (5.20). Also, because of the existence of two values of $C_{\max}$, one has to discriminate between the Δ_1 and Δ_2 that are due to each value of $C_{\max}$. This can be done easily considering that (5.12) and (5.13) show that a larger $C_{\max}$ results in a larger $\Delta_{1,2}$.

To estimate the influence of random error sources on the measurement using (5.21) and (5.22), E is first estimated to be 20V, by a surface potential measurement done 1mm on top of the device's inertial mass, using a contact-less electrostatic voltmeter. The two couples of values of η are first measured by synchronous detection, and the results are depicted in Fig. 5.5a and Fig. 5.5b. The value of δ_V is estimated to be 25mV by averaging the measured voltages across a charged capacitor for which the voltage across is known, using the same setup as for the measurements done for the method. Using (5.22), the theoretical uncertainty on E decreases from 16.6% with the smallest $C_{\max}$, to 4.2% with the largest $C_{\max}$, all with $C_S = 100$pF.

These uncertainty intervals are satisfactory for this example, so the fixed capacitor is chosen as $C_S = 100$pF. As $C_{\min}$ is fixed with our transducer geometry, we measure its value Using a capacitance meter, which yields $C_{\min} = 60$pF. The used diodes are JPAD5, whose parasitic capacitances values are negligible compared to C_S, and V_T is measured as $V_T = 0.7$V for typical values of current in our application. The amplifier used for the measurement is an AD549KHZ.

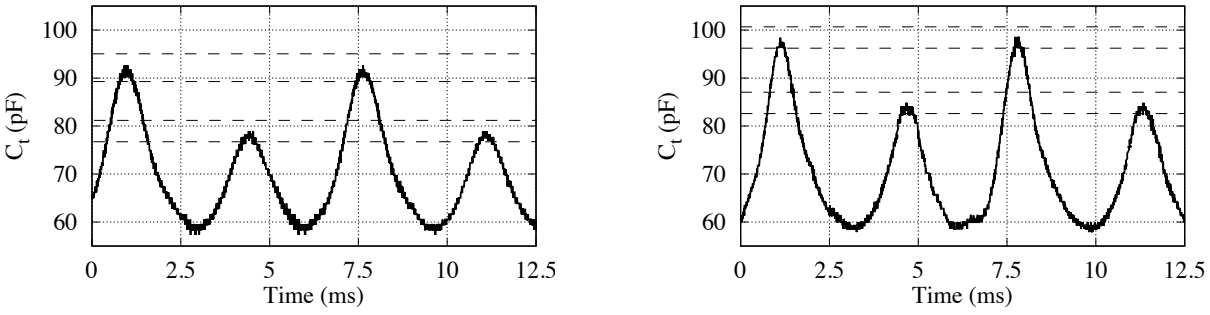

(a) Input amplitude of 1.5g, frequency of 150 Hz.

(b) Input amplitude of 2g, frequency of 150 Hz.

Figure 5.5: C_t variation characterized by synchronous detection for different amplitudes of the input excitation. The dashed lines represent the error on the values of $C_{\max}$.

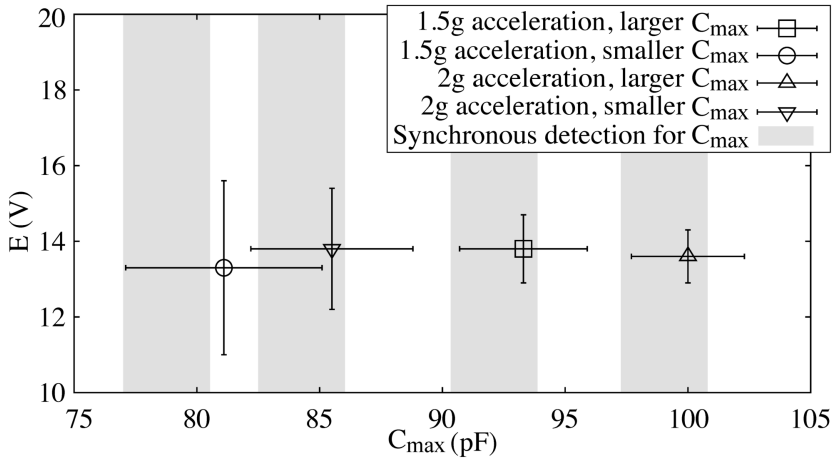

Figure 5.6: Measurement results for E and $C_{\max}$.

The results of the measurement method are depicted in Fig. 5.6. Each point corresponds to $(E, C_{\max})$ obtained by averaging 5 measurements of $(\Delta_1, \Delta_2, V_1, V_2)$. The error bars represent the uncertainties obtained on $(\Delta_1, \Delta_2, V_1, V_2)$ propagated to $(E, C_{\max})$. An example of a

single measurement of $(\Delta_1, \Delta_2, V_1, V_2)$ obtained with the present device is depicted in Fig. 5.3. The results in Fig. 5.6 show that the obtained $C_{\max}$ are in accordance with those measured by synchronous detection. This guarantees that the systematic error due to the electromechanical coupling is negligible. As expected, the uncertainty on E decreases when the input amplitude increases (see end of Section 5.2.3). Using the most accurate result, the electret potential is measured as $E = 13.7\text{V} \pm 5.1\%$. The uncertainty is slightly increased compared to the theoretical uncertainty obtained from (5.22), because of the lower effective value of E compared to its first estimation, and $V_1, V_2 > 0$.

To further validate the method, a voltage source of 5V is added in series with the transducer to simulate a different value of the electret potential, and the measurement is carried out again. The expected value of the lumped voltage source is then of $E + 5$ by superposition, where E is $E = 13.7\text{V} \pm 5.1\%$ measured above. The used input is of 2g amplitude and 150Hz frequency. The synchronous detection method gives $C_{\max} = 102\text{pF} \pm 3\%$ (the lower value of $C_{\max}$ is discarded). From (5.22), keeping $C_S = 100\text{pF}$, with an expected value of $E = 18.7\,\text{V}$, results in an error of 3.7% on E. Using this value of C_S, the measurement yields a value of $E = 23.1\text{V} \pm 3.8\%$ and $C_{\max} = 93\text{pF} \pm 3.1\%$. The value of $C_{\max}$ does not agree with what is measured by synchronous detection, which means that the systematic error due to the electromechanical coupling is large: that is why the measured value of E is measured greater than expected. Hence, the error minimization procedure discussed at the end of section 5.2.3 is applied: the admissible random error on E is relaxed to 7.5%, yielding $C_S = 180\text{pF}$. The new measurement gives $C_{\max} = 103\text{pF} \pm 4.2\%$, which is in accordance with the value measured by synchronous detection. The electret potential is measured as $E = 19\text{V} \pm 6.8\%$, which is the expected value after adding the 5V external voltage.

The value of E characterized is below the value of $E = 20\,\text{V}$ reported in [LOC16], although the same device was used. This can be attributed to two reasons. First, as the last paragraph of Sec. 5.2.3 points out, the method of characterization of E used in [LOC16] is not accurate because it does not take into account the fact that the electromechanical coupling effect on the measurement. Addressing this issue was precisely the role of the error minimizing procedure we carried out. Secondly, the measurements in [LOC16] and in the present work were done separated by a time interval that may have caused the electret charging to degrade.

5.3 Characterization method for $C_{\max}$ and $C_{\min}$ under charge-pump conditioning

5.3.1 Motivation

In the previous chapter, it was emphasized that the overall dynamics, and hence the performances of e-VEHs, are greatly affected by which charge-pump conditioning circuit is used. This is the dependence of the electromechanical coupling effect on the characteristic voltages V_L and V_R of an energy conversion cycle. This was again emphasized above in Sec. 5.2.3 about the systematic error induced by the electromechanical coupling on the measurement of E.

In order to have predictive models from which optimization and comparison can be done, a method was developed in the previous chapter in order to approximate figures such as the

optimum power point (see Sec. 4.3).

To confront the predictions yielded by such models to experiments, it should be checked if they predict accurately the amplitude of the capacitance variation for cycles given in terms of their $(V_{\mathrm{L}}, V_{\mathrm{R}})$. To this end, we present a variant of the method presented above in Sec. 5.2. This new method allows the measurement of the value of $C_{\max}$ and $C_{\min}$ as affected by the biasing imposed by a charge-pump conditioning circuit, for an electrostatic transducer submitted to a given input.

The synchronous detection method mentioned above is hardly usable to carry on this measurement, as the resistance would interfere with the working of the conditioning circuit. Plus, the carrier would be superposed to the voltage across the transducer (which alternates between V_{L} and V_{R} at each cycle of the capacitance variation), which can yield measurement errors when computing the phase shifts. An optical measurement of the capacitance variation during the e-VEH's operation is possible, but the needed equipment is not available in all characterization laboratories.

5.3.2 Description of the method

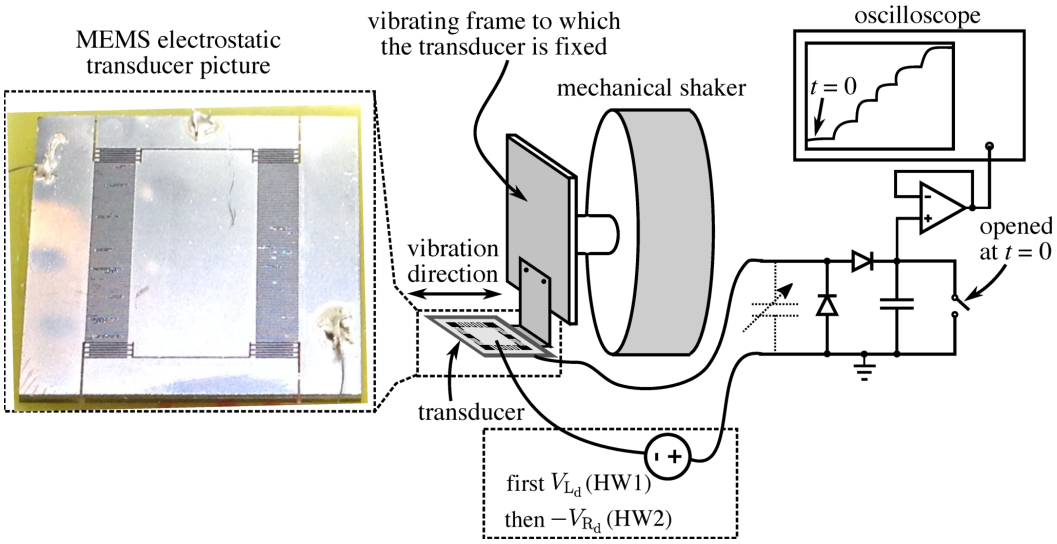

Figure 5.7: Setup used for the measurement of $C_{\max}$ and $C_{\min}$ affected by a charge-pump conditioning circuit biasing of characteristic cycle voltages $V_{\mathrm{L_d}}$ and $V_{\mathrm{R_d}}$. This illustration features the transducer connected to the HW1 and HW2 circuits by setting the right value for the added voltage source, in order to measure (V_1, Δ_1) and(V_2, Δ_2).

The goal is to measure the value of $C_{\max}$ and $C_{\min}$ of a transducer submitted to a given input excitation and for a given charge-pump biasing that we characterize in terms of voltages V_{L} and V_{R}, in the light of the theory exposed in Chap. 2. The essence of the method is to bias the transducer with the rectangular charge-voltage diagram defined by the desired V_{L} and V_{R} (that we will denote in the following by $V_{\mathrm{L_d}}$ and $V_{\mathrm{R_d}}$) using the HW1 and HW2 charge-pumps, while the transducer is submitted to the excitation for which we wish to measure $C_{\max}$ and $C_{\min}$.

Let us suppose that $E = 0$. The method is readily generalizable to a case where $E > 0$. A voltage source is added manually in series with the transducer (at the place of E), of value selected as $V_{\mathrm{L_d}}$. Then, the transducer is put in the experimental set-up depicted in Fig. 5.7,

where the chosen mechanical input has to be that for which it is desired to measure the value of $C_{\max}$. Under the variation of C_t, the voltage across C_S evolves (autonomous operation of a charge-pump). When the voltage across C_S is equal to $V_{R_d} - V_{L_d}$, the transducer is effectively biased following a rectangular charge-voltage diagram of extreme voltages V_{L_d} and V_{R_d}. This is true as long as C_S is large enough so that the rectifier charge-pumps effectively implement an ideal rectangular charge-voltage diagram. The values of (Δ_1, V_1) are measured around this point, that is, where V_1 is as close as possible to $V_{R_d} - V_{L_d}$.

Then, we change HW1 by HW2, that is, we reverse the polarity of the manually added voltage source, and set this time its absolute value to V_{R_d}. As with HW1, we let the voltage across C_S evolve, passing through $V_{R_d} - V_{L_d}$. When this happens, the transducer is again effectively biased following a rectangular charge-voltage diagram of extreme voltages V_{L_d} and V_{R_d}. Again, (Δ_2, V_2) are measured around this point, that is, when V_2 is as close as possible to $V_{R_d} - V_{L_d}$. An example illustrating how $(\Delta_1, \Delta_2, V_1, V_2)$ have to be measured is depicted in Fig. 5.8.

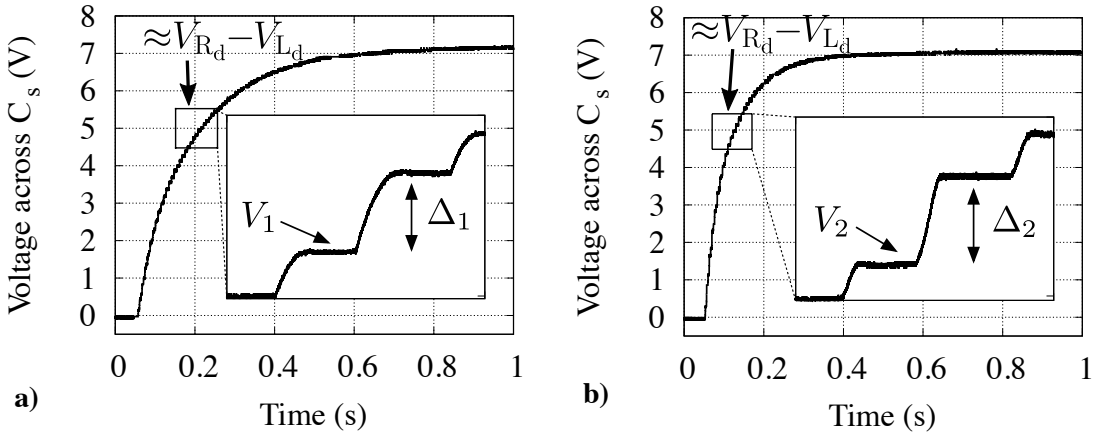

Figure 5.8: Experimental measurement of $(\Delta_1, \Delta_2, V_1, V_2)$, measured on the MEMS electret transducer characterized in section 5.3.4 and reported in [LOC16].
(a) Measured voltage across C_S with HW1 circuit.
(b) Measured voltage across C_S with HW2 circuit.

We are left with a set of measurements $(\Delta_1, \Delta_2, V_1, V_2)$. From (5.12) in which we substitute $E \leftarrow V_{L_d}$, and (5.13) in which we substitute $E \leftarrow V_{R_d}$, we have that

$$C_{min} = C_S \frac{\Delta_2(E_1 - V_T) - \Delta_1(E_2 - V_T - \Delta_2 - V_2)}{(E_1 + \Delta_1 + V_1 + V_T)(E_2 - \Delta_2 - V_2 - V_T) - (E_1 - V_T)(E_2 + V_T)}, \tag{5.23}$$

$$C_{max} = \frac{C_S\Delta_2 + C_{min}(E_2 + V_T)}{E_2 - V_2 - \Delta_2}. \tag{5.24}$$

Let us mention a last point before discussing the measurement errors. As we let the voltage across C_S evolve from 0 to $V_{R_d} - V_{L_d}$, the transducer is biased by cycles $(V_{L_d}, V_{L_d} + V)$ for HW1 and $(V_{R_d} - V, V_{R_d})$, where V denotes the voltage across C_S and evolves from zero to the saturation of the charge-pump. Now, one or both of the charge-pumps may in fact saturate before $V = V_{R_d} - V_{L_d}$ is reached. This means that the evolving value of $C_{\max}/C_{\min}$, as impacted by the evolving biasing of the charge-pump, reaches a point where the converted energy becomes null. We denote here by V_{sat} this saturated value of V. In the light of (2.14) with $E = 0$, this saturation implies that $C_{\max}/C_{\min} = V_{sat}/V_{L_d}$ (if the saturation is observed in the HW1 configuration) or $C_{\max}/C_{\min} = V_{R_d}/V_{sat}$ (if the saturation is observed in the HW2 configuration), for $C_{\max}$ and

$C_{\min}$ impacted as C_{t} is biased by the cycle $(V_{\mathrm{L_d}}, V_{\mathrm{sat}})$ (for HW1) or $(V_{\mathrm{sat}}, V_{\mathrm{R_d}})$ (for HW2). Nothing can be concluded about the value of $C_{\max}$ and $C_{\min}$ when the transducer is biased by the cycle of interest $(V_{\mathrm{L_d}}, V_{\mathrm{R_d}})$. This case is encountered in one of the measurements done below in Sec. 5.3.4 (see the N/A* cell in Table 5.1).

5.3.3 Measurement errors and choice of the parameters

In the same way as it was done in the previous method, it is possible to compute the uncertainty due to random errors on the measurement, as a function of the measurement parameters. As V_1 and V_2 are no longer considered null, the uncertainty on their measurement, due to random error sources, has to be taken into account. Hence, this uncertainty is linked to the measurement parameters and to the effective value of the measurand following

$$\frac{\delta_{C_{\min}}}{C_{\min}} = \frac{\delta_V}{C_{\min}} \sqrt{\left(\frac{\partial C_{\min}}{\partial \Delta_1}\right)^2 + \left(\frac{\partial C_{\min}}{\partial \Delta_2}\right)^2 + \left(\frac{\partial C_{\min}}{\partial V_1}\right)^2 + \left(\frac{\partial C_{\min}}{\partial V_2}\right)^2}, \tag{5.25}$$

$$\frac{\delta_E}{E} = \frac{\delta_V}{C_{\max}} \sqrt{\left(\frac{\partial C_{\max}}{\partial \Delta_1}\right)^2 + \left(\frac{\partial C_{\max}}{\partial \Delta_2}\right)^2 + \left(\frac{\partial C_{\max}}{\partial V_1}\right)^2 + \left(\frac{\partial C_{\max}}{\partial V_2}\right)^2} \tag{5.26}$$

where again Δ_1 and Δ_2 are substituted by their expression in (5.12) and (5.13), whereas V_1 and V_2 have to be both substituted by $V_{\mathrm{R_d}} - V_{\mathrm{L_d}}$. One should note that with the previous method, we could tune two parameters (C_{S} and η) in order to optimize the measurement with regard to both the random and systematic errors. Here, η is a measurand, so only C_{S} remains as a lever. Also note that we still have supposed that the uncertainty on C_{S} and V_{T} are negligible. We add that the uncertainties on the voltages imposed by the voltage sources (first $V_{\mathrm{L_d}}$ then $V_{\mathrm{R_d}}$) are negligible as well.

The expressions arising from (5.25) and (5.26) are rather cumbersome. Let us, in the following, deal with the case of a device where $C_{\min}$ is fixed, essentially because of a symmetrical gap-closing geometry, as for the device above. This allows to only consider (5.24), with $C_{\min}$ supposed known. The random error on $C_{\max}$, as a function of the effective values of the parameters and of the measurand, reads

$$\frac{\delta_{C_{\max}}}{C_{\max}} = \frac{\delta_V}{V_{\mathrm{R_d}} - V_{\mathrm{T}}} \frac{1+\zeta}{\eta}. \tag{5.27}$$

Again, the tolerated uncertainty due to random error sources has to be balanced with the systematic error arising from the electromechanical coupling. We remind that this error is due to the different transducer biasing between the conditioning circuit HW1 and HW2, as is visible on the charge-voltage diagrams of Fig. 5.1c and Fig. 5.1d. As for the previous method, increasing C_{S} reduces the differential effect of the electromechanical coupling between the two configurations HW1 and HW2, and hences lowers the associated systematic error. But additionally, for the present measurement, our goal is to measure $C_{\max}$ and $C_{\min}$ as affected by an idealized charge-pump biasing at the scale of one cycle. This corresponds to the biasing of C_{t} as implemented by the generic circuit of Sec. 2.1.2, or equivalently, described by an ideal, rectangular charge-voltage diagram. This is another reason as of why C_{S} should be chosen large enough: the biasing conditions when measuring $C_{\max}$ and $C_{\min}$ using our method with HW1 and HW2 circuits have to be as close as possible to the biasing described by an ideal, rectangular charge-voltage diagram.

This is illustrated in Fig. 5.9.

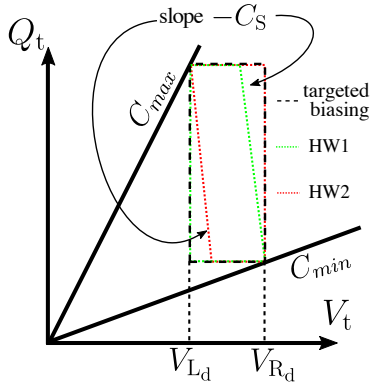

Figure 5.9: Comparison of the non-ideal charge-voltage diagrams of the HW1 and HW2 charge-pumps, with the ideal rectangular charge-voltage diagram given in terms of $(V_{\mathrm{L_d}}, V_{\mathrm{R_d}})$.

The method as is offers no procedure to optimize the value of C_{S} so as to reduce the systematic measurement error due to the differential impact of the electromechanical coupling. However, in the case of fixed $C_{\min}$, (5.23) can be used as a mean of verification. A similar procedure than in the method of Sec. 5.2 can thus be used: a tolerated uncertainty is set on $C_{\max}$, and the measurement is done with the value of C_{S} obtained by solving (5.27) for C_{S}. The measurement with circuits HW1 and HW2 and then carried out, and the measured values of $(\Delta_1, \Delta_2, V_1, V_2)$ are plugged in (5.23), to verify whether it yields a value of $C_{\min}$ corresponding to its known value. If yes, then the measurement can be considered accurate, even if this does not rigorously guarantee the validity of the result, but is rather a necessary condition. If not, the tolerated uncertainty on $C_{\max}$ has to be relaxed, and the measurement is done again. Of course, this has to be done with multiple averaged measurements to accurately estimate the random uncertainty, as well as to converge to the best estimation of the measurand. Finally, note that it should be possible to modify the method so as to allow such a verification for even non fixed $C_{\min}$, by doing the measurement with an additional charge-pump conditioning circuit, such as the full-wave rectifier or the Roundy's charge pump. The equations governing the local dynamics of these circuits can then be added to yield an overdetermined system linking the charge-pump's dynamics to the value of $C_{\max}$ and $C_{\min}$. One can solve the obtained system using, e.g., least-squares approximation.

5.3.4 Application of the method: experimental results

Unfortunately, for reasons linked to the logistics of access to the characterization laboratory, to the accidental breaking of the device first chosen for the characterization, added to time constraints, it has not been possible to carry out an extensive measurement campaign using this second method. Specifically, the measurement was done with only one input excitation namely 1.5 g at 150 Hz frequency. Only three different biasing cycles were tested. Moreover, the error minimization procedure has not been applied even though the symmetrical gap-closing geometry implies that $C_{\min}$ remains constant.

We nevertheless list in Table 5.1 the few results. The used MEMS electrostatic transducer is similar to the device reported characterized above, but its parylene layer was not charged. Hence it has no built-in voltage. The value of $C_{\min}$ was measured using a capacitance meter as

$V_{\mathrm{R_d}}$ \ $V_{\mathrm{L_d}}$	0 V	5 V	10 V
0 V	121.1 pF ± 4.4%	N/A	N/A
5 V	N/A	N/A	N/A
10 V	N/A	121.9 pF ± 5.2%	N/A
15 V	N/A	N/A *	94.7 pF ± 3%

Table 5.1: Some results obtained by the method of $C_{\max}$ characterization under different charge-pump biasing schemes, given in terms of $(V_{\mathrm{L}}, V_{\mathrm{R}})$. The results are the value of $C_{\max}$, the value of $C_{\min}$ being fixed because of the symmetrical gap-closing geometry. The results in the $(0, 0)$ cell are those obtained by synchronous detection. The labels 'N/A' refer to non-admissible cycles because either $V_{\mathrm{R}} \leqslant V_{\mathrm{L}}$, either one of them is equal to zero (so the measurement is not carried out in these cases). The measurement labeled 'N/A*' for $V_{\mathrm{L_d}} = 5$ and $V_{\mathrm{R_d}} = 15$ did not give results for the specified V_{R} and V_{L}, as the voltage across C_{S} saturated before the cycle of interest was reached, at $V = 10.6\,\mathrm{V}$ across C_{S}. The only conclusion we can make is that the values of $C_{\max}$ when biased by $(V_{\mathrm{L}} = 5, V_{\mathrm{R}} = 12)$ is equal to $C_{\min} \times 10.8/5 = 118.8\,\mathrm{pF}$ (see the end of Sec. 5.3.2).

$C_{\min} = 55\,\mathrm{pF}$ (we neglect the uncertainty on it). The value of $C_{\max}$ is measured by synchronous detection as $C_{\max} = 121.1\,\mathrm{pF} \pm 4.4\%$ under the same harmonic input as for the $C_{\max}$ measurement done by the method. Note that the device showed two alternating values of $C_{\max}$ per period of the external forcing at synchronous detection measurement of C_{t}. This is much like the results in Fig. 5.5a. This is in favor of an asymmetry due to the device fabrication or parylene layer deposition process. Indeed, no electrical biasing was applied other than the low-amplitude carrier used for the synchronous detection, as the device has $E = 0$. All the results given below, as well as the synchronous detection measurement, refer to the largest $C_{\max}$ per period of the external forcing.

As mentioned above, the error minimization procedure could not have been carried out, so we cannot guarantee that the results are free of any systematic error due to the electromechanical coupling. We used a value of $C_{\mathrm{S}} = 5\,\mathrm{nF}$, which predicts a random error of 13.5% (see (5.27)) for the values of $C_{\max}$ and $C_{\min}$ above and $V_{\mathrm{Rd}} = 10\,\mathrm{V}$. The uncertainty intervals determined experimentally by averaging multiple measurements were fortunately smaller, probably due to our overestimation of $\delta_V = 25\,\mathrm{mV}$.

5.4 Conclusion and future work

We presented two new characterization methods that are based on the knowledge developed about charge-pump conditioning circuits. These methods are simple and do not require complex instrumentation beyond what is usually found in electrical characterization laboratories.

The first method was used to accurately measure the value of the electret lumped model for an interdigitated e-VEH, for which this measurement is otherwise hardly realizable. Unfortunately, we could not carry out a full measurement campaign for the application of the second method.

Future works may use this second method for the characterization of an e-VEH under various $(V_{\mathrm{L}}, V_{\mathrm{R}})$ biasings. It can also be interesting to vary the types of inputs used, instead of using harmonic inputs. It is also worth to concentrate on making the second method complete, by adding a mean of verification for general transducer structures without fixed $C_{\min}$. This can be done by using additional charge-pump conditioning circuits, as explained at the end of Sec. 5.3.3.

Chapter 6

Principles of near-limits vibration energy harvesting

This chapter presents the concept of near-limits vibration energy harvesting, and attempts to situate it in state-of-the-art works on VEH. Near-limits VEH is a term we use within this chapter and the next to refer to the methodology of VEH design, starting from a system-level view encompassing both electrical and mechanical domains. More precisely, this methodology advocates for designing VEHs that are based on an active control of their mechanical dynamics, through their electrical interface. This control is carried out in order to implement a targeted energy-maximizing inertial mass trajectory. In our case, because of the simple model from which we infer the energy-maximizing dynamics, the resulting VEH systems have the property of being compatible with arbitrary types of input vibrations. This approach is different from that of the former chapters, in which we started the design from an *a priori* choice of electrical interfaces, and only then studied the consequences in the electromechanical domain.

The first section is an introduction in which we stand back from the work presented in the former chapters and summarize the approach that they followed for the design of optimized e-VEHs. We then move on to present some reported works which theoretically study the limits of VEH performances based on generic models. These models can represent VEHs with different electrical interfaces, mechanical parts or even transduction mechanisms.

Next, we present the principle of near-limits VEH itself. We derive, in the context of an idealized model, the dynamics that a controlled VEH must implement so as to maximize the converted power relatively to an upper bound that we also derive in the process. Then, we discuss the formal problem of harvested energy maximization. We highlight the limitations that makes difficult the task of implementing a VEH designed to solve this problem if the form of the input vibrations is not known. We also point out that several works have studied VEHs whose aim are similar to implementing the derived energy-maximizing dynamics. The next chapter of this manuscript (Chap. 7) presents the full quantitative description of the architecture of such a VEH.

The text of this chapter is a part of the article [KJBew] that is submitted for publication and under review at the time of writing of this manuscript.

6.1 Introduction and background

Before we introduce the principles of what we call near-limits vibration energy harvesting, let us stand back from the studies done in the preceding chapters. Specifically, we give a few words about the e-VEH design approach within which these studies fall under. We also go through a quick review of state-of-the-art investigations on the upper bounds of power convertible by a VEH.

6.1.1 More about our approach in the preceding chapters

The Chap. 2 to Chap. 5 were concerned with the study of e-VEHs based on a predetermined electrical interface, namely the charge-pump conditioning circuits. The primary motivation for studying these circuits and using them in e-VEHs was their features such as the self-synchronization with vibrations, or the fact that they are inductor-less.

Only then did we study how e-VEHs using these circuit behave in the electromechanical domain. However as we saw, the study is somewhat complex because of the nonlinear nature of the resulting e-VEHs. In particular, our study was thought as a mean to assess the power yield of e-VEHs using these electrical interfaces, in contexts defined by the characteristics of the vibration input and by the parameters of the mechanical part. This power yield could then be compared between e-VEHs that use other electrical interfaces of the same family. But as is, we did not study how the system had to be parametrized in order to maximize the converted power. By maximizing the converted power, we mean relatively to the necessarily existing upper bound set by the system's physics. In addition, our study in the electromechanical domain was done for harmonic input vibrations, and it is unclear how the e-VEH behaves under more general inputs provided the non-linearity of the system.

6.1.2 Generic vibration energy harvester architectures and limits of energy conversion

In fact, in our studies presented in the previous chapters, once we had selected the charge-pump conditioning circuits as the electrical interface of the studied e-VEHs, we had *de facto* constrained the nature of the electrostatic force. We remind that this electrostatic force is the sole responsible for energy conversion between the electrical and mechanical domains. In the context of previous chapter, this force was expressed as in (4.37), and the function $C_{\mathrm{t}}(x)$ therein accounted for the dependence on the transducer geometry.

If we do not restrain the electrical interface to charge-pump conditioning circuits, then different electrical interfaces and different transducer geometries can result in a wide variety of possible forms for the electrostatic force. If further, we extend our study to other transduction mechanisms than electrostatic, the transducer force can have even more various forms. Therefore, some authors have investigated the *maximum* convertible power of VEHs, in which each VEH was defined in terms of the mathematical form of its transducer force, rather than studying a specific e-VEH configuration as we did in Chap. 4. We list here some of these examples, without explicitly giving each of the used models.

As a fundamental example, the paper of Mitcheson *et al.* [MGY04] presented a study that, instead of being interested in a particular VEH configuration, categorized them into three separate categories defined by the mathematical nature of the force they implement. The models corresponding to each form of the transducer force encompass a various VEH configurations using different transduction mechanisms and using different electrical interfaces. The subsequent developments resulted in finding upper bounds to the amount of power that can be converted from mechanical to electrical domains for each case.

The limits of energy conversion were also sought for more specific VEH configurations that do not fall into the categories coined by Mitcheson *et al.*. For instance, Blokhina *et al.* have studied in [BGH12] the limit of convertible energy for an e-VEH, in which the form of the electrostatic force corresponds to that set by a constant-voltage conditioning circuit, of the type that we have presented in Sec. 1.3.2.2.

Furthermore, the studies in both works cited above make some additional hypotheses, other than on the nature of the transducer force. These take the form of added terms in the mathematical models. These additional assumptions participate in defining the derived energy bounds. For example, in two out of the three configurations studied by Mitcheson *et al.* in [MGY04], a resonant mechanical structure is considered, whereas it is not the case for the third category. The same hypothesis of a resonant structure was made for the study of Blokhina *et al.* in [BGH12].

As a last example, let us cite the work of Daqaq *et al.* in [DME14], which investigates the limits of energy conversion, on yet another generic VEH model. They mention that this model can represent configurations of piezoelectric and electromagnetic VEHs loaded by a resistive element (which therefore constitutes the electrical interface). Other than the model used for the harvesting force, an important difference with both works of Mitcheson *et al.* and Blokhina *et al.* is that the model investigated by Daqaq *et al.* features a more general mechanical potential function than the quadratic mechanical potential function. This allows one to assess the role of mechanical nonlinearities on the performances of VEHs.

6.1.3 Different types of vibrations

The works of Mitcheson *et al.* and Blokhina *et al.* cited above carried out their respective derivation of the upper bound in convertible power for the case of harmonic vibration inputs. Other works investigated the upper bounds of converted power for VEHs described by given models (i.e., given form of the transducer force), submitted to other types of excitations than harmonic. Notably, Halvorsen, in [Hal08], has investigated the case of the two-port linear harvester model that we already mentioned, submitted to inputs given in terms of their probabilistic distribution and their power spectral density.

There are several examples of other works studying the limits of power conversion, which this time make no hypotheses on the form of the transducer force. These works include that of Halvorsen *et al.* in [HLM13], Roundy *et al.* in [HR16], or Hosseinloo *et al.* in [HT15a]. As a result, the limits yielded by these studies are less conservative. This means that, in general, the upper-bound on converted power that they provide is coarser than if the transducer force nature were constrained. On the other hand, this approach enables to consider very general systems and give bounds that must be enforced even by architectures that are yet to be reported.

In the next section, we follow this direction and study a model that makes no hypothesis on the transducer force. The derived bound is valid for arbitrary vibration inputs. In the hypothesis of the model we use, this bound is attained by specific motion of the VEHs inertial mass. Implementing this trajectory is the goal of a near-limits VEH as we hear it. Note that this derivation is similar to that of Hosseinloo *et al.* in [HT15a], the two works having been carried out simultaneously.

6.2 Principles of near-limits vibration energy harvesting

This section is devoted to the derivation of the energy-maximizing dynamics which lie at the core of the near-limits VEH design methodology. These dynamics are in fact a specific trajectory of the VEH's inertial mass. Therefore, we define this methodology as that of designing the VEH with the objective of implementing this trajectory through its transducer force, whilst storing the converted energy in appropriate, usable form. By extension, we call a near-limits VEH (notably the e-VEH whose architecture is the subject of next chapter) a VEH designed following this methodology.

The derivation is done in the context of a generic and simple VEH model, given below in (6.1). In the setting of this model, the derived energy-maximizing dynamics can be implemented by a causal system with a reduced knowledge of the form of the input excitation. Starting the analysis from models comprising sources of energy losses gives more accurate power conversion bounds, but fails to yield energy maximizing dynamics that can be implemented without *a priori* knowledge of the input force $\xi(t)$. This is discussed afterwards in Sec. 6.2.2.

6.2.1 Energy conversion bound and the corresponding inertial mass trajectory

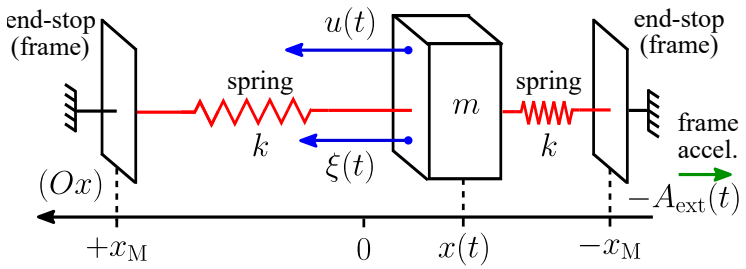

Figure 6.1: A generic model for a 1-dof inertial vibration energy harvester. The inertial mass is supposed to be a point mass.

Let us consider the model in Fig. 6.1. This model is similar to the model presented in Sec. 1.2.2.1, but here no hypothesis is made on the force $u(t)$, except that is has electrical origin. It hence represents a generic transduction mechanism. The VEH is composed of a mass which is supposed to be free to move along one axis in a box, and $x(t)$ denotes its position along this axis at time t, as depicted in the figure. The mass is attached to the frame's end-stops using a suspension modeled as a linear spring of stiffness k. The box in which the mass lies has limited dimensions, and as a result, the mass displacement inside the frame is constrained between positions $\pm x_{\text{M}}$. The box has an acceleration of $-A_{\text{ext}}(t)$: equivalently, the inertial mass

is submitted to an input force $\xi(t) = mA_{\text{ext}}(t)$. The ODE describing the VEH therefore reads

$$\begin{cases} m\ddot{x}(t) & = \xi(t) + u(t) - kx(t), \\ |x(t)| & \leqslant x_{\text{M}}. \end{cases} \tag{6.1}$$

Notice that we have included a term accounting for a linear spring, where the simplest model of VEH may as well not include it. We nevertheless include it to account for a hardly avoidable suspension. In fact, we will see much later in the next chapter that the presence of this spring has implications in the design of near-limits VEH.

Now, let $[t_{\text{i}}\,;t]$ be an interval of time. Let us introduce some notations. In this chapter and the next, the consecutive local extrema of $\xi(t)$ in $]t_{\text{i}}\,;t[$ are represented by the sequence (ξ_{n}). The corresponding times at which they happen are represented by the sequence (t_n). If the extremum is sustained for a non-trivial interval of time, then the corresponding t_n is chosen as the infimum of this interval. The maximums are of even indexes $(\xi_{2\text{n}})$, while the minimum have odd indexes $(\xi_{2\text{n}+1})$. Multiplying (6.1) by $\dot{x}$, integrating over this interval, and rearranging the terms yields the energy balance in the system:

$$\underbrace{\int_{t_{\text{i}}}^{t} \xi(s)\dot{x}(s)\,\mathrm{d}s}_{\text{input energy}} = \underbrace{-\int_{t_{\text{i}}}^{t} u(s)\dot{x}(s)\,\mathrm{d}s}_{\text{converted energy}} + \underbrace{\frac{1}{2}(m\dot{x}^2(t) + kx^2(t))}_{\text{instantaneous mechanical energy}} \tag{6.2}$$

The LHS of this equation is the system's *input energy* from t_{i} to t, and the integral term on the RHS represents the *converted energy* from the mechanical to the electrical domain by the force $u(t)$. Note that we will invariably use the terms converted energy or power, because of the bounded time interval. Also, to lighten notations, we dropped the instantaneous mechanical energy term at t_{i}. Maximizing the converted energy is done by solving the problem

$$\begin{cases} \max\limits_{u} & \left(-\displaystyle\int_{t_{\text{i}}}^{t} u(s)\dot{x}(s)\,\mathrm{d}s\right) \\ \text{s.t.} & m\ddot{x}(t) = \xi(t) + u(t) - kx(t) \\ & |x(t)| \leqslant x_{\text{M}} \end{cases} \tag{6.3}$$

In the light of (6.2), the converted energy equals the input energy modulo the instantaneous mechanical energy of the resonator. If we ignore the latter, then maximizing the converted energy is done by maximizing the input energy in the system. We will assess the validity of ignoring the instantaneous mechanical energy at the end of the derivation. Let us also first ignore the constraint set by the ODE (6.1), i.e., we drop the dependence in the control. Maximizing the input energy integral then reduces to the variational problem of finding the mass trajectory $x_\xi(t)$ that maximizes the input energy integral for any input excitation $\xi(t)$. Let us search for this trajectory, first in the set of bounded piecewise-differentiable functions. As $\int_{t_{\text{i}}}^{t} \xi(s)\dot{x}(s)\,\mathrm{d}s = -\int_{t_{\text{i}}}^{t} \dot{\xi}(s)x(s)\,\mathrm{d}s + \xi(t)x(t)$, if we ignore the $\xi(t)x(t)$ term, this is done by maximizing the integral of the RHS in this equation. The triangular inequality yields that $-\int_{t_{\text{i}}}^{t} \dot{\xi}(s)x(s)\,\mathrm{d}s \leqslant x_{\text{M}} \int_{t_{\text{i}}}^{t} |\dot{\xi}(s)|\,\mathrm{d}s$. From this, one immediately notices that the bound on the

RHS of this latter equation is attained for

$$\tilde{x_\xi}(t) = -x_\mathrm{M}\frac{|\dot{\xi}(t)|}{\dot{\xi}(t)}\mathbb{1}_{\{\dot{\xi}\neq 0\}}. \tag{6.4}$$

and also for

$$x_\xi(t) = \begin{cases} x_\mathrm{M}, t \in \left]t_{2n}\,;t_{2n+1}\right[, \\ -x_\mathrm{M}, t \in \left]t_{2n+1}\,;t_{2(n+1)}\right[. \end{cases} \tag{6.5}$$

the former function being more convenient to evaluate the input energy integral, while the latter carries a straightforward physical meaning that we discuss in the next paragraph. First, let us evaluate the input energy integral, by injecting (6.4) in $\int \xi(s)\dot{x}(s)\,\mathrm{d}s$. In all, we get

$$\int_{t_\mathrm{i}}^{t} \xi(s)\dot{\tilde{x}_\xi}(s)\,\mathrm{d}s = 2x_\mathrm{M}\left(\sum_{\{t_{2n}\leqslant t\}}\xi_{2\mathrm{n}} - \sum_{\{t_{2n+1}\leqslant t\}}\xi_{2\mathrm{n}+1}\right) + M. \tag{6.6}$$

where M is a term bounded by $x_\mathrm{M}(|\xi(t_\mathrm{i})| + |\xi(t)|)$. Notice that evaluating (6.6) for a harmonic input yields the input power bound given in [MMS04]. From (6.5), it is clear that $m\dot{x}^2(t)$ is null. Also, the term kx^2 is bounded. If we further suppose that (i) $\exists\epsilon > 0, \forall\tilde{t} > 0, \exists n \in \mathbb{N}$ such that $t_n > \tilde{t}$ and $|\xi(t_n)| > \epsilon$ and (ii) t is large, then we may neglect the spring's stored energy term in (6.2) when searching for the maximum of converted energy. These two observations justify, *a posteriori*, that we have ignored the instantaneous mechanical energy term when searching for this maximum. In our subsequent references to the energy bound of (6.6), we will omit the M term for the same reasons, as we suppose that the input force $\xi(t)$ is bounded. If the considered that the time interval is infinite (i.e., $t = +\infty$) the converted power reads

$$P_\xi = \lim_{N\to\infty}\frac{2}{t_{2N+1}}x_\mathrm{M}\left(\sum_{\{t_{2n}\leqslant t_{2N}\}}\xi_{2\mathrm{n}} - \sum_{\{t_{2n+1}\leqslant t_{2N+1}\}}\xi_{2\mathrm{n}+1}\right). \tag{6.7}$$

where the t_n are well defined and P is non-null, provided that the condition (i) mentioned earlier in this paragraph is verified.

The motion $x_\xi(t)$ lacks regularity, but a smooth trajectory point-wisely approaching it will result in the input/converted energy approaching the limit (this ensues from a straightforward application of the dominated convergence theorem). Physically, such a trajectory specifies that the inertial mass has to switch from one end-stop $\pm x_\mathrm{M}$ to the other end-stop $\mp x_\mathrm{M}$ as soon as a maximum/minimum of the input force is detected. Returning to the original formulation (6.3), any control $u(t)$ that implements such a trajectory is a solution to the converted energy maximization problem.

To reduce the error between the non-smooth and the smooth point-wisely approaching trajectory, the control has to ensure that the switching between end-stops at each extremum of $\xi(t)$ has to be as brief as possible. Physically, this means that the switching is fast so that it happens while the external force is constant and equal to the detected maximum/minimum value. In addition, the mobile mass must arrive at the other end-stop with ideally zero velocity. As this is not implied by the non-smooth trajectory which is not continuous at the switching events, the reason for the zero-velocity requirement relies on an obvious physical explanation. Indeed, if the mass arrives at the other end with non-zero velocity, the outcome will depend on the physical

implementation of the end-stop (the model (6.1) supposes constrained motion with no definition of the dynamics out of the displacement limits). Bouncing against the end-stop can make the trajectory deviate from the trajectory $x_\xi(t)$. Also, some energy will be wasted in the inelastic collisions with the end-stops. Finally, in between a maximum and a minimum (resp. a minimum and a maximum) of $\xi(t)$, the mobile mass must be kept still at $+x_\mathrm{M}$ (resp $-x_\mathrm{M}$). From now on, $x_\xi(t)$ will denote the smoothened target trajectory fulfilling the requirements listed in this paragraph. This trajectory can be summarized as

$$\forall t \in [t_\mathrm{i}\,;t], x_\xi(t) = \begin{cases} -x_\mathrm{M}, & \text{if } t \in [t_{2n+1} + t^\mathrm{f}_{\xi_{2n+1}}\,;t_{2(\mathrm{n}+1)}] \\ +x_\mathrm{M}, & \text{if } t \in [t_{2n} + t^\mathrm{f}_{\xi_{2n}}\,;t_{2\mathrm{n}+1}] \\ \tilde{x_\xi}^{+\to-}(t), & \text{if } t \in [t_{2n+1}\,;t_{2n+1} + t_{\xi^\mathrm{f}_{2n+1}}] \\ \tilde{x_\xi}^{-\to+}(t), & \text{if } t \in [t_{2n}\,;t_{2n} + t^\mathrm{f}_{\xi_{2n}}]. \end{cases} \tag{6.8}$$

where $\tilde{x_\xi}^{-\to+}(t)$ is a smooth portion of the trajectory $x_\xi(t)$ corresponding to the mass switching from position $-x_\mathrm{M}$ to $+x_\mathrm{M}$ (and symmetrically for $\tilde{x_\xi}^{+\to-}(t)$). It also verifies $|\tilde{x_\xi}^{+\to-}(t)| \leqslant x_\mathrm{M}$. The times t^f_ξ represent the switching time from $\pm x_\mathrm{M}$ to $\mp x_\mathrm{M}$ for an extremum of value ξ. As a result, given our requirements above, these time must be made small by the control $u(t)$ implementing $x_\xi(t)$. An example of smooth trajectory satisfying these requirements is depicted in Fig. 6.2. Note that the requirements on $x_\xi(t)$ to be smooth (say, continuously differentiable) imply the requirement null velocity at both ends of the switching (i.e., for all ξ, n, $\dot{\tilde{x_\xi}}^{-\to+}(t_{2n}) = 0 = \dot{\tilde{x_\xi}}^{-\to+}(t_{2n} + t_{\xi_{2n}})$, and symmetrically for $+x_\mathrm{M}$ to $-x_\mathrm{M}$).

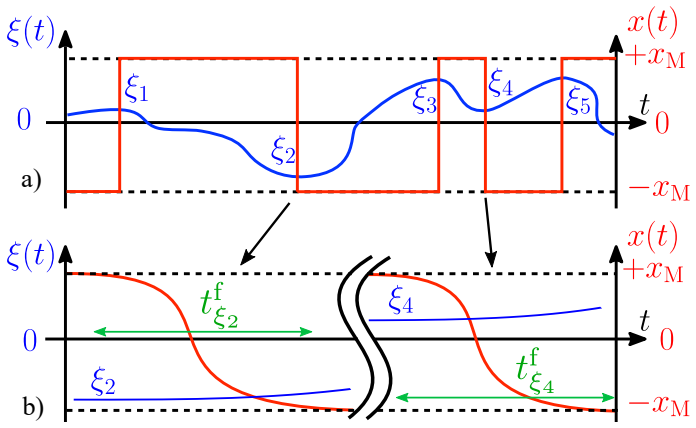

Figure 6.2: Energy-maximizing trajectory $x_\xi(t)$ for an example of input force excitation $\xi(t)$. Two position switching events are time-magnified showing an example of smooth trajectory.

In summary, in the setting of this model, maximizing the converted energy from a given input excitation is done by implementing a control force $u(t)$ that results in the $x_\xi(t)$ trajectory, through the dependence set by the ODE (6.1). We refer to a near-limits VEH as a VEH architecture designed with the goal of implementing this trajectory, while recovering the converted energy. This means that the electrical subsystem responsible for the generation of the control $u(t)$ has to provide a mechanism allowing for the storage of the converted energy, for further processing or use. This is in accordance with the requirements expressed in Sec. 1.3.2.1.

This design approach is much different than that we summarized in Sec. 6.1.1 and that motivated our studies presented in the former chapters. In the present section, we derived the energy-maximizing dynamics of the system, and only after do we care about seeking the

mechanical and associated electrical part that implements these dynamics. This is what we call in this document the "near-limits VEH" methodology. Regarding to the categorization we made in Sec. 1.6 of the introduction chapter, this approach falls within the category of Sec. 1.6.3, whereas our previous works would rather fall into the category Sec. 1.6.2.

6.2.2 On the difference between near-limits VEH and the formal problem of optimal vibration energy harvesting

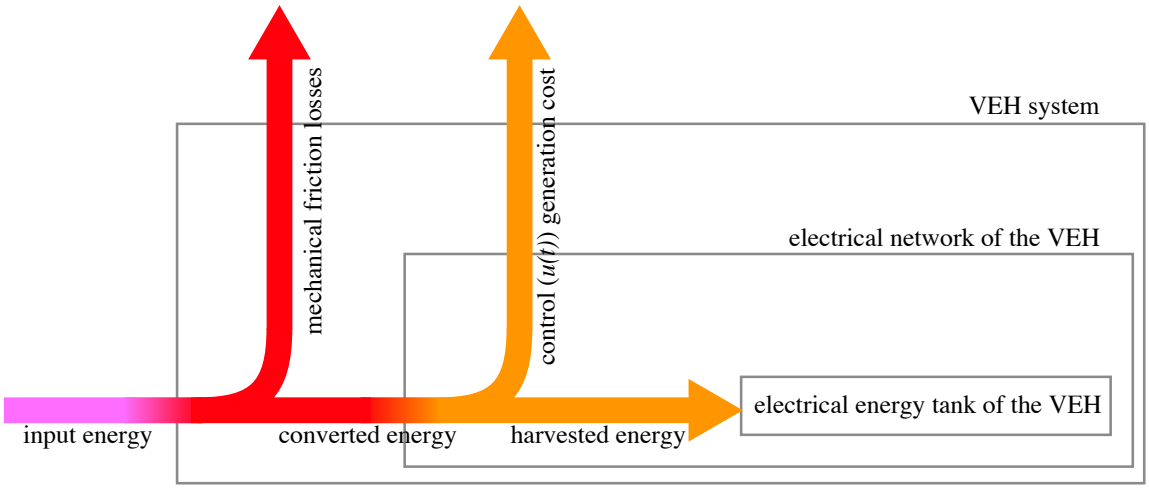

Figure 6.3: Summary of the energy fluxes in a VEH system.

In the hypothesis of (6.1), the input and the converted energy are equal (modulo the system's instantaneous mechanical energy). Thus, the dynamics maximizing the input energy also maximize the converted energy. Yet, a realistic model has to include mechanical friction phenomena, such as air damping or inelastic collisions with the end-stops, due to possible inaccuracy in the implementation of the control. These losses make the converted energy smaller than the input energy. Here and from now on, the term *converted energy* designates the part of the input energy that is converted in the electrical domain. This is exactly the term $-\int u\dot{x}\,\mathrm{d}s$ in (6.1).

Moreover, the ultimate goal of VEH is not the maximization of the converted energy, but rather of the *harvested energy*. From now on, we define this quantity as the part of the converted energy that ends up in the system's electrical energy tank, and that is in a form allowing to supply the electrical load. The harvested energy is smaller than the converted energy, because of the dissipation phenomena that occur in the electrical domain. These losses are the source of the control generation cost.

Indeed, to implement the control $u(t)$, the system must invest energy from its electrical energy tank into the transducer. This energy transfer is done using an interface circuit. This circuit has sources of energy dissipation (e.g., ohmic losses) that result in the loss of part of the invested energy during the transfer. The same phenomenon occurs when the interface circuit transfers the invested energy from the transducer back to the energy tank, with the overhead of converted energy. Also, the interfacing circuit can be controlled by a computation unit, whose decisions are computed as a function of the desired control $u(t)$, as well as, at least, the input $\xi(t)$. The latter hence has to be sensed. The control generation cost also includes the energy consumption of these computation and sensing parts. A diagram summarizing the energy fluxes

in the system is depicted in Fig. 6.3.

In the light of these considerations, the trajectory $x_\xi(t)$ determined above in Sec. 6.2 only results in the maximum of harvested energy in the case of the idealized model (6.1). Its optimality does not extend to the case where a practical model accounting for these various sources of energy losses is considered. If these losses were to be considered, in particular those associated with the control generation cost, then the tasks of determination of optimal trajectory and the control implementing it become entangled: an optimal control problem arises, whereas the two tasks were decoupled in Sec. 6.2.1.

In order to highlight the differences between the strategy derived in Sec. 6.2 and the general optimal energy harvesting problem, let us give a general formulation of the latter. An actual VEH system implements the force $u(t)$ through a transduction mechanism that depends on the mechanical and electrical states of the VEH. The electrical state refers to the currents $\mathbf{I}$ and voltages $\mathbf{V}$, of the electrical circuit the transducer is connected to. This can be summarized by a relation $u(t) = \mathbf{\Phi}(\mathbf{I}, \mathbf{V}, \dot{x}, x)$, where $\mathbf{\Phi}$ describes a particular transduction mechanism. The force $u(t)$ is then synthesized as desired by adequately controlling the currents and voltages of the interface circuit carrying out the corresponding energy transfers between the electrical energy tank and the transducer. This interface circuit can be described by an implicit relation $\mathbf{\Psi}(\dot{\mathbf{I}}, \dot{\mathbf{V}}, \mathbf{V}, \mathbf{I}, \dot{x}, x, t) = \mathbf{0}$. Here, as in the former chapters, $\mathbf{\Psi}$ consists in a set of differential-algebraic relations that describe the circuit's evolution, constrained by the electrical network and components laws. The time dependence accounts for fact that the control of the interface resulting in $u(t)$ is computed as a function of $\xi(t)$. The mechanical suspension can be represented by a force $-k(x)x$, possibly including nonlinear stiffness effects. In the same way, dissipative phenomena in the mechanical domain can be represented by a force $-c(\dot{x}, x)\dot{x}$. Here again, both $k(x)$ and $c(\dot{x}, x)$ are likely to be piecewise-defined to model both the regions when the mass is within $\pm x_\mathrm{M}$ and the collision between the mass and the end-stops [TLH15].The control generation cost $C_e(\mathbf{\Psi})$ arises from the aforementioned dissipation phenomenon in the electrical domain.

Given the previous notations and an input $\xi(t)$, the generic problem of harvested energy maximization is the selection, through the electrical interface described by $\mathbf{\Psi}$, of the adequate control. The formal problem reads:

$$(P)\begin{cases} \max\limits_{\mathbf{\Psi}} & \left(\underbrace{-\int_{t_i}^{t} u(s)\dot{x}(s)\,\mathrm{d}s}_{\text{converted energy}} - \underbrace{C_e(\mathbf{\Psi})}_{\text{control generation cost}} - \underbrace{\int_{t_i}^{t} c(\dot{x}, x)\dot{x}\,\mathrm{d}s}_{\text{mechanical friction losses}} \right). \\ & m\ddot{x}(t) = \xi(t) + u(t) - k(x)x(t) - c(\dot{x}, x)\dot{x}(t) \\ & u = \Phi(\mathbf{I}, \mathbf{V}, \dot{x}, x) \\ & \mathbf{\Psi}(\dot{\mathbf{I}}, \dot{\mathbf{V}}, \mathbf{I}, \mathbf{V}, \dot{x}, x, t) = 0 \end{cases}$$

where the solution $\mathbf{\Psi}$ is sought in Ω, the set of all differential-algebraic relations that can represent the evolution of current and voltage variables of a non-autonomous electrical circuit. The *control generation cost* C_e depends on the control law and on the electrical interface used to implement it, both of which are specified by the choice of $\mathbf{\Psi}$. Therefore, solving the problem (P) for a predefined transduction mechanism Φ consists in choosing the optimal electrical sub-

system $\mathbf{\Psi}^*$ and "simultaneously", through it, the optimal control policy $u^*(t)$. To this control corresponds a trajectory $x^*(t)$. Instead, in Sec. 6.2.1, no mechanical friction phenomenon, no control generation cost, nor any dependence of $u(t)$ on any electrical subsystem were considered.

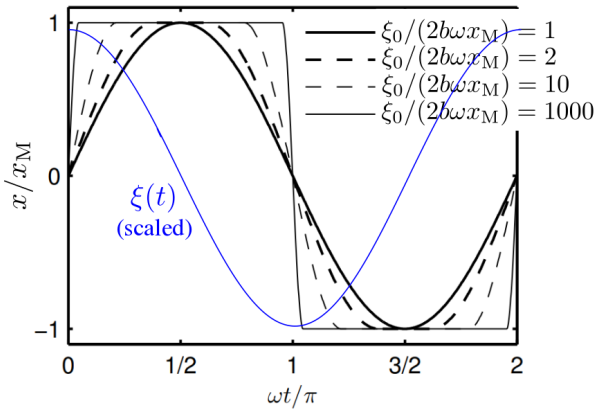

Figure 6.4: The motion maximizing the converted energy for the model (6.9) and different values of the parameter b, the coefficient of a linear mechanical damping force. The results are depicted for one period of the external, harmonic forcing [HLM13].

Designing a VEH maximizing the harvested energy in the general setting of the problem (P) requires, in general, that $\xi(t)$ is known is advance. We show why on an example relying on the work done by Halvorsen *et al.* in [HLM13]. In their work, a particular case of the problem (P) was studied, in which a mere linear mechanical damping force was taken into account, that is, a generic VEH was modeled as

$$\begin{cases} m\ddot{x} & = u(t) - b\dot{x} + \xi(t) \\ |x(t)| & \leqslant x_{\mathrm{M}}. \end{cases} \tag{6.9}$$

Halvorsen *et al.* solved a variational problem associated to this model, which is finding a trajectory $x(t)$ maximizing the converted energy. In this case, the converted energy differs from the input energy because of the losses in mechanical friction $b\int \dot{x}^2 \,\mathrm{d}t$. The considered inputs were harmonic inputs of the form $\xi(t) = \xi_0 \cos(\omega t)$. As in our derivation of Sec. 6.2.1, the control (i.e., the transducer force) $u(t)$ was not made to depend on any electrical interface, nor did have any associated cost or constraint. The problem is therefore basically an ODE-constrained variational problem. Halvorsen *et al.* then derive the resulting energy-maximizing motion as a function of the damping coefficient b. We give their result graphically in Fig. 6.4, copied from [HLM13] with slight modifications to accommodate to our notations and where we added $\xi(t)$.

Two facts can be noted from their results. Firstly, for large value of b (at fixed ξ_0), the trajectory maximizing the input energy becomes sensibly different from $x_\xi(t)$. Secondly, the motion maximizing the converted energy can only be implemented in practice if $\xi(t)$ is known *a priori* by the system. To see this, first let us simplify the matter, and give Halvorsen's result for the energy-maximizing motion in sole the case when b is large enough so that the energy-maximizing motion is harmonic. This corresponds to the case $\xi_0/(2b\omega x_{\mathrm{M}}) \leqslant 1$. It reads

$$x(t) = \xi_0/(2b\omega)\sin(\omega t) \tag{6.10}$$

This motion clearly depends on characteristics of the external forcing that cannot be inferred, at a time t_x, only relying on the knowledge of its values for $t \leqslant t_x$. This is the case at least

because of the dependence of the energy-maximizing trajectory on the frequency and amplitude of the forcing, which has therefore to be known to be harmonic. In the case $\xi_0/(2b\omega x_\mathrm{M}) > 1$, the amplitude of the periodic resulting motion is not anymore a function of that of the input, but the dependence on the input's frequency remains [HLM13]. To conclude, in the particular case of the model (6.9) with limited hypotheses on the input vibrations, a causal control cannot implement the energy-maximizing trajectory for arbitrary $\xi(t)$. Therefore, this ought to be true for more general models and cost functionals that (P) may encompass. Note that the limit in the converted energy decreases when b increases, and approaches that of (6.6) applied to harmonic $\xi(t)$ as $b \to 0$ [HLM13].

In contrast, implementing the control strategy that we described at the end of Sec. 6.2.1 can be done without *a priori* knowledge on the exact form of $\xi(t)$. This is because it relies on the synthesis of the motion $x_\xi(t)$, which in turn merely requires a real-time detection of the extrema of $\xi(t)$. This detection can be done by a causal system without exactly knowing $\xi(t)$, provided that (i) the time resolution of the device measuring $\xi(t)$ is large enough so that $\xi(t)$ remains close to the detected extrema while the position switches from $\pm x_\mathrm{M}$ to $\mp x_\mathrm{M}$ (ii) this position switching can be done fast enough for the same reason (iii) the spatial resolution of the device measuring $\xi(t)$ is high enough. These requirements set practical constraints on the system designed to implement the $x_\xi(t)$ trajectory. This system has to be fast enough to process the highest frequency component of $x_\xi(t)$ (f_max), and accurate enough to correctly measure $\xi(t)$ on its range of values ($[-\xi_\mathrm{max}\,;+\xi_\mathrm{max}]$). The next chapter presenting our near-limits e-VEH architecture explicitly will show that estimates of these two quantities are explicitely needed in order to correctly synthesize $x_\xi(t)$.

The results obtained by Halvorsen *et al.* prove that the strategy of implementing $x_\xi(t)$ cannot possibly yield the upper bound in the harvested energy, even in the simple case of a model featuring a simple linear mechanical damping. This remains certainly true in the case of more general mechanical friction functions. In all generality, it also ought be true when the control is made to depend on an electrical interface to implement it (as in problem (P)), that further sets a non-null control generation cost (i.e., $C_\mathrm{e} > 0$). However, we can suppose as a working hypothesis that this limit is smoothly approached by the strategy of implementing $x_\xi(t)$ as the costs $C_\mathrm{e} + \int_{t_0}^{t} c(\dot{x},x)\dot{x}\,\mathrm{d}s$ approach zero. This reasonable hypothesis is supported by the results of Halvorsen *et al.*'s work described above. Indeed, it is clear from Fig. 6.4 that the trajectory maximizing the converted energy becomes closer to $x_\xi(t)$ as the damping parameter becomes sufficiently small, i.e., as $\int_{t_0}^{t} c(\dot{x},x)\dot{x}\,\mathrm{d}s = \int_{t_0}^{t} b\dot{x}^2\,\mathrm{d}s$ becomes small (because the converted energy bound approaches that yielded by (6.6) for a harmonic input force). As a result of this hypothesis, if the near-limits VEH implementing $x_\xi(t)$ manages to make the control generation cost and the mechanical losses small when implementing $x_\xi(t)$, the harvested energy will approach the upper bound in the harvested energy yielded by solutions of the problem (P), because this upper bound in turn approaches that of (6.6).

Finally, note that other authors have listed several particular cases of the optimal control problem (P), in which various mathematical forms of C_e are considered. For instance, Hosseinloo *et al.* in [HT15a] pose the problem for control generation costs that are quadratic in the transducer force and its first time derivative. They mention that this particular occurrence of the problem can be readily solved using convex optimization techniques. Here again, this has to rely on strong hypotheses on the form of the external excitation $\xi(t)$.

6.2.3 Review of some reported architectures geared towards the implementation of the energy-maximizing dynamics for arbitrary inputs

The first works that investigated VEH systems implementing a trajectory resembling $x_\xi(t)$ defined above can be traced back to Mitcheson's and Miao's *et al.* contributions in [MMS04; MMH06]. In these works, electrostatic transduction is considered. Their works propose an e-VEH system in which the transducer's movable capacitor plate (i.e., the inertial mass) travels from one end-stop to the other when the possibly irregular input force reaches a determined threshold value. It is hence not exactly $x_\xi(t)$ that is the targeted inertial mass trajectory, because $x_\xi(t)$ requires that the switchings are done at the extrema of $\xi(t)$. Moreover, the trajectory they target does not require null velocity at both end of the position switching events. This is fundamentally due to the constrained form of the control considered by Mitcheson *et al.*, which does not formally allow to solve the control problem associated with each position switching event.

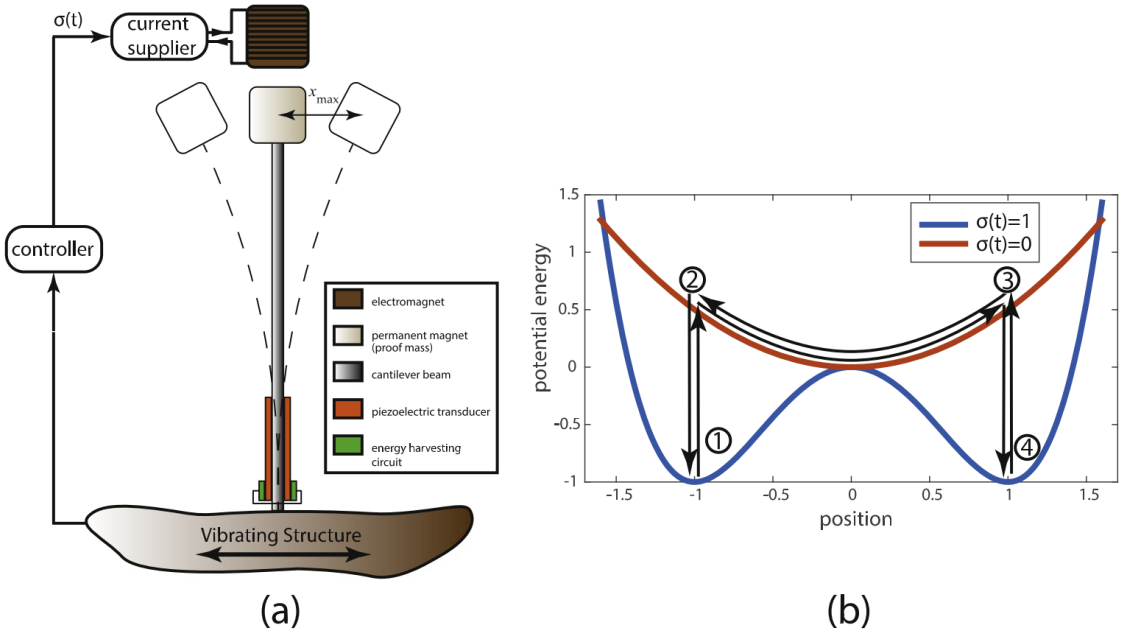

Figure 6.5: An architecture proposed by Hosseinloo *et al.* in order to implement the energy-maximizing trajectory $x_\xi(t)$ [HT15b]. In (a), the schematic of the architecture. In (b), a figure illustrating the two potential functions between which the system switches.

The more recent work by Hosseinloo *et al.* in [HT15b] is of special interest to us, as it proposes the sketch of a VEH system geared towards the implementation of the energy-maximizing trajectory $x_\xi(t)$. Therefore, this system is in essence thought so as to be compatible with a wide range of vibration inputs. The schematic of this system is depicted in Fig. 6.5.a, copied from [HT15b]. In short, $x_\xi(t)$ is implemented by dynamically changing the mechanical potential function of the system, thanks to a controlled magnetic field. First, the mass is kept at one of the end-stops. This corresponds to the mass being "trapped" in one of the wells of the blue bistable potential in Fig. 6.5.b. When an extremum of $\xi(t)$ is detected, the potential function is changed to the red (quadratic) potential function in Fig. 6.5. Therefore, the mass can travel from one end-stop to the other, under the action of the external force. When it reaches the other end-stop, the mass is "trapped" again in the corresponding well of the bistable potential (blue in

Fig. 6.5.b), which is restored. The energy is converted thanks to a piezoelectric patch fixed to the beam supporting the mass, when the mass travels from one end-stop to the other, as well as when the mass eventually oscillates around one of the stable positions (intra-well oscillations). The idealized system was tested in simulation, and Hosseinloo *et al.* report encouraging results of comparison with both bi-stable and linear resonant devices with the same electrical interface, all submitted to both harmonic and walking motion vibrations recorded on a human body.

Even though much of the details of their architecture are not reported by Hosseinloo *et al.* in their paper, we can cite one at least two reasons that makes their proposition different from a near-limits VEH as we hear it. The first of these reasons is that the control considered by Hosseinloo *et al.* obeys a passivity constraint. As a result, the position switching cannot happen on all maxima and minima of $\xi(t)$, but rather only on positive maxima and negative minima. For the near-limits e-VEH we present in the next chapter, we removed the passivity constraint, so that all maxima and minima of $\xi(t)$ can be selected for position switching. The second difference is that the task of putting the energy in correct form for further use is not part of the architecture reported by Hosseinloo *et al.*. In contrast, the near-limits e-VEH described in the next chapter fulfills the task of storing the harvested energy into the system's electrical energy tank.

6.3 Conclusion

This chapter introduced the concept of near-limits VEH, and attempted to situate it in state-of-the-art works in VEH. Specifically, we derived the mass trajectory that a near-limits VEH must implement through its electrical interface. Even though this trajectory formally maximizes the harvested energy only in the case of an idealized, lossless model, we argued that it has the advantage of being implementable in practice with only limited knowledge of the input vibration. Besides, the converted energy can approach the derived upper bound if the costs of control generation are made small. This makes near-limits VEH worthwhile for further investigation in order to convert energy from irregular types of vibrations.

The next and last chapter of this manuscript proposes an architecture for an electrostatic near-limits VEH.

Chapter 7

Architecture of an electrostatic near-limits vibration energy harvester

In this chapter, the architecture of an electrostatic near-limits VEH based on electrostatic transduction is described. Specifically, the VEH implements a control synthesizing the trajectory $x_\xi(t)$ discussed in the previous chapter, from limited hypotheses on the input excitation. The architecture comprises an electrical interface that implements a control synthesizing $x_\xi(t)$, whilst recovering the converted energy. To this end, the interface circuit carries out the necessary energy exchanges between the VEH's electrical energy tank and the electrostatic transducer. The electrical interface is driven by a sensing and computation unit which revolves around a finite-state automaton. Fig. 7.1 presents an overview of the architecture, which is based on a differential electrostatic transducer.

We start the chapter by briefly describing this differential transducer. We then move on to present the control law. Next, an interface circuit is proposed to synthesize the proposed control. The computing and sensing parts commanding the interface circuit are then described. The obtained architecture is sized and modeled in VHDL-AMS for simulation, using realistic models of the electrical components. This simulation constitutes a proof of concept of our architecture. Some comments are given with regard to the full system optimization that can be carried out in future works. We also present some examples of variations of our architecture that are also worth considering to further improve the figures of harvested energy.

As introduced in the previous chapter, here $\xi(t)$ denotes the external input force. Its maxima are indexed by even integers and form a sequence $(\xi_{2\mathrm{n}})$ while its minima are indexed by odd integers and form a sequence $(\xi_{2\mathrm{n}+1})$. The corresponding times of occurrence of each of these maxima and minima are $(t_{2\mathrm{n}})$ and $(t_{2\mathrm{n}+1})$.

The contents of this chapter intersect that of the article [KJBew] that is submitted for publication and under review at the time of writing of this manuscript.

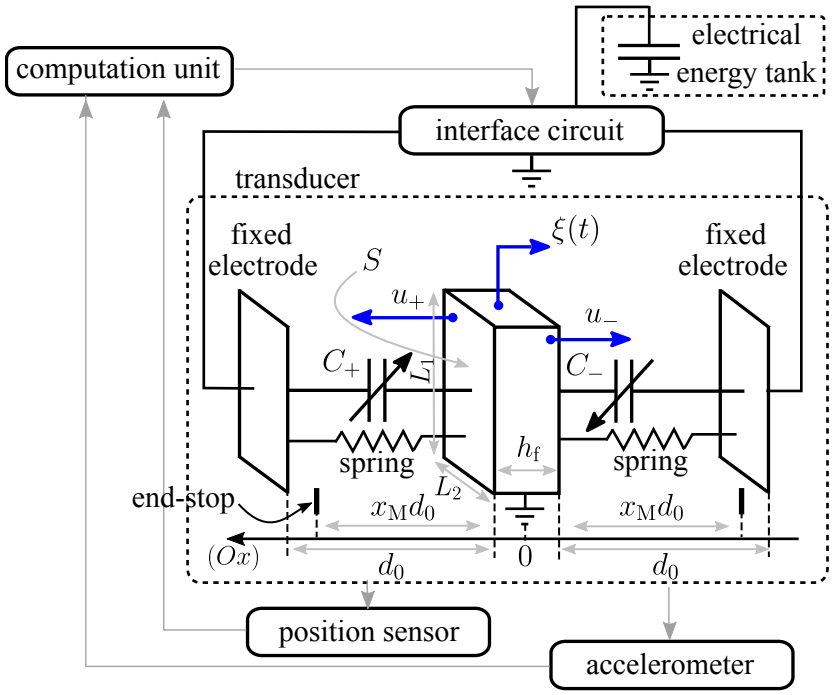

Figure 7.1: Overview of the architecture for a near-limits electrostatic VEH.

7.1 Presentation of the architecture

7.1.1 Differential transducer

To implement the motion $x_\xi(t)$, we need at least a force whose orientation on the (Ox) axis can be controlled. One can check that this is not possible with the three geometries of electrostatic transducer presented so far, as an external biasing manifests through the square of the voltage, and the sign of the term $\partial C/\partial x$ depends on the mass position. Therefore, to be able to generate a force whose orientation on the (Ox) axis can be controlled, a differential transducer composed of two electrostatic transducers C^+ and C^- has to be used. Each of these transducers has one of its electrodes attached to the frame's ends, and the other electrode attached to the VEH's mass. A schematic view of this geometry is depicted in Fig. 7.1, for the gap-closing geometry that we choose. The force u is then the superposition of the two forces:

$$u(t) = u_+(t) - u_-(t) \tag{7.1}$$

with

$$\begin{aligned} u_+(t) &= \frac{1}{2} {V_+}^2(t) \frac{\partial C_+}{\partial x}(x(t)), \\ u_-(t) &= -\frac{1}{2} {V_-}^2(t) \frac{\partial C_-}{\partial x}(x(t)) \end{aligned} \tag{7.2}$$

For the notations of the present chapter, let us define $\kappa := \varepsilon_0 S/{d_0}^2$, a constant that depends on the device's geometry. We remind the signification of the constants: d_0 is the transducer gap at $x = 0$ (hence the same for both C^+ and C^-), S is the capacitance surface of each of C^+ and C^-, and ε_0 represents the permittivity of vacuum (or approximately air). Also, from now on, let us substitute all positions with their value normalized by dividing by d_0, i.e., substitute

$x(t)/d_0 \to x(t)$, $x_\mathrm{M}/d_0 \to x_\mathrm{M}$. However, in the rest of this chapter, we keep all other terms dimensionalized. The capacitance of either of the gap-closing transducers is hence expressed as:

$$C_\pm(x(t)) = \frac{\kappa d_0}{1 \mp x(t)}, \tag{7.3}$$

and hence the (dimensionalized) force reads

$$u_\pm(t) = \frac{1}{2}{V_\pm}^2(t)\frac{\kappa}{(1 \mp x(t))^2}, \tag{7.4}$$

From (7.4), it comes that when the charge of $C_\pm$ is kept constant through the displacement of the mass, the force that the corresponding transducer generates on it is constant. Specifically, if at position $x(t_0) = x_0$, the transducer is charged with $Q_\pm(t_0) = V_\pm(t_0)C_\pm(x_0)$, then the transducer force is constant across the displacement, as long as $Q_\pm(t)$ remains constant. Indeed:

$$u(t) = \frac{1}{2}\frac{{Q_\pm}^2(t_0)}{{C_\pm}^2(t)}\frac{\kappa}{(1 \mp x(t))^2} = \frac{1}{2}\frac{{Q_\pm}^2}{\kappa {d_0}^2} \tag{7.5}$$

so that

$$\begin{aligned} \forall t,\, t_0 \leqslant t \leqslant t_1 \implies u_\pm(t) = u_\pm(t_0) = \frac{1}{2}\frac{{Q_\pm}^2}{\kappa {d_0}^2} = \frac{\kappa}{2}\frac{{V_\pm}^2(t_0)}{(1 \mp x_0)^2} \\ t_1 = \inf\{\, t \geqslant t_0 \,|\, Q_\pm(t) \neq Q_\pm(t_0) \,\} \end{aligned} \tag{7.6}$$

This is referred to as the "constant-charge operation". The corresponding energy in $C_\pm(x_0)$ reads, as a function of the constant force u_0 it implements:

$$W_0 = |u_0| d_0 (1 \mp x_0) \tag{7.7}$$

7.1.2 Control

Let us now describe the control law $u(t)$ that synthesizes the trajectory $x_\xi(t)$ described in Sec. 6.2. We start by an informal description, and then make it mathematically precise. We give some of the underlying motivations for our choice of $u(t)$ later at the end of the subsection. However, let us state from now that the control we implement is a piecewise-constant valued force, so that the foregoing property of constant force for constant charge operation of gap-closing transducers can be turned to good account.

7.1.2.1 Detailed description of the control

The chosen control scheme can be explained as follows. Suppose that initially, the mass is located at $-x_\mathrm{M}$ and $\xi(t)$ is increasing. The control $u(t)$ sustains a large enough force value $-u_\mathrm{max}$ so that the mass, on which $\xi(t)$ and $-kx(t)$ also act, is kept at $-x_\mathrm{M}$ (thanks to the reaction force of the end-stop). Then, as soon as a maximum of $\xi(t)$ is sensed, two cases are possible: either the value of the maximum of $\xi(t)$ is positive, either it is negative. The first case is depicted in Fig. 7.2.a. In this case, the force $u(t)$ first vanishes, and the mass travels towards $+x_\mathrm{M}$ under the action of $\xi(t)$. It is supposed that $\xi(t)$ is varying slowly enough so that its value is equal to the value of the local maximum ξ_0 during the whole position switching process. When the mass reaches a given position $-x_\mathrm{com} \in \,]-x_\mathrm{M}\,; x_\mathrm{M}[$, the control force takes a negative constant value,

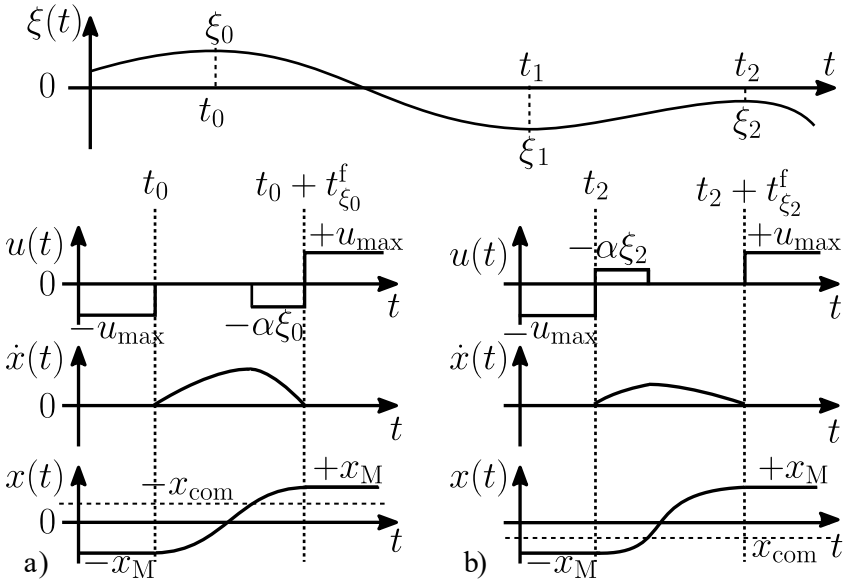

Figure 7.2: Detailed waveforms illustrating the proposed control strategy, on two examples of external force local maximum, in both cases $\xi_{\mathrm{n}} x(t_{\mathrm{n}}) < 0$ (positive force maximum) and $\xi_{\mathrm{n}} x(t_{\mathrm{n}}) > 0$ (negative force maximum).

thus working negatively on the mass. This force value is computed so that the mass arrives at $+x_{\mathrm{M}}$ with zero velocity.

The other case is depicted in Fig. 7.2.b, where the value ξ_2 of the maximum of $\xi(t)$ is negative. In this case, the force $u(t)$ first takes a positive constant value, and works positively on the mass so that it travels towards $+x_{\mathrm{M}}$. When the mass reaches x_{com}, the force $u(t)$ vanishes. The value the positively working force is chosen so that the mass reaches $+x_{\mathrm{M}}$ with zero velocity. In both cases, as soon as the mass reaches $-x_{\mathrm{M}}$, the control force becomes equal to $u_{\max}$, which is large enough so that the mass is kept still at $+x_{\mathrm{M}}$. Then, when a minimum of $\xi(t)$ is sensed, the symmetrical sequence of actions happens, where x_{com} has to be substituted by $-x_{\mathrm{com}}$.

Formally, the control reads:

$$u(t) = \begin{cases} \tilde{u}_n(t), & \text{if } t \in \left]t_{\mathrm{n}}\,; t_{\mathrm{n}} + t^{\mathrm{f}}_{\xi_{\mathrm{n}}}\right[\\ u_{\max}, & \text{if } t \in \left]t_{2\mathrm{n}} + t^{\mathrm{f}}_{\xi_{2\mathrm{n}}}\,; t_{2\mathrm{n}+1}\right[\\ -u_{\max}, & \text{if } t \in \left]t_{2\mathrm{n}+1} + t^{\mathrm{f}}_{\xi_{2\mathrm{n}+1}}\,; t_{2(\mathrm{n}+1)}\right[\end{cases} \tag{7.8}$$

where $\tilde{u}_n(t)$ is a solution to the position switching problem:

$$(Q) \begin{cases} m d_0 \ddot{x}(t) = \xi_{\mathrm{n}} + u(t) - k d_0 x(t) \\ (x(0), \dot{x}(0)) = (-x(t^{\mathrm{f}}_{\xi_{\mathrm{n}}}), \dot{x}(t^{\mathrm{f}}_{\xi_{\mathrm{n}}})) = (\pm x_{\mathrm{M}}, 0)\ , \\ |x(t)| \leqslant x_{\mathrm{M}} \end{cases}$$

and t^{f}_{ξ} denotes the switching duration for an extremum of value $|\xi|$. Here, in the light of the force description qualitatively done in the two paragraphs above, we seek $\tilde{u}_n(t)$ as a constant-piecewise

force that is of the form

$$\tilde{u}_n(t) = \begin{cases} \begin{cases} 0 & x(t) < -x_{\text{com}} \\ -\alpha\xi_{\text{n}} & x(t) \geqslant -x_{\text{com}} \end{cases} & \text{if } \xi_{\text{n}} > 0, \\ \begin{cases} -\alpha\xi_{\text{n}} & x(t) < x_{\text{com}} \\ 0 & x(t) \geqslant x_{\text{com}} \end{cases} & \text{if } \xi_{\text{n}} < 0 \end{cases} \tag{7.9}$$

where α has to be determined so that the mass that leaves $\pm x_{\text{M}}$ with zero velocity and arrives at $\mp x_{\text{M}}$ with zero velocity. One can straightforwardly but tediously solve the boundary problem (Q) to determine its value, but the task is greatly simplified by considering a simple physical argument. This is that the work done by the forces acting on the mass balances, before it reaches $\pm x_{\text{com}}$ and after. For example, for the case (i) $\xi_{\text{n}} > 0$, with $x(0) = -x_{\text{M}}$:

$$\begin{aligned} \int_{-x_{\text{M}}}^{-x_{\text{com}}} \xi_{\text{n}} - kx \,\mathrm{d}x &= -\int_{-x_{\text{com}}}^{x_{\text{M}}} (1-\alpha)\xi_{\text{n}} - kx \,\mathrm{d}x, \\ \implies \alpha &= \frac{2x_{\text{M}}}{x_{\text{M}} + x_{\text{com}}}. \end{aligned} \tag{7.10}$$

The reader may check that the three other cases (ii) $\xi_{\text{n}} > 0$, with $x(0) = x_{\text{M}}$, (iii) $\xi_{\text{n}} < 0$, with $x(0) = -x_{\text{M}}$, and (iv) $\xi_{\text{n}} < 0$, with $x(0) = x_{\text{M}}$, yield the same value for the coefficient α.

Then, injecting $\tilde{u}_n(t)$ in (Q) and solving for t_ξ^{f} using the boundary conditions allows one to find the duration of the position switching from $\pm x_{\text{M}}$ to $\mp x_{\text{M}}$ for an extremum of value ξ. It reads:

$$\begin{aligned} t_\xi^{\text{f}} = \sqrt{\frac{m}{k}} \Bigg(&\delta + \operatorname{acos}\left(\frac{|\xi| + kd_0 x_{\text{com}}}{|\xi| + kd_0 x_{\text{M}}}\right) + \\ &+ \operatorname{atan}\left(\frac{(x_{\text{M}} + x_{\text{com}})\sqrt{kd_0(x_{\text{M}} - x_{\text{com}})(2|\xi| + kd_0(x_{\text{M}} + x_{\text{com}}))}}{|\xi|(x_{\text{M}} - x_{\text{com}}) - kd_0 x_{\text{com}}(x_{\text{M}} + x_{\text{com}})}\right)\Bigg), \end{aligned} \tag{7.11}$$

where

$$\delta := \begin{cases} \pi \text{ if } -\sqrt{1 + \dfrac{4kd_0 x_{\text{M}}|\xi|}{(kd_0 x_{\text{M}} + |\xi|)^2}} < 1 + \dfrac{2kd_0 x_{\text{com}}}{kd_0 x_{\text{M}} + |\xi|} < \sqrt{1 + \dfrac{4kd_0 x_{\text{M}}|\xi|}{(kd_0 x_{\text{M}} + |\xi|)^2}} \\ 0 \text{ otherwise} \end{cases} \tag{7.12}$$

and where $u_{\max} > \xi_{\max} + kd_0 x_{\text{M}}$ ($\xi_{\max} := \max_t |\xi(t)|$). The value of $t_{\xi_{\text{n}}}^{\text{f}}$ is needed to assess if the position switching is fast enough so that $\xi(t) \approx \xi_{\text{n}}$. Otherwise, the control will lack accuracy and the implemented trajectory will deviate from $x_\xi(t)$, which results in a shortfall in the converted energy.

Estimating $t_{\xi_{\text{n}}}^{\text{f}}$ requires some *a priori* information about $\xi(t)$, as it depends on the value of each of $\xi(t)$'s extremum. As hardly any insight can be taken from (7.11), the plots in Fig. 7.3 show the examples of evolution of the switching time for different values of k, ξ_{n} and x_{com}. It is clear that the switching time increases with increasing x_{com} all other variables fixed, decreases with increasing k, and decreases with increasing $|\xi_0|$. The values of d_0, m, x_{M} and k are those used for the architecture as parametrized in Sec. 7.2 (and particularly, corresponding to the results of Fig. 7.11). Note that even if the switching time evaluates to perfectly reasonable values for $x_{\text{com}} = \pm x_{\text{M}}$, theses values of x_{com} are not admissible for the control $u(t)$ to solve (Q).

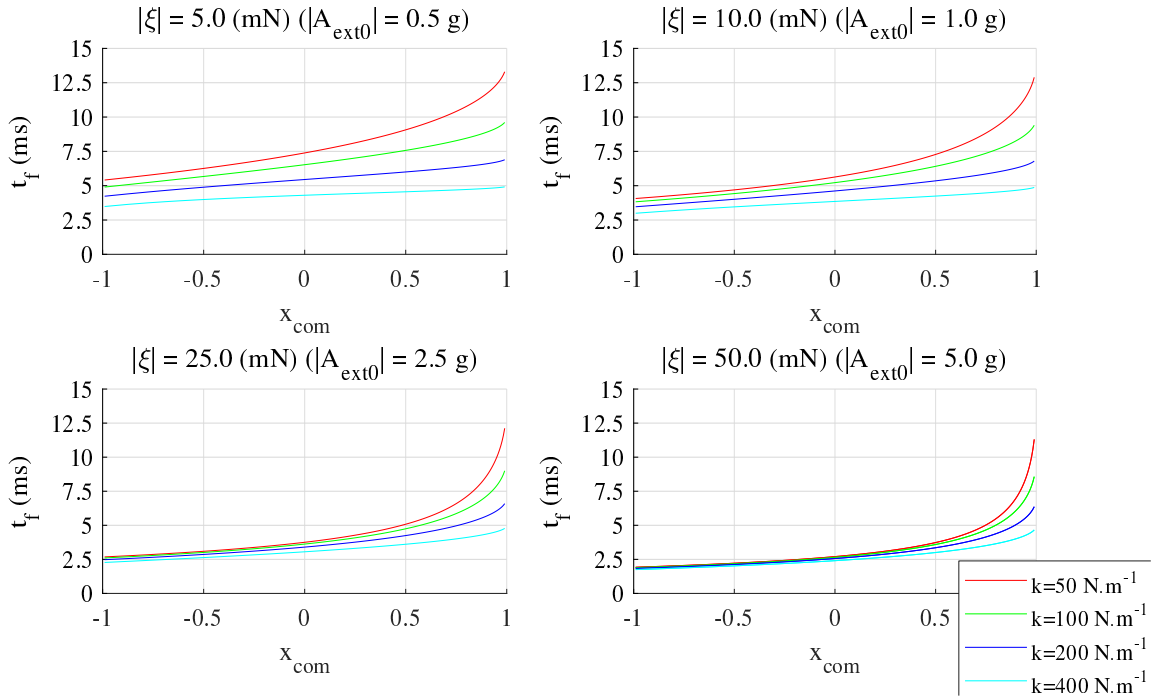

Figure 7.3: Switching duration for the problem (Q) versus the value of x_{com}, for different stiffnesses and extremum values.

In the light of Fig. 7.3, which shows that the switching duration increases when $\xi(t)$ decreases, to guarantee control accuracy, we may conservatively require that

$$\lim_{\xi \to 0} t_{\xi}^{\mathrm{f}} < K/f_{\max}, \tag{7.13}$$

for large enough K depending on the tolerated error, and where $f_{\max}$ denotes the highest frequency component of $\xi(t)$ that has significant amplitude. The term "significant amplitude" has to be given a precise meaning in order to properly choose K and $f_{\max}$. This has to follow from a study of some of the statistical properties of possible inputs $\xi(t)$, that we did not work on. This study would allow to bound the error on the implemented trajectory due to the fluctuation of $\xi(t)$ around. In turn, this bound can be used to control the losses due to the control inaccuracy. Such losses are highlighted in the simulations of Sec. 7.2, in which the control inaccuracy results in inelastic collisions of the mass with the end-stops. This control inaccuracy is in part due to the fluctuation of $\xi(t)$ around its extrema, which in turn results from the fact that the position switching is not carried out fast enough.

7.1.2.2 Energy considerations

The conversion between mechanical and electrical energy occurs during the position switchings at the extrema of $\xi(t)$. In the case of a maximum of positive value or of a minimum of negative value (in these two cases, $x(t_{\mathrm{n}})\xi_{\mathrm{n}} < 0$), the position switching results in an overall conversion of energy from the mechanical to the electrical domain. At each such extremum, from (7.14), it comes that the energy that has first to be invested to implement $\tilde{u}_{\mathrm{n}}(t)$ reads:

$$W_{\mathrm{i,n}}{}^{-} = 2d_0 x_{\mathrm{M}} \frac{1 - x_{\mathrm{com}}}{x_{\mathrm{M}} + x_{\mathrm{com}}} |\xi_{\mathrm{n}}|. \tag{7.14}$$

In the case of a maximum of negative value or of a minimum of positive value (i.e., $x(t_\mathrm{n})\xi_\mathrm{n} > 0$), the position switching results in an overall conversion of energy from the electrical to the mechanical domain, and the next extremum $\xi_{\mathrm{n}+1}$ will necessarily verify $\xi_{\mathrm{n}+1}x(t_{\mathrm{n}+1}) < 0$. From (7.15), the invested energy reads:

$$W_{\mathrm{i,n}}{}^{+} = -2d_0 x_\mathrm{M} \frac{1 + x_\mathrm{M}}{x_\mathrm{M} + x_\mathrm{com}} |\xi_\mathrm{n}|. \tag{7.15}$$

For both cases, the converted energy between the mechanical and the electrical domain (denoted $W_{\mathrm{c,n}}{}^{-}$ for the case $\xi_\mathrm{n}x(t_\mathrm{n}) < 0$ and $W_{\mathrm{c,n}}{}^{+}$ for the case $\xi_\mathrm{n}x(t_\mathrm{n}) > 0$) reads:

$$W_{\mathrm{c,n}}{}^{\pm} = \mp 2d_0 x_\mathrm{M} |\xi_\mathrm{n}|, \tag{7.16}$$

where we have adopted the convention that negative amount of converted energy means that the energy is converted from the electrical to the mechanical domain. Summing (7.16) over n, one obtains the expression (6.6). Note that the case where $x(t_\mathrm{n})\xi_\mathrm{n} > 0$ is precisely the case for which the architecture of Hosseinloo *et al.* cannot select the extremum for position switching, due to the passivity constraint (see Sec. 6.2.3). Indeed, in this case the total energy balance at the end of the position switching is negative, meaning energy has been converted from the electrical to the mechanical domain. Our architectures carries the position switching even at such extrema which, again, will necessarily verify $\xi_{\mathrm{n}+1}x(t_{\mathrm{n}+1}) < 0$.

Finally, an important parameter is the maximum voltage across the transducer. It is reached when the energy on the transducer $C_\pm$ is equal to the sum of invested and converted energy ((7.14) and (7.16)), for an extremum of value ξ_max, at position $\mp x_\mathrm{M}$. It reads

$$V_\mathrm{max} = 2(1 + x_\mathrm{M}) \sqrt{\frac{1}{\kappa} \frac{x_\mathrm{M}}{x_\mathrm{M} + x_\mathrm{com}} \xi_\mathrm{max}} \tag{7.17}$$

Notice that V_max is a decreasing function of x_com, an increasing function of the transducer surface S, of the gap d_0 (through κ) and an increasing function of the mass (through ξ_max). In particular, if the mass and surface are scaled by the same factor, then V_max does not change. This has implications on the choice of the interfacing circuit's switching elements, and on the performances in terms of control generation cost (see Sec. 7.2).

7.1.2.3 Comments

In Sec. 6.2.2 of the previous chapter, it was highlighted that the optimal control maximizing the harvested energy, in the case of the general problem (P), is sought in terms of an electrical interface described by a set of differential-algebraic relations $\mathbf{\Psi}$. This means that the solutions provides simultaneous determination of the mathematical control law and the interface that has to physically implement it. The position switching problem (Q) can itself be enriched with such model details and cost functionals, e.g., adding end-stops model, mechanical friction phenomenon and/or minimizing the energy dissipated in a given interface circuit (see Sec. 7.3.1 below). This allows taking into account the coupling between the choice of both the mathematical control law used to implement the position switchings, and the interface used to implement this control. In other words, the choice of both the mathematical control law and the interface used to implement it are tightly bound to each other when seeking for the best strategy to reduce the

cost of accurately implementing $x_\xi(t)$.

Our choice of the piecewise-constant control (7.8) results from considering this entanglement on a less formal level. Considering the piecewise constant nature of $u(t)$ and the property of the differential gap-closing transducers that they implement constant force at constant charge (see Sec. 7.1.1), the requirement on the electrical interface implementing $u(t)$ is to control the charges on the transducer, at discrete instants corresponding to the force updates of $u(t)$. Such interfaces have been extensively proposed and studied in the literature. For example, the constant-charge electrical interface in Sec. 1.3.2.1 carries out a similar task. The circuit we present in the next section to carry out the energy exchanges described above in Sec. 7.1.2.2 is based on its topology.

In addition, the chosen piecewise-constant force minimizes the number of force updates. It carries only one commutation of the force value in $]t\,;t_\xi^{\mathrm{f}}[$ to solve the problem (Q). It can be easily shown that one commutation is the minimum amount of commutations required for a control solving (Q). The reason why we seek to minimize the number of updates here is because each update will require the interface to perform an action. This action will likely have an associated energy cost. Moreover, one of the constant force values is 0 in order to avoid additional energy investment, at the cost of a slower position switching. Increasing the invested energy to implement the position switchings results in greater losses in the interfacing circuit, i.e., greater control generation cost, for the same value of converted energy per extremum (7.16). Hence, decreasing the invested energy results in larger harvested energy, if this it is done whilst keeping the control accurate. To further decrease the invested energy, x_{com} can be increased, as (7.14) and (7.15) show. Yet, increasing x_{com} makes the position switching slower as (7.11) and Fig. 7.3 show, thus decreasing the control accuracy. The effect of x_{com} is illustrated in the simulations of Sec. 7.2.4.2.

We will also briefly mention in Sec. 7.3.1 some possible alternatives for the control law that require multiple updates between different constant values. This type of control laws can be advantageous because of robustness considerations that we did not address at all in the present section. They can also be advantageous to reduce the energy dissipated in the electrical interface, depending on the implementation of the latter.

7.1.3 Electrical interface

We present in this section an interface circuit to carry out the energy transfers that are needed in order to implement the control described in Sec. 7.1.2. These transfers are done in a way that the converted energy is recovered in a capacitive electrical energy tank. This circuit has a bidirectional DC-DC converter topology. Its schematic is depicted in Fig. 7.4. Let us describe its operation.

Suppose that the transducer capacitance value is constant during the energy transfer processes described hereafter. This implies that the processes of updating the value of the force across the transducers are fast compared to the timescale of the position switching (7.11), so that the mass position can be considered equal to a constant x_0. After the processes are explained in the following, this hypothesis will be assessed at the end of the section.

Setting a force of value u_0 requires to transfer an energy W_{u_0} (see (7.7)) to the corresponding transducer (C_+ if $u_0 > 0$, C_- if $u_0 < 0$). The transducer has then to be disconnected from the

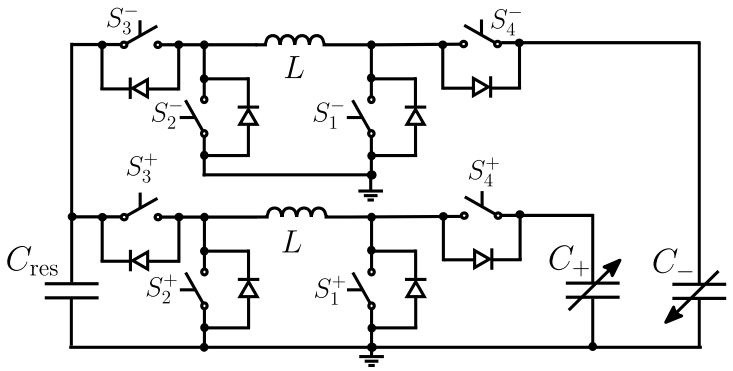

Figure 7.4: Interface circuit carrying out the energy exchanges to implement the control strategy described in Sec. 7.1.2.

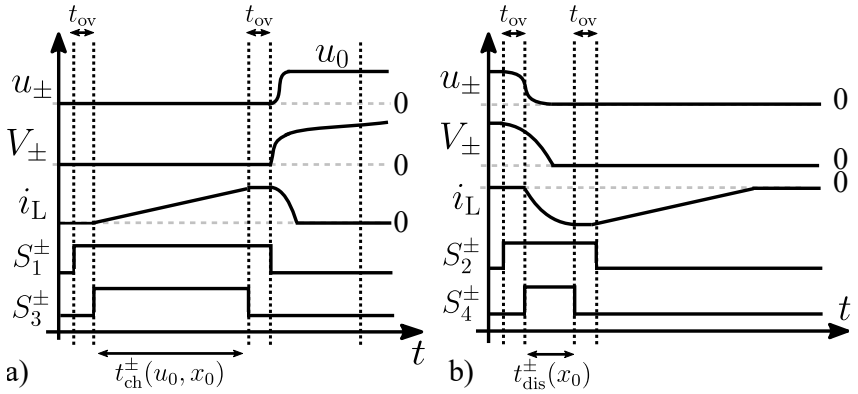

Figure 7.5: Waveforms for the interface circuit switches controls and associated electrical variables for: (a) application of a force u_0 across the transducer (b) nullifying the force across the transducer.

interface circuit, so as to operate at constant charge. Note that we suppose in the following that the architecture only needs to set a force from 0 to u_0, or equivalently, that $C_\pm$ is always discharged at the beginning of this process. This is always the case in the context of implementing of $u(t)$ in (7.8) when $\xi_\mathrm{n} x(t_\mathrm{n}) < 0$, i.e., a maximum of $\xi(t)$ of positive value or a minimum of negative value. In the case $\xi_\mathrm{n} x(t_\mathrm{n}) > 0$, going from the keeping force$\pm u_\mathrm{max}$ to $\alpha\xi_\mathrm{n}$ could be done by merely partially charging or discharge $C_\pm$ so that the force $u_\pm$ increases or decreases in absolute value from u_max to $\alpha|\xi_\mathrm{n}|$ (depending no the relative values of u_max and $\alpha|\xi_\mathrm{n}|$). Yet, here we make the (non-optimal) choice of always first completely discharging $C_\pm$ and then re-charging it afterwards to set the force $\alpha\xi_\mathrm{n}$. Hence, in the context of (7.8), the label u_0 that appears in the description below either denotes u_max (when setting a keeping force) or $\alpha|\xi_\mathrm{n}|$ (when setting a working force carrying out the position switchings).

The first step is to close switches $S_1^\pm$ and $S_3^\pm$ to transfer energy from C_res to L. The switches have to be kept closed for a time $t_\mathrm{ch}^\pm(u_0, x_0)$ to charge the inductor with the energy in (7.7). If we suppose that C_res is large so that the voltage across it V_res can be considered constant, $t_\mathrm{ch}^\pm(u_0, x_0)$ is found as

$$\frac{1}{2}\left(\frac{V_\mathrm{res}}{L} t_\mathrm{ch}^\pm(u_0, x_0)\right)^2 L = W_{u_0} \implies t_\mathrm{ch}^\pm(u_0, x_0) = \frac{\sqrt{2W_{u_0}L}}{V_\mathrm{res}} = \frac{\sqrt{2L|u_0|d_0(1 \mp x_0)}}{V_\mathrm{res}} \tag{7.18}$$

The discharge of the transducer sets the control force to zero, while transferring the transducer energy into the electrical energy tank. It can be in the event of an extremum of the input $\xi(t)$, in which case the invested energy ((7.14) or (7.15)) added to the converted energy (7.16) have to be transferred from $C_\pm$ to C_res. It can also be the keeping force that is being removed prior to the position switching, in which case the energy that was invested to set the keeping force has to be recovered. In all cases, the switches $S_2^\pm$ and $S_4^\pm$ have to be closed for a time $t_\mathrm{dis}(x_0)$ slightly above a quarter period of the $LC_\pm(x_0)$ cell:

$$t_\mathrm{dis}^\pm(x_0) = \frac{\pi}{2}\sqrt{\frac{\kappa d_0 L}{1 \mp x_0}} \tag{7.19}$$

After that, both switches are opened: L discharges through the diodes anti-parallel with $S_1^\pm$ and $S_3^\pm$, and then the transducer is kept at constant charge (if the leakage are negligible for the amount of time specified), generating a constant force u_0.

The waveforms depicted in Fig. 7.5.a summarize the evolution of the involved switches commands and of the electrical variables during the process of updating the force from 0 to u_0. The waveforms depicted in Fig. 7.5.b summarize the evolution of the involved switches commands and of the electrical variables during the process of updating the force from u_0 to 0. Note that these figures feature an additional time margin t_ov that is necessary in practice in order to avoid current discontinuity in the inductors, if the times are not perfectly matched which is always the case in practice.

The validity of the hypothesis that the position does not change during the force update process can now be assessed. The longest force update during the mass motion is when, at $\pm x_\mathrm{com}$, the transducer force is updated from 0 to u_0. In this case, the total duration of the force update is $t_\mathrm{ch}^\pm(\alpha\xi, \pm x_\mathrm{com}) + \pi/2\sqrt{LC_\pm(\pm x_\mathrm{com})}$. As t_ξ^f decreases with ξ and $t_\mathrm{ch}^\pm(\alpha\xi, \pm x_\mathrm{com})$

increases with ξ, the hypothesis that should be assessed is

$$t_{\mathrm{ch}}^{\pm}(\alpha\xi_{\max}, \pm x_{\mathrm{com}}) + \pi/2\sqrt{LC_{\pm}(\pm x_{\mathrm{com}})} < K' t_{\xi_{\max}}^{\mathrm{f}}, \tag{7.20}$$

for large enough K' whose value is dictated by the tolerated inaccuracy on the constant values of the control force.

7.1.4 Computation and sensing parts

This section describes the sensing and computation parts of the architecture. The constituting blocks of this subsystem and their connections are depicted in Fig. 7.6. We do not describe the detailed implementation of these blocks, as they are not exclusive to e-VEH applications. For simplicity, one can assume that all of the inputs and outputs in Fig. 7.6 and that are mentioned below are digital.

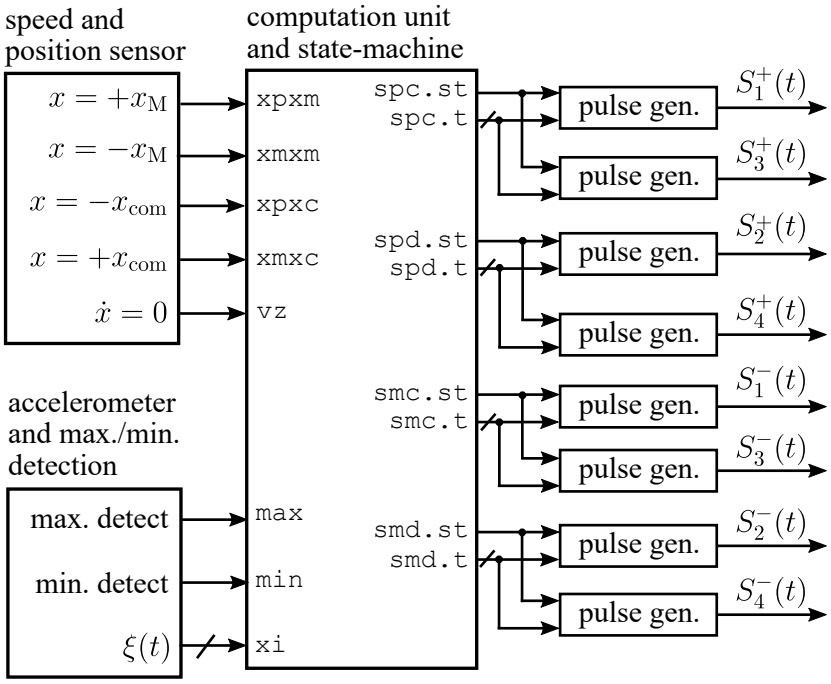

Figure 7.6: Architecture of the computation and sensors subsystem, that drives the interface circuit's switches to implement the control strategy of Sec. 7.1.2. The regular arrows represent "flags", or 1-bit digital signals, whereas the crossed arrows represent quantities (that can be analog or n-bit digital depending on the exact implementation).

Note that the control $u(t)$ as described in Sec. 7.1.2 does not require a measurement of the velocity, which is nevertheless featured in the schematic of Fig. 7.6 (the signal at the input `vz` of the state-machine). This modification slightly changes the control from $u(t)$ discussed in Sec. 7.1.2, in order to make it more robust. Indeed, because of control inaccuracy, the mass velocity may vanish before it reaches the targeted end-stop in the position commutation, hence returning to the end-stop that it has left when the extremum was detected. This would result in losing track of the mass position. To overcome this, when the velocity vanishes during the position commutation, the keeping force is applied so as to move the mass to the targeted end-stop. This induces end-stop collision losses and/or deviation from the optimal trajectory, but in return the mass position is known at all times. The simulations of the next section will

clarify this situation. We will also elaborate on the robustness requirements of the control law in Sec. 7.3.1.3.

The value of the input acceleration and the flags corresponding to the position and velocity of interest, and to the maximum/minimum detection, are fed into the main computation unit. This unit computes the command waveforms that have to be fed to the interface circuit switches in order to implement the control. To this end, it incorporates a finite-state automaton that sets the value of the output according to the sensed events. The graph of this finite-state automaton is depicted in Fig. 7.7 for the mere case of a sensed maximum with $\xi_{\mathrm{n}} x(t_{\mathrm{n}}) < 0$. The outputs of the finite-state automaton are a time value and a pulsed command for each switch in the electrical interfacing circuit. These outputs are fed into a programmable pulse generator. This component generates waveforms corresponding to the delays specified on its input `t`, when it is activated by a rising edge signal on its input `st`. By default, when the component is not generating any waveform, the output is zero. The operation of the pulse generators is described in Fig. 7.8.

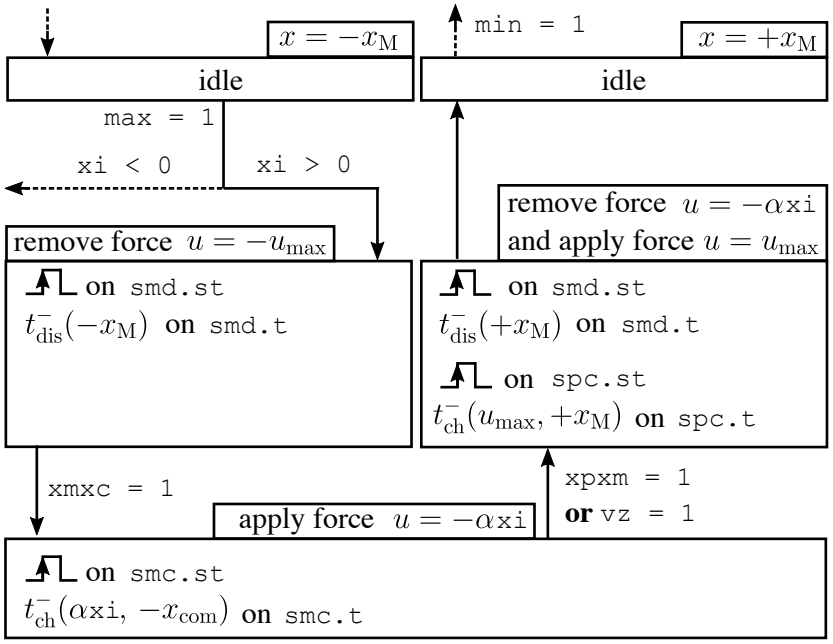

Figure 7.7: Schematic of the finite state automaton of the computation unit implementing the control strategy of Sec. 7.1.2. The part of the automaton that is depicted details the sequence for the position switching from $-x_{\mathrm{M}}$ to $+x_{\mathrm{M}}$ when a maximum of positive value is detected (that is, $\xi_{\mathrm{n}} x(t_{\mathrm{n}}) < 0$. The dotted arrow are connected to states that are not involved in this position switching event.

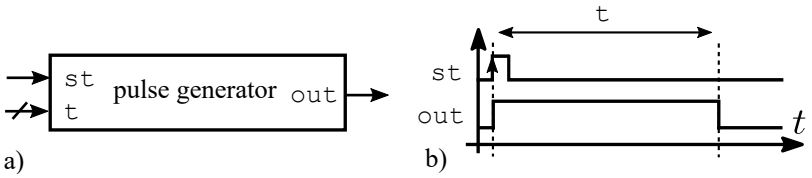

Figure 7.8: (a) Pulse generator block. (b) Waveform describing its operation.

An additional circuit that is not depicted in Fig. 7.6, is needed in order to synthesize the suited driving signals for the switches of the interfacing circuit, from the outputs of the pulse generators. This circuit depends on the chosen technology for the switches (e.g., gate level shifter for power MOSFET switches).

Finally, note that in the architecture as we presented, the interface circuit's switches are controlled in an open-loop manner by the computing unit, in order to implement $u(t)$. In other words, to implement a constant force value u_0, this unit closes the corresponding switches accordingly to (7.18). The inductor magnetizes with some energy W_0, and then discharges into $C_{\pm}$, this energy corresponding to the force u_0 (7.7). But because of parasitic elements (ohmic losses, parasitic capacitances) in the circuit, the total energy ending up in $C_{\pm}$ will be less than W_{u_0}, so that the implemented force will be less than u_0 and inaccuracy in the control follows. We will briefly discuss these robustness concerns in Sec. 7.3.2.2.

7.2 Sizing and simulations

In this section, the architecture described in Sec. 7.1 is tested in simulation. The simulations are carried out using Cadence AMS as for the coupled domain simulations of Chap. 4. This allows for the coupled simulation of the mechanical part described in terms of ODEs, the electrical part using a SPICE engine solver, and the computation/sensing parts of Sec. 7.1.4 using behavioral VHDL-AMS models. The modeling and parameters choice are the subject of Sec. 7.2.1. The results of the simulations for the sized architecture are given in Sec. 7.2.3. Then, the impact of some of the architecture's parameters on the harvested energy is highlighted in Sec. 7.2.4.

The mechanical input excitation used for the simulations is a 1 s sample extracted from a longer recording of the acceleration on a running human, using a smartphone accelerometer. The sample is representative of the recorded signal in its full duration, and corresponds roughly to two steps of running. The acceleration was recorded following the person's height axis. The smartphone was put in the trousers front pocket.

7.2.1 Parametrization of the architecture

Let us start by assigning realistic values to the parameters of architecture for the simulation. To do so, we start from the sole loose constraint that the total volume of the VEH should be of the order of $1\,\mathrm{cm}^3$, and that the mechanical device is made of silicon. The sizing is done in a heuristic manner, in the sense that the values of the parameter are not the result of a formal optimization. This is further discussed in Sec. 7.2.4.3. The mechanical resonator and the associated differential electrostatic transducer are modeled in VHDL-AMS, similarly to what is reported in by Galayko *et al.* in [GPB07]. The interface circuit is described and simulated as a SPICE netlist for the coupled simulation.

7.2.1.1 Mechanical part

For the imagined gap-closing electrostatic transducer, a geometry similar to the schematic structure depicted in Fig. 7.1 is chosen. It is a cuboid-shaped mass sliding in between two electrodes, to which it is connected by spring suspensions. We select a mass of $m = 1\,\mathrm{mg}$, and a spring stiffness of $k = 400\,\mathrm{N\,m^{-1}}$, yielding a resonant frequency of 100 Hz for the subsequent resonator. The transducer surface is of $S = 10\,\mathrm{cm}^2$, and the gap at $x = 0$ is of $d_0 = 50\,\mu\mathrm{m}$. A device with such parameters can be obtained, e.g., by a differential and slightly upscaled version of the

transducer structure reported in [MYR08] fabricated in silicon, and that was already presented in Fig 1.27b of the introduction.

With this geometry, the active area is of 3.16 cm × 3.16 cm for a depth of 450 µm. Referring to the transducer structure in the schematic in Fig. 7.1, this means that $L_1 = L_2 = 3.16\,\text{cm}$, and $h_\text{f} = 450\,\mu\text{m}$. The mechanical device's volume is then of $0.55\,\text{cm}^3$. The maximum and minimum values of the transducer's capacitances are respectively $C_\pm(\pm x_\text{M}) = 3.54\,\text{nF}$ and $C_\pm(\mp x_\text{M}) = 90\,\text{pF}$. The mass, seen as a beam of width 450 µm, length 3.16 cm and height 3.16 cm, has a stiffness of $17.5\,\text{kN}\,\text{m}^{-1}$ in the direction normal to the transducer's electrode plane. This is computed considering a Young modulus of 192 GPa for silicon. Given our ξ_max, this value allows to consider that the mass deflection in the direction normal to the transducer's electrode plane is negligible, so that the lumped mass model used to build the harvester's architecture is accurate. A linear damping effect is incorporated, to model an air friction phenomenon. The corresponding quality factor is of $Q = 1$ for the obtained linear resonator. Note that this value is two orders of magnitudes above what is predicted by (4.60). Plus, non-linear air damping effects can have significant impact on the dynamics as we saw in Chap. 4. Yet, vacuum-packaging [ERK10] or, in a more limited manner, specific transducer geometry designs [LMG17], have both shown to greatly reduce damping effects. This hypothesis also allows us to focus on the role of the control generation and inaccuracy cost on the energy shortfalls with our near-limits VEH architecture. The mechanical end-stops were modeled inspired by [TLH15]: a linear spring $k_\text{st} = 1\,\text{MN}\,\text{m}^{-1}$ associated with a linear damper $\mu_\text{st} = 10\,\text{N}\,\text{s}\,\text{m}^{-1}$.

For the following simulations, we first select x_com as $x_\text{com} = x_\text{M}/2$ (x_com is then varied in Sec. 7.2.4.2). Therefore, $C_\pm(\pm x_\text{com}) = 338\,\text{pF}$. In order to estimate the minimum position switching time as well as to choose the keeping force u_max, an estimate for ξ_max is needed. Let us suppose that $\xi_\text{max} \leqslant 60\,\text{mN}$. Therefore, t_ξ^f ranges from 2.84 ms to 4.97 ms. The keeping force must be chosen greater than $\xi_\text{max} + kd_0x_\text{M}$. We choose $u_\text{max} = 75\,\text{mN}$.

7.2.2 Electrical part

The electrical energy tank is modeled as a large ideal capacitor $C_\text{res} = 10\,\mu\text{F}$ and with $V_\text{res} = 10\,\text{V}$.

The switches $S_1^\pm$ and $S_2^\pm$ block the transducer voltage, that can go to up to 415 V as indicated by (7.17), for $x_\text{com} = x_\text{M}/2$. These four switches are parametrized to model power MOSFETs with their anti-parallel body diodes. The large signal parasitic capacitance at zero blocking voltage is chosen as $C_\text{J0} = 10\,\text{pF}$. This value is selected as the largest C_J0 in the range 5 pF to 50 pF (varied by steps of 2.5 pF) that yields less than 5% error on the transducer force, when the latter ranges from 10 mN to 100 mN, and when the force is set while the transducer capacitance of $C_\pm(\pm x_\text{com})$. As the switches' large signal parallel parasitic capacitance is a nonlinear function of the switch bias – it follows $C_\text{J} \propto 1/\sqrt{V_0 - V}$, where V is the voltage blocked by the switch and V_0 is the junction's potential of the MOSFET – we determined this value of C_J0 under the 5% error constraint by successive simulations, where all ohmic losses were removed.

The value of the ON-state resistance corresponding to C_J0 was determined using the relations provided in [MG12]. In all, we have that

$$R_\text{ON} = \frac{\rho {V_\text{max}}^{3/2}}{C_\text{J0} {V_0}^{1/2}} \tag{7.21}$$

where $\rho = 2.2 \times 10^{-14}\,\Omega\mathrm{CV}^2$ is a constant, $V_{\max}$ is given in (7.17) and $V_0 = 1\,\mathrm{V}$ is the built-in junction potential. Applying (7.21) to power MOSFET blocking up to 420 V and for the chosen value of $C_{\mathrm{J0}} = 10\,\mathrm{pF}$, it comes that $S_1^{\pm}$ and $S_2^{\pm}$'s ON-state resistance is $R_{\mathrm{ON}} \leqslant 19\,\Omega$. Notice that in (7.21), we have eluded that the dependence between R_{ON} and C_{J0} is in fact expressed through their mutual dependence to the area of the MOSFET's conducting epi-layer cross-sectional area. The cross-sectional area corresponding to our parametrization of the switch is of $200\,\mu\mathrm{m}^2$, well within what can be achieved by actual technological processes.

Given our choice of the mechanical system done in (7.2.1.1), and to fulfill the size requirement of the VEH, inductors of size that do not exceed $0.25\,\mathrm{cm}^3$ are considered. At fixed inductor size, smaller-valued inductors have smaller series resistance. But on the other hand, to magnetize the inductor with a given energy amount, the current will be larger with a smaller-valued inductor. Therefore, ohmic losses due to all of the circuit's resistive elements, including the inductor's resistance, are increased. Because of this, there exists an optimum value of the inductor that minimizes ohmic losses. Given the selected value for R_{ON}, we numerically determined that $L = 1\,\mathrm{mH}$, modeled as an ideal inductor element in series with its parasitic DC resistance of $R_{\mathrm{L}} = 6\,\Omega$ and fulfilling our size requirements [14], is nearly optimal regarding to the resistive energy losses. The electrical timescale of the force update can be estimated: $t_{\mathrm{ch}^{\pm}}(\alpha\xi_{\max}, x_{\mathrm{com}}) + \pi/2\sqrt{LC_{\pm}(\pm x_{\mathrm{com}})} = 6.5\,\mu\mathrm{s}$.

The parts that were described in Sec. 7.1.4 are modeled in VHDL-AMS as behavioral blocks, as are the gate level shifters driving the circuit's MOSFETs.

7.2.3 Simulation illustrating the architecture's operation

Results illustrating the operation of the system submitted to the 1 s input excitation are depicted in Fig. 7.9. The plot in Fig. 7.9.a shows the mass trajectory and the input force. A magnified plot of both the mass position and the input force around two extrema, explicating the mass position switching, are depicted in Fig. 7.9.b.

Let us further comment the results in this figure. In (a), the mass position and the input force are depicted. The figure in (b) gives a magnification around two extrema. The minimum of $\xi(t)$ at ⓐ is detected and hence the control makes the mass move from $+x_{\mathrm{M}}$ to $-x_{\mathrm{M}}$. The extrema at ⓑ and ⓒ are ignored because they happen during the position switching. This follows from the specification of the finite state automaton depicted in Fig. 7.7. At ⓓ, the control inaccuracy provokes a collision with the end-stop at $+x_{\mathrm{M}}$. At ⓔ, the control inaccuracy makes the mass velocity vanish before $+x_{\mathrm{M}}$, so that the control applies the keeping force to force the mass to travel to $+x_{\mathrm{M}}$. As a result, the mass collides with the end-stop at $+x_{\mathrm{M}}$ and some energy is dissipated in the collision. In (c) the evolution of the main energies in the VEH are depicted. The harvested energy is defined here as the difference between the energy in C_{res} at $t = 0$ and at $t = 1\,\mathrm{s}$. The figure in (d) shows the magnification of the harvested energy around a maximum ξ_0 of $\xi(t)$ that is such that $\xi_0 x(t_0) < 0$, i.e., ξ_0 is a maximum of positive value. At ①, energy is gathered back from removing the keeping force, so the mass can start travel towards $+x_{\mathrm{M}}$ as $\xi(t)$ acts upon it. At ②, energy is invested to implement the control force working negatively on the mass. At ③, the sum (invested energy + converted energy - energy to implement the keeping force at $+x_{\mathrm{M}}$) is gathered back in C_{res}. Finally, (e) shows the magnification of the harvested energy around a minimum ξ_1 of $\xi(t)$ that is such that $\xi_1 x(t_1) > 0$,

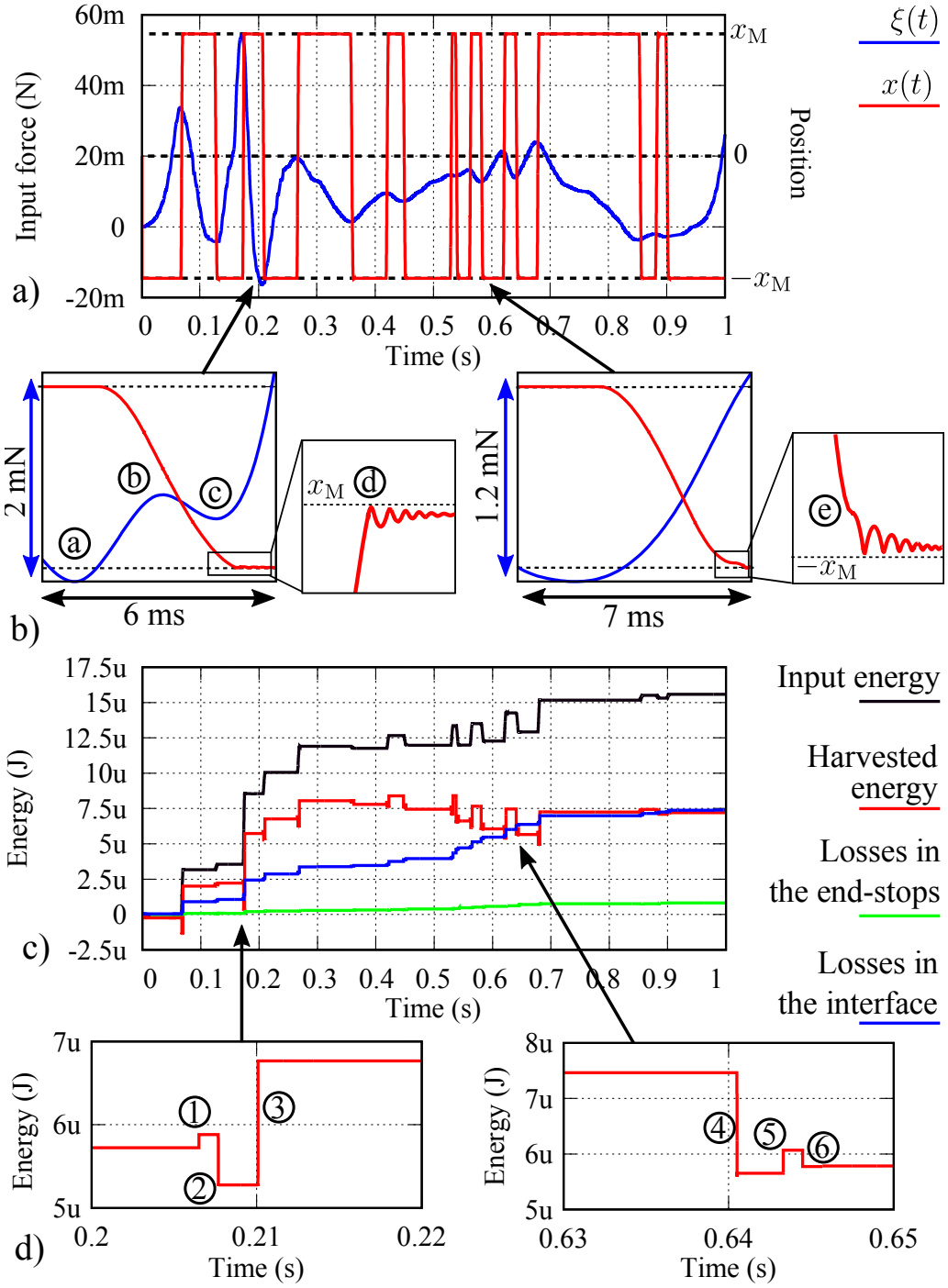

Figure 7.9: Results of the simulation of the near-limits electrostatic VEH.

i.e., ξ_1 is a minimum of positive value. At ④, the energy to implement the negatively working control force is invested, while some energy is being recovered from removing the keeping force at $+x_{\mathrm{M}}$. At ⑤, part of the invested energy is recovered and the mass continues to travel towards x_{M}. At ⑥, some energy is invested from C_{res} to implement the keeping force at $+x_{\mathrm{M}}$.

The evolution of the harvested energy depicted in Fig. 7.9.b. shows that at the end of the sample, it amounts to 7.2 µJ. At the same time, the system input energy is of 15.6 µJ. The sample plot shows the evolution of the total energy lost in the elements of the interface circuit, which amounts to 7.3 µJ. The losses dues to the mass collision with the end-stops, reflecting the control imprecision, are also depicted and amount to 0.8 µJ. For the energy balance to be complete, one has to consider the instantaneous energy in $C_{\pm}$, in the inductors, in the spring and the energy dissipated by the linear damper accounting for air friction. These sum to smaller amounts than the other energies and are not represented in the energy balance of Fig. 7.9.b.

The results show that nearly as much energy is harvested as is lost in the electrical interface. The losses in the end-stops are relatively small, as accuracy in the force was privileged over resistive losses when selecting the electrical components in Sec. 7.2.2. The good accuracy is further reinforced by the relative values of the electrical and mechanical timescales. Let us now discuss how some slight modifications in the control law can help increase the harvested energy.

7.2.4 Impact of some of the parameters

7.2.4.1 Extremum selection

One can immediately notice by inspecting the results in Fig. 7.9.b that the consecutive extrema happening between 0.5 s and 0.7 s lead to an overall decrease in the harvested energy. This is because the cost of carrying out the position switchings overcomes the converted energy for these pair of extrema. In such a case, it can be beneficial to ignore them and not carry out the position switching.

To this end, we add a primitive criterion of extremum selection for the position switching. It consists in carrying out the position switching only if the difference of values between the sensed extremum with the previously selected extremum exceeds a threshold value. We select this threshold value to be 15 mN. This results in skipping the extrema that led to a decrease of the harvested energy at the end of the sample.

The system is then simulated, and the results are depicted in Fig. 7.10. The trajectory deviates from $x_\xi(t)$ in that the extrema of $\xi(t)$ happening between 0.4 s and 0.8 s are now skipped. These extrema were shown in Fig. 7.9 to result in a shortfall in the harvested energy (see Fig. 7.9.b). Compared to the previous simulation without a selection threshold, this results in a decreased input energy (14.1 µJ) but increased harvested energy (9.4 µJ). Both the losses in the electrical interface (4.2 µJ) and in the end-stops (0.3 µJ) are decreased. This is an obvious example where a different trajectory than $x_\xi(t)$ yields higher harvested energy than $x_\xi(t)$ because of impact of the control generation cost on the harvested energy (see Sec. 6.2.2).

Note however that the maximum at 0.62 s is selected, whereas it would have been more beneficial to skip it and select the next maximum at 0.67 s. Nonetheless, increasing the threshold value so as to select the latter for position switching would in fact make the extremum at 0.35 s

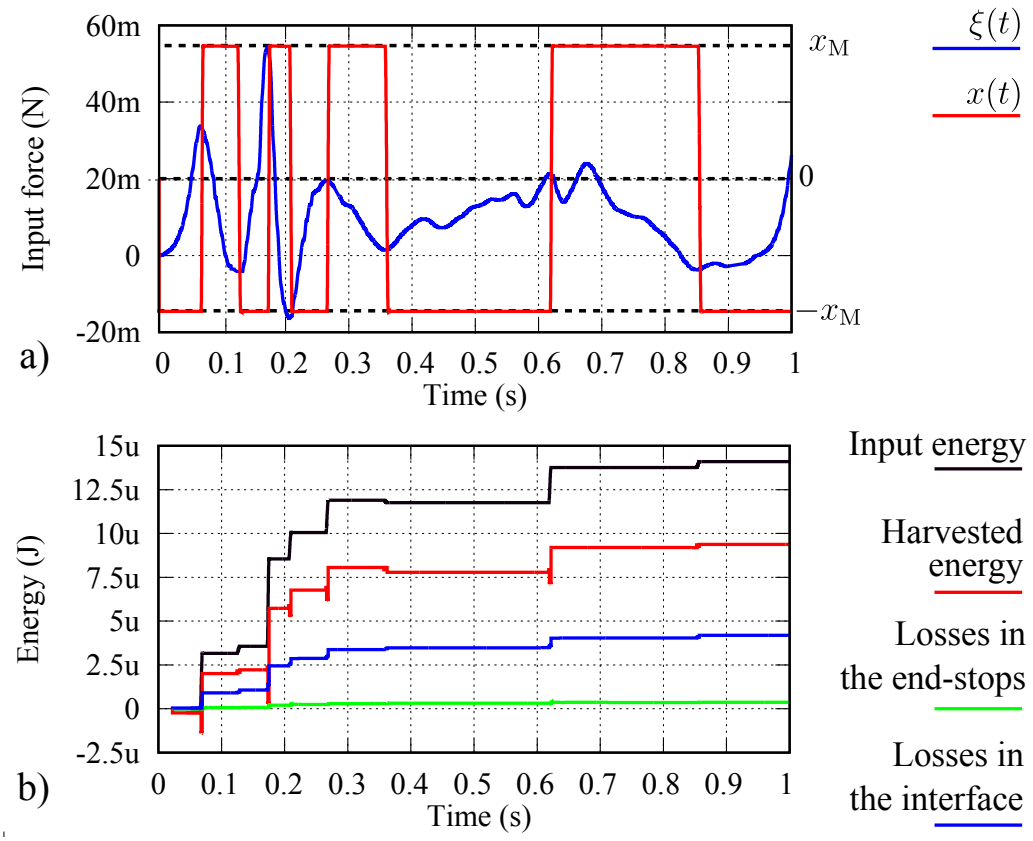

Figure 7.10: Results of the simulation of the near-limits electrostatic VEH, in the same setting as for the results depicted in Fig. 7.9 but with a threshold for extremum detection of 15 mN. — (a) Mass position and input force. — (b) Evolution of the energies.

to be skipped. The subsequent sequence of selected extremum would then result in a decreased amount of harvested energy. This shows that smarter algorithms of extremum selection are needed in order to yield better figures of harvested energy.

7.2.4.2 x_{com} parameter

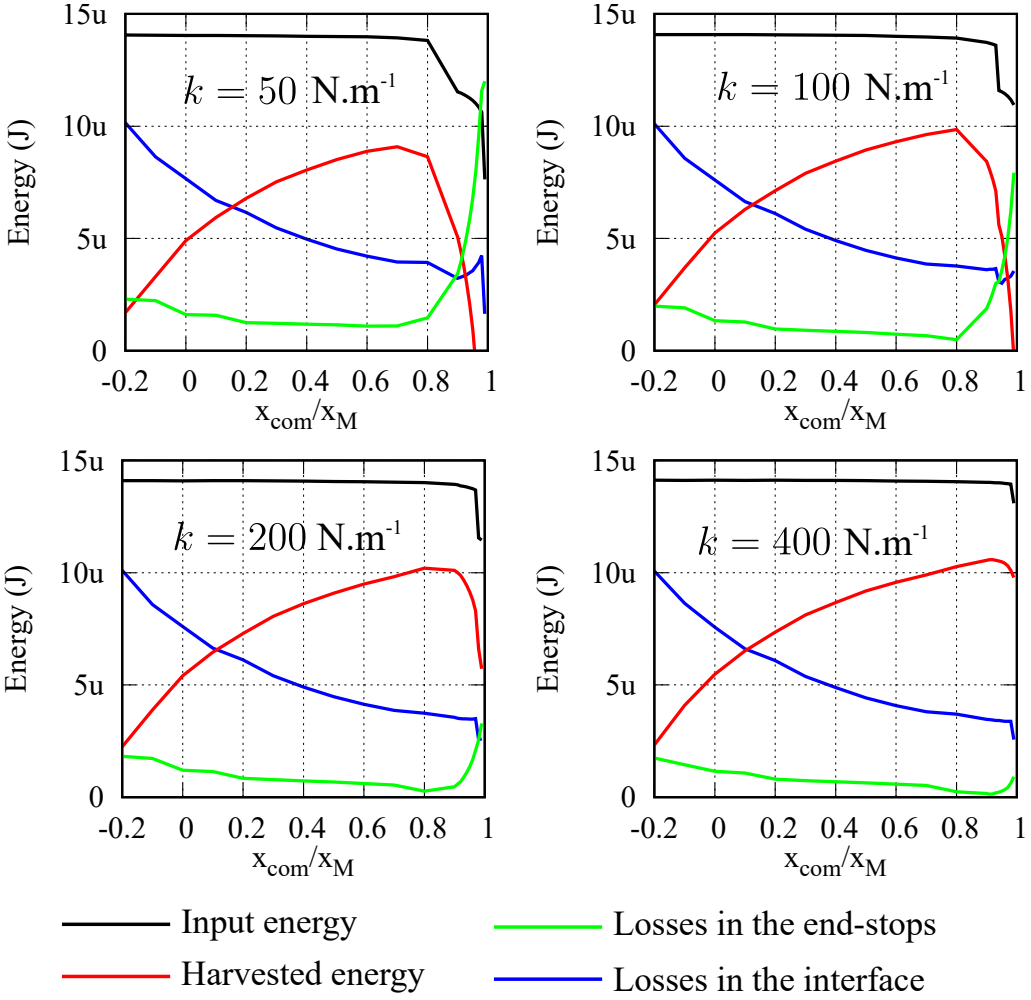

Figure 7.11: Results of the simulation of the near-limits electrostatic VEH, varying x_{com}, k and the switches parameters R_{ON} and C_{JO} accordingly. The other parameters have the values chosen in Sec. 7.2.1. The results are obtained with the 15 mN extremum selection threshold.

The role of the control-related parameter x_{com} was discussed in Sec. 7.1.2.2. In addition to the decreased invested energy, increasing x_{com} allows to chose switches with reduced resistance and parasitic capacitance, thanks to the reduced maximum transducer voltage, as follows from (7.17) and (7.21). Another advantage in increasing x_{com} comes from the cases of extrema such that $\xi_n x(t_n) < 0$. Indeed, in such cases, the non-zero force is applied when the transducer's capacitance is $C_{\pm}(\pm x_{\text{com}})$, which increases with x_{com}. Thus, the inaccuracy in the force value due to the parasitic capacitances of the interfacing circuit is decreased, as the transducer capacitance is large compared to the parasitic capacitances of the switches.

The simulation results depicted in Fig. 7.11 show the energy balance at the end of the 1 s input, for values of x_{com} ranging from $-x_{\text{M}}$ to x_{M} (excluded), and for different k. The extremum selection threshold of 15 mN is used. For each point, a new value of R_{ON} is used accordingly to

(7.21) in which the value of V_{max} computed from (7.17) is injected.

The results are slightly improved compared to Sec. 7.2.4.1 ($k = 400\,\mathrm{N\,m^{-1}}$). The harvested energy is increased from 9.4 µJ with $x_{com} = 0.5x_M$ to 10.6 µJ with $x_{com} = 0.9x_M$. This is the highest value of harvested energy obtained from this sample. It amounts to 68% of the absolute limit in *input energy* that can be obtained with the considered mechanical device and input excitation. This value of $x_{com} = 0.9$ yields a maximum transducer voltage of 370 V, so that, according to (7.21), R_{ON} was reduced from 19 Ω with $x_{com} = x_M/2$, to $R_{ON} = 15\,\Omega$.

One notes that when k is high, increasing x_{com} is beneficial up to values that are very close to x_M. This is because the high value of k ensures that the position switching remains fast enough, despite the increase of x_{com}, so that the control is able to accurately implement $x_\xi(t)$ (see (7.11) and Fig. 7.3). As k is decreased, the position switching becomes slower. Hence, the value of x_{com} for which the control becomes inaccurate so that the implemented trajectory significantly deviates from $x_\xi(t)$ is reduced. The decrease in the input energy for higher-end values of x_{com} corresponds to significant deviation of the implemented trajectory from $x_\xi(t)$. For example, with $k = 50\,\mathrm{N\,m^{-1}}$ and $x_{com} = 0.9x_M$, the position switching time for the maximum at 0.17 s (the largest extremum of the sample) is of 6.8 ms, during which the value of $\xi(t)$ decreases of 30% from its value at the extremum. In this case, the hypothesis that $\xi(t)$ remains approximately equal to its extremum is largely violated. The control subsequently fails to correctly carry out the position switching.

7.2.4.3 Discussion on the optimization through the system's parameters

In the above simulations, a $1\,\mathrm{cm^3}$ size constraint was considered. A mechanical device inspired from existing designs and compatible with this constraint was chosen *a priori* (Sec. 7.2.1.1). Only then, the electrical part was optimized under a transducer force accuracy constraint (Sec. 7.2.2), hence predefining the balance between the control accuracy and the energy losses in the interface circuit. This determined the value of the resistive components of the circuit elements, which are the origin of a major component of energy loss in the electrical interface. Finally, after both the mechanical part and the electrical part were fixed, the control was tuned in order to maximize the harvested energy (Sec. 7.2.4).

In fact, an optimized design flow would consists in allowing customized sizing of the mechanical device, and different balances between the control accuracy and the losses in the electrical interface. Carrying out this optimization, instead of the sequential design choices that we did in Sec. 7.2.1, will undoubtedly improve the figures of harvested energy. The subsequent optimization includes parameters related to the control, to the mechanical part, and to the circuit components, under constraint that are dictated by the application (e.g., maximum size constraint) and for known characteristics of the input (at least ξ_{max}). Also, the sole premise of using power MOSFET switches may be detrimental to the harvested energy, compared to other technologies [SG05].

This work being thought as a starting for further investigations of near-limits VEHs, we did not carry out such an optimization procedure yet, which has to be the subject of future works. Also, below in Sec. 7.3, we discuss others avenues worth exploring, that do not fall within the optimization on parameters of the presenter architecture. Rather, the variations that we present

below are structural changes to the architecture.

Before describing such architecture variations, as a final note, it has to be considered that a limitation of the above simulations is that they do not take into account the consumption of the blocks of Sec. 7.1.4. This is because these blocks were described using behavioral models. Some of these parts have to be taken into account in the overall system optimization, as their energy consumption depends on the system's parameters. For example, the temporal resolution of the position detector should be low enough compared to the position switching time, which goes with increased power consumption. Likewise, the computation time should be negligible with respect to the position switching time. State-of-the-art realizations of each of the blocks constituting the computing and sensing part show micro-watt or sub-micro-watt energy consumption figures [17; SLN15; 15; KBH13; GAW13; JMV10; JJO15]. These consumption figures are comparable with the amount of harvested energy in our simulated example, further reinforcing the need for a fine system optimization.

7.3 Variations of the presented architecture

This section deals with variations of the architecture of near-limits VEH described in Sec. 7.1. Each idea is mentioned very briefly and only reviewed on surface, so that this section stands for a "future works" list, in the sense that we did not had the time to explore most of these ideas in deep.

Each of the variations presented here constitute paths that we think are worth pursuing in order to enable the realization of practical near-limits VEH that effectively come close to the limits of energy conversion. The variety of application contexts will certainly make some of these ideas useful in some situations. Contrarily to the optimization procedure discussed above in Sec. 7.2.4.3 – which is also yet to be carried out – the variations we present here deal with the structure of the architecture, in that they imply a change in the architecture itself, rather than merely tuning the value of a parameter that already appears in it.

These variations are given for the three principal constituents of the architecture, namely, the control law, the electrical interface, and the mechanical structure of the near-limits VEH.

7.3.1 Variations in the control

7.3.1.1 Time-optimal controls

A legitimate modification of the control as presented in our first architecture is to put emphasis on reducing the mass position switching duration at each extremum detection. This is because reduced switching duration improves the accuracy of the control, as was discussed in Sec. 7.1.2 and observed in the simulations of Sec. 7.2.

The time-optimal control problem at each extremum detection reads

$$(Q_{\mathrm{T}}) \begin{cases} md_0\ddot{x}(t) = \xi_{\mathrm{n}} + mu(t) - kd_0x(t) \\ (x(0), \dot{x}(0)) = (-x(t^{\mathrm{f}}_{\xi_{\mathrm{n}}}), \dot{x}(t^{\mathrm{f}}_{\xi_{\mathrm{n}}})) = (\pm x_{\mathrm{M}}, 0) \\ |x(t)| \leqslant x_{\mathrm{M}}, \\ \min\limits_{\|u\|_\infty \leqslant u_{\mathrm{M}}} t^{\mathrm{f}}_{\xi_{\mathrm{n}}} \end{cases},$$

Notice that $u(t)$ has the dimension of an acceleration here, to lighten the forthcoming notations. In the case of $k = 0$, it is easy to show that the solution to this problem is a bang-bang command with one commutation [Tré08]. In practice, this also encompasses cases where the stiffness k is low. In this case, we can show that the solution of the minimum-time control problem (Q_{T}) is given by

$$\tilde{u_n}(t) = \begin{cases} \pm\mathrm{sign}(\xi_{\mathrm{n}})u_{\mathrm{M}} & \forall t \leqslant t_x, \\ \mp\mathrm{sign}(\xi_{\mathrm{n}})u_{\mathrm{M}} & \forall t > t_x. \end{cases} \tag{7.22}$$

Here, $\pm$ has to be chosen as $+$ if ξ_{n} is a maximum of negative sign or a minimum of positive sign, and as $-$ otherwise (and conversely for $\mp$). The commutation has to be carried out at time t_x

$$t_x := \sqrt{2d_0 \frac{x_{\mathrm{M}}}{u_{\mathrm{M}}} \frac{u_{\mathrm{M}} \mp \xi_{\mathrm{n}}}{u_{\mathrm{M}} \pm \xi_{\mathrm{n}}}}, \tag{7.23}$$

and the total position switching duration time amounts to

$$t^{\mathrm{f}}_{\xi_{\mathrm{n}}} = 2\sqrt{2d_0 u_{\mathrm{M}} x_{\mathrm{M}} ({u_{\mathrm{M}}}^2 - {\xi_{\mathrm{n}}}^2)^{-1}} \tag{7.24}$$

Because $x(t)$ is monotonic during the position switching, the commutation event can be specified in terms of position $x(t_x)$ instead of time t_x. In (7.22), u_{M} refers to the maximum value that the control can take in absolute value, that is, $-u_{\mathrm{M}} \leqslant u(t) \leqslant u_{\mathrm{M}}$. In our architecture, this maximum can be defined as a function of the amount of energy we are willing to invest (and therefore, can afford to lose) in order to implement the position switchings. Thus, a first observation is that the larger u_{M}, the larger the control generation cost will be. A second observation is that, compared to (7.8), the control (7.22) takes two non-null values instead of just one. The two latter observations support the general trend that a faster control is achieved at the price of larger control generation cost, calling for a trade-off.

When $k \gg 0$, then the problem (Q_{T}) becomes more difficult because of the state constraint $|x| \leqslant x_{\mathrm{M}}$. We did not further push investigations, and there are certainly cleverer ways known to the research community in optimal control to tackle the problem given its simple linear form, but a naive way would consist in a "raw" application of the Pontryagin Maximum Principle (PMP). The cost functional has to be completed by a penalty that weights the displacement excedient. However, to the best of our knowledge, computing solutions from the application of the PMP in such cases often require the numerical solving of boundary-value problems [Tré08]. This task can be rather computationally intensive. It is questionable if it is realistic to provide the e-VEH with a computing unit capable to resorting to such calculations in real-time, because of the associated energy consumption.

7.3.1.2 Energy-optimal controls

In the simulations of our near-limits VEH architecture, the mechanical friction did not play a large role. This is because we used a high value of the mechanical quality factor, compared to what can be estimated for our geometry using, e.g., the relation (4.60).

Let us consider a context where these losses are large and have more influence on the system's dynamics. The first thing to note in this case is that the control to carry out the position switching has to be changed in order to be accurate. That is, the control has to solve

$$(Q_{\mathrm{F1}}) \begin{cases} md_0\ddot{x}(t) = \xi_{\mathrm{n}} + u(t) - kd_0x(t) - c(x,\dot{x})d_0\dot{x} \\ (x(0),\dot{x}(0)) = (-x(t_{\mathrm{n}}^{\mathrm{f}}),\dot{x}(t_{\mathrm{n}}^{\mathrm{f}})) = (\pm x_{\mathrm{M}},0) \\ |x(t)| \leqslant x_{\mathrm{M}} \end{cases},$$

Furthermore, we have seen in Sec. 6.2.2 of Chap. 6 that minimizing both the costs of control generation and the losses in mechanical friction mechanisms makes the implemented trajectory approach the optimal, energy-maximizing trajectory. In our discussion, we took the example of a linear damping and its effect in the shortfall of converted energy, as investigated by Halvorsen *et al.* in [HLM13]. Therefore, it is naturally worth investigating controls that specifically aim to reduce the amount of energy lost in mechanical friction in the position switching. This is readily put into the form of an optimal control problem

$$(Q_{\mathrm{F2}}) \begin{cases} md_0\ddot{x}(t) = \xi_{\mathrm{n}} + u(t) - kd_0x(t) - c(x,\dot{x})d_0\dot{x} \\ (x(0),\dot{x}(0)) = (-x(t_{\mathrm{n}}^{\mathrm{f}}),\dot{x}(t_{\mathrm{n}}^{\mathrm{f}})) = (\pm x_{\mathrm{M}},0) \\ |x(t)| \leqslant x_{\mathrm{M}}, \\ \min\limits_{u\in\mathcal{U}} \int_0^{t_{\xi_{\mathrm{n}}}^{\mathrm{f}}} c(x(s),\dot{x}(s))\dot{x}^2(s)\,\mathrm{d}s \end{cases},$$

Here, $\mathcal{U}$ refers to the set of piecewise-constant controls, bounded by some value u_{M}. We require that the sought control belong to this set because this is the form of control force that can be implemented by our architecture as we presented it. This problem is a fixed final time problem [Kir12]. In practice, the time $t_{\xi_{\mathrm{n}}}^{\mathrm{f}}$ has to be specified so as to enforce the hypothesis that $\xi(t) \approx \xi_{\mathrm{n}}$ during the position switching .

If one removes the state constraint $|x| \leqslant x_{\mathrm{M}}$ and the constraint of piecewise-constant u, the (Q_{F2}) problem with linear damping ($c(x,\dot{x}) = b$ constant) becomes the classical linear-quadratic optimal control problem. Still, extensions of the classical linear-quadratic theory for sampled-data controls are investigated by the optimal control research community [BT17], and many results are also available for the state-constrained case.

An interesting question is to compare the converted energy yielded by implementing $x_\xi(t)$ using a control that solves (Q_{F2}) at each position switching event, with the converted energy from the energy-maximizing motion derived by Halvorsen *et al.* in [HLM13], but whose implementation requires *a priori* knowledge of $\xi(t)$'s harmonic nature. Answering this question can provide a first benchmark on how much can near-limits VEHs approach the upper bound of *converted energy*.

Also, the problem (Q_{F2}) with more general cost functionals can be considered, such that

those arising from the nonlinear squeeze-film damping already encountered in Sec. 4.3.1.1. Such nonlinear optimal control problems can be tackled starting from the PMP, in a form allowing to account for the piecewise-constant nature of u. This type of control constraint was investigated by Bourdin and Trélat in [BT15]. As for the state-constrained time-optimal controls, resorting to this approach may require involved numerical methods that can violate the low-power consumption requirement for the computing unit.

In the same way, we can consider optimal control formulations seeking to minimize the control generation cost at each position switching event. The costs functionals that are ought to be considered in this case must result from a detailed analysis of the source of energy losses in the interface circuit. It is also naturally possible to consider position switching problems with cost functionals that account for both the electrical control generation cost and the mechanical friction induced losses.

7.3.1.3 Robust controls

An important consideration that we have eluded in our description of the architecture is the robustness of the control. Our control law presented in Sec. 7.1.2 is an open-loop control. Hence, the change of $\xi(t)$ from its extremum values during the position switching, as well as model and state estimation uncertainties, can have a large impact on the accuracy with which of our control law synthesizes the mass position switchings.

A first possibility to implement robust position switchings is to stabilize the mass at $\pm x_{\mathrm{M}}$, until an extremum of $\xi(t)$ is sensed. When this happens, the position switching is carried out by changing the reference position to $\mp x_{\mathrm{M}}$. The $|x(t)| \leqslant x_{\mathrm{M}}$ constraint can be enforced by requiring no overshoot in the response to the change in reference position, while requiring an acceptable settling time in order to enforce the hypothesis that $\xi(t) \approx \xi_{\mathrm{n}}$. Such a controller can be readily synthesized using classical methods from control theory (e.g., pole-placement). We can also explicitly account for the discrete nature of our transducer force to implement such stabilization mechanism using a deadbeat controller [Son13].

Another conceptually simple possibility to implement robust position switching from $\pm x_{\mathrm{M}}$ to $\mp x_{\mathrm{M}}$ is to use linear-quadratic theory. More precisely, a pre-determined switching trajectory from $\pm x_{\mathrm{M}}$ to $\mp x_{\mathrm{M}}$ can be specified. A LQ regulator can be used in order for the mass to track this pre-determined trajectory, while rejecting external disturbances (e.g., changes in $\xi(t)$ from its detected extremum value). Once again, one has to weigh the pros and cons to such possibly computation-intensive methods, here because of the real-time computation of the controller gains.

7.3.1.4 Extremum selection

Finally, in addition to the three variations in the control law listed above, we can add the concept of extremum selection that was illustrated in the simulations of Sec. 7.2.4.1. Improvements upon our rather primitive extremum selection criterion used therein include the implementation of algorithms that based on a statistical treatment of the input force history.

7.3.2 Changes in the interface circuit

7.3.2.1 Slightly modified energy transfer circuit

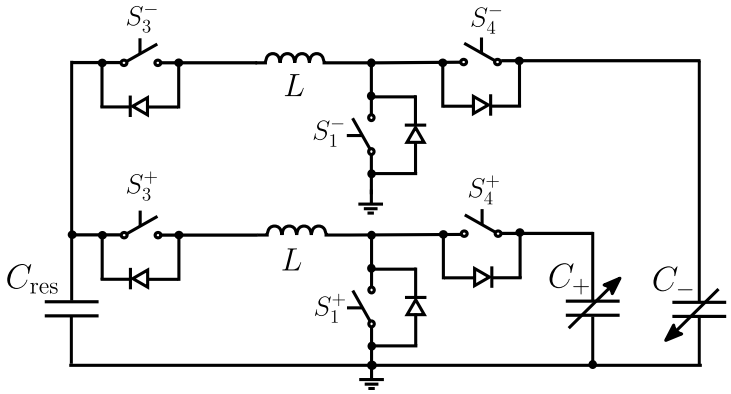

Figure 7.12: A slightly modified version of the circuit in Fig. 7.4 to implement the energy transfers for the control of the electrostatic near-limits VEH.

The circuit in Fig. 7.12 is a slightly modified version of the interface circuit in Fig. 7.4 that our architecture was originally presented with. Here, the switch $S_2^{\pm}$ is removed. Therefore with this circuit, charging the transducer is done by closing switches $S_1^{\pm}$ and $S_3^{\pm}$ so to magnetize the corresponding inductor. Then, when $S_1^{\pm}$ is opened, the transducer $C_{\pm}$ is charged through the loop $C_{\text{res}}, L, C_{\pm}$, through the anti-parallel diode with $S_4^{\pm}$. Compared to the circuit of Fig. 7.4, one switch command is saved. Also, the current flows through less switches than with the circuit of Fig. 7.4, which required to first magnetize L through two elements, and demagnetize it in $C_{\pm}$ through two other switches.

The drawback of this circuit is that the voltage to which $C_{\pm}$ has to be charged has to exceed V_{res}. Thus, this interface circuit does not allow to implement forces that are too small in absolute value.

7.3.2.2 Robust force implementation

In the end of Sec. 7.1.4, we pointed out that the forces values are set through a direct timed-command of the switches of the interface circuit. This timed-command is done by the computing unit. We mentioned that this induces possible errors in the implemented force value, due to, e.g., parasitic elements in the circuit, or timing errors. Later in the simulation section, we chose the values of the parasitic capacitances of our MOSFET switches so as to reduce the inaccuracy on the force. However, this forced us to select MOSFET switches with high ON-state resistance value, in the light of (7.21). This resulted in a large control generation cost that was observed in the simulations: the losses in the interface circuit amounted for about half of the input energy in the e-VEH, and were the major source of shortfall in the harvested energy. Therefore, it may be of interest to relax the requirements on the switches, for example by allowing for larger parasitic capacitance.

To do so without inducing a large error on the implemented value of the force, an electrical feedback mechanism has to be used. In short, the computing unit should monitor the energy in $C_{\pm}$ after it has charged it from a first time-based actuation of the interface circuit switches.

Therefore, it can compensate a possible deficit or overhead of energy in $C_{\pm}$, subsequent to losses in the parasitic elements of the circuit, or to timing errors in the first transfer.

This electrical feedback mechanism for the interface circuit is independent from the mechanical feedback discussed in Sec. 7.3.1.3, as it only ensures that the transducer force is set to the desired value. Hence, this electrical feedback mechanism can be of interest in both an open-loop or closed-loop mechanical control context.

7.3.2.3 Multiple-shot energy transfer

Finally, considering our original electrical interface of Sec. 7.1.3 that is depicted in Fig. 7.4, one can easily show that it is advantageous in terms of reducing the ohmic losses to transfer energy from V_{res} to $C_{\pm}$ (and conversely) by breaking down the transfer into several smaller transfers. In [BKG17], we have already used this technique of "multiple-shot" energy transfer to design energy-extracting interfaces for charge-pump conditioning circuits. These energy-extracting interfaces have similar topology and similar high-voltage requirements to those of the electrical interface of our near-limits VEH architecture.

7.3.3 Mechanical structures

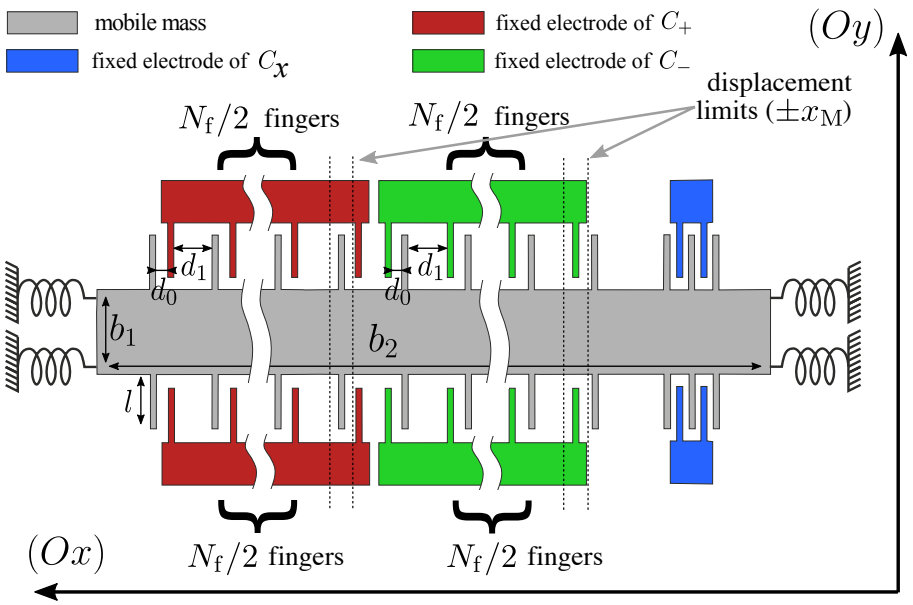

Figure 7.13: Top-view schematic of an interdigitated differential transducer geometry for electrostatic near-limits VEH.

In the presentation of the architecture done in Sec. 7.1, we did not mention a specific mechanical structure for our near-limits VEH. We only required that the corresponding transducer has a differential gap-closing geometry. We nevertheless parametrized a possible structure in Sec. 7.2.1.1, loosely based on the device fabricated by Miao *et al.* and reported in [MMH06]. It is also depicted in Fig. 1.27 of the introduction chapter. Let us give here an example of a different structure that could be used instead, and give advantages and drawbacks.

The starting point for our example is similar to the interdigitated structure presented in Sec. 1.24, used in the experiments done in Chap. 4 and 5. Now, this latter structure has a

geometrical gap-closing geometry, but we need a differential transducer structure. Therefore, we propose the structure depicted in Fig. 7.13.

The structure depicted in Fig. 7.13 allows for generating forces of both orientations on the (Ox) axis on the inertial mass. The green transducer generates positively oriented forces, while the red transducer is used for negatively oriented forces. With the notations of the present chapter, the red transducer is C_+ and the green transducer is C_-. We have also represented an additional symmetrical gap-closing transducer C_x in blue, which is used for monitoring the mass' position and speed, through a readout circuit.

The major drawback of this architecture is that when generating a force of positive sign, a parasitic force of negative sign will be generated, and conversely. This is because the consecutive pairs of digits (or fingers) of each transducer are separated by a gap d_1, so that they also form an electrostatic transducer with the next pair of digit. The capacitance versus displacement function for $C_\pm$ reads

$$C_\pm(x) = \kappa d_0 \left(\frac{1}{1 \mp x} + \frac{1}{d(1 \pm d^{-1}x)} \right) \tag{7.25}$$

where we have introduced $d \coloneqq d_1/d_0$. In the equation above, $\kappa \coloneqq \varepsilon_0 S/{d_0}^2$. The transducer surface S has the expression $N_\mathrm{f} l h_\mathrm{f}$ where N_f is the number of fingers of each transducer, l their length (see Fig. 7.13), and h_f is the height of the structure. The generated force reads

$$u_\pm(x) = \frac{1}{2}\kappa {V_\pm}^2 \left(\frac{1}{(1 \mp x)^2} \quad \underbrace{-\frac{1}{d^2(1 \pm d^{-1}x)^2}}_{\text{parasitic force component } u_\pm^\mathrm{p}} \right) \tag{7.26}$$

The parasitic force component is obviously non-desirable, because it increases the energy that has to be invested from C_res to effectively implement a force of desired value. Increasing the invested energy, in turn, results in increased losses in the interface circuit, and thus in increased control generation cost.

The relation (7.26) shows that the parasitic component of the force decreases relatively to the useful component by increasing d. Hence, the parasitic force component can be bounded as desired, and this yields a corresponding d that has to be used for our structure. At constant gap d_0, by increasing dn the device length b_2 (see Fig. 7.13) increases. To keep the maximum voltage constant, it is required that this change in length does not change the mass. Otherwise the mass would change at constant transducer surface S, and V_max would in turn increase, as (7.17) indicates. As a result, the central part has to be made thinner for its mass to remain constant, i.e., b_1 has to be reduced. Slenderizing the inertial mass in this way may pose problems related to the structure deflecting in the (Oy) direction. Indeed, the central part of the mass, of dimensions $b_1 \times b_2 \times h_\mathrm{f}$ and seen as a beam deflecting in the (Oy) direction, has a stiffness proportional to $(b_1/b_2)^3$. As the deflection of the structure following the (Oy) direction is obviously non desirable, the value of this stiffness has to be kept as high as possible. *In fine*, a trade-off between the parasitic force ratio and the ratio b_1/b_2 has to be determined.

Now, let us mention the main advantage of this structure. The expression that links the damping coefficient of an interdigitated structure such as in Fig. 7.13, to its geometrical param-

eters, reads [Bao05]

$$B_1 = 2N_{\mathrm{f}} l \frac{{h_{\mathrm{f}}}^3}{{d_0}^3} \mu_{\mathrm{air}} \tag{7.27}$$

The meaning of the geometrical parameters appearing above are clarified in Fig. 7.13. Notice that in (7.27), we have neglected the contribution of the consecutive pairs of digits separated by a gap d_1, because we assume that $d_0 \ll d_1$. This is the condition to have a small parasitic force component. For a structure with square parallel-plates as the one we have sized in the simulations of Sec. 7.2, this expression is no longer valid. But we may assume that the following inequality is verified

$$B_2 \geqslant L \frac{L^3}{{d_0}^3} \mu_{\mathrm{air}} \tag{7.28}$$

The meaning of the geometrical parameters appearing above are clarified in Fig. 7.1 in the beginning of the present chapter, where in addition we consider that $L_1 = L_2 = L$.

Considering the interdigitated structure of Fig. 7.13 at fixed structure height h_{f} and digit length l, the number of fingers N_{f} have to be chosen as

$$N_{\mathrm{f}} = \lfloor \frac{L^2}{l h_{\mathrm{f}}} \rfloor \tag{7.29}$$

for the transducer surface to be the same as for the square parallel-plate differential transducer of square side length L. It then comes that

$$B_1 < B_2 \iff h_{\mathrm{f}} < \frac{L}{\sqrt{2}}, \tag{7.30}$$

i.e., the damping effect on the interdigitated structure is reduced compared to the square parallel-plate structure, when the rightmost condition of (7.30) is enforced.

Finally, this interdigitated structure can be adapted to have triangular-shaped electrodes. Interdigitated structures with such electrode shapes are a mean to reduce the air damping effect, as shown by Lu *et al.* in [LMG17].

7.4 Conclusion and future works

In this chapter, we proposed a possible electrostatic implementation of a VEH design following the near-limits principles presented in Chap. 6. In accordance with these principles, our architecture can implement the energy maximizing trajectory $x_\xi(t)$, relying on a reduced set of hypothesis on the input excitation $\xi(t)$.

This work is thought as a starting point in the quest for optimized architectures based on the near-limits VEH principles. The results of simulation of our architecture, sized with realistic values of the electrical interface and mechanical parameters, constitutes a first proof of concept for the near-limits design principles. A figure of harvested energy that amounts to up to 10.6 µJ is attained, from a 1 s sample of vibrations recorded on a running human. This amounts to 68% of the absolute limit set by the device size and the input force. Nonetheless, it remains true that, for instance, the consumption of the parts responsible for the computation and sensing was not taken into account. But at the same time, it is important to note that these results

were obtained without a formal optimization procedure on the system's parameters.

Beyond such an optimization procedure, we gave some other routes to explore in order to improve our architecture. Some of the architecture variations presented at this occasion will necessarily have to be investigated, in particular those related to the robustness of $x_\xi(t)$ implementation. After these ways for improvements have been investigated, the next milestone would be to build a prototype of a near-limits VEH. Finally, let us mention that implementing a near-limits VEH using different transduction mechanisms, or for multiple degrees-of-freedom inertial VEHs, are also long-term objectives that are worth investigating.

General conclusion

The studies reported in this Ph.D thesis resulted in new knowledge geared towards enhancing the performances of inertial electrostatic vibration energy harvesters (e-VEHs) by improving their electrical interfaces. Rather than working on the optimization of a particular device, this work was dedicated to the building of an understanding of various electrical interfaces, paving the way for systematic e-VEH design flows. Our work was subdivided into two parts. In the first part, we focused on the study of conditioning circuits based on charge-pumps, whose main advantage is an automatic synchronization with the motion of the e-VEHs mobile mass. In the second part, a novel e-VEH architecture was proposed, that on the contrary, relies on the active synthesis of the mobile mass' dynamics.

We first presented an introduction that summarized some of the existing knowledge in the field of e-VEH (Chap. 1). Then, we reported the results of our effort to unify some state-of-the-art electrical interfaces used in e-VEHs, that all have the feature of being auto-synchronized with the electrostatic transducer's capacitance variation. We presented these electrical interfaces within a unique framework of charge-pump conditioning circuits (Chap. 2). We also completed the subfamily of unstable charge-pump conditioning circuits, by introducing a new generic topology. We gave a formal analysis and proof of operation of this generic topology (Chap. 3). Specifically, from this analysis resulted a characterization of our generic topology in terms of its γ-ratio, a sufficient parameter that characterizes any unstable charge-pump conditioning circuit within our framework. A general and complete underlying theory of charge-pump conditioning circuits in the electrical domain is yet to build. Our contribution in Chap. 2 and Chap. 3 is a starting point towards such a theory.

Next in Chap. 4, we moved on to show that our endeavor of extending the family of unstable conditioning circuits has more than a sole theoretical motivation. Indeed, the need for a wide range of different unstable charge-pump conditioning circuits was made clear by first considering a comparison in the electrical domain. This comparison also showed that the circuits of the unstable family have the advantage, over their stable counterparts, of maximizing the rate of energy conversion through their autonomous evolution, starting from an arbitrarily low initial energy amount in the circuit. Therefore, we conducted experiments to assess to what extent this property remains valid in the electromechanical domain. These experiments showed the prominent role of the electromechanical coupling on the dynamics of e-VEHs using unstable charge-pump conditioning circuits. The unstable behavior that allowed reaching arbitrarily high levels of converted power from low pre-charge was shown to be mitigated. This was clear as the tested e-VEH, which was coupled to the Bennet's doubler, exhibited a maximum power-point when submitted to harmonic input excitations.

To quantitatively link this maximum power point to the vibration input and system parameters, including the charge-pump's γ-ratio, we proposed a novel semi-analytical method based on the study of the averaged dynamics of the e-VEH. After we had presented our method and carefully outlined some of its limitations, we applied it to several cases with different input excitation characteristics, different sizings of the mechanical part, and different γ-ratios of the charge-pump. The results showed that, contrarily what was inferred from the electrical domain analysis, the pre-charge energy in the charge-pump is an important design parameter of e-VEHs using unstable conditioning circuits. The results also highlighted that, at the cost of this larger pre-charge, the unstable charge-pump conditioning circuits allow converting energy in larger amounts from frequencies that are lower than that of the e-VEH's mechanical resonator. This property can be turned into good account in order to design e-VEHs targeting lower frequency inputs, a task that is otherwise difficult considering small-scale resonant structures. Although the method as we presented it still relies on numerically solving sets of algebraic equations, we finished the chapter by mentioning future developments of our method which can ultimately lead to an analytical parameter sensitivity analysis. These developments will enable a more straightforward optimized design of e-VEHs using unstable charge-pump conditioning circuits, thus participating to the conception of a systematic e-VEH design flow.

In Chap. 5, we exposed a method of characterization for e-VEHs that are charged by an electret layer. This method allows for a simple and non-destructive measurement of the voltage source modeling the electret in electrical lumped models of e-VEHs. We gave an error-minimization procedure in order to improve the accuracy of the measurement. In particular, this procedures allows reducing the systematic measurement error due to the impact of the electromechanical coupling. We then applied the method to the characterization of an electret-charged MEMS e-VEH. In the same chapter, we presented a second method, which serves to measure the extremal capacitance variation of an e-VEH as impacted by the electromechanical coupling imposed by a charge-pump biasing scheme. This second method has still to undergo deeper experimental validation.

In the two last chapters of this manuscript, we moved to a completely different approach of e-VEH design. We settled the principles of what we called near-limits vibration energy harvesting (Chap. 6). These principles advocate for an active implementation of specific dynamics of the e-VEH's mobile mass. We have shown that these dynamics maximize the converted energy relatively to the physical limit in the case of an idealized system, and from arbitrary types of input vibrations. This approach is therefore much different than that of using charge-pump conditioning circuits in e-VEHs, which were considered precisely because of the passive synchronization with the mechanical dynamics. We identified the differences between near-limits VEH as we defined it and the formal problem of harvested energy maximization. Nevertheless, by reducing the energy cost of the implementation of the custom e-VEHs dynamics, a near-limits VEH can approach the physical upper-bound in harvested energy.

In the last chapter of the manuscript (Chap. 7), we explicitly described an architecture of e-VEH implementing the near-limits VEH principles discussed above. We thoroughly described the different constituents of the architecture, that are transducer geometry, the control law, the interface circuit and the computation and sensing part. After proper sizing using realistic models of electrical components, the system was simulated, submitted to non-harmonic vibrations recorded on the human body. The results proved the feasibility of near-limits e-VEHs. Our study

is hence a starting point towards more optimized architectures of near-limits VEHs. To this end, we gave various directions which are worth investigating in order to further make the architecture approach the limits of harvested energy. It is also worth investigating different transduction mechanisms than electrostatic to implement these principles. Finally, possible mixing of the two approaches followed in this manuscript can lead to interesting future developments. That is, we can assess in what extent e-VEHs using charge-pump conditioning circuits can implement the energy maximizing dynamics required for near-limits VEH. This may be done using a proper asynchronous control of the charge-pump's state.

In conclusion, our study contributed to assessing the role of different types of electrical interfaces in e-VEHs. We carried out the first systematic study of e-VEHs using charge-pump conditioning circuits. The results of our study give some keys to improve the operation of e-VEHs using this type of conditioning circuits. We also explored a radically different approach based on the active synthesis of the e-VEHs dynamics, opening routes for optimized e-VEH compatible with arbitrary types of input vibrations. Each of these two approaches may prove useful in different situations. Therefore, our contribution is a step towards the conception of systematic e-VEH design flows, which can draw from the results of our work and follow one of the two presented approaches depending on the application context.

List of publications

Journal articles under review

Armine Karami, Jérôme Juillard, Elena Blokhina, Philippe Basset, and Dimitri Galayko. "Electrostatic Near-Limits Kinetic Energy Harvesting". In: *IEEE Transactions Mechatronics* (Under review)

Published journal articles

Armine Karami, Dimitri Galayko, and Philippe Basset. "A Novel Characterization Method for Accurate Lumped Parameter Modeling of Electret Electrostatic Vibration Energy Harvesters". In: *IEEE Electron Device Letters* 38.5 (2017), pp. 665–668

Armine Karami, Dimitri Galayko, and Philippe Basset. "Series-Parallel Charge Pump Conditioning Circuits for Electrostatic Kinetic Energy Harvesting". In: *IEEE Transactions on Circuits and Systems I: Regular Papers* 64.1 (2017), pp. 227–240

Hakim Takhedmit, Zied Saddi, **Armine Karami**, Philippe Basset, and Laurent Cirio. "Electrostatic vibration energy harvester with 2.4-GHz Cockcroft–Walton rectenna start-up". In: *Comptes Rendus Physique* 18.2 (2017), pp. 98–106

Dimitri Galayko, Andrii Dudka, **Armine Karami**, Eoghan O'Riordan, Elena Blokhina, et al. "Capacitive Energy Conversion with Circuits Implementing a Rectangular Charge-Voltage Cycle – Part 1: Analysis of the Electrical Domain". In: *IEEE Transactions on Circuits and Systems I: Regular Papers* 62.9 (2015)

Vitaly Dorzhiev, **Armine Karami**, Philippe Basset, Frédéric Marty, Valery Dragunov, and Dimitri Galayko. "Electret-free micromachined silicon electrostatic vibration energy harvester with the Bennet's doubler as conditioning circuit". In: *IEEE Electron Device Letters* 36.2 (2015), pp. 183–185

Published conference proceedings

Armine Karami, Dimitri Galayko, Mohammed Bedier, and Philippe Basset. "Analysis and comparison of charge-pump conditioning circuits for capacitive electromechanical energy conversion". In: *Circuits and Systems (ISCAS), 2017 IEEE International Symposium on*. IEEE. 2017, pp. 1–4

Mohammed Bedier, **Armine Karami**, Dimitri Galayko, and Philippe Basset. "Autonomous energy management interface for electrostatic series-parallel charge pump vibrational energy harvester". In: *New Circuits and Systems Conference (NEWCAS), 2017 15th IEEE International*. IEEE. 2017, pp. 385–388

Zied Saddi, Hakim Takhedmit, **Armine Karami**, Philippe Basset, and Laurent Cirio. "Electrostatic Vibration Energy Harvester Pre-charged Wirelessly at 2.45 GHz". In: *Journal of Physics: Conference Series*. Vol. 773. 1. IOP Publishing. 2016, p. 012111

Armine Karami, Philippe Basset, and Dimitri Galayko. "Electrostatic vibration energy harvester using an electret-charged mems transducer with an unstable auto-synchronous conditioning circuit". In: *Journal of Physics: Conference Series* 660.1 (2015), p. 012025

Armine Karami, Andrii Dudka, Dimitri Galayko, Frédéric Marty, and Philippe Basset. "The limiting effect of electromechanical coupling in self-biased electrostatic Vibration Energy Harvester". In: *Design, Test, Integration and Packaging of MEMS/MOEMS (DTIP), 2015 Symposium on*. IEEE. 2015, pp. 1–4

Vitaly Dorzhiev, **Armine Karami**, Philippe Basset, Valery Dragunov, and Dimitri Galayko. "MEMS electrostatic vibration energy harvester without switches and inductive elements". In: *Journal of Physics: Conference Series*. Vol. 557. 1. IOP Publishing. 2014, p. 012126

Oral presentations

"*Near-limits electrostatic kinetic energy harvesting from arbitrary input vibrations*"
Presentation at the Microenergy conference, Gubbio, Italy, July 2017.

"*Smart electronic interfaces for electrostatic vibration energy harvesters*"
Seminar in Konstantin Turitsyn's group, Massachusetts Institute of Technology, Cambridge, USA, June 2017.

"*Analysis and comparison of charge-pump conditioning circuits for capacitive electromechanical energy conversion*"
Presentation at the International Symposium on Circuits and Systems, Baltimore, USA, May 2017.

"*Series-parallel charge-pump conditioning circuits for electrostatic kinetic energy harvesting*"
Presentation at the International Symposium on Circuits and Systems, Baltimore, USA, May 2017.

"*Advances in circuits and systems for electrostatic kinetic energy harvesting*"
Seminar of the system-on-chip department, computer science laboratory, Sorbonne Université, Paris, France, May 2017.

"*Characterization of the capacitance variation of electrostatic vibration energy harvesters biased following rectangular charge-voltage diagrams*"
Presentation at the 16$^{\text{th}}$ PowerMEMS Conference, Paris, France, December 2016.

"*Electrostatic vibration energy harvester using an electret-charged MEMS transducer with an unstable auto-synchronous conditioning circuit*"
Presentation at the 15$^{\text{th}}$PowerMEMS Conference, Boston, USA, December 2015.

Bibliography

[KJBew] **Armine Karami** et al. "Electrostatic Near-Limits Kinetic Energy Harvesting". In: *IEEE Transactions Mechatronics* (Under review).

[BK87] Abraham Bennet and Richard Kaye. "An Account of a Doubler of Electricity". In: *Philosophical Transactions of the Royal Society of London* 77 (1787), pp. 288–296.

[Lev60] Edwin S Levitan. "Forced Oscillation of a Spring-Mass System having Combined Coulomb and Viscous Damping". In: *the Journal of the Acoustical Society of America* 32.10 (1960), pp. 1265–1269.

[Van68] Wallace E Vander Velde. *Multiple-input describing functions and nonlinear system design*. McGraw-Hill, New York, 1968.

[Til96] Harrie AC Tilmans. "Equivalent circuit representation of electromechanical transducers: I. Lumped-parameter systems". In: *Journal of Micromechanics and Microengineering* 6.1 (1996), p. 157.

[PFC97] José-Philippe Pérez, Robert Fleckinger, and Robert Carles. *Électromagnétisme: fondements et applications: avec 300 exercices et problèmes résolus*. Masson, 1997.

[KK00] John Kuffel and Peter Kuffel. *High voltage engineering fundamentals*. Elsevier, 2000.

[MMA01] Scott Meninger et al. "Vibration-to-electric energy conversion". In: *IEEE Transactions on Very Large Scale Integration (VLSI) Syst.* 9.1 (2001), pp. 64–76.

[Kha02] H.K. Khalil. *Nonlinear Systems*. Pearson Education. Prentice Hall, 2002. ISBN: 9780130673893. URL: https://books.google.fr/books?id=t%5C_d1QgAACAAJ.

[RWR03] Shad Roundy, Paul K Wright, and Jan Rabaey. "A study of low level vibrations as a power source for wireless sensor nodes". In: *Computer communications* 26.11 (2003), pp. 1131–1144.

[RS03] Carl Johan Rydh and Bo Svärd. "Impact on global metal flows arising from the use of portable rechargeable batteries". In: *Science of the Total Environment* 302.1-3 (2003), pp. 167–184.

[MGY04] Paul D Mitcheson et al. "Architectures for vibration-driven micropower generators". In: *Journal of microelectromechanical systems* 13.3 (2004), pp. 429–440.

[MMS04] Paul D Mitcheson et al. "MEMS electrostatic micropower generator for low frequency operation". In: *Sensors and Actuators A: Physical* 115.2 (2004), pp. 523–529.

[Bad05] Adrien Badel. "Récupération d'énergie et contrôle vibratoire par éléments piézoélectriques suivant une approche non linéaire". PhD thesis. Université de Savoie, 2005.

[Bao05] Minhang Bao. *Analysis and design principles of MEMS devices*. Elsevier, 2005.

[DJJ05] Ghislain Despesse et al. "Fabrication and characterization of high damping electrostatic micro devices for vibration energy scavenging". In: *Proc. Design, Test, Integration and Packaging of MEMS and MOEMS*. 2005, pp. 386–390.

[SG05] Bernard H Stark and TC Green. "Comparison of SOI power device structures in power converters for high-voltage, low-charge electrostatic microgenerators". In: *IEEE Transactions on Electron Devices* 52.7 (2005), pp. 1640–1648.

[MMH06] P. Miao et al. "Mems inertial power generators for biomedical applications". In: *Microsystem Technologies* 12.10 (Sept. 2006), pp. 1079–1083. ISSN: 1432-1858. DOI: 10.1007/s00542-006-0152-9.

[YL06] Bernard C. Yen and Jeffrey H. Lang. "A variable-capacitance vibration-to-electric energy harvester". In: *IEEE Transactions on Circuits and Systems I: Regular Papers* 53.2 (2006), pp. 288–295. ISSN: 10577122. DOI: 10.1109/TCSI.2005.856043.

[GPB07] D. Galayko et al. "AMS modeling of controlled switch for design optimization of capacitive vibration energy harvester". In: *2007 IEEE International Behavioral Modeling and Simulation Workshop*. Sept. 2007, pp. 115–120. DOI: 10.1109/BMAS.2007.4437536.

[Sen07] Stephen D Senturia. *Microsystem design*. Springer Science & Business Media, 2007.

[AB08] Vincent Acary and Bernard Brogliato. *Numerical methods for nonsmooth dynamical systems: applications in mechanics and electronics*. Springer Science & Business Media, 2008.

[Hal08] Einar Halvorsen. "Energy harvesters driven by broadband random vibrations". In: *Journal of Micromechanics and Microengineering* 17.5 (2008), pp. 1061–1071.

[MYR08] P. D. Mitcheson et al. "Energy Harvesting From Human and Machine Motion for Wireless Electronic Devices". In: *Proceedings of the IEEE* 96.9 (Sept. 2008), pp. 1457–1486. ISSN: 0018-9219. DOI: 10.1109/JPROC.2008.927494.

[Tré08] Emmanuel Trélat. *Contrôle optimal: théorie & applications*. Vol. 865. Vuibert Paris, 2008.

[BGP09] P Basset et al. "A batch-fabricated and electret-free silicon electrostatic vibration energy harvester". In: *Journal of Micromechanics and Microengineering* 19.11 (Oct. 2009), p. 115025.

[CVG09] F Cottone, H Vocca, and L Gammaitoni. "Nonlinear energy harvesting". In: *Physical review letters* 102.8 (2009), p. 80601.

[MSK09] Daigo Miki, Yuji Suzuki, and Nobuhide Kasagi. "Effect of nonlinear external circuit on electrostatic damping force of micro electret generator". In: *2009 Transducers - 2009 15th International Conference on Solid-State Sensors, Actuators and Microsystems*. IEEE, June 2009, pp. 636–639. ISBN: 978-1-4244-4190-7. DOI: 10.1109/SENSOR.2009.5285405.

[SJ09] Jeff Scruggs and Paul Jacob. "Harvesting ocean wave energy". In: *Science* 323.5918 (2009), pp. 1176–1178.

[ABB10] Vincent Acary, Olivier Bonnefon, and Bernard Brogliato. *Nonsmooth modeling and simulation for switched circuits*. Vol. 69. Springer Science & Business Media, 2010.

[AIM10] Luigi Atzori, Antonio Iera, and Giacomo Morabito. "The internet of things: A survey". In: *Computer networks* 54.15 (2010), pp. 2787–2805.

[DSP10] Reinhilde D'hulst et al. "Power processing circuits for piezoelectric vibration-based energy harvesters". In: *IEEE Transactions on Industrial Electronics* 57.12 (2010), pp. 4170–4177.

[ERK10] R Elfrink et al. "Vacuum-packaged piezoelectric vibration energy harvesters: damping contributions and autonomy for a wireless sensor system". In: *Journal of Micromechanics and Microengineering* 20.10 (2010), p. 104001.

[JMV10] Mohamad Al Kadi Jazairli et al. "An ultra-low-power frequency-tunable UWB pulse generator using 65nm CMOS technology". In: *Ultra-Wideband (ICUWB), 2010 IEEE International Conference on*. Vol. 1. IEEE. 2010, pp. 1–4.

[MOC10] Thomas McKay et al. "Self-priming dielectric elastomer generators". In: *Smart Materials and Structures* 19.5 (2010), p. 055025.

[TR10] Erick O Torres and Gabriel A Rincón-Mora. "A 0.7-μm BiCMOS Electrostatic Energy-Harvesting System IC". In: *IEEE Journal of Solid-State Circuits* 45.2 (2010), pp. 483–496.

[DD11] Antonio Carlos M De Queiroz and Marcelo Domingues. "The doubler of electricity used as battery charger". In: *IEEE Transactions on Circuits and Systems II: Express Briefs* 58.12 (2011), pp. 797–801. ISSN: 15497747. DOI: 10.1109/TCSII.2011.2173963.

[Suz11] Yuji Suzuki. "Recent progress in MEMS electret generator for energy harvesting". In: *IEEJ Transactions on Electrical and Electronic Engineering* 6.2 (2011), pp. 101–111. ISSN: 19314973. DOI: 10.1002/tee.20631.

[BGH12] Elena Blokhina et al. "Limit on converted power in resonant electrostatic vibration energy harvesters". In: *Applied Physics Letters* 101.17 (2012), p. 173904.

[GBA12] Carmina Georgescu, Bernard Brogliato, and Vincent Acary. "Switching, relay and complementarity systems: A tutorial on their well-posedness and relationships". In: *Physica D: Nonlinear Phenomena* 241.22 (2012), pp. 1985–2002.

[Gui12] Raphaël Guillemet. "Etude et réalisation d'un récupérateur d'énergie vibratoire par transduction électrostatique en technologie MEMS silicium". PhD thesis. Université Paris-Est, 2012.

[KBH12] Asantha Kempitiya, D-A Borca-Tasciuc, and Mona Mostafa Hella. "Analysis and optimization of asynchronously controlled electrostatic energy harvesters". In: *IEEE Transactions on Industrial Electronics* 59.1 (2012), pp. 456–463.

[Kir12] Donald E Kirk. *Optimal control theory: an introduction*. Courier Corporation, 2012.

[MG12] Paul D Mitcheson and Tim C Green. "Maximum effectiveness of electrostatic energy harvesters when coupled to interface circuits". In: *IEEE Transactions on Circuits and Systems I: Regular Papers* 59.12 (2012), pp. 3098–3111.

[BO13] Carl M Bender and Steven A Orszag. *Advanced mathematical methods for scientists and engineers I: Asymptotic methods and perturbation theory*. Springer Science & Business Media, 2013.

[BGB13] Elena Blokhina et al. "Steady-State Oscillations in Resonant Electrostatic Vibration Energy Harvesters". In: *IEEE Transactions on Circuits and Systems I: Regular Papers* 60.4 (Apr. 2013), pp. 875–884. ISSN: 1549-8328. DOI: 10.1109/TCSI.2012.2209295.

[BCD13] S Boisseau et al. "Stable DRIE-patterned SiO 2/Si 3 N 4 electrets". In: *2013 Transducers & Eurosensors XXVII: The 17th International Conference on Solid-State Sensors, Actuators and Microsystems (TRANSDUCERS & EUROSENSORS XXVII)*. IEEE. 2013, pp. 1942–1945.

[DST13] Eddy Dascotte, Jacques Strobbe, and Ulf T Tygesen. "Continuous stress monitoring of large structures". In: *Proceeding of 5th International Operational Modal Analysis Conference, Portugal*. 2013.

[Det13] Martin Deterre. "Toward an energy harvester for leadless pacemakers". PhD thesis. Paris 11, 2013.

[DD13] V Dragunov and V Dorzhiev. "Electrostatic vibration energy harvester with increased charging current". In: *Journal of Physics: Conference Series*. Vol. 476. 1. IOP Publishing. 2013, p. 012115.

[GBB13] Dimitri Galayko et al. "Tools for analytical and numerical analysis of electrostatic vibration energy harvesters: Application to a continuous mode conditioning circuit". In: *Journal of Physics: Conference Series*. Vol. 476. 1. IOP Publishing. 2013, p. 012076.

[GAW13] P. Gasnier et al. "An ultra low power maximum voltage detector for piezoelectric and electrostatic energy harvesters". In: *2013 IEEE 11th International New Circuits and Systems Conference (NEWCAS)*. June 2013, pp. 1–4. DOI: 10.1109/NEWCAS.2013.6573613.

[GH13] John Guckenheimer and Philip Holmes. *Nonlinear oscillations, dynamical systems, and bifurcations of vector fields*. Vol. 42. Springer Science & Business Media, 2013.

[Hal13] Einar Halvorsen. "Fundamental issues in nonlinear wideband-vibration energy harvesting". In: *Physical Review E* 87.4 (2013), p. 042129.

[HLM13] E Halvorsen et al. "Architecture-independent power bound for vibration energy harvesters". In: *Journal of Physics: Conference Series*. Vol. 476. 1. IOP Publishing. 2013, p. 012026.

[KBH13] A. Kempitiya, D. A. Borca-Tasciuc, and M. M. Hella. "Low-Power ASIC for Microwatt Electrostatic Energy Harvesters". In: *IEEE Transactions on Industrial Electronics* 60.12 (Dec. 2013), pp. 5639–5647. ISSN: 0278-0046. DOI: 10.1109/TIE.2012.2230891.

[NHP13] Son D Nguyen, Einar Halvorsen, and Igor Paprotny. "Bistable springs for wideband microelectromechanical energy harvesters". In: *Applied Physics Letters* 102.2 (2013), p. 023904.

[RAG13] M Renaud et al. “A high performance electrostatic MEMS vibration energy harvester with corrugated inorganic SiO 2-Si 3 N 4 electret”. In: *Solid-State Sensors, Actuators and Microsystems (TRANSDUCERS & EUROSENSORS XXVII), 2013 Transducers & Eurosensors XXVII: The 17th International Conference on*. IEEE. 2013, pp. 693–696.

[Son13] Eduardo D Sontag. *Mathematical control theory: deterministic finite dimensional systems*. Vol. 6. Springer Science & Business Media, 2013.

[BGC14] P Basset et al. “Electrostatic vibration energy harvester with combined effect of electrical nonlinearities and mechanical impact”. In: *Journal of Micromechanics and Microengineering* 24.3 (2014), p. 035001.

[CBM14] Francesco Cottone et al. “Electrostatic generator with free micro-ball and elastic stoppers for low-frequency vibration harvesting”. In: *Micro Electro Mechanical Systems (MEMS), 2014 IEEE 27th International Conference on*. IEEE. 2014, pp. 385–388.

[DME14] Mohammed F Daqaq et al. “On the role of nonlinearities in vibratory energy harvesting: a critical review and discussion”. In: *Applied Mechanics Reviews* 66.4 (2014), p. 040801.

[DKB14] Vitaly Dorzhiev et al. “MEMS electrostatic vibration energy harvester without switches and inductive elements”. In: *Journal of Physics: Conference Series*. Vol. 557. 1. IOP Publishing. 2014, p. 012126.

[Dud14] Andrii Dudka. “etude, optimisation et implémentation en silicium du circuit de conditionnement intelligent haute-tension pour le système de récupération électrostatique d’énergie vibratoire”. PhD thesis. Paris 6, 2014.

[LRW14] E Lefeuvre et al. “Self-Biased Inductor-less Interface Circuit for Electret-Free Electrostatic Energy Harvesters”. In: *Journal of Physics: Conference Series*. Vol. 557. 2014, p. 012052.

[Que14] Antonio Carlos M. de Queiroz. “Electrostatic energy harvesting without active control circuits”. In: *2014 IEEE 5th Latin American Symposium on Circuits and Systems* (2014), pp. 1–4. DOI: 10.1109/LASCAS.2014.6820274.

[VC14] Helios Vocca and Francesco Cottone. “Kinetic energy harvesting”. In: *ICT-Energy-Concepts Towards Zero-Power Information and Communication Technology*. InTech, 2014.

[14] *WE-PD HV SMD Power Inductor*. 7687779102. Rev. 1.2. Wurth Electronics. June 2014.

[BT15] Loïc Bourdin and Emmanuel Trélat. “Optimal sampled-data control, and generalizations on time scales”. In: *arXiv preprint arXiv:1501.07361* (2015).

[DKB15] Vitaly Dorzhiev et al. “Electret-free micromachined silicon electrostatic vibration energy harvester with the Bennet’s doubler as conditioning circuit”. In: *IEEE Electron Device Letters* 36.2 (2015), pp. 183–185.

[GDK15] Dimitri Galayko et al. “Capacitive Energy Conversion with Circuits Implementing a Rectangular Charge-Voltage Cycle – Part 1: Analysis of the Electrical Domain”. In: *IEEE Transactions on Circuits and Systems I: Regular Papers* 62.9 (2015).

[HT15a] Ashkan Haji Hosseinloo and Konstantin Turitsyn. "Fundamental limits to nonlinear energy harvesting". In: *Physical Review Applied* 4.6 (2015), p. 064009.

[HT15b] Ashkan Haji Hosseinloo and Konstantin Turitsyn. "Non-resonant energy harvesting via an adaptive bistable potential". In: *Smart Materials and Structures* 25.1 (2015), p. 015010.

[Jui15] Jérôme Juillard. "Analysis of resonant pull-in of micro-electromechanical oscillators". In: *Journal of Sound and Vibration* 350 (2015), pp. 123–139.

[JJO15] Wanyeong Jung et al. "27.6 A 0.7 pF-to-10nF fully digital capacitance-to-digital converter using iterative delay-chain discharge". In: *Solid-State Circuits Conference-(ISSCC), 2015 IEEE International*. IEEE. 2015, pp. 1–3.

[KBG15] **Armine Karami**, Philippe Basset, and Dimitri Galayko. "Electrostatic vibration energy harvester using an electret-charged mems transducer with an unstable auto-synchronous conditioning circuit". In: *Journal of Physics: Conference Series* 660.1 (2015), p. 012025.

[KDG15] **Armine Karami** et al. "The limiting effect of electromechanical coupling in self-biased electrostatic Vibration Energy Harvester". In: *Design, Test, Integration and Packaging of MEMS/MOEMS (DTIP), 2015 Symposium on*. IEEE. 2015, pp. 1–4.

[KHS15] Sukhdeep Kaur et al. "Characterization and modeling of nonlinearities in in-plane gap closing electrostatic energy harvester". In: *Journal of Microelectromechanical Systems* 24.6 (2015), pp. 2071–2082.

[RAE15] M Renaud et al. "Modeling and characterization of electret based vibration energy harvesters in slot-effect configuration". In: *Smart Materials and Structures* 24.8 (July 2015), p. 085023.

[SLN15] Stefano Stanzione et al. "20.8 A 500nW batteryless integrated electrostatic energy harvester interface based on a DC-DC converter with 60V maximum input voltage and operating from 1μW available power, including MPPT and cold start". In: *Solid-State Circuits Conference-(ISSCC), 2015 IEEE International*. IEEE. 2015, pp. 1–3.

[TLH15] B. D. Truong, C. P. Le, and E. Halvorsen. "Experimentally verified model of electrostatic energy harvester with internal impacts". In: *2015 28th IEEE International Conference on Micro Electro Mechanical Systems (MEMS)*. Jan. 2015, pp. 1125–1128. DOI: 10.1109/MEMSYS.2015.7051162.

[15] *Ultra-Low Power, Ultra-Small Size, 12-Bit, 1-MSPS, SAR ADC*. ADS7042. Rev. C. Texas Instruments. Dec. 2015.

[BBG16] Philippe Basset, Elena Blokhina, and Dimitri Galayko. *Electrostatic kinetic energy harvesting*. John Wiley & Sons, 2016.

[HR16] John D Heit and Shad Roundy. "A framework to determine the upper bound on extractable power as a function of input vibration parameters". In: *Energy Harvesting and Systems* 3.1 (2016), pp. 69–78.

[KGB16] **Armine Karami**, Dimitri Galayko, and Philippe Basset. "Characterization of the capacitance variation of electrostatic vibration energy harvesters biased following rectangular charge-voltage diagrams". In: *Journal of Physics: Conference Series*. Vol. 773. 1. IOP Publishing. 2016, p. 012015.

[LOC16] Y Lu et al. “A batch-fabricated electret-biased wideband MEMS vibration energy harvester with frequency-up conversion behavior powering a UHF wireless sensor node”. In: *Journal of Micromechanics and Microengineering* 26.12 (Sept. 2016), p. 124004.

[OGB16] Eoghan O’Riordan et al. “Complete electromechanical analysis of electrostatic kinetic energy harvesters biased with a continuous conditioning circuit”. In: *Sensors and Actuators A: Physical* 247 (2016), pp. 379–388.

[QO16] A. C. M. de Queiroz and L. C. M. de Oliveira Filho. “Energy harvesting with 3D-printed electrostatic generators”. In: *2016 IEEE 7th Latin American Symposium on Circuits Systems (LASCAS)*. Feb. 2016, pp. 127–130. DOI: 10.1109/LASCAS.2016.7451026.

[STK16] Zied Saddi et al. “Electrostatic Vibration Energy Harvester Pre-charged Wirelessly at 2.45 GHz”. In: *Journal of Physics: Conference Series*. Vol. 773. 1. IOP Publishing. 2016, p. 012111.

[TLH16] Binh Duc Truong, Cuong Phu Le, and Einar Halvorsen. “Power optimization and effective stiffness for a vibration energy harvester with displacement constraints”. In: *Journal of Micromechanics and Microengineering* 26.12 (2016), p. 124006.

[UJM16] Gilberto A Urzúa et al. “Radiative effects and the missing energy paradox in the ideal two capacitors problem”. In: *Journal of Physics: Conference Series*. Vol. 720. 1. IOP Publishing. 2016, p. 012054.

[WLM16] J Wei et al. “Interface circuit with adjustable bias voltage enabling maximum power point tracking of capacitive energy harvesting devices”. In: *Journal of Micromechanics and Microengineering* 26.12 (2016), p. 124008.

[BKG17] Mohammed Bedier et al. “Autonomous energy management interface for electrostatic series-parallel charge pump vibrational energy harvester”. In: *New Circuits and Systems Conference (NEWCAS), 2017 15th IEEE International*. IEEE. 2017, pp. 385–388.

[BT17] Loïc Bourdin and Emmanuel Trélat. “Linear–quadratic optimal sampled-data control problems: Convergence result and Riccati theory”. In: *Automatica* 79 (2017), pp. 273–281.

[Gei17] Matthias Geisler. “Récupération d’énergie mécanique pour vêtements connectés autonomes”. PhD thesis. Université Grenoble Alpes, 2017.

[ITK17] Patrin Illenberger et al. “A Mathematical Model for Self-Priming Circuits: Getting the Most From a Dielectric Elastomer Generator”. In: *IEEE Transactions on Power Electronics* 32.9 (2017), pp. 6904–6912.

[KGB17a] **Armine Karami**, Dimitri Galayko, and Philippe Basset. “A Novel Characterization Method for Accurate Lumped Parameter Modeling of Electret Electrostatic Vibration Energy Harvesters”. In: *IEEE Electron Device Letters* 38.5 (2017), pp. 665–668.

[KGB17b] **Armine Karami**, Dimitri Galayko, and Philippe Basset. “Series-Parallel Charge Pump Conditioning Circuits for Electrostatic Kinetic Energy Harvesting”. In: *IEEE Transactions on Circuits and Systems I: Regular Papers* 64.1 (2017), pp. 227–240.

[KGB17c] **Armine Karami** et al. "Analysis and comparison of charge-pump conditioning circuits for capacitive electromechanical energy conversion". In: *Circuits and Systems (ISCAS), 2017 IEEE International Symposium on*. IEEE. 2017, pp. 1–4.

[KMH17] Hideaki Koga et al. "Development of a cantilever-type electrostatic energy harvester and its charging characteristics on a highway viaduct". In: *Micromachines* 8.10 (2017), p. 293.

[LH17] Cuong Phu Le and Einar Halvorsen. "Equivalent-circuit models for electret-based vibration energy harvesters". In: *Smart Materials and Structures* 26.8 (2017), p. 085042.

[LHG17] Yingxian Lu et al. "Bennet's Doubler Working as a Power Booster for Triboelectric Nano Generators". In: *Electronics Letters* (2017).

[LMG17] Y Lu et al. "New comb geometry of capacitive vibration energy harvesters miniaturizing the air damping effect". In: *Micro Electro Mechanical Systems (MEMS), 2017 IEEE 30th International Conference on*. IEEE. 2017, pp. 857–860.

[17] *MEMS digital output motion sensor: high-performance ultra-low-power 3-axis femto accelerometer*. LIS2DW12. Rev. 4. STMicroelectronics. 2017.

[TSK17] Hakim Takhedmit et al. "Electrostatic vibration energy harvester with 2.4-GHz Cockcroft–Walton rectenna start-up". In: *Comptes Rendus Physique* 18.2 (2017), pp. 98–106.

[TWT17] Kai Tao et al. "Enhanced electrostatic vibrational energy harvesting using integrated opposite-charged electrets". In: *Journal of Micromechanics and Microengineering* 27.4 (2017), p. 044002.